

PH.D. DISSERTATION



**UNIVERSIDAD
DE GRANADA**

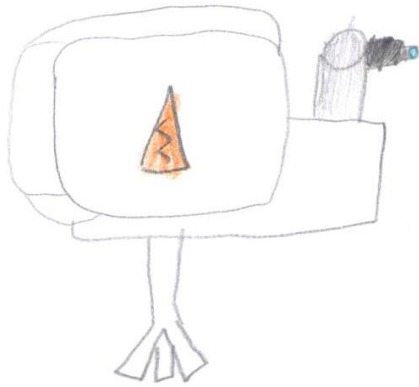
Programa de Doctorado en Física y Ciencias del
Espacio

ATMOSPHERIC PROFILING BASED ON AEROSOL AND DOPPLER LIDAR

Pablo Ortiz Amezcuca



Editor: Universidad de Granada. Tesis Doctorales
Autor: Pablo Ortiz Amezcua
ISBN: 978-84-1306-353-9
URI: <http://hdl.handle.net/10481/57771>



*To my family
To my friends
To my wife*

CONTENTS

ABSTRACT	13
RESUMEN	21
PART I: BASIS AND INSTRUMENTAL WORK	29
I INTRODUCTION AND OBJECTIVES	31
II FUNDAMENTALS	37
2.1 Atmospheric boundary layer and turbulence	37
2.2 Atmospheric aerosol	41
2.2.1 Aerosol microphysical properties.....	44
2.2.2 Aerosol optical properties.....	47
2.3 Remote sensing	51
2.3.1 Active remote sensing of aerosols: elastic and Raman lidar technique.....	55
2.3.2 Active remote sensing of wind: Doppler lidar.....	58
III EXPERIMENTAL SITE AND INSTRUMENTATION.....	63
3.1 Elastic-raman lidar system	66
3.2 Doppler lidar system.....	69
3.3 Ancillary instrumentation and modelling tools.....	71
3.3.1 Ceilometer	71
3.3.2 Sun/sky/lunar-photometer.....	72
3.3.3 Star-photometer.....	73
3.3.4 CALIOP lidar onboard CALIPSO satellite	74
3.3.5 HYSPLIT model.....	74
3.4 Implementation of rotational raman channels to improve aerosol retrievals	75
3.4.1 Instrumental modification	77

3.4.2	Systematic error due to temperature dependence ..	79
3.4.3	Elastic crosstalk avoidance	80
3.4.4	Test cases	81
3.5	Calibration of the doppler lidar signal	86
3.5.1	Background correction	87
3.5.2	Focus correction	89
3.6	Conclusions.....	96

PART II: AEROSOL OPTICAL AND MICROPHYSICAL PROFILING
..... 99

IV INVERSIONS USING SPHERICAL APPROXIMATION.....105

4.1 Hybrid regularization algorithm. UP software.....106

4.2 Microphysical characterization of long-range transported biomass burning particles from North America..111

4.2.1 Experimental sites and instrumentation.....113

4.2.2 Methodology.....115

4.2.3 Results I: Characterization of sources and transport of the smoke plumes

4.2.4 Results II: Optical properties

4.2.5 Results III: Microphysical properties

4.3 Improving Raman lidar aerosol microphysical retrievals with star- and lunar-photometry

4.3.1 Sensitivity study

4.3.2 Experimental cases.....

4.4 Summary and conclusions.....

V INVERSIONS FOR NON-SPHERICAL PARTICLES

5.1 SphInX software

5.2 Example cases.....

5.2.1 Case I: 18th May 2016.....

5.2.2	Case II: 9 th June 2016	175
5.3	Summary and Conclusions.....	185
PART III: WIND AND TURBULENCE PROFILING		187
VI	CHARACTERIZATION OF THE ATMOSPHERIC BOUNDARY LAYER WITH DOPPLER LIDAR.....	189
6.1	Wind retrieval and ABL classification	191
6.1.1	Wind vector field retrieval	191
6.1.2	ABL classification with Halo lidar toolbox.....	196
6.2	Statistical characterization of horizontal wind field over Granada	201
6.2.1	Methodology and data availability	201
6.2.2	Results	205
6.3	Characterization of the ABL turbulent sources over three sites	211
6.3.1	Methodology	212
6.3.2	Additional experimental sites: AMAPOLA and POLIMOS campaigns	212
6.3.3	Results	214
6.4	Conclusions and future work	224
PART IV: CONCLUSIONS		227
VII	CONCLUSIONS AND OUTLOOK.....	229
	CONCLUSIONES Y PERSPECTIVAS	235
	APPENDIX.....	243
	LIST OF SYMBOLS AND ABBREVIATIONS.....	255
	ACKNOWLEDGEMENTS	261
	REFERENCES	265

ABSTRACT

The observation and study of the Earth's atmosphere have become of increasing concern because of the interest on weather prediction, air quality and climate change. Among all the atmospheric components and processes related to those topics, atmospheric aerosol particles (defined as solid and/or liquid particles suspended on the atmospheric air, excluding clouds) and the dynamic and turbulent properties of the atmospheric boundary layer (ABL, the lowermost part of the atmosphere, that is directly influenced by the Earth's surface) represent two of the most active research fields due to the lack of knowledge about the uncertainties of their effects. Lidar (Light detection and ranging) is a key technique in atmospheric research because it provides atmospheric information with high spatial and temporal resolution.

In this context, this thesis is the result of an effort of compiling, understanding and applying some of the most recent lidar techniques in the field of atmospheric profiling. The work done to this end includes instrumental set up, calibration and improvement, regular measurements and several field campaigns, algorithm development, knowledge of several specific and complex software and application to the analysis and interpretation of a variety of atmospheric situations.

The experimental work is based on the use of two different lidar systems, namely a Raman lidar and a Doppler lidar. Some ancillary tools have also been used, as co-located ceilometer and photometers, simultaneous satellite-based lidar and HYSPLIT (Hybrid Single-Particle Lagrangian Integrated Trajectory) backward-trajectory model. The instrumentation is located at the UGR station in the city of Granada (southeastern Spain, 680 m above sea level, a.s.l.) and in Cerro Poyos station (1830 m a.s.l.) as ancillary mountain station at close distance for certain studies. They are part of the experimental observatory AGORA (Andalusian Global Observatory of the Atmosphere), included in ACTRIS (Aerosol, Clouds and Trace Gases Research Infrastructure) that is in the way to be constituted as a permanent European Research Infrastructure Consortium (ERIC). An important part of the measurements were taken in the framework of SLOPE I (Sierra Nevada Lidar Aerosol Profiling Experiment I) campaign. This thesis includes lidar measurements from two additional rural sites, an olive orchard in Úbeda (Spain) and a peatland in Rzecin (Poland), gathered respectively during AMAPOLA (Atmospheric Monitoring of Aerosol Particle Fluxes in Olive Orchard) and POLIMOS-2018 (Polish Radar and Lidar Mobile Observation System 2018) field campaigns.

The multiwavelength Raman lidar system MULHACEN is used to retrieve vertical profiles of aerosol particle optical and microphysical properties. It emits pulsed laser radiation at 355, 532 and 1064 nm wavelengths and collects the elastic and inelastic backward-scattered radiation, also with depolarization capabilities. This spectral and polarization information is useful for retrieving size and shape properties of the aerosol particles and as an indicator of the aerosol type. The system is part of EARLINET (European Aerosol Research Lidar Network) in the frame of ACTRIS activities.

The Raman radiation collected by MULHACEN corresponds to changes in the vibrational energy states of molecules, a widely used effect in aerosol Raman lidars although it has the disadvantage of a low Signal-to-Noise Ratio (SNR) that usually

limits the retrievals to nocturnal measurements with 30-60 min time resolution. We have implemented a new setup in the UV of MULHACEN system in order to measure Raman lines corresponding to rotational energy states, enhancing the measured signal and diminishing the wavelength shift between elastic and Raman radiation (a key point for diminishing uncertainties due to spectral dependence). The rotational lines have some issues related to temperature dependence, but we demonstrate that, with an appropriate filter wavelength selection, this accounts for an additional uncertainty of less than 4 % on the retrieved aerosol optical properties. With this new setup, we have been able to retrieve aerosol extinction and backscatter coefficients profiles with 1-h time resolution during daytime and up to 1-min time resolution during nighttime. Nevertheless, this study has an exploratory nature within this thesis and the database used in the rest of the sections corresponds to the extended vibrational Raman measurements previously obtained.

The Doppler lidar system Stream Line emits pulsed infrared radiation at 1500 nm and measures the Doppler frequency shift in the backscattered radiation due to the aerosol particles movement with wind. This instrument is used for the first time at UGR station, and we have set it up to retrieve vertical profiles of wind field within the ABL and its turbulent properties. Thanks to this, the instrument has become part of Cloudnet in the frame of ACTRIS activities.

The signal measured by the Doppler lidar is optimized for directly obtaining radial velocities, but the the signal intensity presents some artifacts that have to be corrected if this signal is to be used for further purposes. We have applied a correction algorithm developed at the Finnish Meteorological Institute (FMI), in the frame of ACTRIS, to correct for two kind of artifacts affecting background subtraction, specifically certain range-independent step changes with time and time-independent residual structures at different altitudes. A third issue is the signal magnification around certain range and reduction at higher ranges due to the instrument optical

system focal length, set at that range. We have proposed in collaboration with FMI a methodology to calculate experimental focal length and lens diameter as calibration parameters for our Doppler lidar. It consists of an iterative method based on comparing the Doppler lidar corrected signal with a co-located ceilometer (that needs no focus correction), and we have obtained the calibration parameters for our system with less than 20 % standard deviation. The corrected signal allows for estimating more advanced quantities as velocity errors and attenuated backscatter.

The vertical profiles of aerosol optical and microphysical properties have been retrieved with several inversion algorithms from Raman lidar measurements. The starting point is the retrieval of particle backscatter and extinction coefficients at three wavelengths, and their derived intensive particle properties, by using Klett-Fernald method or Raman methods for elastic or inelastic signals, respectively, and depolarization method for polarization measurements. Our work is then focused on employing the set of optical properties to obtain more complex particle optical and microphysical properties (i.e., particle volume concentration, effective radius, complex refractive index and single scattering albedo) using a regularization algorithm.

In particular, two different software tools developed at the University of Potsdam (Germany) have been used. The first software, called here UP, is built upon Mie model for spherical particles and can be used for forward or inverse calculations using simulated or measured inputs. The inversion algorithm is a hybrid regularization method based on explicitly solving the mathematical equations that relate the particle microphysical and optical properties according to the spherical model, obtaining the particle size distribution as output. The second software is called SphInX (Spheroidal Inversion Experiments) and is based on an extension of Mie model in two dimensions in order to account for non-spherical particles by assuming an ensemble of spheroids characterized by their volume-equivalent radius and aspect ratio. The regularization methods

are similar to the one in UP, but SphInX uses a precalculated database for the calculation of the kernel equations for certain cases, due to the higher complexity of the model. An additional difference between the two tools is that depolarization measurements are only input for SphInX software, because UP assumes no depolarization by spherical particles.

We have applied UP software for the characterization of long-range transported biomass burning particles from strong plumes that were detected during July 2013 at Granada and two more ACTRIS-EARLINET stations, namely Leipzig (Germany) and Warsaw (Poland). A deep analysis on the sources and transport paths of the particles has been performed using satellite observations and modelling tools, confirming the arrival of the smoke plumes to the studied stations several days after being emitted from forest fires in North America. The observed optical and microphysical properties correspond then to aged smoke particles and reveal their small and mostly spherical shape with weak absorption.

SphInX software has also been used for the study of different types of transported aerosol particles. A first case with biomass burning particles has been selected in order to compare with UP software and assess for the impact of the additional depolarization measurement and the extended 2D model for particles. The second selected case corresponds to mineral dust particles from Sahara desert as well-known large and non-spherical aerosol type. The limited size range of the precalculated SphInX database due to lidar measured wavelengths has limited the application of this software to the submicrometric and micrometric part of the distribution, but the rest of the microphysical properties agree with the literature, with the added value of detailed information on particle shape according to spheroidal model.

The minimum requirement to retrieve particle properties from multiwavelength Raman lidar systems with UP or SphInX software tools is to have 3 particle backscatter coefficient (at 355, 532 and 1064 nm) profiles and 2 particle extinction

coefficient (at 355 and 532 nm) profiles (plus a particle depolarization profile in case of SphInX retrievals). Since this is not always the case, but global aerosol networks need as many and complete measurements as possible, we have proposed a methodology for systems with one missing channel. It is based on using spectral measurements from co-located star- or lunar-photometer to reproduce the missing profile, using Angström equation. This methodology can be applied using both UP and SphInX tools, although the results here refer only to UP.

The proposed methodology has been tested with a sensitivity study in order to assess for the additional errors introduced in the microphysical retrievals. We have used UP software in forward mode to simulate different aerosol cases in terms of size distributions and complex refractive indices, and the suggested method has been applied for three different scenarios (according to the lidar channel that is missing). The same scenarios have been used for applying the methodology to real data measured with MULHACEN lidar at UGR station. All the results from simulated and real cases have been compared with the retrievals using the complete lidar setup without photometer information. Maximum deviations of 20 % have been found for simulated cases with an input error of 5 %, and deviations less than 40 % for real cases with input errors up to 40 %.

The vertical profiles of wind field and turbulent properties within the ABL have been retrieved from vertical and scanning Doppler lidar measurements using several linked algorithms. We have used a software processing chain, the Halo lidar toolbox developed at the FMI, that includes the most recent methodologies to calculate vertical profiles of horizontal wind field and turbulent properties (namely vertical velocity statistical moments, wind shear and turbulent kinetic energy dissipation rate). The chain culminates with the combination of all the retrieved information to create a classification mask of the turbulence sources with temporal and vertical resolution within the ABL.

We have used the horizontal wind product of the Halo lidar toolbox to carry out a statistical study over Granada using a two-year database of regular measurements. The data availability in terms of maximum analyzed altitudes for statistically significant results is limited to around 1000-1500 m above ground level (a.g.l.) due to the decreasing signal intensity with height that also depends on aerosol load. We have analyzed the differences and similarities in the diurnal evolution of the vertical wind profiles for different seasons, and diurnal and nocturnal wind roses have also been calculated for the whole dataset at three altitude intervals.

Finally, we have studied the turbulent properties of the ABL with the corresponding Halo lidar toolbox products. We have evaluated the diurnal development of the ABL for two days from AMAPOLA campaign, one with clear-sky conditions and the other with clouds, observing their effect on the lower altitude reached by the ABL and on the top-down turbulent movements. For Granada and Rzecin sites, where the available databases were of two years and four months, respectively, we have been able to perform a statistical analysis of the main turbulent sources within those analyzed periods, with temporal (for each hour of the day) and height resolution. A seasonal distinction has been done only for Granada. Both sites show a clear convective activity during daytime at altitudes increasing with time, and a significant wind-shear driven turbulence during nighttime, in special in Rzecin. We have also found at both sites an important contribution of nocturnal turbulence with unknown sources (labelled as 'intermittent') although in Rzecin it is mostly concentrated around 600 m a.g.l., while in Granada it is present at all heights.

RESUMEN

La observación y estudio de la atmósfera terrestre se han convertido en motivo de creciente preocupación debido al interés en la predicción meteorológica, la calidad del aire y el cambio climático. Entre los componentes y procesos atmosféricos relacionados con esos temas, el aerosol atmosférico (definido como la suspensión de partículas sólidas y/o líquidas en el aire atmosférico, excluyendo las nubes) y las propiedades dinámicas y turbulentas de la capa límite atmosférica (en inglés, *atmospheric boundary layer*, ABL, la capa más baja de la atmósfera, que está directamente influenciada por la superficie terrestre) representan dos de los campos de estudio más activos debido a la falta de conocimiento sobre las incertidumbres de sus efectos. Lidar (Light detection and ranging) es una técnica clave en investigación atmosférica, ya que proporciona información atmosférica con gran resolución espacial y temporal.

En este contexto, esta tesis es el resultado de un esfuerzo por compilar, comprender y aplicar algunas de las técnicas lidar más recientes en el campo del perfilado atmosférico. Para este fin, se ha realizado un trabajo que incluye instalación, calibración y mejoras de instrumentos, realización de medidas regulares y participación en campañas de campo, desarrollo de algoritmos, conocimiento de varios programas específicos y

complejos, y su aplicación al análisis e interpretación de situaciones atmosféricas variadas.

El trabajo experimental se basa en el uso de dos sistemas lidar distintos, un lidar Raman y un lidar Doppler. También se han empleado algunas herramientas auxiliares, como ceilómetro y fotómetros próximos, lidar a bordo de satélite y el modelo de retrotrayectorias HYSPLIT (Hybrid Single-Particle Lagrangian Integrated Trajectory). La instrumentación se encuentra en la estación UGR en la ciudad de Granada (al sudeste de España, 680 m sobre el nivel del mar, s.n.m.) y la estación de Cerro Poyos (1830 m s.n.m.) como estación auxiliar de montaña para algunos estudios. Estas estaciones son parte del observatorio AGORA (Andalusian Global Observatory of the Atmosphere), incluida en ACTRIS (Aerosol, Clouds and Trace Gases Research Infrastructure) que está en proceso de constituirse como infraestructura permanente en el *European Research Infrastructure Consortium* (ERIC). Una parte importante de las medidas se tomaron en el marco de la campaña SLOPE I (Sierra Nevada Lidar Aerosol ProfilinG Experiment I). Esta tesis incluye medidas lidar de dos sitios rurales adicionales, un olivar en Úbeda (España) y una turbera en Rzecin (Polonia), medidas en las campañas AMAPOLA (Atmospheric Monitoring of Aerosol Particle Fluxes in Olive Orchard) y POLIMOS-2018 (Polish Radar and Lidar Mobile Observation System 2018), respectivamente.

El sistema lidar Raman multiespectral MULHACEN se ha usado para obtener perfiles verticales de propiedades ópticas y microfísicas de las partículas de aerosol. Este sistema emite radiación láser pulsada a longitudes de onda de 355, 532 y 1064 nm y recibe las señales retrodispersadas elástica e inelásticamente, también con capacidad de despolarización. Esta información espectral y de polarización es útil para la obtención de propiedades de tamaño y forma de las partículas de aerosol, y como indicador del tipo de aerosol. Este sistema es parte de EARLINET (European Aerosol Research Lidar Network) en el marco de las actividades de ACTRIS.

La señal Raman detectada por MULHACEN corresponde a cambios de estados vibracionales de energía de las moléculas, un efecto ampliamente usado en los lidars Raman de aerosol, aunque tiene la desventaja de una Razón Señal-Ruido (SNR) baja que suele limitar a medidas nocturnas con 30-60 min de resolución temporal. Hemos implementado una nueva configuración en la rama UV del sistema MULHACEN para medir líneas RAMAN correspondientes a estados rotacionales de energía, aumentando así la señal medida y disminuyendo la diferencia de longitud de onda entre la radiación elástica y Raman (un punto clave para disminuir las incertidumbres debidas a la dependencia espectral). Las líneas rotacionales muestran también algunos problemas relacionados con la dependencia con la temperatura, pero se demuestra que, con una selección apropiada de los filtros usados, esta dependencia supone una incertidumbre adicional de menos del 4 % en las propiedades ópticas obtenidas. Con esta nueva configuración hemos podido obtener perfiles de extinción y retrodispersión de partículas con resolución temporal de 1 h durante el día y hasta 1 minuto durante la noche. Sin embargo, este estudio tiene un carácter exploratorio en esta tesis, y la base de datos usada en el resto de secciones corresponde a la amplia base de medidas Raman vibracional obtenidas con anterioridad.

El sistema lidar Doppler Stream Line emite radiación infrarroja pulsada a 1500 nm y mide el cambio de frecuencia Doppler en la radiación retrodispersada, debido al movimiento de las partículas de aerosol con el viento. Este instrumento se ha utilizado por primera vez en la estación UGR, y lo hemos configurado para obtener perfiles verticales de campo de viento en la ABL y sus propiedades turbulentas. Gracias a esto, el instrumento ha pasado a formar parte de la red Cloudnet en el marco de las actividades de ACTRIS.

La señal medida por el lidar Doppler está optimizada para obtener directamente velocidades radiales, pero la intensidad de la señal presenta algunos artefactos que deben ser corregidos si esta señal se quiere utilizar con otros fines. Hemos aplicado un algoritmos de corrección desarrollado en el

Instituto Meteorológico de Finlandia (FMI), en el marco de ACTRIS, para corregir dos tipos de artefactos que afectan a la sustracción de la señal de fondo, específicamente ciertos cambios temporales bruscos independientes de la distancia y estructuras residuales a distintas alturas constantes con el tiempo. Un tercer problema es el aumento de señal en torno a cierta distancia y su reducción a mayores distancias debido a la distancia focal del sistema óptico del instrumento, configurada a esa distancia. Hemos propuesto, en colaboración con el FMI, una metodología para calcular la distancia focal y el diámetro de la lente como parámetros de calibración para nuestro lidar Doppler. Consiste en un método iterativo basado en comparar la señal lidar Doppler corregida con un ceilómetro próximo (que no necesita corrección de foco), y hemos obtenido parámetros de calibración para nuestro sistema con desviación estándar de menos del 20 %. La señal corregida permite estimar cantidades más avanzadas como los errores en la velocidad y el coeficiente de retrodispersión atenuado.

Los perfiles verticales de propiedades ópticas y microfísicas de las partículas de aerosol se han obtenido con varios algoritmos de inversión a partir de medidas lidar Raman. El punto de partida es la obtención de coeficientes de retrodispersión y extinción de partículas a tres longitudes de onda, y sus propiedades intensivas derivadas, usando el método Klett-Fernald o el método Raman para señales elásticas o inelásticas, respectivamente, y el método de despolarización para medidas de polarización. Así, nuestro trabajo se centra en emplear un conjunto de propiedades ópticas para obtener propiedades ópticas y microfísicas más complejas (por ejemplo, concentración volúmica de partículas, radio efectivo, índice de refracción complejo y albedo de dispersión simple) usando un algoritmo de regularización.

En particular, se han usado dos programas desarrollados en la Universidad de Potsdam (Alemania). El primero, llamado aquí UP, está basado en el modelo de Mie para partículas esféricas y se puede usar para cálculos directos o inversos usando datos de entrada simulados o medidos. El algoritmo de inversión es

un método de regularización híbrido basado en resolver explícitamente las ecuaciones matemáticas que relacionan las propiedades microfísicas y ópticas de las partículas según el modelo esférico, obteniendo la distribución de tamaño de partículas como resultado. El segundo programa se llama SphInX (Spheroidal Inversion Experiments) y se basa en una extensión del modelo de Mie en dos dimensiones para tener en cuenta partículas no esféricas asumiendo un conjunto de esferoides caracterizados por su radio equivalente volumétrico y su razón de aspecto. Los métodos de regularización son similares a los de UP, pero SphInX usa una base de datos precalculada para obtener los *kernel* para ciertos casos concretos, debido a la mayor complejidad del modelo. Una diferencia adicional entre los dos programas es que las medidas de despolarización solo las utiliza SphInX, ya que UP asume partículas esféricas que no producen despolarización.

Hemos aplicado el programa UP para la caracterización de partículas de combustión de biomasa transportadas a larga distancia y contenidas en intensas plumas que fueron detectadas en julio de 2013 en Granada y dos estaciones ACTRIS-EARLINET más, Leipzig (Alemania) y Varsovia (Polonia). Se ha realizado un análisis profundo de las fuentes y los caminos de transporte de las partículas usando observaciones de satélite y herramientas de modelización, confirmando la llegada de plumas de humo a las estaciones de estudio varios días después de haber sido emitidas en incendios forestales en el Norte de América. Las propiedades ópticas y microfísicas observadas corresponden, por tanto, a partículas de humo envejecido, y revelan su pequeño tamaño y forma casi esférica con absorción muy débil.

El programa SphInX también se ha usado para el estudio de distintos tipos de partículas de aerosol transportadas. Un primer caso, con partículas de combustión de biomasa, ha sido seleccionado para comparar con el programa UP y evaluar el impacto de las medidas adicionales de despolarización y el modelo 2D extendido para las partículas. El segundo caso seleccionado corresponde a partículas de polvo mineral del

desierto del Sahara, como ejemplo conocido de partículas gruesas y no esféricas. El rango de tamaños limitado de la base de datos precalculada de SphInX, debido a las longitudes de onda medidas con el lidar, ha limitado la aplicación de este programa a la parte micrométrica y submicrométrica de la distribución total, pero el resto de las propiedades microfísicas son coherentes con lo encontrado en las referencias bibliográficas, con el valor añadido de la información detallada sobre forma de las partículas según el modelo de esferoides.

El requisito mínimo para obtener propiedades de las partículas a partir de sistemas lidar Raman multiespectrales con UP o SphInX es tener 3 perfiles de coeficientes de retrodispersión de partículas (a 355, 532 y 1064 nm) y 2 perfiles de extinción de partículas (a 355 y 532 nm), y un perfil de despolarización de partículas solo en el caso de SphInX. Ya que ésta no es siempre la situación, pero las redes globales de aerosol necesitan tantas medidas completas como sea posible, hemos propuesto una metodología para sistemas que no incluyen todos los canales requeridos. Se basa en el uso de medidas espectrales de un fotómetro estelar o lunar próximo para reproducir el perfil que falta, usando la ecuación de Angström. Esta metodología puede ser aplicada usando tanto UP como SphInX, aunque los resultados aquí se refieren solo a UP.

La metodología propuesta se ha probado con un estudio de sensibilidad para evaluar los errores adicionales introducidos en las inversiones microfísicas. Hemos usado el programa UP en modo directo para simular distintos casos de aerosol según su distribución de tamaño y su índice de refracción complejo, y se ha aplicado el método propuesto a tres escenarios diferentes (según el canal lidar eliminado). Se han usado esos mismos escenarios para aplicar la metodología a datos reales medidos con MULHACEN en la estación UGR. Todos los resultados de casos reales y simulados se han comparado con las inversiones usando la configuración lidar completa, sin información de fotómetro. Se han encontrado desviaciones máximas del 20 % para los casos simulados con un error de entrada del 5 %, y

desviaciones menores del 40 % para los casos reales, con errores iniciales hasta del 40 %.

Los perfiles verticales de campo de viento y propiedades turbulentas en la ABL se han obtenido a partir de medidas lidar Doppler verticales y de escaneos usando varios algoritmos conectados entre sí. Hemos usado una cadena de procesamiento, *Halo lidar toolbox* desarrollada en el FMI, que incluye las metodologías más recientes de cálculo de perfiles verticales de viento horizontal y propiedades turbulentas (momentos estadísticos de la velocidad vertical, cizalla del viento y tasa de disipación de la energía cinética turbulenta). La cadena culmina con la combinación de toda la información obtenida para crear una máscara de clasificación de las fuentes de turbulencia con resolución temporal y vertical en la ABL.

Hemos usado el producto de viento horizontal de *Halo lidar toolbox* para llevar a cabo un estudio estadístico en Granada usando una base de datos de dos años de medidas regulares. La disponibilidad de datos, según la altura máxima analizada para que los resultados sean representativos, limita el análisis hasta 1000-1500 m sobre el nivel del suelo (s.n.s.) debido a la decreciente intensidad de la señal con la altura, que también depende de la carga de aerosol. Hemos analizado las diferencias y semejanzas en la evolución diaria de los perfiles verticales de viento para distintas estaciones del año, y se han obtenido también rosas de los vientos diurnas y nocturnas para la base de datos completa a tres alturas diferentes.

Finalmente, hemos estudiado las propiedades turbulentas de la ABL con los productos correspondientes de *Halo lidar toolbox*. Hemos evaluado el desarrollo diurno de la ABL para dos días de la campaña AMAPOLA, uno con condiciones despejadas y otro con nubes, observando el efecto de éstas en la menor altura alcanzada por la ABL y en los movimientos turbulentos descendentes. Para Granada y Rzecin, donde las bases de datos disponibles eran de dos años y cuatro meses, respectivamente, hemos podido realizar un análisis estadístico de las fuentes principales de turbulencia en esos periodos

analizados, con resolución temporal (para cada hora del día) y en altura. En Granada, además, fue posible hacer distinción por estaciones de año. Ambos sitios muestran una clara actividad convectiva durante el día en altitudes que aumentan con el tiempo, y una importante turbulencia debida a la cizalla durante la noche, especialmente en Rzecin. También hemos encontrado en ambos lugares una importante contribución de turbulencia nocturna debida a fuentes desconocidas (etiquetada como 'intermitente') aunque en Rzecin está principalmente concentrada en torno a 600 m s.n.s., mientras que en Granada está presente a todas las alturas.

PART I

BASIS AND INSTRUMENTAL WORK

I INTRODUCTION AND OBJECTIVES

In the last decades, there is an increasing concern about the climate change and also about the air quality, and how natural and anthropogenic processes affect them. According to a special report of the Intergovernmental Panel on Climate Change (IPCC, 2018), human activities are estimated to have caused approximately 1.0°C of global warming above pre-industrial levels, and this warming is likely to reach 1.5°C between 2030 and 2052 if it continues to increase at the current rate. However, there are several atmospheric components and mechanisms that are not sufficiently understood, measured or whose effect still presents high uncertainties according to the Fifth IPCC Assessment Report (Myhre et al., 2013) and some related studies (e.g. Myhre et al., 2017). This is the case of atmospheric aerosols and the vertical distribution of their particle optical and microphysical properties, which modify the vertical profile of heating rate of the atmosphere (e.g. Quijano et al., 2000). Since that Fifth IPCC Report, some new conclusions have been found for greenhouse gases radiative forcing (Etminan et al., 2016), but no conclusive revision has been done for aerosol forcing, what remains an active field of research (Allen et al., 2018).

Lidar (light detection and ranging) technique, used both in ground-based, satellite and airborne systems, has become a strategic methodology to obtain vertical profiles of tropospheric aerosol particles using one or several wavelengths with high spatial and temporal resolution. Multiwavelength lidar systems are specially convenient since the spectral dependence of the main aerosol optical properties is used as an indicator of the type of aerosol (*aerosol typing technique*). Moreover, measuring the change on the polarization state of the received light provides additional information on the sphericity of the aerosol particles.

Aerosol particles can undergo regional and long-range transport that modify their properties. Therefore, the study of these aerosol transport processes is relevant for all aerosol types, since this information is crucial in modelling the global impact of aerosol particles and monitoring events of social relevance (Pappalardo et al., 2013).

In this sense, global and continental networks are necessary, as they can provide appropriate spatial distribution of measurements with enough quality to fairly account for both the impact of isolated events and for the climatological effect of atmospheric aerosol particles (as opposed to satellites, with much higher spatial coverage but less likely to be equipped with instruments with the same potential and complexity as the ground-based systems). EARLINET, the European Aerosol Research Lidar Network (Pappalardo et al., 2014), is an established network with the main goal of providing a database for distribution and properties of the aerosol over Europe, which is exhaustive and complete enough to be climatologically significant. Thanks to the use of lidar techniques as the basis of the network, information on the vertical distribution of atmospheric aerosol particles with large spatial and temporal resolution is provided.

The behaviour of the lowermost region of the atmosphere has also a crucial role in modelling and understanding climate and air quality. This layer, known as *Atmospheric Boundary Layer*

(ABL), is the place where the emission of pollutants occurs, is directly responsible for the dispersion processes, and its correct modelling is essential for the numeric weather prediction and climate models (Baklanov et al., 2011; Li et al., 2017). It is characterized by a turbulent behaviour with significant temporal and spatial variations, which makes the accurate measurement and modelling of its internal mixing and its interactions with the surface and the rest of the atmosphere a challenging task.

In this different context, lidar technique represents again a powerful tool to retrieve profiles of several ABL properties. In particular, Doppler lidars (those measuring the Doppler shift due to the movement of aerosol particles with the wind) can be used to retrieve the 3D wind field inside the ABL and to retrieve turbulent properties with high temporal and vertical resolution, which can be combined to classify turbulence basing on its source (Harvey et al., 2013; Manninen et al., 2018).

In this context, the present thesis aims to address the profiling of atmospheric properties with a synergic approach, i.e., with the use of different instrumentation and methodologies that provide complementary information. Therefore, the core work done in this thesis is the deep understanding and application of different methodologies and algorithms to retrieve a set of atmospheric properties from lidar measurements. This kind of work is crucial to improve the methodologies themselves and to increase the knowledge on atmospheric processes, as well as to monitor extreme events of social impact and to create harmonized data sets of atmospheric quantities.

In this framework, the specific objectives of the thesis are:

- Improvement of the lidar measuring and pre-processing techniques in order to maximize the retrieved information from Raman and Doppler lidars.
- Characterization of aerosol optical and microphysical properties from Raman lidar measurements using spherical model. Application to the analysis of

transported smoke particles and extension of the algorithm to cases with non-ideal lidar setup.

- Characterization of aerosol optical and microphysical properties from Raman lidar measurements using spheroidal model for non-spherical particles. Application to the analysis of transported mineral dust and other aerosol types, and comparison with spherical model.
- Characterization of the wind field and turbulent structure of the ABL over Granada and other experimental sites using Doppler lidar measurements.

This thesis contains seven chapters structured in four parts. The first part sets the theoretical and experimental basis to develop the different studies and includes the instrumental work done. After the present first chapter with an introduction and an overview of the objectives and outline of the thesis, the second chapter includes a complete review of the concepts, definitions and equations describing the lowermost atmospheric layers, the turbulence, the aerosol particles and the remote sensing profiling techniques. The third chapter presents the main meteorological features of the experimental site where the majority of the measurements for this thesis have been performed and the instrumentation used, namely the Raman and the Doppler lidars and other ancillary systems. There are also two subsections with the instrumental work that has been done in order to improve the quality of the measured signals with Raman and Doppler lidars.

The second part of the thesis is devoted to the retrieval of optical and microphysical aerosol properties vertical profiles. Chapter four focuses on retrievals using a spherical approximation to model aerosol particles, and contains a description of the main algorithm applied, a study of the long-range transport of smoke particles over three European sites and a sensitivity study for a methodology using nocturnal photometry to complete Raman lidar measurements. In chapter five, we describe a different software based on a spheroidal model for non-spherical aerosol particles and we

apply it to some cases including mineral dust transport from Sahara Desert.

Part III aims its attention at wind and turbulence profiling within the low atmosphere. It includes a single chapter (six) where we describe a complete software toolbox to calculate wind field and turbulent properties of the atmosphere from Doppler lidar measurements. We then apply the software to characterize the atmosphere in terms of mean horizontal winds and turbulent sources.

Finally, the fourth part of the thesis includes chapter seven with the general conclusions drawn from all the studies. After that, there are some appendices including additional tables, acknowledgement to the institutions and people that have supported this thesis, and a short CV of the author.

II FUNDAMENTALS

The atmosphere is the gaseous layer that surrounds the Earth due to gravitational attraction and is composed by gases, clouds and aerosol particles. It plays a crucial role on the life development due to its greenhouse effect (modulating the planetary temperature) and its capability for absorbing ultraviolet solar radiation. For that reason, atmospheric research and observation is important, and remote sensing is a powerful technique to obtain valuable information with spatial and temporal resolution

The aim of this chapter is to provide an overview of the relevant physical concepts about atmosphere and remote sensing upon which this work is based. Sections 2.1 and 2.2 describe the targets and processes studied in this thesis, i.e., the atmospheric aerosols and wind field in the low atmosphere. The techniques used to explore those targets, encompassed in the remote sensing framework, are explained in section 2.3.

2.1 ATMOSPHERIC BOUNDARY LAYER AND TURBULENCE

The Earth's atmosphere can be divided into regions according to different criteria, one of them being its average thermal structure (Seinfeld and Pandis, 1998). With this criterion, the

regions from outside inward are the exosphere, the thermosphere, the mesosphere, the stratosphere and the troposphere. This lowest layer, which extends from the Earth's surface up to the tropopause (~12 km height, depending on location and season) is the one that contains 75% of the total atmospheric mass, and where weather-related and vertical mixing processes occur.

The lowermost region of the troposphere is usually called *Atmospheric Boundary Layer* (ABL), in contrast to the *free troposphere* (FT), although its proper definition is still uncertain. Here we present some of the most relevant definitions:

- Stull (1988): 'the part of the troposphere that is directly influenced by the presence of the Earth's surface, and responds to surface forcings with a time scale of about an hour or less'.
- Garrat (1992): 'the layer of air directly above the Earth's surface in which the effects of the surface (friction, heating and cooling) are felt directly on time scales less than a day, and in which significant fluxes of momentum, heat or matter are carried by turbulent motions on a scale of the order of the depth of the boundary layer or less'.
- Geer (1996): 'the atmospheric layer from the Earth's surface up to an altitude about 1 kilometer in which wind speed and direction are affected by frictional interaction with objects on the Earth's surface'.
- American Meteorological Society (2000): 'the bottom layer of the troposphere that is in contact with the surface of the Earth. It is often turbulent and is capped by a statically stable layer of air or temperature inversion. The ABL depth (i.e., the inversion height) is variable in time and space, ranging from tens of meters in strongly statically stable situations, to several kilometers in convective conditions over deserts'.
- Bravo-Aranda et al. (2019): 'the part of the troposphere that is directly or indirectly influenced by the Earth's

surface (land and sea), and responds to gases and aerosol particles emitted at the Earth's surface and to surface forcing at time scales less than a day. Forcing mechanisms include heat transfer, fluxes of momentum, frictional drag and terrain-induced flow modification'.

All definitions coincide in the permanent surface-ABL interaction, and in its turbulent nature that makes its properties (gas and particles concentrations, temperature, momentum) to be mixed and thus vertically homogeneous.

The turbulent structures in the ABL are called eddies, and transport and disperse matter of other atmospheric properties in a process known as *turbulent* diffusion. These eddies are either caused by mechanical processes (wind shear, surface roughness and friction) or thermal processes (buoyancy, produced by surface heating which creates updrafts or by cloud-top radiative cooling which creates downdrafts). When present, buoyancy driven turbulence is the most dominant source for mixing (Oke, 1992).

The height of the ABL (ABLH) varies over a wide range, particularly over land surfaces (Arya, 1995). It shows large diurnal variations in response to the diurnal cycle of heating and cooling of the surface under clear skies, being the maximum ABLH around several kilometers and its minimum around several tens of meters in mid-latitudes (e.g. de Arruda Moreira et al., 2018b; Baars et al., 2008; Bedoya-Velásquez et al., 2019; Granados-Muñoz et al., 2012). The ABLH, important for pollutant dispersion and meteorological modelling, can be determined by strong variations in some variables like potential temperature, vertical wind speed or particle concentration, although these determinations may not always agree or be precise due to the different tracers and observed quantities involved in the applied methods, particularly when complex structures are present (see Figure II-1).

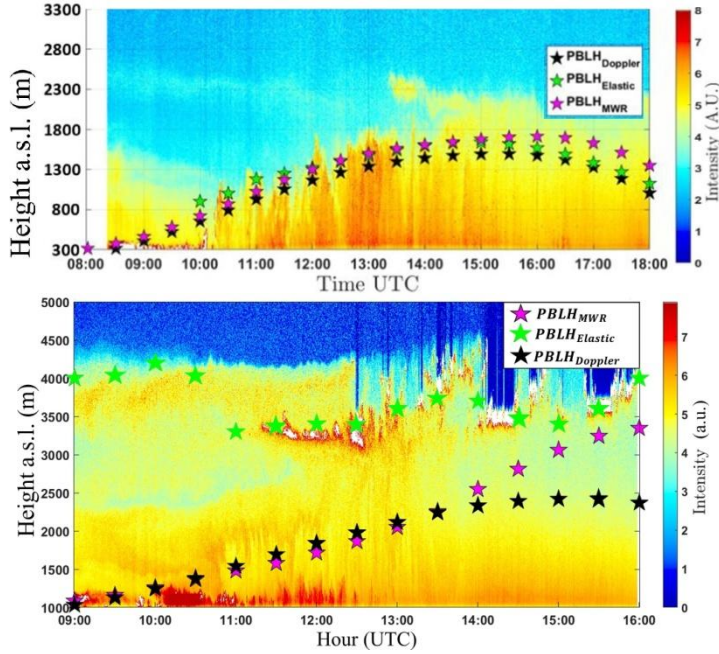


Figure II-1: ABLH determination based on temperature (pink stars), aerosol concentration (green stars) and vertical wind (black stars), when all methods agree (upper panel) and when they disagree due to complex structures (lower panel). Color map stands for aerosol load. From de Arruda Moreira et al. (2018a, 2018b).

An important aspect in turbulence studies is that a statistical approach rather than a deterministic approach is necessary, since fluctuations are unpredictable in detail. For this approach, Reynold's decomposition is applied to a variable $q(t)$, that is composed of a mean value $\langle q \rangle$ and its fluctuations $q'(t)$:

$$q(t) = \langle q \rangle + q'(t) \quad (\text{II-1})$$

From this concept, the second, third and fourth order moments of $q(t)$ can be calculated and interpreted in terms of turbulence. For the case when $q = w$, i.e., the vertical component of the wind field, the moments directly give information about the air updrafts and downdrafts:

- Variance: defined as the second order statistical moment of q . Using Reynold's decomposition $qt = \langle q \rangle + q'(t)$ (II-1):

$$\sigma_q^2 = \frac{1}{N} \sum_{i=0}^{N-1} (q_i - \langle q \rangle)^2 = \frac{1}{N} \sum_{i=0}^{N-1} q_i'^2 = \langle q_i'^2 \rangle \quad (\text{II-2})$$

where N is the total number of discrete measurements. Variance measures how far are the fluctuations spread out from the mean. Therefore, σ_w^2 (vertical velocity variance) is a direct measurement of turbulence, and actually the *Turbulent Kinetic Energy* (the part of the kinetic energy per unit mass associated with velocity fluctuations, TKE; Stull, 1988) is proportional to σ_w^2 .

- Skewness: third order moment normalized to the variance:

$$S_q = \frac{\langle q_i^3 \rangle}{\langle q_i^2 \rangle^{3/2}} \quad (\text{II-3})$$

In the case of vertical wind, S_w measures the dominant direction of the turbulent movements. A positive (negative) S_w implies strong but narrow updrafts (downdrafts) surrounded by weaker but more widespread downdrafts (updrafts).

- Kurtosis: fourth order moment normalized to the variance:

$$K_q = \frac{\langle q_i^4 \rangle}{\langle q_i^2 \rangle^2} \quad (\text{II-4})$$

This moment is more meaningful when calculated for other physical quantities, such as temperature or aerosol concentration, because it provides the level of mixing of this quantity. Since a normal distribution has a kurtosis of 3, $K_q < 3$ means that q is well mixed (the distribution has fewer and less extreme outliers than normal distribution) and $K_q > 3$ means low mixing.

2.2 ATMOSPHERIC AEROSOL

The atmospheric aerosol is defined as the suspension of solid and/or liquid particles in the atmospheric air, excluding clouds, which are considered a separate phenomenon (Horvath, 1998). These particles arise from natural sources as wind-blown dust, sea spray, volcanoes, smoke from fires and pollen or other biogenic material, and from anthropogenic activities, such as combustion of fuels or agricultural biomass burning.

These particles range in size from a few nanometers to tens or hundreds of micrometers, and can be directly emitted as particles (*primary aerosol*) or formed in the atmosphere by gas-to-particle conversion processes (*secondary aerosol*). They are removed from the atmosphere by two mechanisms: dry deposition at Earth's surface and wet deposition after being incorporated into cloud droplets during the formation of precipitation. These mechanisms make aerosol residence times in atmosphere span from a few days to a few weeks, excepting stratospheric aerosol (mainly from volcanic eruptions, e.g. Brasseur and Granier, 1992) that can stay for years. Due to those lifetimes, aerosol particles can be transported over several thousands of kilometers (eg. Ansmann et al., 2003; Ortiz-Amezcuca et al., 2017).

The main constituents of the atmospheric aerosol are inorganic species (sulphate, nitrate, ammonium, sea salt), organic species (also called organic aerosol, OA), black carbon (formed from the incomplete combustion of fuels under certain conditions), mineral species and primary biological aerosol particles (PBAPs). Table II-1 lists the characteristic sources and lifetimes of the main aerosol species.

Atmospheric aerosol plays an important role in cloud formation processes, since they act as condensation nuclei or ice formation nuclei (Andreae and Rosenfeld, 2008). They also take part in chemical and electrical processes in the atmosphere (Hallquist et al., 2009; Seinfeld and Pandis, 1998). When they are present in large concentrations, they can be even dangerous to health. They have also an effect on climate, because they are responsible for a radiative forcing (RF) through their interaction with radiation, and also as a result of their interaction with clouds. However, quantification of this forcing, in particular the anthropogenic aerosol RF, has still large uncertainties (Haywood and Boucher, 2000; Haywood and Schulz, 2007; Lohmann and Feichter, 2005; Myhre et al., 2013).

Table II-1: Properties of principal aerosol species in the atmosphere. Terminology about size distribution (in second column) is explained later on subsection 2.2.1. Adapted from Boucher et al. (2013).

Aerosol species	Size distribution	Main sources	Tropospheric lifetime
Sulphate	Primary: Aitken, accumulation and coarse modes Secondary: Nucleation, Aitken, and accumulation modes	Primary: marine and volcanic emissions. Secondary: oxidation of SO ₂ and other S gases from natural and anthropogenic sources	~ 1 week
Nitrate	Accumulation and coarse modes	Oxidation of NO _x	~ 1 week
Black carbon	Freshly emitted: <100 nm Aged: accumulation mode	Combustion of fossil fuels, biofuels and biomass	1 week to 10 days
Organic aerosol	Prim. OA: Aitken and accumulation modes. Sec. OA: nucleation, Aitken and mostly accumulation modes. Aged OA: accumulation mode	Combustion of fossil fuel, biofuel and biomass. Continental and marine ecosystems. Some anthropogenic and biogenic non-combustion sources	~ 1 week
... of which brown carbon	Freshly emitted: 100–400 nm Aged: accumulation mode	Combustion of biofuels and biomass. Natural humic-like substances from the biosphere	~ 1 week
...of which terrestrial PBAP	Mostly coarse mode	Terrestrial ecosystems	1 day to 1 week depending on size
Mineral dust	Coarse and super-coarse modes, with a small accumulation mode	Wind erosion, soil resuspension. Some agricultural practices and industrial activities (cement)	1 day to 1 week depending on size
Sea spray	Coarse and accumulation modes	Breaking of air bubbles induced e.g., by wave breaking. Wind erosion.	1 day to 1 week depending on size
... of which marine primary OA	Preferentially Aitken and accumulation modes	Emitted with sea spray in biologically active oceanic regions	~ 1 week

2.2.1 Aerosol microphysical properties

A complete physical description of aerosol would describe the composition and geometry of each particle of the whole ensemble. In practice, such an approach cannot be taken since atmospheric aerosol can present concentrations of several thousands of particles per cm^3 (Seinfeld and Pandis, 1998) and sizes in a range of several orders of magnitude. For that reason, a statistical approach is taken.

For a chemically homogeneous aerosol, this problem becomes one of representing the *size distribution*, i.e., the density distribution of particles for each radius (considering only spherical particles). The numeric size distribution is then described as:

$$n(r) = \frac{dN}{dr} \quad (\text{II-5})$$

representing the number of particles with radius r (μm) in the interval $(r, r + dr)$ per unit air volume. The total number of particles per unit volume, is then given by:

$$C_N = \int_0^{\infty} n(r) dr \quad (\text{II-6})$$

The size distribution $n(r)$ is then a statistical density function, and thus one can define its statistical momenta (mean, variance, etc.). The effective radius (or area-weighted mean radius) of an aerosol distribution is defined as the ratio of the third moment to the second moment of the size distribution:

$$r_{eff} = \frac{\int_0^{\infty} r^3 n(r) dr}{\int_0^{\infty} r^2 n(r) dr} \quad (\text{II-7})$$

The usefulness of r_{eff} comes from the fact that energy removed from a radiation beam by a particle is proportional to its area (provided the particle radius is similar to or larger than the wavelength of the incident radiation).

Analogous to the description of the distribution of particle number with radius it is also possible to describe particle surface area, volume and mass with equivalent expressions. Then, the surface size distribution $s(r)$, volume size distribution $v(r)$, and mass size distribution $m(r)$, representing the area,

volume and mass, respectively, of particles with each radius per unit volume, are:

$$s(r) = \frac{dS}{dr} \quad (\text{II-8})$$

$$v(r) = \frac{dV}{dr} \quad (\text{II-9})$$

$$m(r) = \frac{dM}{dr} \quad (\text{II-10})$$

And the total particle area (C_S), volume (C_V) and mass (C_M) are calculated by integrating the corresponding distributions as in Equation (II-6). Figure II-2 depicts a typical distribution of surface size distribution, showing also the phenomena that influence particle sizes in aerosol ensemble (Seinfeld and Pandis, 1998).

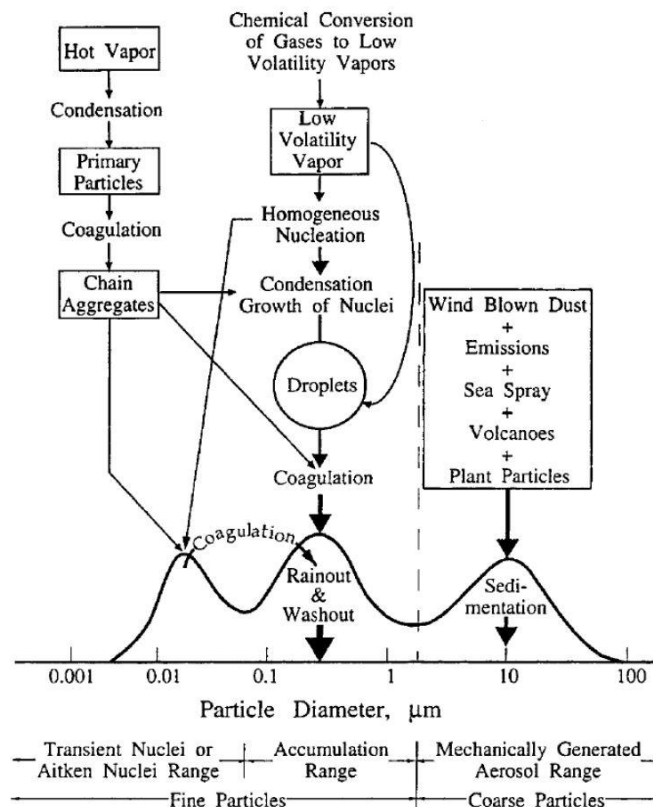


Figure II-2: Idealized schematic of the distribution of particle surface area of an atmospheric aerosol. Principal modes, sources and particle formation and removal mechanisms are indicated. From (Seinfeld and Pandis, 1998), originally adapted from Whitby and Cantrell (1976).

In the light of the observed size distributions, aerosol particles can be divided roughly into *modes* of those distributions. The modes and their corresponding diameter (d) ranges are: *nucleation* mode (d < 10 nm), *Aitken* mode (10 nm < d < 100 nm), *accumulation* mode (0.1 < d < 2.5 μm) and *coarse* mode (d > 2.5 μm). Particles from nucleation and Aitken modes are also known as ultrafine particles or nanoparticles. These particles, together with accumulation mode particles form the called *fine* mode.

The typically observed aerosol distributions present common features that allow for their modelling. The most extended model to represent aerosol distributions is the multi-modal *log-normal function* (Aitchison and Brown, 1957):

$$n(r) = \sum_{j=1}^M \frac{c_{N,j}}{r \cdot \ln \sigma_j \cdot \sqrt{2\pi}} \exp \left[-\frac{(\ln r - \ln r_{med,j})^2}{2(\ln \sigma_j)^2} \right] \quad (\text{II-11})$$

where the j corresponds to each mode until M , the geometric standard deviation is σ_j and $r_{med,j}$ is the median radius.

This statistical description of aerosol is of extended use, although it only accounts for particle size characterization, assuming approximately spherical particles. However, in the recent years it has been shown that this approximation is not precise enough for the non-spherical case such as mineral dust particles and volcanic ashes, and a better description of particle shape is needed (Mishchenko et al., 2000). Since there is no complete formula to cover every possible shape, it has to be modelled for a certain geometry, and the *spheroidal approximation* is usually taken. Particles are then approximated to have a spheroidal shape, i.e., the geometrical shape of the revolution of an ellipse about one of its principle axes. Denoting one semiaxis as r_h and the other as r_v , one can define the *aspect ratio* as:

$$a = \frac{r_v}{r_h} \quad (\text{II-12})$$

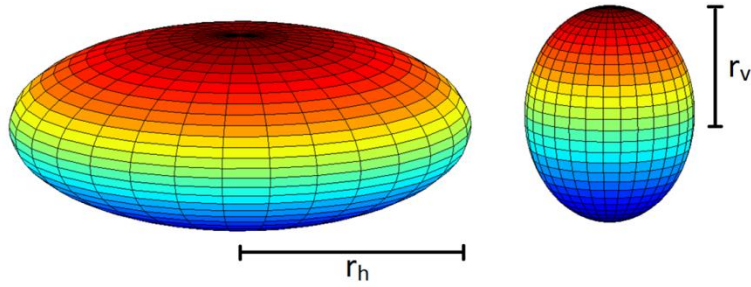


Figure II-3: Example of an oblate spheroid (left) and a prolate spheroid (right), showing their semiaxes r_h and r_v .

Three possible shapes can be then distinguished: the oblate spheroid ($a < 1$), the sphere ($a = 1$), and the prolate spheroid ($a > 1$), see Figure II-3.

The previously described size distribution is then generalized to a *shape-size* distribution in two dimensions (Böckmann and Osterloh, 2014; Osterloh, 2011; Samaras, 2017). The particle distributions are then generalized to $n(r, a)$, $s(r, a)$, $v(r, a)$ and $m(r, a)$, and the total particle number, area, volume and mass are obtained by double integration of the distribution over radius and aspect ratio. Finally, the *effective aspect ratio* (a_{eff}) can be introduced to give us an estimation and a direct look of a central tendency of the a , analogously to Equation (II-7) as:

$$a_{eff} = \frac{\int_0^{\infty} a \int_0^{\infty} v(r, a) dr da}{C_v} \quad (\text{II-13})$$

and the spread of the a values from a_{eff} , the *aspect ratio width*:

$$a_{width} = \frac{\int_0^{\infty} (a - a_{eff})^2 \int_0^{\infty} v(r, a) dr da}{C_v} \quad (\text{II-14})$$

2.2.2 Aerosol optical properties

When electromagnetic radiation propagates through the atmosphere, it is attenuated via scattering and absorption by aerosol particles, gases and clouds.

Absorption occurs when the radiative energy becomes part of the internal energy of the interacting object. It is described by

the *absorption coefficient*, $\sigma_{ab}(\lambda)$ that depends on radiation wavelength and has units of inverse longitude (m^{-1}).

Scattering occurs when the incident radiation is redirected in all spatial directions. It is described by the *scattering coefficient*, $\sigma_{sc}(\lambda)$ (m^{-1}), or by the *backscatter coefficient*, $\beta(\lambda)$ ($\text{m}^{-1}\text{sr}^{-1}$) if we refer only to the radiation scattered in the elemental solid angle corresponding to 180° with respect to incident direction. Scattering strongly depends on the size of the interacting objects, distinguishing between Rayleigh scattering for small scatterers (size parameter $x = \frac{2\pi r}{\lambda} \ll 1$) and Mie scattering for larger scatterers ($x \sim 1$). Rayleigh scattering holds, in the solar and atmospheric radiation ranges, for air molecules, and is characterized by wavelength dependence as λ^{-4} and by full symmetry with respect to the orthogonal direction of propagation. In the aforementioned spectral ranges, Mie scattering is applied to aerosol particles, and the backscattered radiation is less than the forward scattered (see Figure II-4).

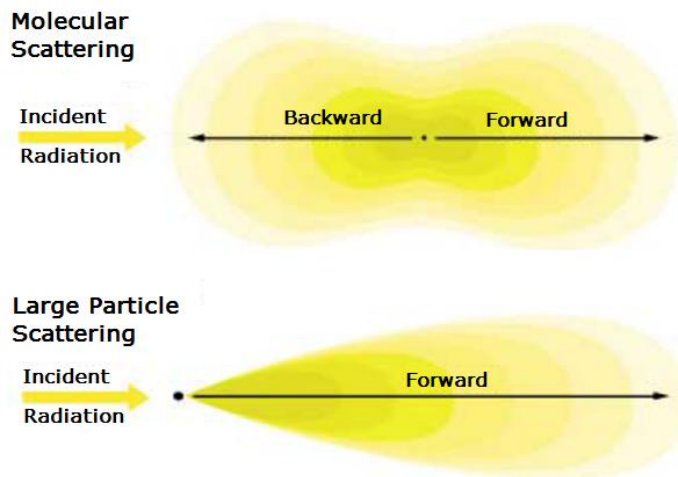


Figure II-4: Rayleigh (upper picture) and Mie (lower picture) scattering patterns. Adapted from Malm (2017).

A special type of scattering is linked to Raman effect in molecules, due to which the radiation is scattered with a wavelength shift respect to the incident radiation. It is also called *inelastic* scattering (as opposed to *elastic* scattering, where there is no wavelength shift), and is due to variations in

the vibrational and/or rotational quantum state of molecules. The *Raman spectrum* of a molecule therefore presents some discrete lines corresponding to rotational state variations (pure rotational Raman, RR) and some others corresponding vibrational (usually combined with rotational) state variations (vibrational-rotational Raman, VR). The wavenumber shift and relative cross sections of several relevant atmospheric molecules are depicted in Figure II-5, compared to elastic scattering. It can be observed that RR scattering lines present much shorter wavenumber shift (a few cm^{-1}) and much higher cross section than VR scattering (for example Inaba (1976) calculated a factor 32 for the 337.1 nm laser wavelength, if all rotational lines are integrated).

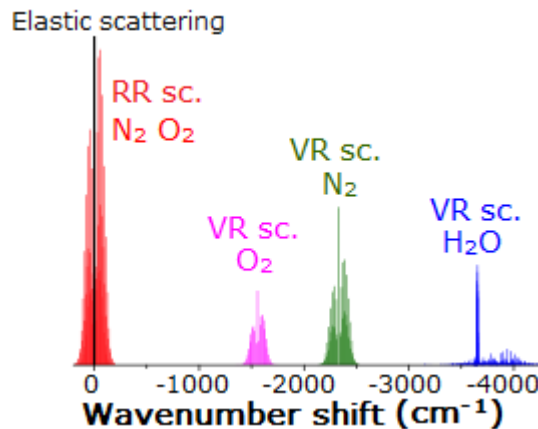


Figure II-5: Pure rotational Raman scattering (PRRS) and rotational-vibrational Raman scattering (ro-vib.) lines for Nitrogen, Oxygen and water vapor molecules. Adapted from mpimet.mpg.de.

The combination of both absorption and scattering processes (which usually occur simultaneously) is called extinction, and is described by the *extinction coefficient* (m^{-1}):

$$\alpha(\lambda) = \sigma_{ab}(\lambda) + \sigma_{sc}(\lambda) \quad (\text{II-15})$$

Absorption, extinction, scattering and backscattering coefficients can be modelled for a certain aerosol size distribution $n(r)$. For spherical particles, Lorenz-Mie model holds (Mie, 1908), and the coefficient $\Gamma(\lambda)$ (meaning any of the coefficients) is calculated as (Bohren and Huffman, 1983):

$$\Gamma(\lambda) = \int_{r_{min}}^{r_{max}} K_{\Gamma}(r, \lambda, CRI) \cdot n(r) dr \quad (II-16)$$

where $K_{\Gamma}(r, \lambda, CRI)$ is the cross section (of absorption, extinction, scattering or backscattering, respectively) and depends on particle size (r) and complex refractive index (CRI). The CRI is another optical property of the particles, whose real part (RRI) is related to the scattering efficiency and depends on size and shape of particles, and imaginary part (IRI) is related to the absorption efficiency.

For non-spherical particles, T-matrix theory (Mishchenko et al., 1996; Waterman, 1965) is among the most powerful techniques for solving the electromagnetic scattering problem. For the case of spheroidal model, the resulting cross sections $K_{\Gamma}(r, a, \lambda, CRI)$ depend also on the aspect ratio (Dubovik et al., 2006; Osterloh, 2011; Samaras, 2017; Veselovskii et al., 2010).

The extinction of radiation along a slant path from s_1 to s_2 can be evaluated using the *optical thickness*:

$$OT(\lambda) = \int_{s_1}^{s_2} \alpha(\lambda) ds \quad (II-17)$$

or more commonly using the equivalent definition for a vertical path (z), the *optical depth*:

$$OD(\lambda) = \int_{z_1}^{z_2} \alpha(\lambda) dz \quad (II-18)$$

If one refers only to the aerosol contribution to extinction, the *aerosol optical depth* (AOD) is defined. The spectral dependence of AOD is parameterized by means of the Angström Law (Ångström, 1961):

$$AOD(\lambda) = AOD(1\mu m) \cdot \lambda^{-AE} \quad (II-19)$$

where AE is the *Angström Exponent*, which is related to the size of the particles. Large AE values (around 2) indicate the prevalence of fine particles, while low values (around 0) are related to the presence of coarse particles (Dubovik et al., 2002b). The AE can be also defined for other quantities (q), and calculated for two wavelengths as:

$$AE_q(\lambda_1, \lambda_2) = -\frac{\log(q(\lambda_1)/q(\lambda_2))}{\log(\lambda_1/\lambda_2)} \quad (\text{II-20})$$

The relative importance of the scattering and absorption processes is characterized by the *single scattering albedo* (*SSA*), a key parameter for the estimation of the direct radiative impact of aerosols:

$$SSA(\lambda) = \frac{\sigma_{sc}(\lambda)}{\sigma_{ab}(\lambda) + \sigma_{sc}(\lambda)} = \frac{\sigma_{sc}(\lambda)}{\alpha(\lambda)} \quad (\text{II-21})$$

It mainly depends on the sources of the various aerosol substances and on aging during transport.

It is well known that particles change the polarization state of a fraction of the incident light (Bohren and Huffman, 1983), depending on the size parameter and particle shape. In order to quantify the depolarization capability of the atmospheric aerosol, different variables have been defined in scientific literature (Cairo et al., 1999). Among them, the most used is the *volume linear depolarization ratio*, δ , defined as the ratio between the perpendicular (\perp) and parallel (\parallel) backscatter coefficient produced by a linear-polarized incident radiation. In order to separate the molecular and particle contribution, the *linear particle depolarization ratio* is defined, as

$$\delta_p = \frac{\beta_{\perp}^a}{\beta_{\parallel}^a} \quad (\text{II-22})$$

Depolarization values range between 0 and 1, and depend on the predominance of spherical versus non-spherical particles (0 corresponding to perfect spheres).

2.3 REMOTE SENSING

The exploration of the atmosphere, particularly the troposphere and the ABL, has been of interest for a long time for several reasons, including weather forecast or research on surface-atmosphere interactions. First observations started with in situ measurements at the ground or from towers, and soon the development of remote data transfer allowed also for measurements away from the surface with tethered ballons and radiosondes. These observations are constrained by spatial

or temporal sampling limitations, or both. The development of remote sensing techniques allowed the continuous probing of the whole ABL and troposphere with high spatial resolution.

Remote sensing is defined as “the technology of measurement or acquiring data and information about an object or phenomena by a device that is not in physical contact with it” (Geer, 1996). It is based on the detection and measurement of changes that the target produces on the surrounding field, including electromagnetic field emitted or reflected by the object or acoustic waves reflected or perturbed by it, but also gravity or magnetic potential field due to its presence (Elachi, 1987).

For atmospheric research purposes, mainly electromagnetic waves are used. These waves have to verify that their wavelength must be of the order of the size of the atmospheric objects and processes to be sensed, in order to maximize the scattering cross section (Bragg and Bragg, 1913). The size range of the main ABL compounds and processes goes from nanometers (molecules and aerosol particles) to millimeters (cloud droplets and precipitation) and decens and hundreds of meters (turbulent eddies). Therefore, the corresponding detection wavelengths for remote sensing of ABL have to cover the same range (see Figure II-6).

In the case of electromagnetic waves, another condition for remote sensors wavelengths is that the atmosphere do not absorb the used radiation or absorbs only weakly in those wavelengths. The bands of the electromagnetic spectrum within which the atmosphere is not absorbing are called atmospheric windows (Geer, 1996).

Remote sensing instruments can be divided into:

- Passive remote sensors, that record naturally occurring waves (usually electromagnetic radiation) that are either emitted or reflected from areas and targets of interest. Examples of them for atmospheric observation are the microwave radiometers (detecting microwave part of the electromagnetic spectrum emitted by the Earth or the

atmosphere), or the photometers (detecting the visible, ultraviolet and near-infrared part of the radiation coming from the Sun, the sky, the Moon or the stars after passing through the atmosphere).

- Active remote sensors, that send artificial waves toward the target or features of interest and then record the part that is reflected back to the system. Examples of atmospheric active remote sensors are radar and lidar systems (that emit and detect radio and optical electromagnetic waves, respectively), or sodar systems (that work with acoustic waves).

The main advantage of the active over the passive sensors is that the emitted radiation is controlled and usually pulsed, and thus it is possible to determine distances (so called ranging) by measuring the time lapse between the emission and the detection of each pulse. In addition, the changes in certain properties (such as wavelength or polarization) of the emitted radiation can be tracked and used to extract more information.

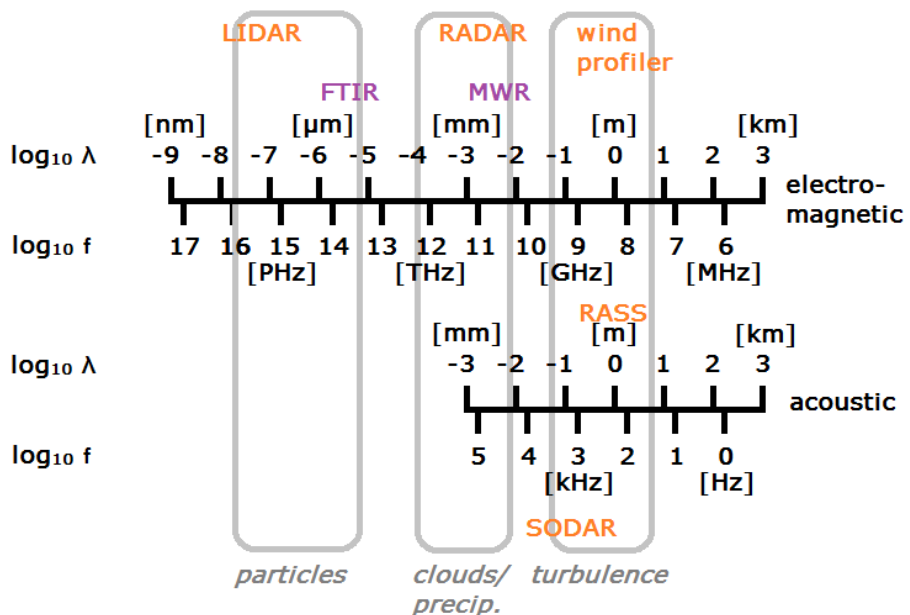


Figure II-6: Size ranges of the ABL objects of interest (grey boxes), and the corresponding frequency ranges for some active (orange labels) and passive (purple labels) remote sensing, for electromagnetic and acoustic waves.

Adapted from Emeis (2011).

Remote sensing usually implies the detection of a physical quantity that is a more or less complicated function of the quantity that is actually required. This kind of problems are known as *Inverse Problems*, and the study and retrieval of their solutions is known as *Inversion Theory* (Rodgers, 2000).

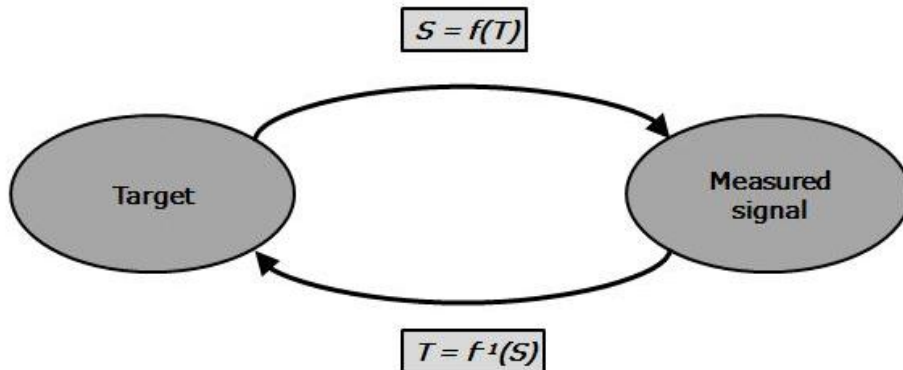


Figure II-7: Schematic explanation of the inversion problem inherent to remote sensing.

In Figure II-7, the inversion problem is schematically explained. The direct or *forward* problem would be to calculate the signal S generated by the interaction of radiation with target T , described by the function f . The inverse problem is to calculate the properties of the target given the signal measured, $T=f^{-1}(S)$. Solving the inverse problem is complicated by a number of difficulties. From a mathematical point of view, we can see this as an *ill-posed* problem, as it usually breaches one of the conditions defined by Hadamard (1923):

- Existence of at least one solution of the problem. This could be violated if the experiment had been set up incorrectly and there was no data on the properties of the substance in the scattered beam.
- Uniqueness of the solution. This condition can be not fulfilled in remote sensing because there are several unknown parameters, which can be combined in different ways to generate the same observed signal.

- Stability of the solution in the sense that small perturbations or errors in the observations should not produce large changes in the retrieved properties.

It is therefore important to have a general method for solving ill-posed problems. There exist different approaches for this purpose, but all are based on the idea of incorporating extra information into the method of solution (Shifrin, 2003). During this process, called *regularization*, the problem becomes *well-posed*, reducing the number of solutions by two operations: (1) formulation of additional conditions which eliminate physically absurd solutions; and (2) with a formal algorithm that finds the best solution in terms of the minimum difference $|f(T')-S|$, where T' is the estimated solution.

2.3.1 Active remote sensing of aerosols: elastic and Raman lidar technique

Lidar is an active remote sensing technique that is known to be a strong approach for atmospheric research since it provides profiles of aerosol particles using one or several wavelengths, with very high spatial and temporal resolution. Lidar systems are laser-based and operate emitting light pulses into the atmosphere (usually in the vertical, but also in other directions). The portion of the light that is backscattered to the system is collected by a telescope and focused upon a photodetector that measures the amount of light as a function of distance from the lidar (Kovalev and Eichinger, 2004).

In its simplest form, the detected signal by lidar can be written as:

$$P(z, \lambda) = K \cdot G(z) \cdot \beta(z, \lambda) \cdot T^2(z, \lambda) = K \cdot G(z) \cdot \beta(z, \lambda) \cdot \exp\left[-2 \int_0^z \alpha(z', \lambda) dz'\right] \quad (\text{II-23})$$

i.e., the power P receiver from a distance z is made up of four factors: K is a system constant, containing all range-independent information about the system performance; $G(z)$ describes the range-dependent measurement geometry, including the *overlap function* that accounts for the incomplete overlap between the laser beam and the receiver field of view;

$\beta(z, \lambda)$ is the atmospheric backscatter coefficient, and $T^2(z, \lambda)$ is the transmission term that describes the light loss on the way from and back to the lidar due to extinction (α) by molecules, aerosol particles and clouds. The two first factors are completely determined by the lidar setup and can thus be controlled, while the information on the atmosphere (and thus the subject of investigation) is contained in the two last terms.

The algorithm used for solving the inverse problem of retrieving aerosol extinction and backscatter coefficients profiles, $\alpha^a(z, \lambda)$ and $\beta^a(z, \lambda)$, is usually referred as Klett-Fernald inversion (Fernald, 1984; Fernald et al., 1972; Klett, 1981). This method assumes a known extinction-to-backscatter ratio of particles or *aerosol lidar ratio* ($LR^a(z, \lambda)$). This parameter depends on the aerosol type and could vary with the height, although a constant value is assumed.

Under these assumptions, the equation for $\beta^a(z, \lambda)$ can be solved as follows:

$$\beta^a(z, \lambda) = -\beta^m(z, \lambda) + \frac{RCS(z, \lambda) \exp\left\{-2 \int_{z_0}^z [LR^a(z', \lambda) - LR^m(z', \lambda)] \beta^m(z', \lambda) dz'\right\}}{\frac{RCS(z_0, \lambda)}{\beta^a(z_0, \lambda) + \beta^m(z_0, \lambda)} - 2 \int_{z_0}^z LR^a(z', \lambda) RCS(z', \lambda) T(z', z_0, \lambda) dz'} \quad (\text{II-24})$$

where the superscripts 'm' and 'a' indicate molecular and aerosol components of the coefficients, and $RCS(z, \lambda) = P(z, \lambda) \cdot z^2$ is the *range corrected signal*. Molecular terms can be calculated using standard atmosphere conditions or an atmospheric profile from radiosondes launched nearby. An additional assumption is needed, the aerosol backscatter coefficient at a specific height z_0 , normally selected such that $\beta^a(z_0, \lambda) \approx 0$ (true for clear air conditions in the upper troposphere).

When the lidar system detects inelastically backscattered radiation due to Raman effect (see section 2.2), it is said that the system has Raman configuration, and the detected signal is:

$$P_R(z, \lambda) = K_R \cdot G(z) \cdot \beta_R(z, \lambda) \cdot \exp\left\{-\int_0^z [\alpha(z', \lambda) + \alpha(z', \lambda_R)] dz'\right\} \quad (\text{II-25})$$

where the subscript 'R' indicates the Raman-shifted wavelength. This additional equation allows for independent $\alpha^a(z, \lambda)$ and $\beta^a(z, \lambda)$ retrieval without LR^a assumption.

The algorithm for the retrieval of $\alpha^a(z, \lambda)$ and $\beta^a(z, \lambda)$ coefficient using elastic and Raman lidar signals was first shown by (Ansmann et al., 1990) and then reviewed by (Whiteman, 2003a, 2003b). In this review, the temperature dependence of the Raman scattering was shown to be important under certain conditions, by including a temperature-dependent factor $F_R(z, \lambda)$ in Equation (II-25). This effect can be neglected for elastic signal except for the case of very light aerosol loading (Whiteman, 2003a).

The equations for the calculation of $\alpha^a(z, \lambda)$ and $\beta^a(z, \lambda)$ profiles, respectively, as derived by (Whiteman, 2003a) and (Veselovskii et al., 2015b) are:

$$\beta^a(z, \lambda) = \beta^m(z, \lambda) + \beta^m(z_0, \lambda) \cdot \frac{P_R(z_0, \lambda)P(z, \lambda)N(z)F_R(z, \lambda)}{P(z_0, \lambda)P_R(z, \lambda)N(z_0)F_R(z_0, \lambda)} \cdot \exp\left\{\int_{z_0}^z \left[\alpha^a(z', \lambda) \cdot \left(1 - \left(\frac{\lambda}{\lambda_R}\right)^A\right) + \alpha^m(z', \lambda) - \alpha^m(z', \lambda_R) \right] dz'\right\} \approx \beta^m(z, \lambda) + \beta^m(z_0, \lambda) \cdot \frac{P_R(z_0, \lambda)P(z, \lambda)N(z)}{P(z_0, \lambda)P_R(z, \lambda)N(z_0)} X(z) \quad (\text{II-26})$$

$$\alpha^a(z, \lambda) = \frac{\frac{d}{dz} \ln\left(\frac{N(z)}{P_R(z, \lambda) \cdot z^2}\right) + \frac{d}{dz} \ln F_R(z, \lambda) - \alpha^m(z, \lambda) - \alpha^m(z, \lambda_R)}{1 + \left(\frac{\lambda_L}{\lambda_R}\right)^A} \quad (\text{II-27})$$

where $N(z)$ is the air molecular density. For vibrational Raman scattering the ratio $F_R(z, \lambda)/F_R(z_0, \lambda)$ in Equation (II-26) can be

well approximated to 1, as can the contribution provided by the term $\frac{d}{dz} \ln F_R(z, \lambda)$ in Equation (II-27). However, these approximations may not be valid for pure-rotational Raman scattering.

Some aerosol lidars have also the capability of measuring the perpendicular and parallel components of the elastic backscattered light by particles, and the linear particle depolarization ratio (Equation II-22) can be calculated as (Cairo et al., 1999):

$$\delta_p(z, \lambda) = \frac{R(z, \lambda) \cdot \delta(z, \lambda) \cdot [\delta^m(z, \lambda) + 1] - \delta^m(z, \lambda) \cdot [\delta + 1]}{R(z, \lambda) \cdot [\delta^m(z, \lambda) + 1] - [\delta + 1]} \quad (\text{II-28})$$

where $R(z, \lambda)$ is the *backscattering ratio*, defined as the ratio of total (particle plus molecule) to molecular backscatter coefficients, δ is the volume linear depolarization ratio and δ^m is the molecular linear depolarization ratio.

Statistical error in lidar analyses is mainly due to signal detection noises and to operational procedures such signal averaging (Ansmann et al., 1992a; Bösenberg, 1998). Moreover, there is error propagation due to the application of the algorithm for the inversion of particle optical properties, and thus the analytical calculation of the uncertainties becomes very complex.

The usual technique to assess for this statistical error is based on Monte Carlo method, extracting new random lidar signals following a certain probability distribution with the measured mean and standard deviation. Then, a set of solutions are calculated with the same inversion algorithm from the generated signals, and the standard deviation is taken as the statistical error. This technique is accepted and systematically used in EARLINET (Guerrero-Rascado et al., 2008; Mattis et al., 2016; Pappalardo et al., 2004).

2.3.2 Active remote sensing of wind: Doppler lidar

The measurements of winds in the Earth's atmosphere by remote sensing have been performed with different approaches. Because of the small physical size of the laser beam and the shortness of the laser pulses, lidar has a big potential to make wind measurements with higher spatial and temporal resolution than other active methods as wind radars (also called wind profilers) and sodars.

There is a variety of approaches to estimate wind velocities with lidars, but they can be divided into correlation methods and Doppler spectral methods (Kovalev and Eichinger, 2004; Werner, 2005). The first group includes crosswind determination by pattern correlation (using the lidar ability to track structures in time), laser time of flight velocimetry (using two laser beams close to each other), or laser Doppler velocimetry.

All the techniques in the second group are based in the well-known Doppler effect, the change of perceived frequency of radiation when the source or the receiver move relative to one another. Measuring this frequency change, the relative speed of the source with respect to the medium can be determined. Lidar techniques based on this effect send laser radiation with frequency f_0 to the atmosphere and detect the backscattered radiation by aerosols (that are assumed to move with air with velocity v), shifted to the frequency $f_0 + \Delta f$:

$$f = f_0 + \Delta f = f_0 \cdot (1 + 2v_r/c) \quad (\text{II-29})$$

where c is the speed of light and v_r is the *radial velocity*, or velocity component along the line of sight (positive toward the lidar and vice versa). The measuring principle is depicted in Figure II-8.

The Doppler shift of the backscattered radiation is quite small relative to the outgoing pulse. As an example, a wind velocity of $30 \text{ m}\cdot\text{s}^{-1}$ would result in a Doppler shift of 10 MHz at a wavelength of $1.5 \mu\text{m}$.

Some Doppler lidar methods use direct detection (also called incoherent techniques) of this frequency shift, by different detection approaches as high-dispersion multichannel spectrometry or the use of filters such as Fabry-Perot interferometers or etalons operating in the edge of their transmission curve.

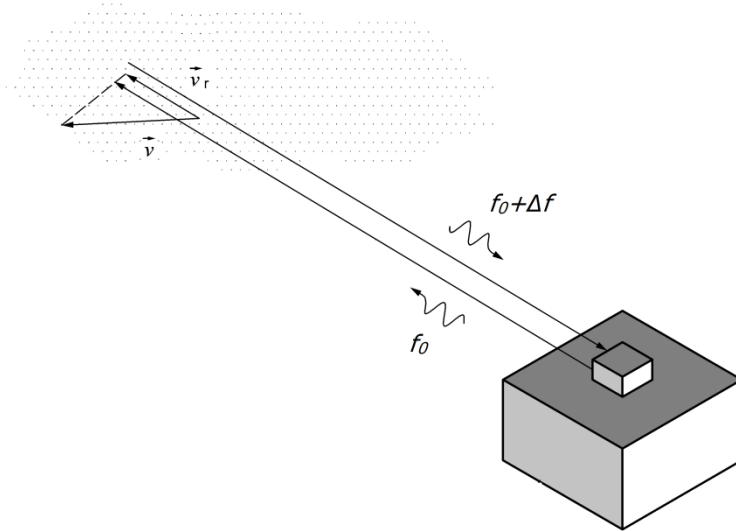


Figure II-8: Measurement principle of Doppler lidars.

The other option for measuring the frequency shift is demodulating the detected signal using optical mixing, so called *coherent detection*. In coherent Doppler lidar the backscattered radiation is mixed with light from a frequency-stable continuous-wave laser, i.e., the so-called local oscillator (LO). The mixed signal exhibits a temporal modulation in the amplitude that oscillates at the frequency difference between the two beams. This is the signal that is detected, and the modulation frequency indicates the Doppler shift (Grund et al., 2001).

As an example (Newsom, 2012), we assume a simple monochromatic backscattered field given by

$$E = A \cos(2\pi f t + \varphi) \quad (\text{II-30})$$

where A is the amplitude, f is the frequency, t is time, and φ is an arbitrary phase. The frequency is given by the known frequency of the outgoing pulse f_0 plus a small Doppler shift, i.e., $f = f_0 + \Delta f$

The LO field is similarly represented as:

$$E_{LO} = A_{LO} \cos(2\pi f_{LO} t + \varphi_{LO}) \quad (\text{II-31})$$

where f_{LO} is the known LO frequency. This specific coherent detection scheme, where the LO and the outgoing pulse frequencies (f_0 and f_{LO}) are different is also known as *heterodyne detection*. The irradiance at the photodetector, after mixing detected and LO signals is given by:

$$I \propto (E + E_{LO})^2 = E^2 + E_{LO}^2 + AA_{LO} \cos(2\pi f_+ t + \varphi_+) + AA_{LO} \cos(2\pi \delta f t + \delta \varphi) \quad (\text{II-32})$$

where the subscript $+$ means the sum of the backscattered and the LO frequencies or phases, and δ stands for the difference. The first three terms on the right-hand side of Equation (II-32) oscillate at optical frequencies, and thus fall well outside of the photodetector's pass band. The last term in Equation (II-32) oscillates at the difference frequency δf , which is typically on the order of 10 MHz and well within the detector's pass band. Thus, the signal coming off the photo-detector can be written as:

$$s(t) \propto \cos(2\pi \delta f t + \delta \varphi) \quad (\text{II-33})$$

where

$$\delta f = f - f_{LO} = \Delta f + f_0 - f_{LO} \quad (\text{II-34})$$

Equation (II-33) represents the raw heterodyne signal that is detected. By knowing the frequency difference between the outgoing pulse and the LO, it is possible to determine the Doppler shift of the backscattered radiation from an analysis of the Fourier transform of the raw heterodyne signal (Frehlich, 1999; Rye and Hardesty, 1993b, 1993a). In practice, the raw signal is first downmixed to baseband and then digitized at an appropriate sampling rate.

In addition to radial velocity, the Doppler lidar produces estimates of the wideband Signal-to-Noise-ratio (SNR), which by definition is the coherent signal divided by the noise in the full bandwidth.

III EXPERIMENTAL SITE AND INSTRUMENTATION

This thesis has been mostly developed using the instrumentation operated by the Atmospheric Physics Group (*Grupo de Física de la Atmósfera*, GFAT) at the experimental observatory AGORA (*Andalusian Global Observatory of the Atmosphere*). In particular, the instrumentation used were remote sensors located in the UGR station, at the Andalusian Institute for Earth System Research (IISTA-CEAMA) in Granada (37.16° N, 3.61° W, 680 m a.s.l.). In some cases, an additional station in Sierra Nevada mountain range was used, Cerro Poyos station (37.11° N, 3.49° W, 1830 m a.s.l., see Figure III-1) in order to characterize regional and long-range transport episodes with less influence of the urban background.

Granada is a medium-size city in southeastern Spain located in a natural basin delimited by Sierra Nevada mountain range, that reaches more than 3000 m a.s.l. This city is climatically characterized for having large seasonal temperature differences, with winter average minima of 2°C and summer average maxima of 33°C (according to Spanish Meteorological Agency, AEMET). It is a dry area, in terms of low relative humidity (year average of 57 %) and scarce precipitation (year average around 350 mm).



Figure III-1: Aerial view of the locations of IISTA-CEAMA (in the city of Granada), Armilla airbase station and Cerro Poyos station. Adapted from Google Maps.

Mean surface winds are also light (less than 2 m/s in average with more than 50 % of calms), coming predominantly from West and Northwest according to historical records (Bosque Maurel, 1959; Viedma Muñoz, 1998). Figure III-2 shows a wind rose obtained with diurnal and nocturnal measurements of wind speed and direction, obtained from AEMET database at Armilla airbase station (3.14 km apart from IISTA-CEAMA, see Figure III-1) for a period from 1992 to 2018. In that figure, a strong variation in the wind direction from day to nighttime is observed, with predominant southerly nocturnal winds. An important factor that characterizes the diurnal wind regime in Granada is the local mountain-valley thermal flow, that forms katabatic winds from Sierra Nevada mainly in the early night (Montávez et al., 2000).

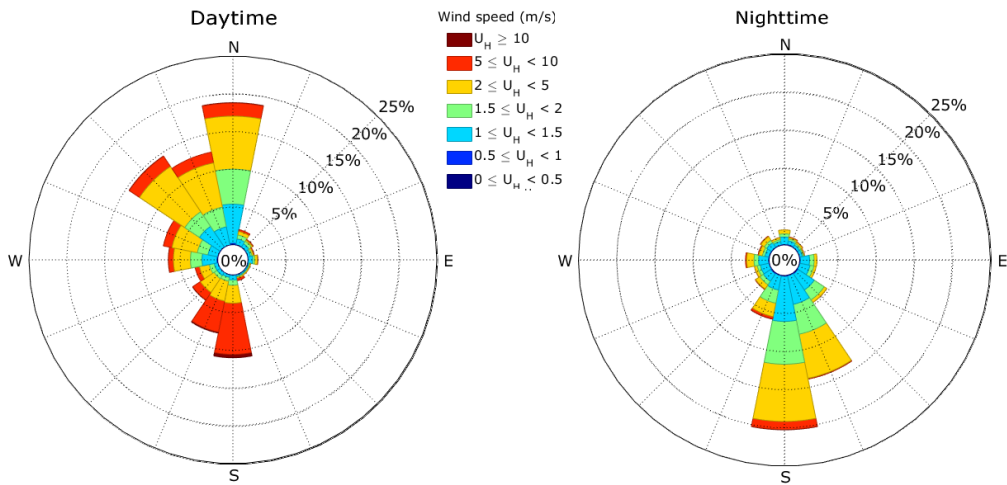


Figure III-2: Wind roses showing the prevailing wind speeds and directions in Granada during day and nighttime, with measurements obtained from AEMET database at Armilla airbase station from 1992 to 2018.

Concerning aerosol sources and types in Granada, there are differences between local and transported particles. Most part of the local aerosols are anthropogenic carbonaceous particles from road traffic, domestic heating and biomass burning (Lyamani et al., 2010; Titos et al., 2017), but pollen grains can also represent an important contribution (Cariñanos et al., 2014, 2016). Despite the short distance to Mediterranean Sea (around 50 km), the contribution of marine aerosols is negligible due to the natural barrier of Sierra Nevada mountain range (Titos et al., 2014b).

Transported aerosols are mainly mineral dust from Sahara Desert (Benavent-Oltra et al., 2017; Bravo-Aranda et al., 2013, 2015; Cazorla et al., 2017; Córdoba-Jabonero et al., 2011; Granados-Muñoz et al., 2014, 2016; Guerrero-Rascado et al., 2008, 2009; Horvath et al., 2018; Mandija et al., 2016, 2017; Sicard et al., 2019a; Soupiona et al., 2019), European mixed and anthropogenic aerosols, and biomass-burning particles from the northwestern Iberian Peninsula, North Africa and North America (Alados-Arboledas et al., 2011; Ortiz-Amezcuca et al., 2014, 2017; Sicard et al., 2019b).

The subsections below describe the remote sensing instrumentation used in this thesis, that are included in several

research networks, namely EARLINET, Cloudnet (Illingworth et al., 2007), AERONET (Aerosol Robotic Network) (Holben et al., 1998), and ICENET (Iberian Ceilometer Network) (Cazorla et al., 2017), and that contribute to ACTRIS (Aerosol, Clouds and Trace Gases Research Infrastructure).

3.1 ELASTIC-RAMAN LIDAR SYSTEM

The vertical profiles of particle optical and microphysical properties were obtained using the measurements from the multiwavelength Raman lidar system MULHACEN (Figure III-3), based on a LR331D400 manufactured by Raymetrics Inc. (with several upgrades). A technical description of the main instrumental features is detailed in Table III-1. It has monostatic biaxial alignment pointing vertically to the zenith. The light source is a Nd: YAG pulsed laser (Quantel CFR Series) with emission wavelengths at 1064, 532 and 355 nm and output energies of 110, 65 and 60 mJ, respectively.

The radiation is collected by a 40 cm-diameter Cassegrainian telescope, split into several detection branches with dichroic mirrors (DM) and then each detected wavelength is isolated with interference filters. The infrared (IR) channel detects the elastic signal at 1064 nm with an Avalanche Photodiode Detector (APD) working in analog (An) mode. The ultraviolet (UV) branch includes the elastic detection at 355 nm with a photomultiplier (PMT) working in An and photon-counting (Pc) modes (Hamamatsu, 2005), but also the detection of Raman shifted signals from nitrogen at 386.1 nm and from water vapor at 408 nm with PMT's in Pc mode. The visible (VIS) branch detects firstly the Raman shifted signal from nitrogen at 607 nm with a PMT in Pc mode, and then includes a polarizing beam splitter (PBS) for detecting parallel (P) and perpendicular (S) components of the elastic signal at 532 nm, with PMT's in An and Pc modes. Figure III-4 shows an scheme of the described optical detection branches.

The nominal spatial resolution of MULHACEN is 7.5 m and the maximum temporal resolution is 2 s. Due to the instrument

setup, the incomplete overlap between the emitted laser and the telescope field of view limits the lowest possible detection height to 500 m (Guerrero-Rascado et al., 2010b; Navas-Guzmán et al., 2011).

Table III-1: Technical details of the main optical elements of MULHACEN.

Emission	
Wavelength (nm)	355, 532, 1064
Pulse energy (mJ)	60, 65, 110
Pulse duration (ns)	8
Adjusted Pulse repetition rate, PRR (Hz)	10
Beam diameter/divergence (mm/rad)	6/0.1
Reception optics	
Telescope primary/secondary mirror diameter (mm)	400/90
Telescope focal length (mm)	3998
Interference filter wavelength (nm) and FWHM	355 (1.0), 386.1 (2.7), 408 (1.0), 532 (0.5), 607 (2.7) and 1064 (1.0)
Polarization beam splitter reflectance for p-component / transmittance for s component	0.995 / 0.99
Detection Unit	
Detector type	APD
Transient recorder	LICEL
Nominal Range resolution (m)	7.5
Temporal resolution (s)	2

This system was modified during this thesis, substituting the interference filter at 386.1 nm by a new one at 353.9 nm. However, the measurements taken with this new setup are only used in section 3.4, where a full description of the instrument modification is given. A more detailed description of MULHACEN before the implementation of the new filters can be found in (Bravo-Aranda et al., 2013; Guerrero-Rascado et al., 2008, 2009; Navas-Guzmán et al., 2013b).

The version of the instrument used in this thesis does not allow for continuous and unattended operation. Therefore the measurement database is limited, especially for Raman measurements that can be only done during nighttime. This system is part of EARLINET since 2005 and contributes to the ACTRIS research infrastructure.



Figure III-3: Multiwavelength Raman lidar system.

Regular quality checks (Belegante et al., 2018; Freudenthaler, 2016; Freudenthaler et al., 2018; Guerrero-Rascado et al., 2011c) have been performed during this thesis, with the support of ACTRIS-2 activities LiCoTest (Lidar Components Testing Laboratory) and LiReQA (Lidar Remote Quality Assurance). This activities are managed by the Lidar Calibration Centre (LiCal, <http://lical.inoe.ro/>, Pappalardo et al., 2016), a multi-installation facility located in Romania (National Institute of R&D for Optoelectronics, INOE), Germany (Ludwig Maximilians University – Meteorological Institute, LMU) and Italy (Institute of Methodologies for Environmental Analysis – National Research Council, CNR-IMAA).

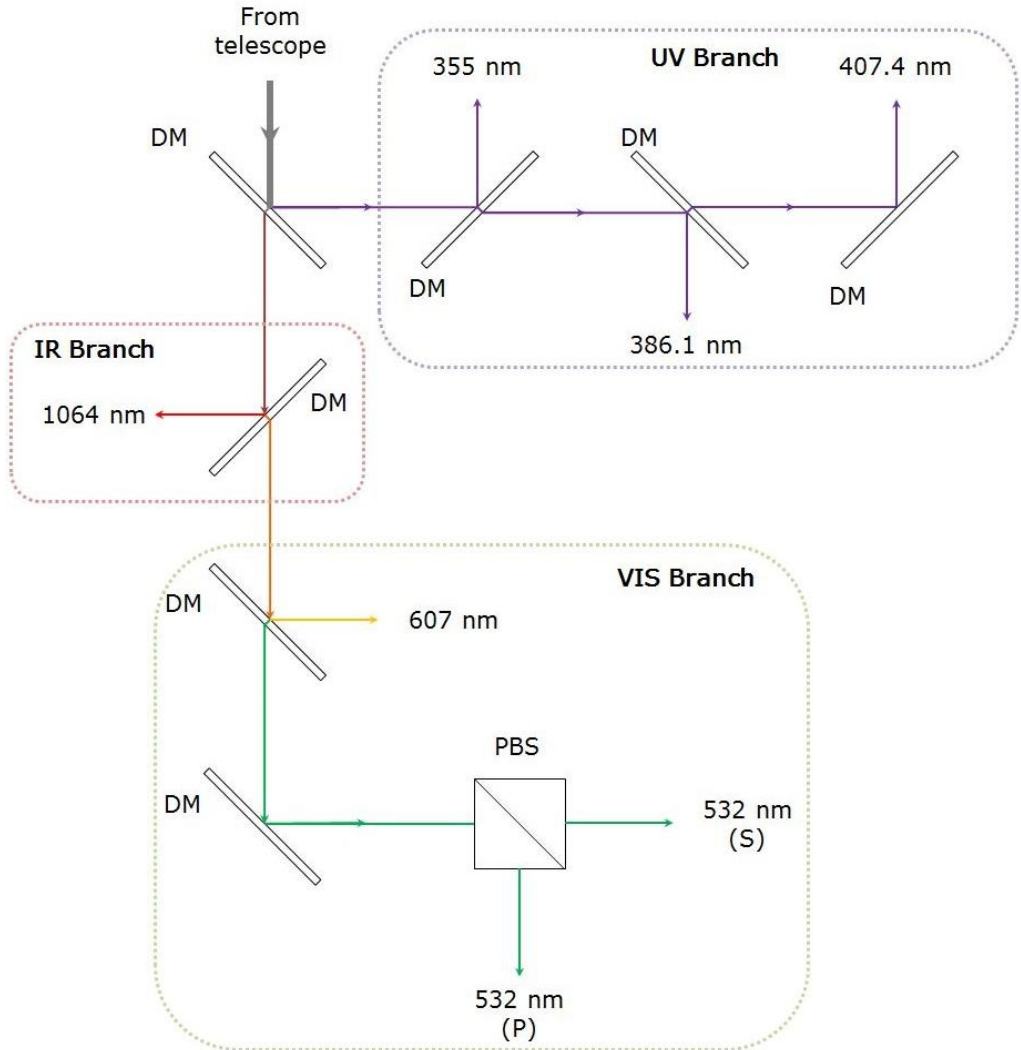


Figure III-4: Scheme of MULHACEN receiving optics, divided in three branches (UV, IR and VIS). Optical paths are represented by colored arrows, dichroic mirrors (DM) by thin rectangles and polarizing beam splitter (PBS) by divided square. Different wavelength values stand for the corresponding interference filters.

3.2 DOPPLER LIDAR SYSTEM

The vertical profiles of wind and of ABL turbulent properties in this thesis were obtained using the measurements of the Doppler lidar Stream Line (Halo Photonics, Figure III-5). In Table III-2, a description of the main instrumental features is

given. The system consist of a solid-state pulsed laser emitting at $1.5 \mu\text{m}$ and a heterodyne detector using fibre-optic technology. The emission is done with low pulse energy ($100 \mu\text{J}$) and high pulse repetition rate (15 kHz), what makes the instrument eye-safe. The signal acquisition is performed continuous and autonomously in vertical stare mode with a temporal resolution around 2 s , and it also has full hemispheric scanning capability. For the regular measurements, conical scans with constant elevation of 75° and 12 equidistant azimuth points have been performed every 10 min.



Figure III-5: Doppler lidar system on UGR station roof.

Some operational parameters can be configured by the user, but the instrument has been operating during this thesis at 30 m vertical resolution and an effective range from 90 m to $6000\text{-}9000 \text{ m}$. The focus of the optical system is set around 700 m , increasing the instrument sensitivity at this height, but reducing it above 2 km (see Section 3.5). A more detailed description of the instrument can be found in (Pearson et al., 2009).

Table III-2: Technical details of the main optical elements of the Doppler lidar system.

Emission	
Wavelength (nm)	1500
Pulse energy (μJ)	100
Pulse duration (ns)	200
Pulse repetition rate, PRR (kHz)	15
Reception optics	
Telescope	monostatic optic-fibre coupled
Lens diameter (cm)	8
Lens divergence (μrad)	33
Focal length (m)	700
Detection	
Detection type	Heterodyne
Range resolution (m)	30
Points per range bin	10
Sampling frequency (MHz)	50
Velocity resolution (ms^{-1})	0.0382
Nyquist velocity (ms^{-1})	20

3.3 ANCILLARY INSTRUMENTATION AND MODELLING TOOLS

In addition to the lidar systems described, other instruments (some of them also operated by GFAT at AGORA station) and model outputs were used in this thesis to compare, complement and/or support the analyses. These additional systems and tools are briefly described hereinafter.

3.3.1 Ceilometer

Ceilometer measurements have been used as ancillary source of vertical atmospheric profiles. The system CHM15k-Nimbus (Jenoptik S.A.) is installed at UGR station, and is a one-wavelength backscatter lidar with technical specifications allowing for unattended continuous operation. It consists of a pulsed Nd:YAG laser with fundamental emission at 1064 nm, a pulse energy of 8.4 μJ and a PRR in the range of 5-7 Hz. The instrument detects the elastically backscattered signal of molecules and particles with APD detectors in Pc mode and a LICEL Transient recorder. It operates with a spatial resolution

of 15 m and temporal resolution up to 15 s, although the usual operation is at 1 min time resolution. The manufacturer provides a default overlap function so that the 90 % complete overlap is obtained between 555 and 885 m above the instrument. A more detailed description of the system and its calibration and products can be found in (Cazorla et al., 2017).

3.3.2 Sun/sky/lunar-photometer

Column-integrated aerosol properties have been obtained by means of the standard AERONET photometers CIMEL CE318 (Cimel Electronique). From 2004 to 2011, CE318-4 model was in operation at UGR station taking diurnal Sun and sky measurements and processing the data at AERONET server. From 2011 to 2016, the model was CE318-NE, with the same operation procedure. A CE318-T model started to operate in 2016 in order to extend the diurnal performance to nocturnal measurements. Their optical design is similar, consisting of an optical head with two collimators, a robotic arm for Sun tracking and sky positioning and an electronic box.

In the diurnal mode, both photometers perform direct Sun irradiance and sky radiance measurements with a 1.2° full field of view every 15 min at nominal wavelengths of 340, 380, 440, 500, 675, 870, 940 and 1020 nm. The sky radiances are measured in the principal plane (measurements at different zenith angles with fixed azimuth angle) and almucantar configuration (different azimuth angles with constant zenith angle). In CE318-T model, principal plane measurements are replaced by hybrid plane observations, a mix between principal and almucantar planes.

In the nocturnal mode, CE318-T measures the lunar irradiance at nominal wavelengths of 440, 500, 670, 870, 1020 and 1640 nm. A sequence of three measurements of the radiation reflected by the Moon is taken every 30 s at each wavelength. Aerosol optical depth (*AOD*) is obtained from these irradiances following the method of Barreto et al. (2016), which uses the ROLO model (Kieffer and Stone, 2005) to calculate the lunar extraterrestrial irradiance. Barreto et al. (2019) showed that

the *AOD* uncertainty with this method is dependent on the calibration technique, ranging from 0.012 up to 0.1. The nocturnal measurements can be taken during 50% of the Moon cycle, extending the diurnal measurements during this period.

The calibration of the photometers is annually carried out by RIMA network (*Red Ibérica de Medida fotométrica de Aerosoles*, www.rima.uva.es), which is also one of the Central Facilities of ACTRIS infrastructure and AERONET-EUROPE, so-called GOA Calibration Facility. The diurnal photometric measurements are automatically transferred to the GOA Calibration Facility, where they are processed by the AERONET algorithm (Dubovik and King, 2000; Holben et al., 1998), that has several versions. In this thesis, AERONET algorithm Version 2 is used, and the data provided have several quality levels: Level 1.0, corresponding to unscreened data; Level 1.5, corresponding to cloud-screened data and Level 2.0, corresponding to reprocessed data after calibration and manual check to fulfill a set of criteria (Holben et al., 2006).

Dubovik et al. (2000) described the uncertainty of the AERONET inversion products. According to them, errors in size distributions are around 10-35 % for particles in the size range [0.1, 7] μm , while for sizes outside this range retrieval errors rise up to 80-100%. The uncertainty in the *SSA* retrieval is <0.03 , and in the *IRI* is about 30-50% for data products of Version 2 Level 2.0. The products Version 2 Level 1.5 accuracy levels drop down to 0.05-0.07 for *SSA*, to 80-100% for the *IRI* and to 0.05 for the *RRI*.

3.3.3 Star-photometer

In some parts of this thesis, nocturnal photometric measurements measured with a star-photometer were also used. The system, called EXCALIBUR, was designed by GFAT and Andalusian Institute of Astrophysics (IAA) (Pérez-Ramírez et al., 2008), and consists of a Schmid-Cassegrain telescope with a CCD Camera SBIG ST-8XME as a detector. Starlight collected by the telescope passes through a filter wheel with narrowband filters at 380, 440, 500, 670, 880, 940 and 1020

nm. The target star is selected using astronomical coordinates, and then, a 'centre field' routine is used to move the telescope so that the brightest point falls into the central pixels of the CCD camera.

A detailed description including the data analysis technique is given by Pérez-Ramírez et al. (2008) and references therein.

3.3.4 CALIOP lidar onboard CALIPSO satellite

The observations of the spaceborne CALIOP (Cloud-Aerosol Lidar with Orthogonal Polarization) were used in several studies carried out during this thesis to track the aerosol plumes during their transport. This lidar system, with two wavelengths (532 and 1064 nm), polarization channels at 532 nm, an infrared radiation radiometer and a wide-field camera, is onboard the CALIPSO (Cloud-Aerosol Lidar and Infrared Pathfinder Satellite Observation) mission, launched in 2006. Its main products are attenuated backscatter profiles and also clouds and aerosol information together with layer properties (Winker et al., 2009).

3.3.5 HYSPLIT model

The analysis of backward trajectories (temporal evolution of the coordinates of a certain air parcel before reaching its position at the study time) has been widely used in this thesis in order to characterize the origin and followed path of the air masses analyzed with the remote sensing instruments. This analysis was performed by means of the HYSPLIT model (Hybrid Single-Particle Lagrangian Integrated Trajectory; Rolph, 2016; Stein et al., 2015) developed by the NOAA (National Oceanographic and Atmospheric Administration) in collaboration with Australia's Bureau of Meteorology. The meteorological database used for the calculations was the GDAS (Global Data Assimilation System) database.

Three types of multiple trajectory analyses were carried out for the different studies in this thesis: single trajectories, ensemble calculation and cluster analysis. The single trajectories are usually calculated for several altitudes using the meteorological

database and the trajectory model. The ensemble form of the model is used to trace back the history of the detected layers with the objective of improving plume simulations and accounting for possible uncertainties. With this method, multiple trajectories start from the selected starting point, and each member of the trajectory ensemble is calculated by offsetting the meteorological data by a fixed grid factor, resulting in 27 members for all possible offsets in longitude, latitude and altitude. Finally, for the illustration of airflow patterns in order to interpret the transport over different spatial and temporal ranges, trajectories that have some commonalities in space and time can be merged into groups, called clusters, and represented by their mean trajectory. Differences between trajectories within a cluster are minimized while differences between clusters are maximized (Draxler et al., 2009).

3.4 IMPLEMENTATION OF ROTATIONAL RAMAN CHANNELS TO IMPROVE AEROSOL RETRIEVALS

In lidar applications, Raman effect between vibrational energy states of molecules (vibrational Raman, VR) is widely used. In particular, Raman scattering from N_2 and O_2 provides additional information to the elastic scattered lidar signal that makes possible the independent retrieval of particle extinction (α^a) and backscatter (β^a) coefficients (Ansmann et al., 1990, 1992a), as we showed in Section 2.3.1. This reduces the errors introduced with Klett-Fernald method for elastic lidars, since Raman signal constitutes an additional information vector and less assumptions must be taken. Moreover, vertical profiles of particle lidar ratio (LR^a) can be retrieved and used as an indicator of the aerosol type. Another advantage of Raman method is that it can be used to determine the overlap function, an experimental function to correct system alignment and unknown parameters (Wandinger and Ansmann, 2002).

Lidar systems that are part of lidar networks as EARLINET or LALINET (Latin American Lidar Network) (Antuña-Marrero et

al., 2017; Guerrero-Rascado et al., 2016) usually measure wavelengths corresponding to VR effect, but there are some disadvantages. On one hand, the SNR is very low for the power of the lasers commonly used, what makes the retrieval of aerosol optical properties quite noisy. In order to increase this SNR, the signals are usually collected during certain integration time, resulting in profiles with temporal resolution of 30-60 min during nighttime. Daytime retrievals are not usually available for VR systems, excepting those with very powerful lasers (e.g. Goldsmith et al., 1998). On the other hand, the significant wavelength shift of the scattered radiation (30 -75 nm) is an important source of uncertainty in α^a and β^a calculation, since the spectral dependence of the radiation has to be assumed (Ansmann et al., 1992b).

The issues of VR can be overcome by measuring at wavelengths corresponding to the pure rotational energy states (rotational Raman, RR) of the considered molecules. These spectral lines present much higher SNR, thus allowing for detection of much less noisy Raman signals. Therefore, they need shorter integration time and the temporal resolution of the retrieved profiles can be around 1-5 min during nighttime, as it is shown in this section. This technique allows even for diurnal retrievals (Arshinov et al., 2005; Zeyn et al., 2008), with temporal resolution of 60 min in our case. Another advantage is the significantly smaller wavelength shift for RR (a few nm) than for VR. This means that the assumption needed for Raman inversion method, that particle extinction-related Angström Exponent (AE_α) equals 1, introduces much smaller α^a and β^a uncertainties.

RR measurements have already been used for lidar applications, very often to obtain temperature profiles (e.g. Chen et al., 2015; Di Girolamo et al., 2004, 2006; Kim and Cha, 2007; Vaughan et al., 1993; Wu et al., 2016). However, when the aim of the lidar measurements is to retrieve α^a and β^a profiles, the temperature dependence of RR lines becomes an issue. This has already been overcome using different approaches, like collecting signals from lines with opposite

temperature dependence (Di Girolamo et al., 2006; Kim and Cha, 2007). The approach used in this section was already presented by Veselovskii et al. (2015b) for 532 nm and by Haarig et al. (2016) for 1064 nm and is based on selecting only a part of the spectrum with low temperature sensitivity. The main advantage of this method is that the implementation of the RR channel can be done with few modifications on an existing VR lidar.

3.4.1 Instrumental modification

In order to measure RR signals to improve α^a and β^a retrievals, the UV detection branch of MULHACEN system was modified (see scheme of the detection branches in Figure III-4).

Table III-3: Technical details of some optical elements of MULHACEN emitter system and UV detection branch.

Optical system (UV branch)	
Interference filter wavelengths, nm (FWHM, nm /Tmax, %)	355 (1.0/57), 353.9 (0.8/59), 407.4 (1.0/67)
Dichroic mirrors transmittance (T) or reflectance (R) , % (wavelength)	
DM1	R > 99% (< 410 nm)
DM2	R > 15% (407.4 nm), T > 90% (< 360 nm)
DM3	R > 96% (353.9 nm)
DM4	R > 99% (355 nm)

The 386.1 nm interference filter was substituted in December 2016 by a filter centered in 353.9 nm. With this filter, it was possible to detect some lines of the rotational Raman spectra of N₂ and O₂. Figure III-6 shows those spectral lines obtained from Compaan et al. (1994) for a laser wavelength of 355 nm. The filter transmittance is also included in the figure, to show the selected lines. A new configuration of dichroic mirrors was necessary in order to get enough intense signals for all channels. With this new setup (Figure III-7), a total transmittance close to 90% was achieved for the rotational Raman channel, without losing elastic and water vapor

channels signals. A detailed description of the interference filters and dichroic mirrors (DM) is presented in Table III-3.

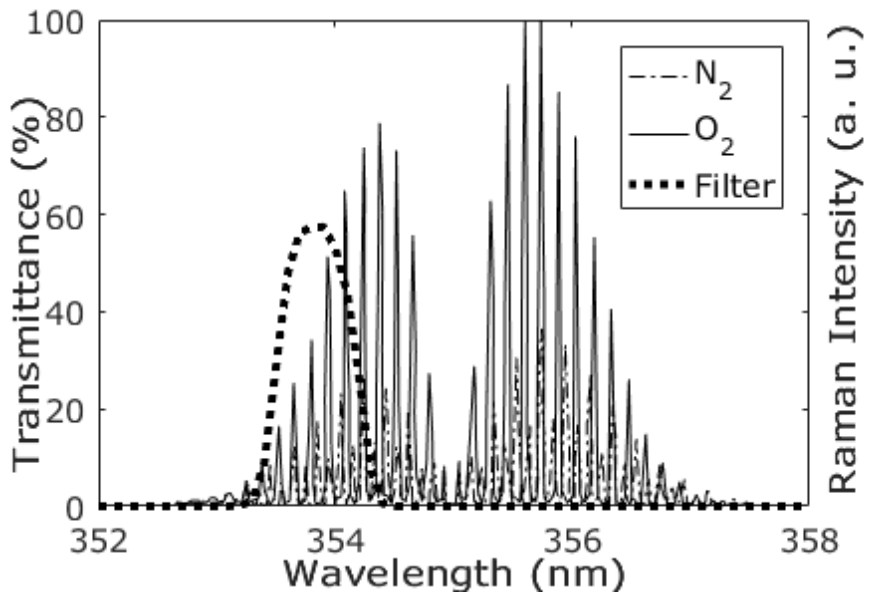


Figure III-6: Rotational Raman spectral lines (intensity in arbitrary units) of molecular oxygen (solid line) and nitrogen (dash-dot line) at 300 K, together with interference filter transmittance (dotted line).

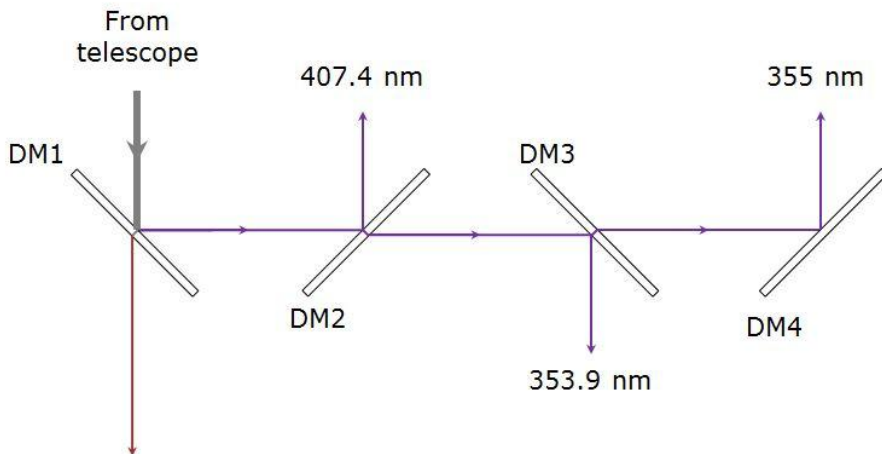


Figure III-7: Configuration of the UV detection branch of MULHACEN lidar system. Optical paths are represented by arrows and dichroic mirrors (DM). Different wavelength values stand for the corresponding interference filters.

3.4.2 Systematic error due to temperature dependence

In equations (II-26 and (II-27), the terms $X(z)$ and $\Delta\alpha = \frac{1}{2} \frac{d}{dz} \ln F_R(z, \lambda)$ depend on the effective differential cross section of the atmosphere (that contains the contribution of the individual RR lines of N_2 and O_2). Since the intensity of these lines are temperature-dependent, the retrieved α^a and β^a profiles present a systematic error that could be significant if the temperature gradient with altitude is strong. This effect does not appear for vibrational Raman scattering, where terms $X(z)$ and $\frac{1}{2} \frac{d}{dz} \ln F_R(z, \lambda)$ can be assumed to be 1 and 0, respectively.

Veselovskii et al. (2015b) showed that this temperature effect is small for an emission of 532.12 nm and a pure-rotational Raman filter selecting a certain spectral range. They obtained a relative error in aerosol backscatter coefficient below 1 %, and absolute error of aerosol extinction coefficient below 2 Mm^{-1} for heights up to 10 km. A similar procedure has been applied in the present work for an emission at 355 nm and the implemented RR interference filter.

For β^a , the relative error (ε_β) introduced if temperature dependence is neglected can be calculated from Equation (II-26) when $X(z) = 1$, obtaining for high aerosol loads ($\beta^a \gg \beta^m$) that $\varepsilon_\beta \approx \frac{X-1}{X}$. We calculated this ε_β for our interference filter and temperatures varying in the range 230-300 K (Figure III-8a). Therefore, it can be concluded that we can neglect the temperature dependence for β^a calculation, introducing an additional uncertainty of less than 4%.

For α^a , we have estimated the error due to temperature ($\Delta\alpha$) using the temperature variation with height, given by the US Standard Atmosphere (1976) model. The results of this simulation are shown in Figure III-8b, where we can see an always negative contribution up to -1.6 Mm^{-1} . This means that the uncertainty introduced by neglecting this term is less than 2% for $\alpha^a > 80 \text{ Mm}^{-1}$.

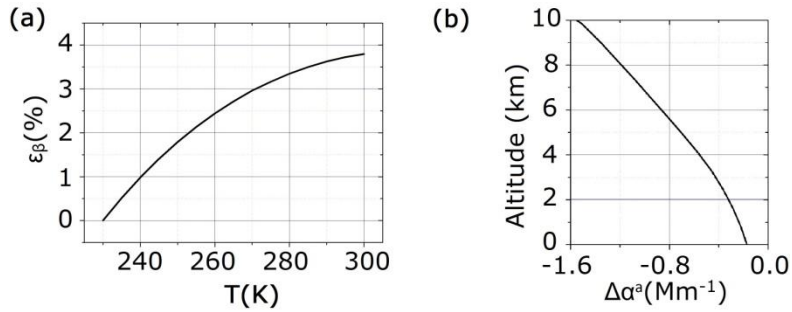


Figure III-8: (a) Relative error in β^a due to temperature for usual tropospheric temperature range. (b) Absolute error in α^a due to temperature variations with altitude, using US Standard Atmosphere (1976) temperature profile.

3.4.3 Elastic crosstalk avoidance

Another possible error source is the measurement of some elastic signal by the detector at the RR channel. This is known as elastic crosstalk, and it could appear in our system due to the close RR and elastic wavelengths, and the bandwidth of the interference filters. This effect has been tested by analyzing both signals under cloudy conditions, when the elastic signal is very strong (scattering ratio can be around 300 or more). In Figure III-9, the elastic and RR range-corrected signals (RCS) measured in an example of such test are depicted, together with the modelled molecular signal. During the measurement, some aerosol load was present until 4 km a.s.l., and the cloud base was at 4.5 km a.s.l. The strong enhancement of the elastic signal can be observed, while the RR signal remains unperturbed. We can then be sure that the elastic crosstalk is negligible in our system even for strong elastic signals.

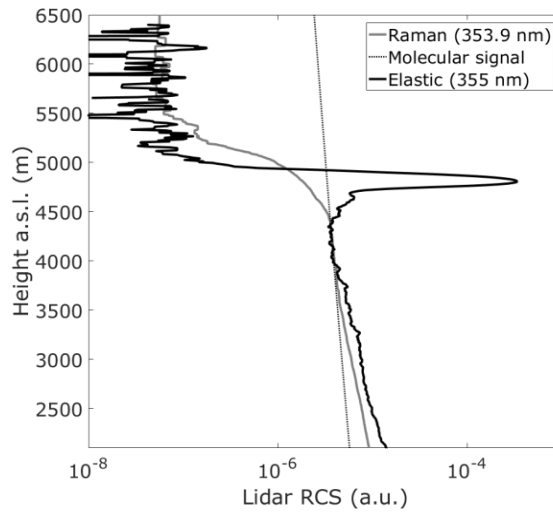


Figure III-9: Range-corrected elastic (355 nm, black solid line) and Raman (353.9 nm, grey solid line) lidar signals in the presence of clouds. Modelled molecular backscattering is indicated by dotted line.

3.4.4 Test cases

Several cases were analyzed to evaluate the performance of the new lidar setup. The examples correspond to measurements on 25th June 2018 during night and daytime. This case was selected because the aerosol load and type was the usual for Granada (Lyamani et al., 2010), with AOD around 0.35 at 440 nm and AE_{AOD} around 0.6 at 440-870 nm. In Figure III-10 we can see the evolution of the lidar RCS at 532 nm (a), and of the AOD and AE_{AOD} (b) obtained from AERONET (Holben et al., 1998) during daytime and using the algorithm described in Barreto et al. (2016) during nighttime. It can be seen that the aerosol load was roughly constant during the whole day, with only a small decrease during the first hours of the night.

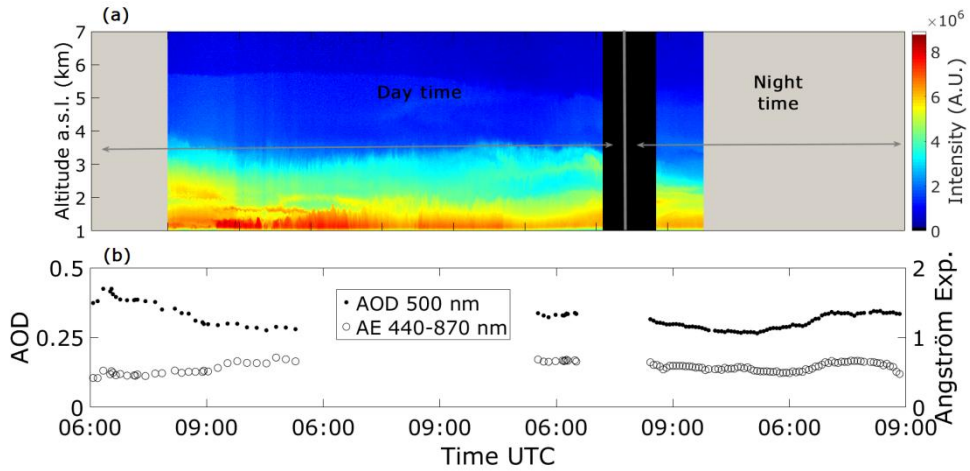


Figure III-10: (a) Time evolution of measured lidar RCS on 25th June 2018 from day to nighttime. (b) Time evolution of AOD at 500 nm and AE_{AOD} at 440-870 nm, measured with triple photometer.

With this dataset, we performed two different evaluations. Firstly, the nocturnal signals were averaged using different integration times with the aim of reducing the usual 30 min intervals. In the second part, diurnal signals were used to obtain profiles of optical properties, with a time resolution of 1 h. These profiles were then compared with the nocturnal ones, taking into account the small variations expected in the view of Figure III-10.

Figure III-11 shows the retrieved optical properties, i.e., α^a , β^a and LR^a , for the time interval from 20:34 to 21:04 UTC. The black thick lines stand for the profiles obtained from signals previously averaged for the whole period, as it was usually done for our VR lidar system. However, the increase of SNR due to RR detection allowed us to calculate the optical properties with integration times down to 1 min. The results are shown with dots in the same figure, and the differences observed with the 30-min-integrated profiles are up to 20 % for α^a and β^a , and up to 30 % for LR^a . The average of the 1-min-integrated optical profiles (represented as dashed lines) differ less than 10 % for all profiles below 2 km a.s.l., thus we could interpret the 1-min differences as part of the real variability of the atmosphere.

In Figure III-12, the time evolution of the α^a and β^a profiles with 1 min temporal resolution is shown. With this resolution, certain thin structures can be detected.

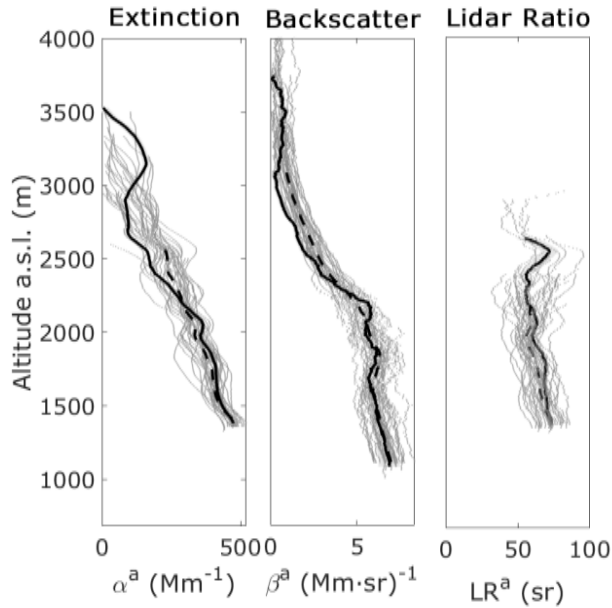


Figure III-11: Nocturnal profiles of particle backscatter and extinction coefficients and lidar ratio for a 30-min time interval (thick lines), together with profiles obtained with 1-min resolution (dots) and their average (dashed lines).

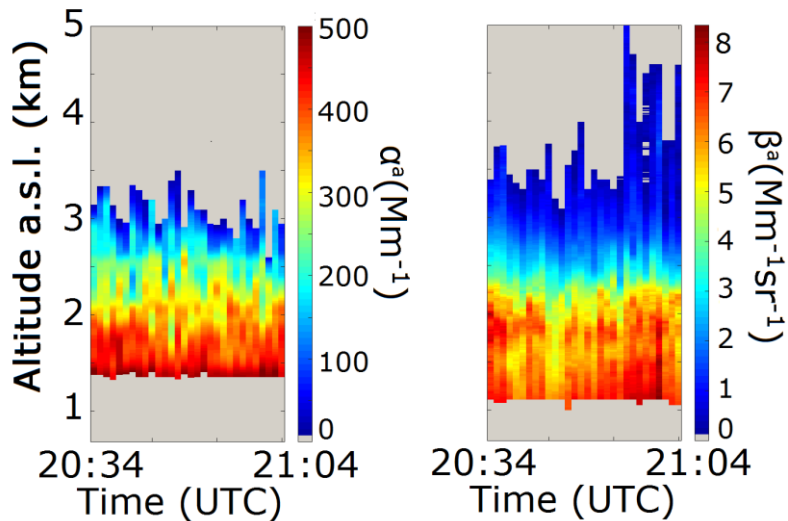


Figure III-12: Temporal evolution of particle extinction and backscatter coefficients during a nocturnal period, with 1 min resolution.

For the diurnal measurements, it was necessary the use of hourly signal averages in order to increase the SNR. The resulting elastic and RR signals allowed for obtaining aerosol optical properties with the Raman algorithm. The overlap function could also be calculated using the method in Wandinger and Ansmann (2002). The retrieval of such correction during daytime is an added value even to apply it to the elastic signals in Klett-Fernald inversions. In spite of this correction, the signal quality was not good enough to retrieve β^a values below 320 m (1 km a.s.l.) and α^a values below 720 m (1.4 km a.s.l.).

In order to check the reliability of the retrieved profiles, the elastic signal was also processed with Klett-Fernald algorithm, although only β^a can be compared using this method. For these elastic retrievals, the reference height in Equation (II-24) (let us call it $z_{0,KF}$ for Klett-Fernald algorithm) was selected between 6.5 and 7 km a.s.l. to ensure that $\beta_{KF}^a(z_{0,KF}) \approx 0 \text{ m}^{-1}\text{sr}^{-1}$ (see Figure III-10). The RR signals did not have enough quality at that height, and thus the reference height for Raman method in Equation (II-26) (let us call it $z_{0,R}$) was selected in the range between 2.5 and 3 km a.s.l., calibrating the retrieved β_R^a profiles so that $\beta_R^a(z_{0,R}) = \beta_{KF}^a(z_{0,KF})$. The constant LR^a values selected for Klett-Fernald algorithm were between 55 and 80 sr, selecting in each case the average of the profiles obtained with Raman method. The validation for α^a profiles was done by comparing their height-integral (AOD_{lidar}) with the AOD from AERONET (AOD_{AER}), interpolated to 355 nm.

Figure III-13 and Figure III-14 show the obtained α^a and β^a profiles from 8:14 to 19:14 UTC with 1 h time resolution. For the sake of clarity, error bars have not been plotted, but the obtained uncertainties were around 10-20 % for the statistical part (we should also add 2 % and 4 % in the α^a and β^a uncertainties, respectively, to include the temperature-derived uncertainty, as shown in Section 3.4.2).

The comparison of AOD_{lidar} versus AOD_{AER} gave us mean differences of 30 %, being the minimum differences (around 15

%) in the latests hours, when the background signal is smaller. These differences are reasonable, taking into account that the first 720 m of the α^a profiles were not included because of incomplete overlap effect in lidar (despite the correction applied). On the other hand, the comparison between β_{KF}^a and β_R^a gave differences less than 10 % at altitudes from 1 to 2 km a.s.l. and less than 20 % for higher altitudes.

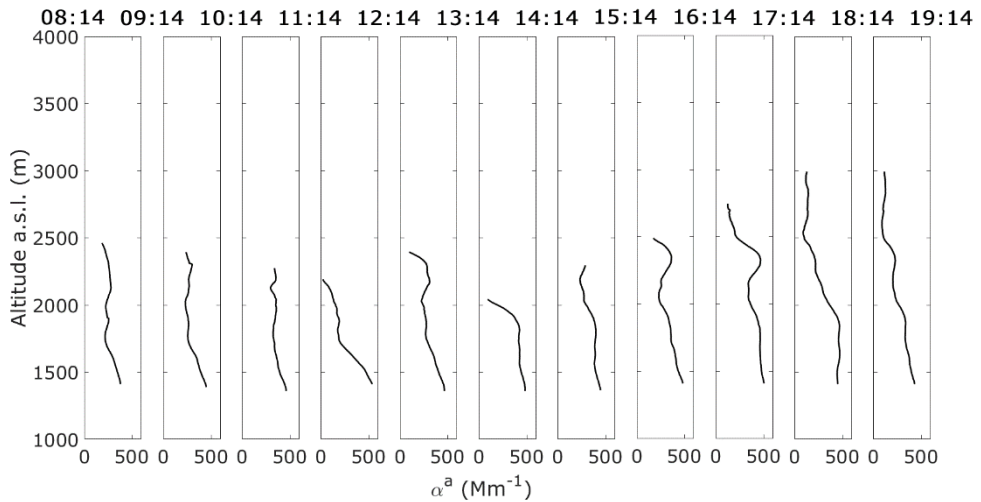


Figure III-13: Particle extinction coefficient retrieved with Raman signals during daytime for 25th June 2018.

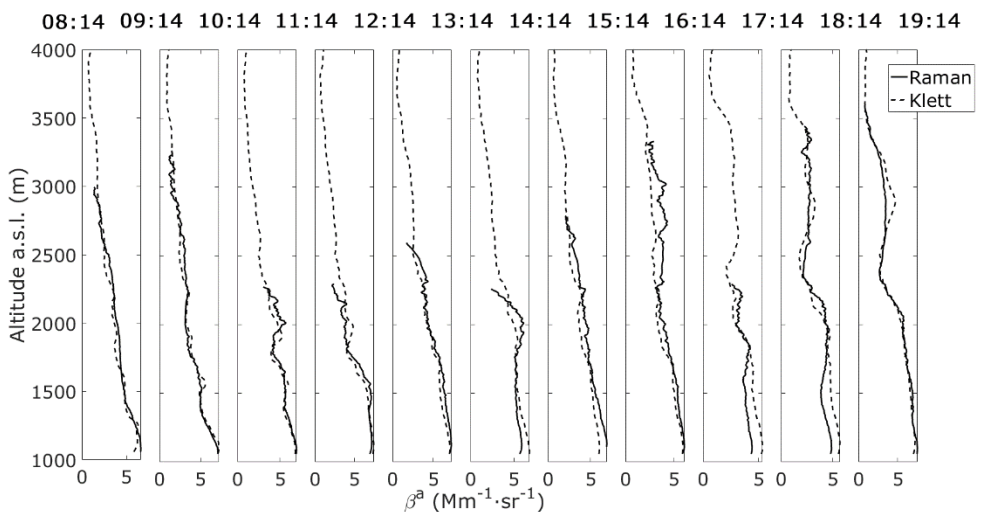


Figure III-14: Particle backscatter coefficient retrieved with Raman (solid lines) and elastic (dashed lines) signals during daytime for 25th June 2018.

The last part of the diurnal profiles validation was to compare two close retrievals, one corresponding to daytime and another to nighttime. This is the case of 18:14 – 19:14 UTC (diurnal) and 20:34 – 21:04 UTC (nocturnal). Optical properties, together with the calculated overlap function are shown in Figure III–15. There is an evident agreement between diurnal and nocturnal profile, except for the β^a above 2.5 km a.s.l. However, it can be seen in the RCS time evolution (Figure III–10) that the aerosol load in this part of the profile actually disappears during nighttime.

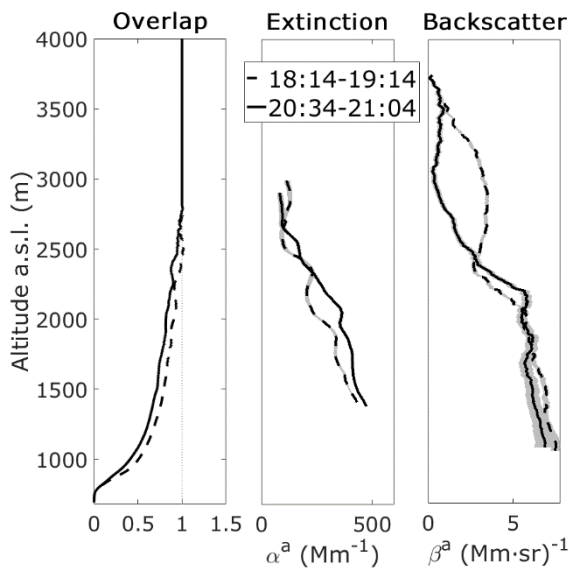


Figure III–15: Particle backscatter and extinction coefficients retrieved with Raman signals during two close intervals (daytime and nighttime) for 25th June 2018.

3.5 CALIBRATION OF THE DOPPLER LIDAR SIGNAL

The Doppler lidar system used in this thesis (Halo Photonics Stream Line model, see section 3.2) provides profiles of backscattered radiation intensity in terms of SNR together with profiles of radial wind velocity obtained from the Doppler shift of the backscattered radiation (section 2.3.2). These profiles

are retrieved with high temporal resolution, allowing for using them to determine turbulent properties of the ABL.

The instrument performs a periodical signal background noise determination (typically every hour), but Manninen et al. (2016) and Vakkari et al. (2019) showed that further post-processing is needed to properly calculate SNR profiles with high temporal resolution. Moreover, the instrument optics are configured so that the focus is set around 700 m to increase the sensitivity in the ABL, but this implies an additional range-dependent bias of the detected signals (Hill, 2018). Those issues do not affect radial velocity measurements (related to signal frequency and not to intensity), but they directly bias the radial velocity uncertainty estimates and therefore, turbulent properties as the TKE dissipation rate (O'Connor et al., 2010). The corrected SNR is also used to calculate attenuated backscatter (β_{att}), which is used by the algorithm applied in this thesis to classify turbulent mixing sources (subsection 6.1.2).

In this section, we describe the application of the Doppler lidar signal correction algorithms to the data measured by the Halo system at UGR station. Those algorithms have been developed in the Finnish Meteorological Institute (FMI, Helsinki, Finland) in the framework of Cloudnet activities within ACTRIS, and tested with different Doppler lidars systems in several locations as Finland, Greece, South Africa or Germany (Manninen et al., 2016, 2018; Tuononen et al., 2017; Vakkari et al., 2019). In subsection 3.5.1, the improvement of the background noise retrieval is applied. In subsection 3.5.2, we have applied a method to determine the necessary instrumental parameters to apply the focus correction to the signal.

3.5.1 Background correction

Manninen et al. (2016) and Vakkari et al. (2019) detected two different artifacts in the Doppler lidar output signals from different Halo systems, and created algorithms to correct those artifacts.

The first one is the presence of step changes in the background which normally occur due to the periodic background determinations carried out by the instrument (typically every hour). These biases become visible as vertical stripes in the signal, as can be observed for instance between 15 h and 17 h UTC in the example shown in the solid black box in Figure III-16a. The method developed by Manninen et al. (2016) detects and corrects those step changes after signal cloud- and aerosol-screening.

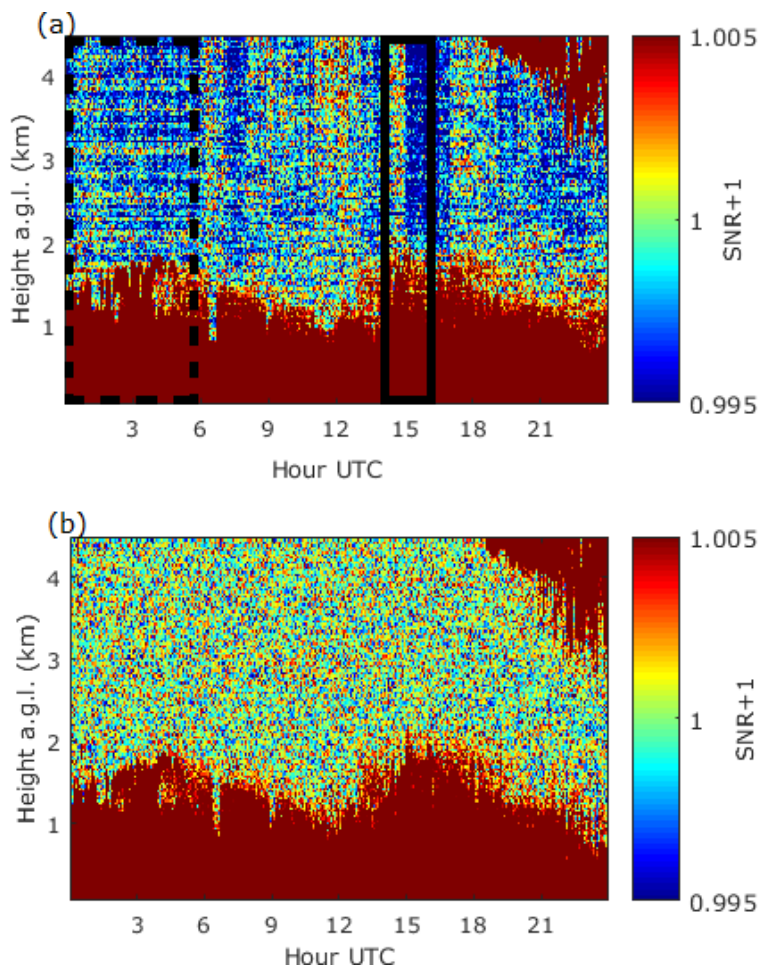


Figure III-16: Time evolution of backscattered signal intensity measured by Doppler lidar on 21st April 2016 in vertically pointing mode. (a) Signal before post-processing and (b) Background-processed signal. Black solid and dashed boxes correspond to artifacts described by Manninen et al. (2016) and Vakkari et al. (2019), respectively.

The second signal artifact is the presence of persistent residual structures that vary with range and are originated in the amplifier response of the transmitted pulse (Vakkari et al., 2019). The biases produced in the signals can be observed as horizontal stripes that are constant between two instrument background checks, as for instance before 6 h UTC in dashed black box in Figure III-16a. Vakkari et al. (2019) developed an algorithm for correcting this effect and combined it with the previous signal screening and step correction algorithm.

We applied the final algorithm with both corrections to data measured with our Halo Doppler lidar system at UGR station with satisfactory results, showing the robustness of the scripts for different Halo systems. The final effect of the corrections can be observed in Figure III-16b. Thanks to these corrections, the noise can be more easily separated from the measured signal and the calculated SNR is directly used to calculate radial velocity uncertainties and turbulent properties (O'Connor et al., 2010).

3.5.2 Focus correction

The usual configuration of ground-based Doppler lidars is optimized for ABL observation by focusing the instrument optics around ABL region. This has an effect on instrument sensitivity, increasing it around the focus height and decreasing it above that height. For a Gaussian beam, this sensitivity or collection efficiency follows a Lorentzian function, although Lindelöw (2008) proposed a slightly different model. Figure III-17 shows examples of the relative effect on the instrument sensitivity following Lorentzian and Lindelöw models for different focal lengths.

This effect has to be corrected (in addition to the background corrections presented before) if the backscattered signal intensity is used to calculate β_{att} . The correction can be done by using one of the mentioned models as e.g. in Hill (2018), but the actual focus height (f_h) and also the system lens diameter (l) have to be known. The manufacturer provides those values (included in Table III-2 for the system used in

this thesis), but we checked that they may not coincide with the actual values. For this reason, we propose here in collaboration with Doppler lidar group at FMI a method to calibrate the signals and calculate the actual focal length and lens diameter as calibration parameters.

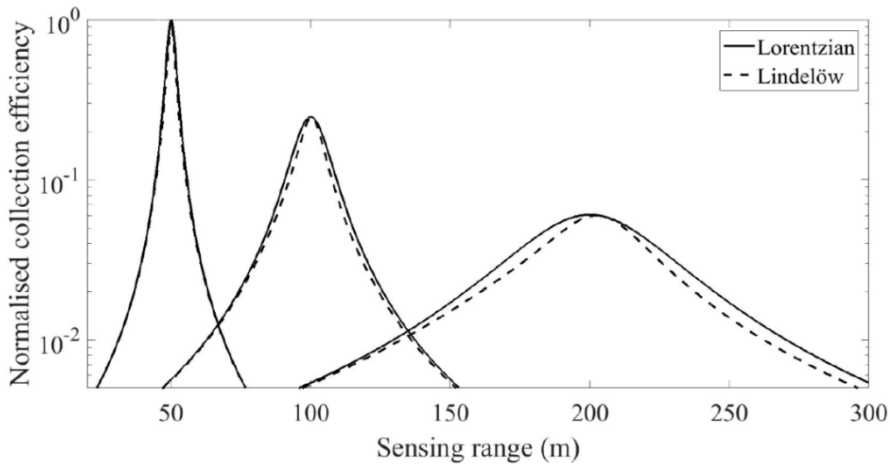


Figure III-17: Normalised curves of range dependence for three different fixed focus ranges (50 m, 100 m, 200 m), calculated with Lorentzian (solid lines) and Lindelöw (dashed lines) models. From (Hill, 2018).

The method is based on comparing Doppler lidar signals from a certain dataset with simultaneous signals from a co-located ceilometer. We followed the subsequent steps:

1. Doppler lidar and ceilometer data are homogenized in terms of range and time. To this end, 10-min temporal averages are taken for both instruments and the height resolutions are interpolated (to the one with less resolution, the Doppler lidar in our case).
2. For each 10-min averaged profile, different corrected Doppler lidar signals are calculated in an iterative process using several f_h and l values in a certain range.
3. Certain height ranges are also selected in an iterative process and linear correlations between Doppler lidar and ceilometer profiles are calculated for each height range, as first order approximation taking into account the different measured wavelengths. Figure III-18 shows an example of the resulting R^2 grid for f_h between

400 m and 1000 m and l between 0.039 m and 0.076 m (with respective steps of 10 m and 0.001 m), for measurements taken at UGR station with Halo Doppler lidar and the ceilometer described in 3.3.1.

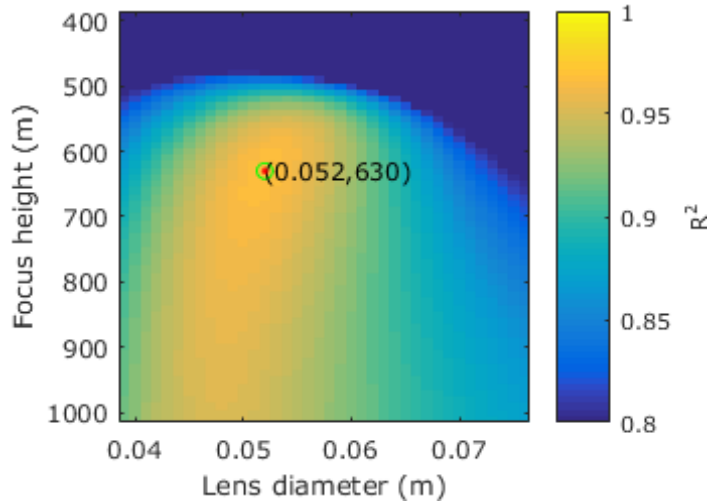


Figure III-18: Determination of the instrument lens diameter and focus height (red dot and values in brackets) for an example measurement at UGR station. Each pixel stands for a linear correlation between the corrected Doppler signal (with certain focus height and lens diameter values) and the simultaneous ceilometer signal.

4. The best f_h and l values are then selected for each height range using the best linear correlation in terms of R^2 , and then the best height range is selected for a single 10-min profile.

In order to include possible variations of the calibration parameters, we performed a statistical analysis using a dataset of Doppler lidar and ceilometer measurements from 26th June to 5th July 2017, rejecting profiles with clouds to avoid comparison of saturated profiles. We selected a height range width of 1000 m for comparing Doppler lidar and ceilometer profiles in the iteration described in step 3, for heights between 0 and 1500 m a.g.l. Figure III-19 shows the relative frequency with which each height range was selected by the algorithm (each bar stands for the central height of each possible height range). The first valid range for comparison was from 215 to

1215 m a.g.l. (centered in 715 m a.g.l.), also coinciding with the most frequently selected range.

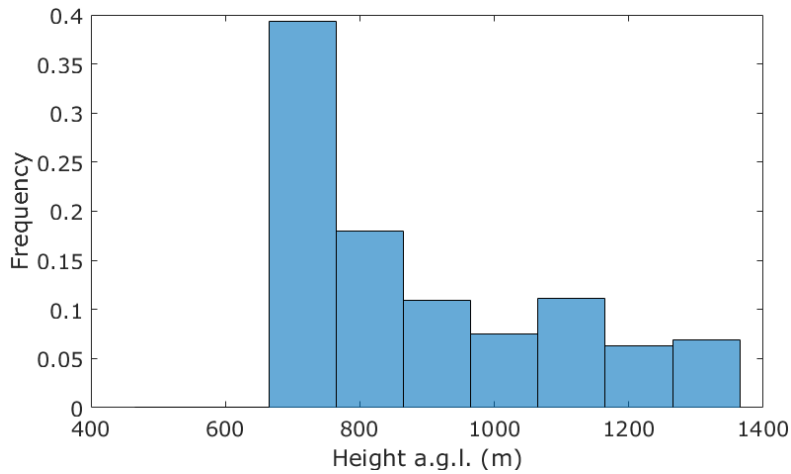


Figure III-19: Histogram showing the frequency of the selected 'best height' within each of the analyzed profiles. Values in x-axis refer to the center of the corresponding 1000 m height range used for the linear correlations.

With the f_h and l values corresponding with all those selected heights, we formed two histograms, depicted in Figure III-20. We can observe that the histograms are distributed around certain f_h and l values, making possible to take the mean and the standard deviation. These values were taken as calibration parameters for our system:

$$f_h = 630 \pm 120 \text{ m} \quad (\text{III-1})$$

$$l = 0.054 \pm 0.007 \text{ m} \quad (\text{III-2})$$

This statistical study should ideally have been performed over the whole Doppler lidar database, but the algorithm used was not fully optimized and the computation time would have been too high. Instead of that, we performed the analysis using several short datasets, and we obtained values coinciding with (III-1) and (III-2) within their uncertainty intervals. Therefore, we took those values for the calibration of the Doppler lidar signals used in this thesis.

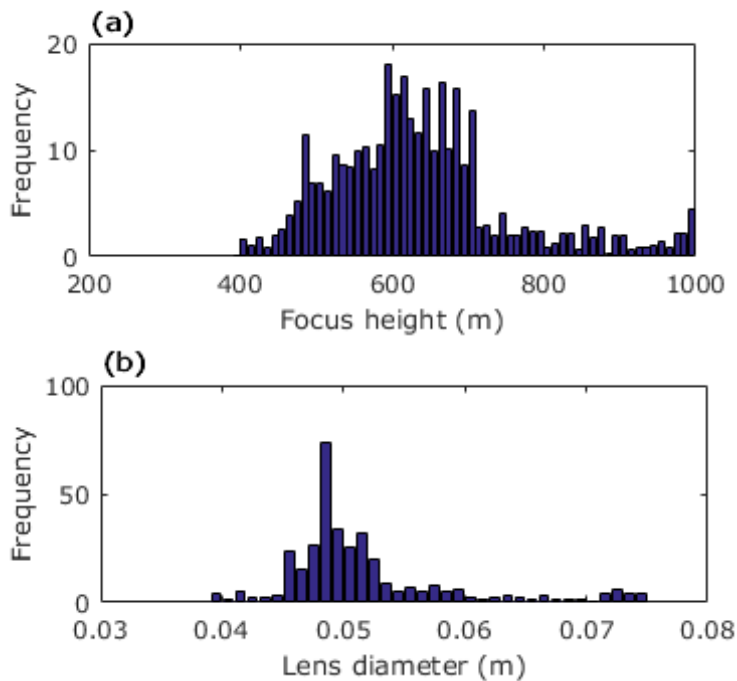


Figure III-20: Histograms corresponding to the retrieved Doppler lidar calibration parameters using a dataset of 10 days. (a) Focus height histogram. (b) Lens diameter histogram.

One of the direct effects of the Doppler lidar calibration appears on the cloud detection mask used by the ABL classification algorithm applied in chapter IV. In the present version of the software described in 6.1.2, clouds are detected from the β_{att} values by selecting a threshold of $10^{-5} \text{ m}^{-1}\text{sr}^{-1}$ from the literature (e.g., Harvey et al., 2013; Hogan et al., 2009; Westbrook et al., 2010). The increased intensity of the focused Doppler lidar signal around the focus height may lead to β_{att} values over that threshold in cases when no clouds but high aerosol load is present.

Figure III-21 shows an example of wrong cloud detection due to the focused signal. In Figure III-21a, the calculated Doppler lidar β_{att} profiles are shown in logarithmic scale for a whole day, applying only the background corrections. An intensified layer is noticeable below 1 km a.g.l. and before 9 h UTC. Co-located ceilometer provided cloud base heights between 1 km and 2 km a.g.l. before 6 h UTC, and only lower clouds during

short periods between 6 h and 9 h UTC (as can also be seen in the Doppler lidar signal as saturated signal). The intensified layer corresponded, therefore, to aerosol particles. However, the described threshold-based cloud detection scheme on Doppler lidar signal (Figure III–21b) assigned the cloud flag to the aerosol layer. Without further correction, this wrong cloud identification would propagate in the ABL classification algorithm and affect any study performed with it.

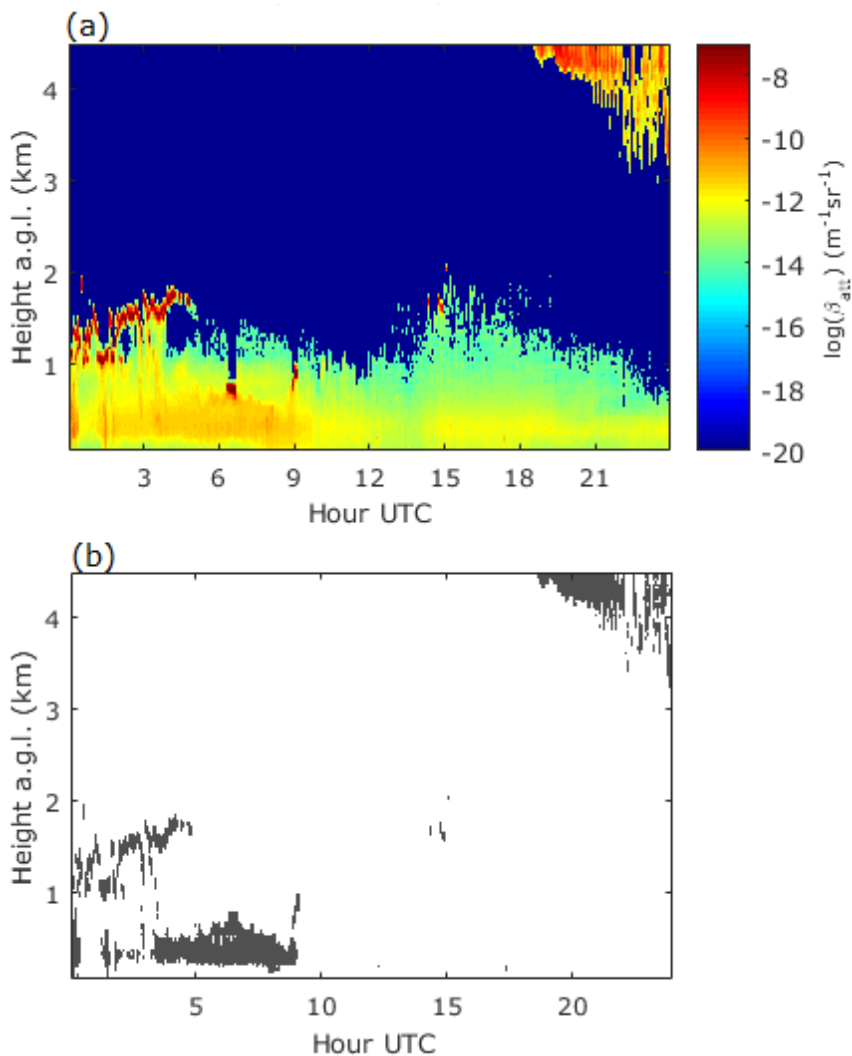


Figure III–21: (a) Attenuated backscatter and (b) cloud detection mask corresponding to background-corrected Doppler lidar measurements on 21st April 2016, with no focus correction.

In Figure III-22, the same example is shown after applying the focus correction with the calibration parameters (III-1) and (III-2). The β_{att} in Figure III-22a still presents the signal increase below 1 km a.g.l. due to the aerosol particles. However, the cloud mask (Figure III-22b) is now able to successfully identify the actual clouds.

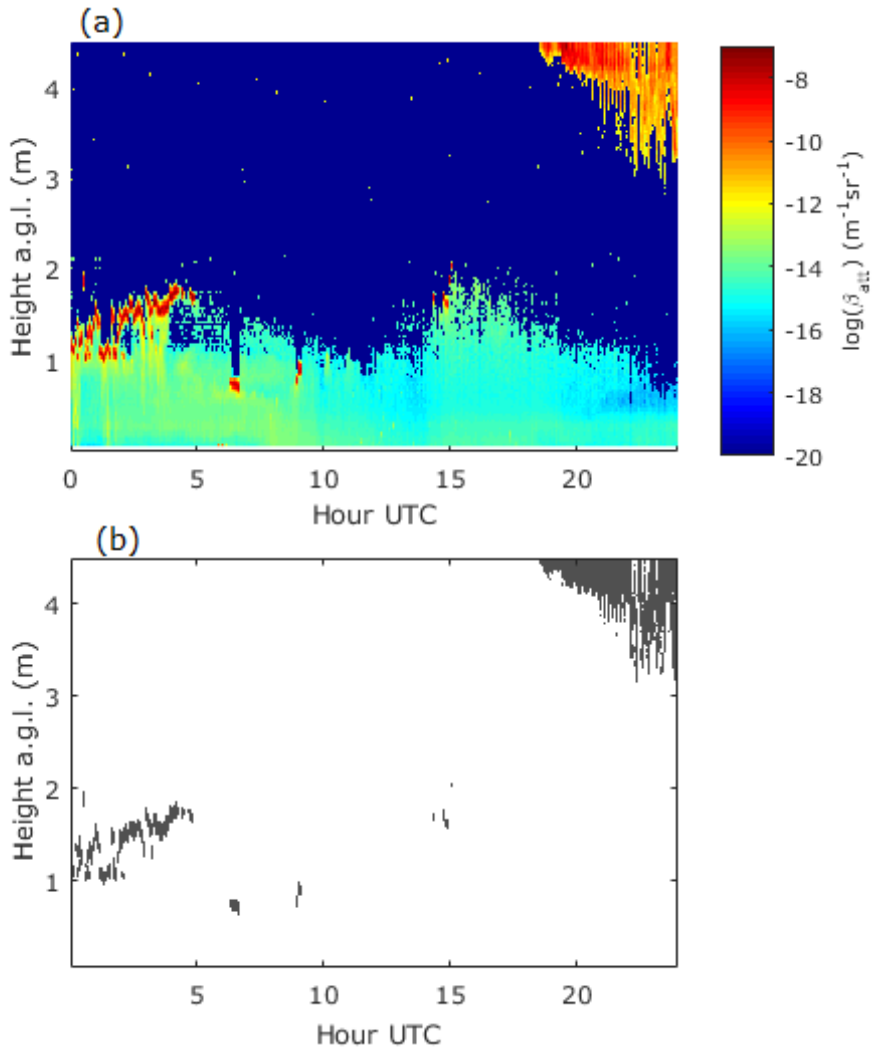


Figure III-22: Same as Figure III-21, but applying also focus correction to the measured signal.

3.6 CONCLUSIONS

This chapter is a combination between describing the experimental site and the instrumentation used in this thesis and developing new methods to improve the measurements. In this section, we present the main conclusions from the developments that we proposed.

In section 3.4 we implemented a new setup in the already existing Raman lidar MULHACEN at Granada station. This system used to measure vibrational Raman signals of molecules for the emission wavelengths of 355 and 532 nm. With few and simple instrumental modifications, a new interference filter was installed in order to measure rotational Raman signal at 353.9 nm (corresponding to emission at 355 nm). The main advantages of measuring pure rotational Raman signals are the enhanced SNR and the negligible wavelength shift between elastic and Raman returns.

With this upgrade, MULHACEN is now able to provide improved measurements, with enough quality to retrieve particle backscatter and extinction coefficient profiles during daytime (with a time resolution of 1h) and during nighttime (with an improved time resolution up to 1 min). We assessed the different error sources with the conclusion that the only significant uncertainty that has to be added to the statistical uncertainty is less than 2 % and 4 % for α^a and β^a , respectively, due to the temperature dependence of the signals.

We compared diurnal retrievals under typical aerosol load conditions, obtaining mean differences less than 30 % with photometer retrievals (without considering the incomplete overlap region for lidar) and less than 20 % with elastic retrievals. As an added value, we were able to calculate the correction for the incomplete overlap (overlap function) during daytime. Nocturnal retrievals with 1-min time resolution showed to reflect the variability of the atmosphere without losing the quality of the usual 30-min-averaged profiles.

The Doppler lidar measured signal was also improved within this chapter with several post-processing algorithms in section 3.5. Firstly, we applied the algorithms by Manninen et al. (2016) and Vakkari et al. (2019) to improve the background signal, routinely measured every hour. These algorithms correct the background signal for artifacts due to the instrumental response and to the measurement protocol itself. After the corrections, the actual atmospheric signal can be better separated from the noise, allowing a lowering of the SNR threshold to detect weaker signals.

The second improvement applied to the Doppler lidar signal was its calibration in terms of focus height and lens diameter of the optical system. These quantities are provided by the manufacturer, but an empirical and more accurate determination was needed in order to apply a correction in the effective collection efficiency of the instrument. We applied a systematic procedure for retrieving the calibration parameters by comparing the corrected signals with a co-located ceilometer. Thanks to the values obtained, we were able to calculate corrected attenuated backscatter from Doppler lidar signal intensity, a key magnitude for the subsequent turbulence retrievals.

PART II

AEROSOL OPTICAL AND MICROPHYSICAL PROFILING

Atmospheric aerosol is an important source of uncertainty on the radiative forcing models and therefore on Climate Change projections, as explained in section 2.2. One of the reasons for these uncertainties is the wide range of particle sizes, shapes and compositions, which depend on sources and on transformation processes while they are in the atmosphere, and that directly affect their interaction with radiation. The characterization of optical and microphysical properties of aerosol particles of different type, but also measured in different environments or after different residence times in atmosphere while being transported through different paths is, therefore, crucial for the decrease of modelling uncertainties. The importance of aerosol characterization and their effect in the atmosphere a in the necessity of monitoring events of social relevance, as Saharan dust intrusions or volcanic eruptions (Pappalardo et al., 2013).

In situ techniques are widely used for aerosol characterization, since they allow for direct measurement of different properties such as size distribution, absorption or scattering. However, the scope of these techniques is limited to the air volume close to the sampling device (usually at ground level or on board an aircraft), and some particle properties can be modified due to the sampling technique itself (impact, drying, etc.). On the contrary, with active remote sensing we can study the processes at different altitudes and without perturbing the aerosol.

In particular, we explained in section 2.3.1 that that Raman lidar signals are used to obtain particle backscatter (β^a) and extinction (α^a) coefficient profiles using the Raman algorithm. In this part of the thesis we retrieve these optical properties and their derived intensive properties to characterize different aerosol types, and we employ the resulting set of $3\beta^a$ (at 355, 532 and 1064 nm) and $2\alpha^a$ (at 355 and 532 nm) as input to obtain particle microphysical properties. Mathematically, this means solving an inverse ill-posed problem, for which a theoretical model and a regularization method is needed. The amount of regularization imposed to the problem is crucial for

the usefulness of the inversion result, since too much of it can eliminate important information together with noise. Therefore, special techniques called parameter choice rules (PCR) are also needed.

The theoretical framework to relate particle optical and microphysical properties is also decisive to characterize aerosols from lidar measurements. In this part, two approaches are applied, the Mie model for spherical particles and T-matrix model for spheroidal particles. The main difference between them, regarding the modelled particle ensemble, is the assumption about particle shape. The actual shape of aerosol particles is diverse and, thus, it is not possible to account for all real particle shapes in the aerosol ensemble. Spherical model has shown to be a good approximation, in special for fine particles (with respect to the measurement wavelength) such as biomass burning particles or anthropogenic pollution (e.g. Böckmann et al., 2001; Müller et al., 2001). However, this approximation is not enough for other aerosol as mineral dust or volcanic ashes, formed by coarser and more irregular particles.

The algorithms used in this part for microphysical retrievals share also the minimum requirement of having $3\beta^a$ and $2\alpha^a$ from Raman lidar (and depolarization information also in the case of spheroidal model). With this setup, the microphysical retrievals can be performed without external information, the reason why we called them *lidar stand-alone* retrievals. However, this ideal lidar setup is sometimes not available, and photometry information is usually combined with lidar measurements. Some algorithms, such as Lidar-Radiometer Inversion Code (LIRIC, Chaikovsky et al., 2016) or Generalized Retrieval of Atmosphere and Surface Properties algorithm (GRASP, Dubovik et al., 2014; Lopatin, 2013) are able to provide vertically resolved particle optical and microphysical properties from elastic lidar measurements combined with Sun photometry. In this part of the thesis, we include an alternative methodology for using the lidar stand-alone retrieval algorithm

when some of the complete setup is missing, by combination with nocturnal photometry.

This part of the thesis is divided in two chapters. Chapter IV provides a complete insight into the monitoring and description of aerosol events of different nature basing on inversion of Raman lidar measurements. In particular, a first section focuses on the use of a regularization algorithm using spherical model to characterize the transport and ageing of biomass burning particles, and a second section tests that algorithm when using nocturnal photometry data.

In chapter V, we explore the advantages of using a spheroidal model in a similar regularization algorithm by adding depolarization measurements to the Raman lidar dataset. This algorithm is applied to aerosol particles of different types in order to exploit the advantages of having shape information from the retrievals, and the results are discussed to better understand the strengths and limitations of this approach.

IV INVERSIONS USING SPHERICAL APPROXIMATION

The retrieval of aerosol size distribution and the derived particle microphysical properties from Raman lidar measurements is an issue that has been addressed for several decades. In particular, the use of regularization techniques applied to Lorenz-Mie model (Mie, 1908) has been shown to provide satisfactory solutions for particles with approximate spherical shape, such as biomass burning particles (e.g. Alados-Arboledas et al., 2011), anthropogenic pollution (e.g. Guerrero-Rascado et al., 2011b) or stratospheric sulphate particles from volcanic eruptions (Navas-Guzmán et al., 2013a).

Several algorithms sharing this same concept have been developed since late 90's. Müller et al. (1999b) and Böckmann (2001) created their algorithm in the framework of EARLINET standards. Other authors (Kolgotin and Müller, 2008; Veselovskii et al., 2002; Wang et al., 2007) have explored the effect of different regularization methods and a priori information, and the application to bimodal size distributions

(Veselovskii et al., 2004) or new mathematical methods (Böckmann and Kirsche, 2006; Wang, 2008) has also been considered.

This chapter is based on the hybrid regularization algorithm developed by Böckmann (2001) and its application to real and simulated cases. This algorithm and the corresponding software to apply it for forward and inverse calculations is described in section 4.1.

The aim of section 4.2 is to give a complete description of an important event of biomass burning particles transported from North America to Europe. The use of different tools and models to properly monitor and characterize the transport path of the air masses containing the smoke plumes is combined in that section with optical and microphysical characterization of the detected particles with Raman lidar and regularization algorithms.

In section 4.3, a sensitivity study is performed to a proposed methodology with the purpose of using the regularization algorithm even if a complete measurement dataset is not available. The combination of Raman lidar technique with nocturnal photometry is explored first with simulated aerosol size distributions and then is applied to real cases measured at UGR station in Granada.

Finally, a summary, some general conclusions and future work proposals are included in section 4.4.

4.1 HYBRID REGULARIZATION ALGORITHM. UP SOFTWARE

This section is focused on explaining the basis of the algorithm used in this thesis to retrieve particle microphysical properties basing on the assumption of spherical particles. It is an inversion algorithm developed at the University of Potsdam (Germany) in the framework of EARLINET (Müller et al., 2016), known as UP software (Böckmann et al., 2001, 2005). It is based on explicitly solving the mathematical equations that

relate the particle microphysical and optical properties by means of regularization techniques, an approach that is shared with Müller et al. (1999a), and Veselovskii et al. (2002) inversion algorithms. That means that forward computations using look-up tables containing microphysical versus optical properties are not carried out, having the advantage that particle size distribution shape is not assumed as input, but approximately calculated as output.

As explained in section (2.2.2) assuming spherical particles the model relating the optical parameters $\Gamma(\lambda)$ with the particle size distribution $n(r)$ is described by Equation (II-16), which can be also expressed in terms of volume particle size distribution $v(r)$ adapting the kernel functions $K_{\Gamma}(r, \lambda, m)$ accordingly:

$$\Gamma(\lambda) = \int_{r_{min}}^{r_{max}} K_{\Gamma,v}(r, \lambda, CRI) \cdot v(r) dr \quad (IV-1)$$

These kernel functions (that physically are the scattering or absorption cross sections) are calculated from Mie-scattering theory (Bohren and Huffman, 1983), assuming spherical shape of the aerosol particles. In our case, $\Gamma(\lambda)$ represents the particle backscatter or extinction coefficients, $\beta^a(\lambda)$ and $\alpha^a(\lambda)$, retrieved from lidar measurements with Raman method. For $\beta^a(\lambda)$ we only have information for the wavelengths 355, 532 and 1064 nm, while for $\alpha^a(\lambda)$ we are limited to the first two. This is also known as '3 β + 2 α ' setup, or simply '3 + 2' setup.

The problem reduces then to the inversion of Equation (IV-1), which is an ill-posed inverse problem. An additional issue for this problem is that the kernel functions are not known, since they depend on the *CRI*. For the sake of simplicity, *CRI* is usually assumed to be λ -independent (Böckmann, 2001; Müller et al., 1999a, 1999b; Samaras et al., 2015). Solving this problem requires then discretization, regularization (with a regularization method, RM) and a parameter choice rule (PCR).

Equation (IV-1) is discretized with spline collocation, i.e., approximating $v(r)$ by a finite linear combination of B-spline functions of order d :

$$v_n(r) = \sum_{j=1}^n b_j \phi_j(r^{d-1}) \quad (IV-2)$$

where the spline functions are denoted as $\phi_j(r^{d-1})$ since they are polynomials of degree $d - 1$. This reduces the problem to a discrete one to determine the coefficients b_j , i.e., $Ab = \Gamma$ with

$$A_{ij} = \int_{r_{min}}^{r_{max}} K_{\Gamma}(\lambda_i, r, CRI) \phi_j(r^{d-1}) dr \quad (IV-3)$$

This problem is solved by a hybrid regularization method (Böckmann, 2001) based on a technique called *Truncated Singular Value Decomposition* (TSVD). This technique consists on expanding A using a very useful factorization generalizing the concept of eigenvalues and diagonalization, known as the *Singular Value Decomposition* (SVD, e.g., Hansen, 2010; Trefethen and Bau, 1997). The potential noise in the matrix, magnified in the smallest singular values, is avoided by including only a part of the SVD defining a certain cut-off level k , what makes the method be *Truncated*. In order to overcome the unknown CRI to calculate the elements of A , a grid of physically viable options for the real and imaginary parts ($RRI \times IRI$) is defined. The solution space is then created for each CRI and all possible TSVD with triplets (n, d, k) . This space is restricted by picking the best (n, d, k) in terms of least residual error with respect to forward calculation of Equation (IV-1), and the resulting solution grid is presented with a color scale relevant to the error magnitude (Figure IV-1). Finally a few solutions (15-30) are manually selected based on the best size distributions. For more details and recommendations on selection procedure, see (Müller et al., 2016).

After retrieving the volume distribution and the CRI , the rest of particle optical and microphysical properties can be extracted, namely number, surface-area and volume concentration (C_N , C_S and C_V), effective radius (r_{eff}), and single scattering albedo (SSA). It has to be noted that due to the smoothness of the kernel functions in Equation (IV-1), the UP algorithm should not be used for $r > 5-7 \mu m$ because of the ill-posedness (Osterloh et al., 2013; Samaras et al., 2015).

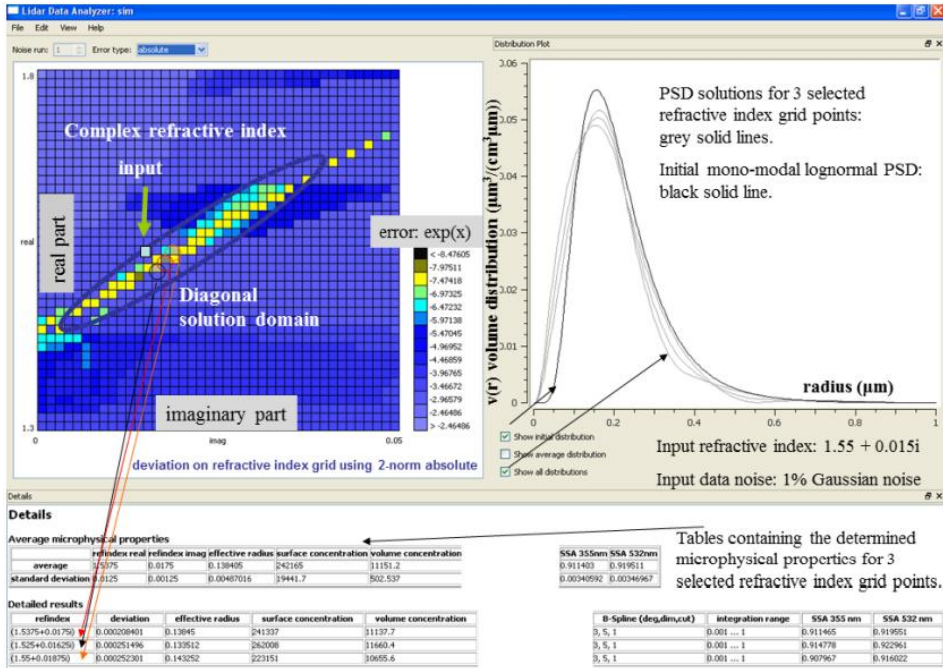


Figure IV-1: Screen shot of the evaluation panel of the UP software and explanation of the post-processing procedure: selection of suitable grid points of *CRI* clustering along the diagonal domain (left), corresponding size distributions and initial distribution (right), and tables with retrieved microphysical parameters for each selected *CRI* and mean values with standard deviation (bottom). The residual errors on the right hand side of the grid appear in ascending order from top to bottom on a logarithmic scale.

From Müller et al. (2016).

The calculations are done with a software which has three phases, namely setup, computation and evaluation, and can be used in *measurement mode* (to invert experimental optical data) or in *simulation mode* (to set up a certain aerosol distribution to make inversion tests). A schematic view of these three phases is depicted in Figure IV-2. In the setup phase, the input optical data are specified, together with the *CRI* grid limits, the $[r_{min}, r_{max}]$ interval and the parameter space to search (n, d, k) . A different retrieval method called *Padé regularization* (Böckmann and Kirsche, 2006; Kirsche and Böckmann, 2006) can also be selected on this phase, although it has not been used in this thesis, since TSVD gave better solution for our cases. The computation phase is run with a software that allows for parallel execution on a supercomputer

or computer cluster, if needed (Osterloh et al., 2009). The evaluation phase is shown in Figure IV-1, where the user can explore the results (bottom box) and plot the distributions (right box) for selected *CRI* (left box) thanks to an interactive frontend.

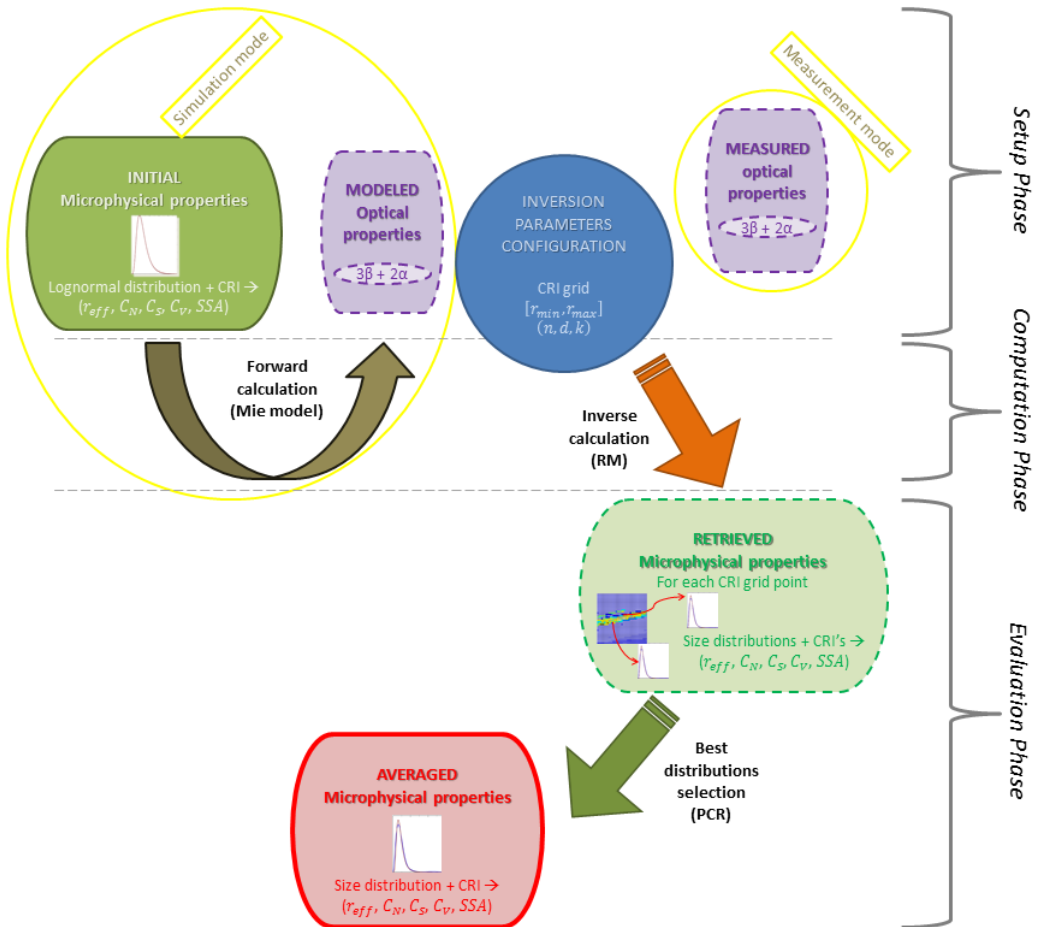


Figure IV-2: Scheme of the phases and steps of UP software.

4.2 MICROPHYSICAL CHARACTERIZATION OF LONG-RANGE TRANSPORTED BIOMASS BURNING PARTICLES FROM NORTH AMERICA

This section is adapted from 'Microphysical characterization of long-range transported biomass burning particles from North America at three EARLINET stations' by Ortiz-Amezcuca, P., Guerrero-Rascado, J. L., Granados-Muñoz, M. J., Benavent-Oltra, J. A., Böckmann, C., Samaras, S., Stachlewska, I. S., Janicka, L., Baars, H., Bohmann, S. and Alados-Arboledas, L. (2017), published in Atmospheric Chemistry and Physics, 17, 5931-5946, doi:10.5194/acp-17-5931-2017.

In this section, we show the potential of multiwavelength Raman lidar technique to obtain vertically resolved properties of biomass burning particles. We apply the UP software described before in order to have a complete optical and microphysical description of those particles.

As explained in section 2.2, atmospheric aerosols play an important role on effective radiative forcing because of their interactions with radiation and clouds. These interactions are strongly dependent on the scattering and absorption capabilities of the aerosol particles and on their vertical distribution along the atmospheric column. In particular, biomass burning particles can have a completely opposite behaviour, depending on their content in organic and black carbon, on their size and on their spatial distribution in the atmosphere. These properties of the biomass aerosol particles are affected by source type, combustion type and phase (Jacobson, 2001; Martins et al., 1998; Reid et al., 2005a, 2005b) and so-called aging processes caused by different mechanisms such as photochemical oxidation (Grieshop et al., 2009a, 2009b), hygroscopic growth (Granados-Muñoz et al., 2015; Hobbs, 1997; Ritter et al., 2018; Titos et al., 2014a, 2014c, 2016) or coagulation (Fiebig et al., 2003).

It has been demonstrated that large smoke plumes from large forest fires can be injected into the free troposphere, and then easily transported by air masses along the Earth, presenting long residence times in the atmosphere (Andreae, 1991; Ansmann et al., 2018; Fromm and Servranckx, 2003; Guerrero-Rascado et al., 2010a, 2011a; Haarig et al., 2018; Jost et al., 2004; Peterson et al., 2014; Ritter et al., 2018; Seinfeld and Pandis, 1998; Sicard et al., 2019b). The study of these transport process is crucial for modelling the global impact of this type of aerosol particles.

In this chapter, intense events of biomass burning particles released from North American forest fires during summer 2013 are analyzed in terms of their particle microphysical properties when they reached different EARLINET stations after being transported by air masses across the Atlantic Ocean. The summer of 2013 was one of the driest in the previous decades in the USA and Canada. Large forest fires caused by thunderstorms started at the end of June 2013 and continued being active during July and August, causing vast forest areas to burn up (Ancellet et al., 2016). In a previous work (Ortiz-Amezcuca et al., 2014), a preliminary optical description was given for the lidar detection of a smoke event over Granada (Spain) in July 2013. Markowicz et al. (2016) used in situ measurements, passive and active remote sensing observations and numerical simulations to describe the temporal variability of aerosol optical properties for the same period over Poland, and Janicka et al. (2017) studied the properties of the mixing of those smoke particles with dust particles over Warsaw. Ancellet et al. (2016) reported optical properties of the smoke plumes transported over some stations in the western Mediterranean Basin in June 2013. Veselovskii et al. (2015a) described vertically resolved optical and microphysical properties of particles detected in Washington, DC coming from similar forest fires after regional transport in August 2013.

Given the importance of smoke transport events, several attempts have been made at establishing mean values and

ranges for the reported main optical and microphysical properties of the biomass burning particles, classifying them according to source regions, combustion phase and aging (Dubovik et al., 2002b; Müller et al., 2007a; Reid et al., 2005a, 2005b). These estimations are strongly dependent on the detection type (in situ measurements and passive or active remote sensing), and every new measurement can show a different feature which does not fit with those reported in the mentioned works. This chapter intends to make a significant contribution to the general knowledge about biomass burning events detected after transatlantic transport, not only giving new observed values of intensive properties of the particles, but highlighting the similarities and differences among presumptive different events. These concordances or discrepancies will be meaningful, taking into account that the three analyzed plumes are different in terms of origin, transport path and conditions at each observation site, and they will allow for the extracting of some common pattern for transatlantic transport to be applied in future events.

We present a complete microphysical characterization of the smoke particles released into the free troposphere during different North American forest fires at the beginning of July 2013 and detected 8–10 days after, over three EARLINET stations (Granada, Leipzig and Warsaw) at different times and altitudes. Vertically resolved microphysical properties after such long-range transport are necessary in order to account for the particle properties that might have changed during the process and that might then directly affect their radiative impact.

4.2.1 Experimental sites and instrumentation

Three European experimental sites were selected in this work for characterizing the detected smoke plumes (Table IV–1). These stations are part of the EARLINET network and have lidar systems that fit the conditions for retrieving particle microphysical properties using regularization algorithms. That is, the so-called ' $3\beta + 2\alpha'$ ' optical data set can be obtained, since the three lidar systems are able to detect elastic signals at the

emitted wavelengths 355, 532 and 1064 nm as well as N₂ Raman-shifted signals at 387 and 607 nm.

Table IV–1: Geographical location of the selected EARLINET stations and lidar system providing data for this study.

Station	Location	Lidar name and/or model	References
Atmospheric Physics Group, University of Granada, Spain (GR)	37.16°N, 3.61°W, 680 m a.s.l.	MULHACEN, LR331-D400	This thesis (Section 3.1)
Leibniz Institute for Tropospheric Research, Leipzig, Germany (LE)	51.35°N, 12.43°E, 90 m a.s.l.	Polly ^{XT}	Althausen et al. (2009); Baars et al. (2016); Engelmann et al. (2016)
Radiative Transfer Laboratory, University of Warsaw, Poland (WA)	52.21°N, 21.03°E, 100 m a.s.l.	Polly ^{XT}	Althausen et al. (2009); Baars et al. (2016); Engelmann et al. (2016)

Moreover, columnar microphysical data from Sun-photometers at three AERONET stations have been used. The sites were selected to be the nearest AERONET stations to the EARLINET stations GR, LE and WA. For Granada, where two photometers from the network were working during the studied period, the one located on the hill 'Cerro de los Poyos' (37.11° N, 3.49° W, 1830 m a.s.l.) was selected because it presents the advantage of being more than 1 km higher than the lidar station, making it easier to study aerosol layers decoupled from ABL (Granados-Muñoz et al., 2014). In Leipzig, the selected photometer was co-located with the lidar system. In the case of Warsaw, the nearest AERONET station was found at the Geophysical Observatory at Belsk (51.84° N, 20.79° E, 190.0 m a.s.l.).

Cerro de los Poyos is around 12 km apart from Granada, and the observatory at Belsk is located at a distance of about 50 km south of Warsaw. Although these distances can be

considered negligible compared to the much larger horizontal scale of the common air masses (Holton, 1992), special care was taken when comparing the results from Raman lidar and from Sun-photometer techniques.

4.2.2 Methodology

In the first part of this work, satellite observations and models were used to study the sources and transport mechanism of the detected aerosol particles.

The Active Fire Mapping Program (<https://fsapps.nwcg.gov/afm/>), a satellite-based fire detection and monitoring program managed by the USDA Forest Service Remote Sensing Applications Center, was used to analyze the distribution of fires in the United States and Canada during the studied period. High temporal image data collected by the NASA's Moderate Resolution Imaging Spectroradiometer (MODIS) on Terra and Aqua platforms are currently the primary remote sensing data source of this fire detection program. MODIS provides multiple daily observations of the United States and Canada, which is ideal for continuous operational monitoring and characterization of wildland fire activity.

The NAAPS (Navy Aerosol Analysis and Prediction System) model of the Marine Meteorology Division, Naval Research Laboratory (NRL; <http://www.nrlmry.navy.mil/aerosol/>), was used for forecasting *AOD* and particle density of smoke at the Earth's surface, using smoke emissions derived from satellite-measured thermal anomalies.

The analysis of backward trajectories was performed by means of the HYSPLIT model (see section 3.3.5). In particular, cluster analysis and ensemble calculation were used. The observations of the spaceborne CALIOP (see section 3.3.4) were used to track the aerosol plumes during their transport.

In the second part of the work, vertical profiles of optical properties (independently retrieved particle backscatter and extinction coefficients, Angström exponents and lidar ratios)

were obtained from nighttime lidar measurements applying the Raman methodology (Section 2.3.1).

The set of ' $3\beta + 2\alpha$ ' obtained from Raman lidar observations was employed to obtain particle microphysical properties (i.e., particle volume concentration, effective radius, complex refractive index and single scattering albedo) using the UP algorithm described in Section 4.1.

4.2.3 Results I: Characterization of sources and transport of the smoke plumes

According to MODIS fire detection maps (Figure IV–3a), several active forest fires were detected at the United States and Canada, releasing large amounts of biomass burning particles during July 2013. Figure IV–3b shows the smoke surface concentration at the beginning of that month, given by the NAAPS model. High concentrations can be observed in almost all North America, reaching values more than $64 \mu\text{g m}^{-3}$ in several regions. Markowicz et al. (2016) studied the relative *AOD* changes in several North American AERONET stations during the first weeks of July 2013, finding values reaching 1.5 (at 500 nm), which implies mean *AOD* anomalies (with respect to long-term means for July) up to 0.42.

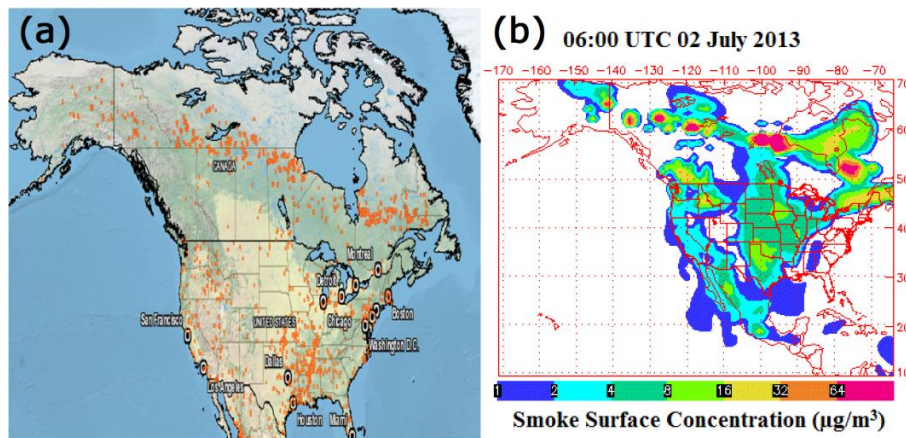


Figure IV–3: Active fire map for the period from 1st to 15th July 2013 (a) and concentration of smoke particles at the surface according to the NAAPS model, for a specific time (2nd July 2016 at 06:00 UTC) within the period of intense forest fires in North America (b).

The cluster analysis performed using HYSPLIT software revealed that, during June and July 2013, the prevailing synoptic situation favored the transport of these aerosol particle plumes across the Atlantic Ocean to Europe. In Figure IV-4, the most relevant 10-day backward-trajectories clusters for each of the studied stations and layers are represented. This figure shows the main influence of air masses coming from North America, accounting for 59 % of all the trajectories ending at Granada, 64 % for Leipzig and 61 % for Warsaw.

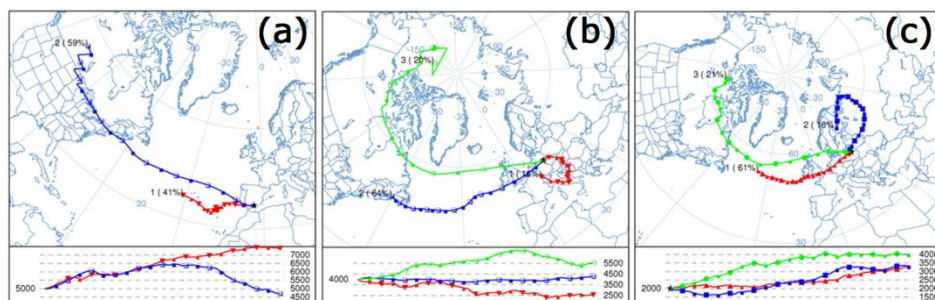


Figure IV-4: Coordinates and altitude in meters above ground level (black lines) of the 10-day backward-trajectories clusters during the period June–July 2013 arriving at Granada (a), Leipzig (b) and Warsaw (c).

Using the EARLINET database, the detection of possible smoke particles for the three selected stations was confirmed. In Figure IV-5, the lidar raw corrected signal in the selected locations shows the presence of aerosol layers at different altitudes. In Granada and Leipzig, multilayer structures were found and smoke particles appeared in the free troposphere, between 4 and 6 km a.s.l., while in Warsaw, the high load of aerosol particles was observed at a lofted aerosol layer between 1.5 and 3 km a.s.l. This layer was decoupled from the aerosol layer near the surface, as it can be seen in Figure IV-5, and was over the lifted condensation level according to the nearest radiosonde at Legionowo (<http://weather.uwyo.edu/upperair/sounding.html>).

Ensembles of backward trajectories generated with the HYSPLIT model were used to determine the origin of the air masses carrying aerosol plumes arriving at the studied stations at the relevant heights (Figure IV-6). They confirmed that the

relevant air masses came from areas over North American forest fires detected by MODIS, and that they were advected for around 8–10 days before reaching the stations.

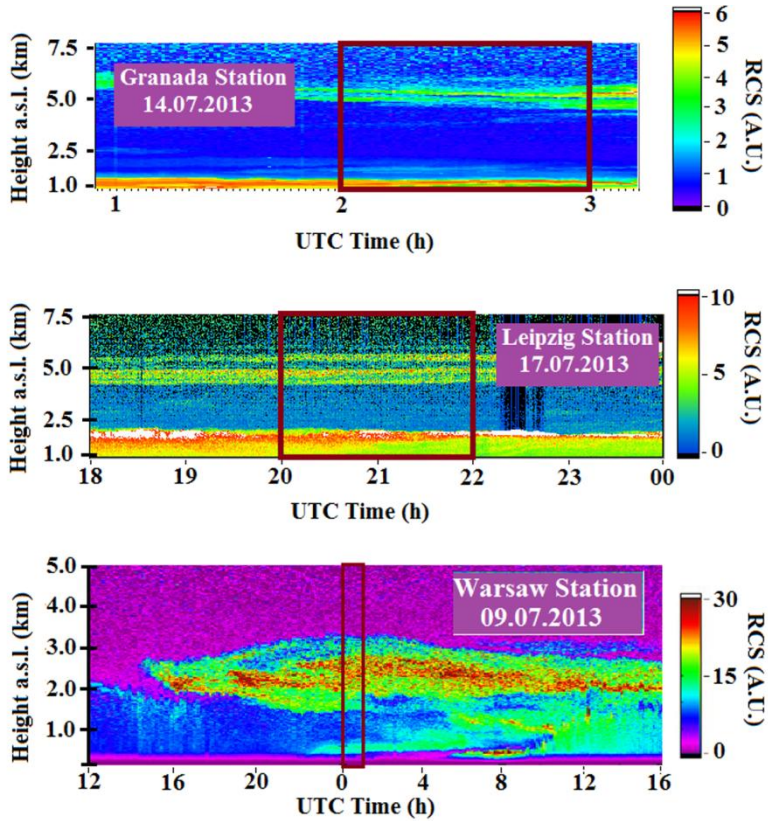


Figure IV–5: Time evolution of lidar raw corrected signal (in arbitrary units) at 1064 nm showing the detection of the smoke plumes at Granada, Leipzig and Warsaw stations, with analyzed intervals inside red boxes.

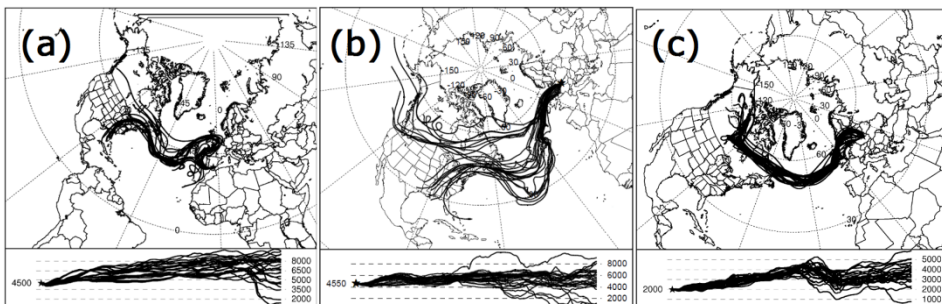


Figure IV–6: Coordinates and altitude in meters above ground level (black lines) of the ensembles of probable air masses' trajectories ending at the investigated layer on 14th July 2013 above Granada (a), on 17th July 2013 above Leipzig (b) and on 9th July 2013 above Warsaw (c).

These ensemble trajectories in Figure IV–6 also show that in contrast to the aforementioned general transport from North America (as seen in the cluster analysis, Figure IV–4), there are two clearly different source zones for the specific analyzed layers. While the layer arriving to Warsaw unequivocally comes from west Canada, the corresponding layers arriving at Granada and Leipzig might come from both west Canada and from the eastern USA. This difference in source region implies different types of forest: coniferous forests predominate in Canada, while in that part of USA, deciduous forests are the most important (David and Holmgren, 2001). This might be crucial, since it implies a different fuel and combustion type (modifying the black carbon content) and thus has to be taken into account when analyzing the physical properties of the detected particles.

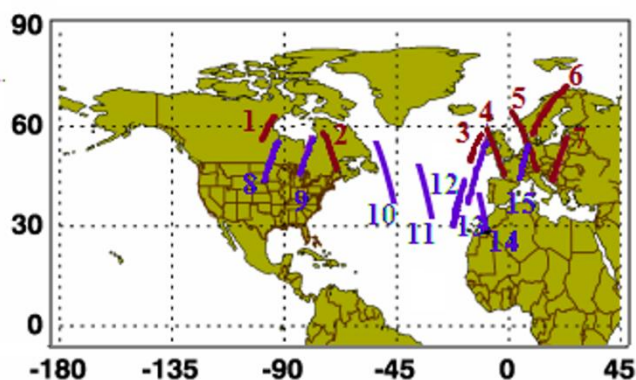


Figure IV–7: Map showing the relevant CALIPSO overpasses tracking some smoke plumes being transported to Europe. Brown lines stand for plumes arriving at Warsaw on 9th July 2013, and purple lines stand for plumes arriving at Granada on 14th July 2013 and Leipzig on 17th July 2013.

The geolocation of CALIPSO overpasses and backward trajectories on Figure IV–6 provide a reliable tool to assess the involvement of those air masses in the transportation of the smoke plumes which finally reached Europe. Figure IV–7 illustrates some of the overpasses of this satellite coinciding in space and time with parts of the back-trajectories on 1st–8th July 2013 for Warsaw case and 5th–16th July for Granada and Leipzig cases. The aerosol type product (Omar et al., 2009)

provided by CALIPSO (Figure IV–8 and Figure IV–9) confirmed that the smoke columns reached 5 km altitude over the sources, and the smoke content on the transported air plumes, as indicated by the black color.

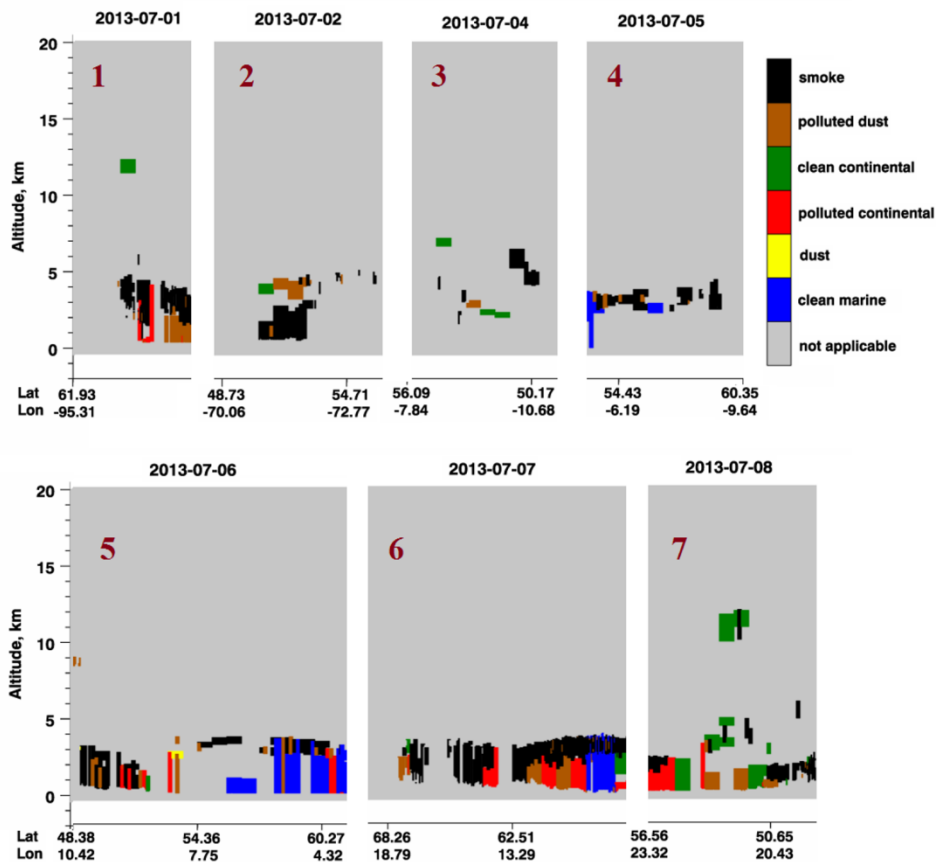


Figure IV–8: Position (altitude, latitude and longitude) and type of the aerosol layers detected by CALIPSO for each of the overpasses tracking the masses arriving at Warsaw (depicted in Figure IV–7 as 1–7), with black color indicating smoke aerosol particles.

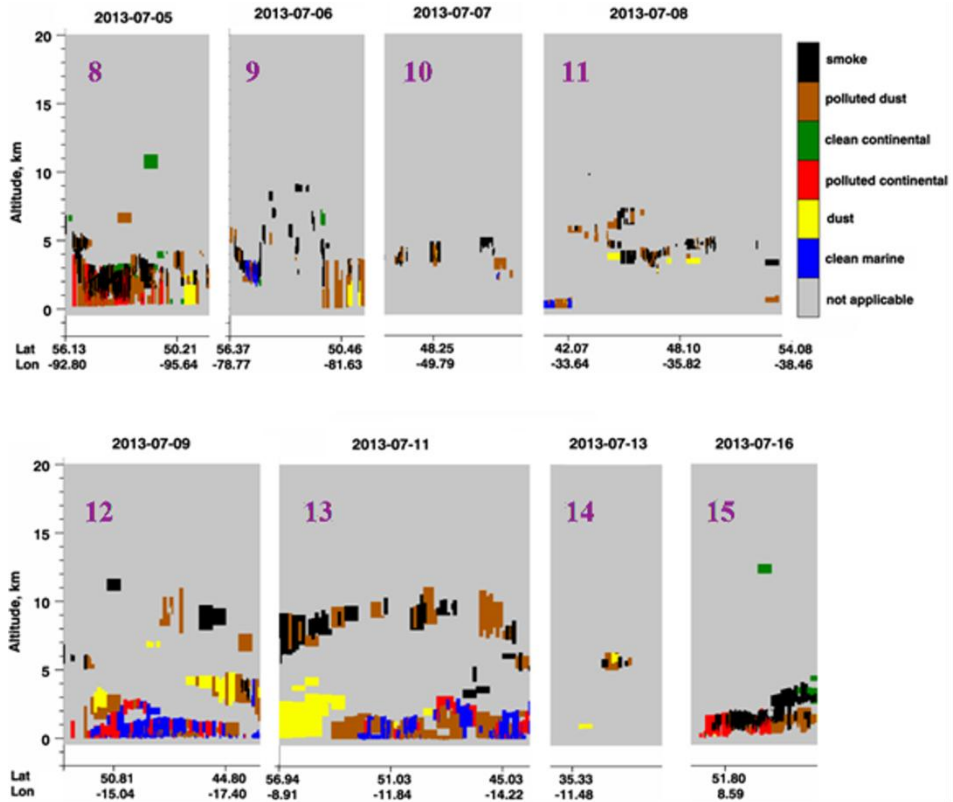
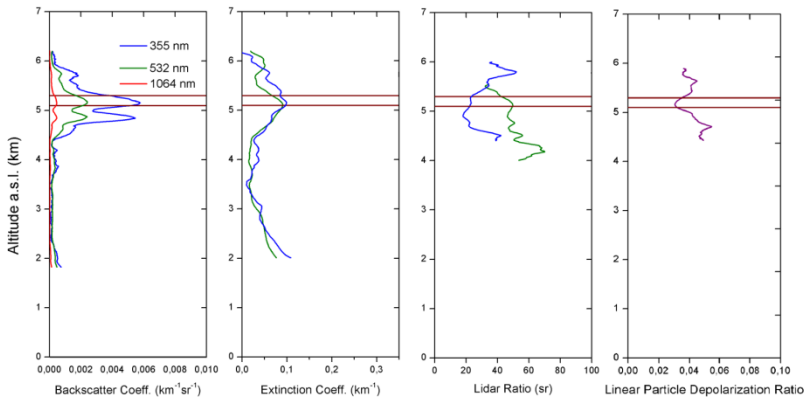


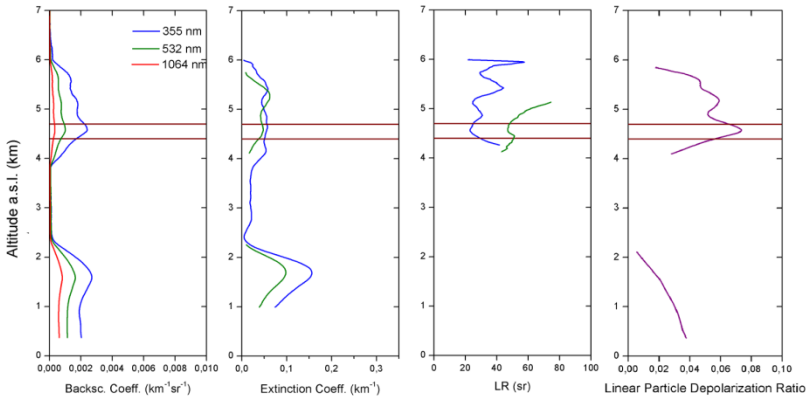
Figure IV-9: Position (altitude, latitude and longitude) and type of the aerosol layers detected by CALIPSO for each of the overpasses tracking the masses arriving at Granada and Leipzig (depicted in Figure IV-7 as 8–15), with black color indicating smoke aerosol particles.

4.2.4 Results II: Optical properties

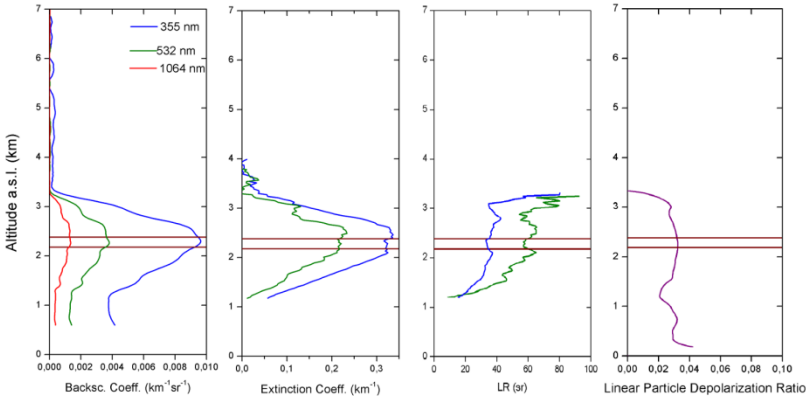
In order to characterize the optical properties of the biomass burning particles, the Raman algorithm was applied to lidar data corresponding to 02:00–03:00 UTC on 14th July for Granada, 20:00–22:00 UTC on 17th July for Leipzig and 00:00–01:00 UTC on 9th July for Warsaw. The particle backscatter coefficient (β^a), particle extinction coefficient (α^a), lidar ratio (LR^a) and linear particle depolarization ratio (δ_p) profiles are plotted in Figure IV-10. The regions of profiles affected by incomplete overlap and by too-low backscatter ratios are not shown. The β^a and α^a profiles highlighted that the smoke layers were intense in terms of optical properties, and the low δ_p values (less than 0.04 for Granada and Warsaw and less than 0.08 for Leipzig) indicate the large proportion of spherical,



Granada Station 14.07.2013 02-03 h UTC



Leipzig Station 17.07.2013 20-22 h UTC



Warsaw Station 09.07.2013 00-01 h UTC

Figure IV-10: Vertical profiles of β^a and α^a , LR^a and linear particle δ_p obtained for Granada, Leipzig and Warsaw cases. The layers analyzed to obtain the optical and microphysical description of the transported particles are marked with brown rectangles.

fine-particles (Bravo-Aranda et al., 2015; Granados-Muñoz et al., 2014; Navas-Guzmán et al., 2013b).

The thickness of each smoke layer was calculated using the gradient method (Flamant et al., 1997), and it was obtained that the bottom and top of each layer was 4.3–6.1 km at GR, 4.2–5.7 km at LE and 1.5–3.3 km at WA. By the integration of the particle extinction coefficient over the smoke layer, the fraction of the total *AOD* associated to the smoke plume was derived, showing that it accounted for more than 40 % of the total *AOD* (532 nm) in the case of Granada, more than 30 % in Leipzig and more than 70 % in Warsaw. In these calculations, the α^a along the region of incomplete overlap were approximated by multiplying the β^a profile at this region (which is not affected by incomplete overlap) by a constant LR^a .

Table IV–2: Average particle optical properties for the selected thin layers within the smoke zone.

	Layer Height a.s.l. (km)	$\beta^a(355)$ ($Mm^{-1}sr^{-1}$)	$\alpha^a(532)$ (Mm^{-1})	AE_α (355, 532)	AE_β (355, 532)	$LR^a(355)$ (sr)	$LR^a(532)$ (sr)	CR_{LR}
GR	5.20±0.10	2.20±0.09	82±16	0.2±1.2	1.2±0.5	23±10	47±11	2±1
LE	4.55±0.15	0.93±0.14	48±5	0.3±0.3	1.9±0.4	25±4	51±9	2.1±0.5
WA	2.28±0.10	3.7±0.5	216±6	0.98±0.06	1.9±0.2	34±6	58±10	1.7±0.4

In each case, a single thin layer (200 m thick for GR and WA and 300 m for LE) was selected (pointed with brown rectangles in Figure IV–10) to obtain an optical and microphysical description of the transported particles. In Table IV–2, the main optical properties of the analyzed aerosol layers are shown. Very similar properties were found for GR and LE, with low extinction-related Angström exponents (AE_α) and LR^a of 23 ± 10 and 25 ± 4 sr for 355 nm as well as 47 ± 11 sr and 51 ± 9 sr for 532 nm. The very low measured LR^a values at 355 nm represent a feature to point out, since they indicate low absorption from the smoke particles, compared to the mean value of 46 ± 13 sr for North American biomass burning

particles reported by Müller et al. (2007a). However, Müller et al. (2005) already found LR_{355}^a ranging from 21 to 67 sr for biomass burning aerosol, which agrees with the values presented here. The 'color ratio of lidar ratios' ($CR_{LR} = LR_{532}^a / LR_{355}^a$) reached values around 2 for GR and LE, which hints towards the aging process. It has been demonstrated that $CR_{LR} < 1$ is usual for fresh smoke particles, while $CR_{LR} > 1$ corresponds to aged smoke (Alados-Arboledas et al., 2011; Müller et al., 2005, 2007a; Nicolae et al., 2013). The latter comparison among the results obtained and other values found in the literature about biomass burning events detected in Europe is summarized in Table IV-3.

Concerning the values obtained for WA, there are noticeable differences with the other two stations: higher AE_α (reaching 0.98 ± 0.06) and LR^a and slightly lower CR_{LR} (although it keeps well over 1, being consistent with the aging during transport). These discrepancies might be due to the different smoke sources as observed before, but may also be attributed to a different aging process.

4.2.5 Results III: Microphysical properties

The UP algorithm was applied to the layers in Table IV-2 in order to retrieve a microphysical description of the detected aerosol particles. Table IV-4 shows the results obtained.

The retrieved particle volume concentrations (C_V) present values over $10 \mu\text{m}^3 \text{cm}^{-3}$, reaching almost $35 \mu\text{m}^3 \text{cm}^{-3}$ in WA. The r_{eff} 's present high values in agreement with the aging process and fit the exponential curve derived by Müller et al. (2007b) with a discrepancy below 15 % for GR and LE and 20 % for WA. Complex refractive indices that have real parts (RRI) a bit lower than 1.50, which represents the typical value for boreal forest fire particles according Dubovik et al. (2002) see Table IV-3.

Table IV-3: Optical and microphysical properties found in the literature about BB events detected in Europe.

Ref.	Meas. Type	Source region	Aging	LR_{355}^a	LR_{532}^a	AE_{α}^a (355-532)	δ_p	CR_{LR}	RRI	IRI	r_{eff} (μm)	SSA 355 nm	SSA 532 nm
				(sr)	(sr)								
Dubovik et al. (2002b)	Sun phot.	USA/Canada	All types	-	-	1.0-2.3	-	-	1.50±0.04	0.0094±0.003	-	0.94 (440 nm)	0.935 (670 nm)
				-	-	-	-	-	-	-	-	-	0
Wandinger et al. (2002)	Lidar	NW Canada	6-10 days	-	40-80	-	-	-	1.64-1.77	0.043-0.053	0.16-0.27	-	0.79-0.83
				-	-	-	-	-	-	-	-	-	-
Müller et al., (2005)	Lidar	Canada	14 days	21-49	26-61	0.00-1.10	-	-	1.39-1.56	0.001-0.006	0.24-0.4	-	0.89-0.98
				21-67	31-87	0.27-1.10	-	-	1.37-1.6	0.001-0.007	0.24-0.38	-	0.89-0.98
				-	-	-	-	-	-	-	-	-	-
Müller et al., (2007a)	Lidar	Siberia/Canada	aged	46±13	53±11	1.0±0.5	<5%	(0.8±0.2) ⁻¹	-	-	-	-	-
				-	-	-	-	-	-	-	-	-	-
Alados-Arboledas et al. (2011)	Lidar	South Spain	1 day	60-65	60-65	1.16-1.3	-	1	1.49-1.53	0.02±0.02	0.13-0.17	0.76-0.83	0.80-0.87
				Star phot.	-	-	1.61±0.10	-	-	-	-	-	0.19±0.05

Table IV-3 (cont.): Optical and microphysical properties found in the literature about BB events detected in Europe.

Ref.	Meas. Type	Source region	Aging	LR_{355}^a (sr)	LR_{532}^a (sr)	$AE_a^{(355-532)}$	δ_p	CR_{LR}	RRI	IRI	r_{eff} (μm)	SSA ₃₅₅ nm	SSA ₅₃₂ nm
Nicolae et al. (2013)	Lidar	Romania	Fresh	43-73	43-46	1.37-1.93	-	0.6-1	1.61-1.66	0.009-0.05	0.27-0.4	0.74-0.92	0.77-0.94
		Greece	2 days	41 \pm 7	56 \pm 8	1.28 \pm 0.01	-	1.4 \pm 0.05	1.65 \pm 0.13	0.012 \pm 0.08	0.34 \pm 0.09	0.87 \pm 0.07	0.92 \pm 0.07
		Ukraine/Russia	2-3 days	32-48	52-54	0.64-0.99	-	1.1-1.6	1.41-1.59	0.003-0.014	0.19-0.44	0.85-0.97	0.91-0.97
		Iberian Peninsula	Fresh	51 \pm 17	55 \pm 30	1.4 \pm 0.5	-	-	-	-	-	-	-
Preigler et al. (2013)	Lidar	North America	5-10 days	58 \pm 17	56 \pm 30	2.2 \pm 0.7	-	-	-	-	-	-	-
		Iberian Peninsula	1-2 days	52-66	49-66	1.2-1.6	3.8-5%	0.93-1.04	1.49-1.61	0.01-0.024	0.14-0.19	0.89-0.86	0.82-0.92
Samaras et al. (2015)	Lidar	East Europe	-	-	27-55	1.2-2.3	4-8%	-	1.352-1.368	2.9 \cdot 10 ⁻⁴ -0.0024	0.275-0.325	-	0.942-0.997
Ancelet et al. (2016)	Satellite-based lidar	North America	aged	42-59	45-60	-	5-10%	-	-	-	-	-	-
Markowicz et al. (2016)	Sun phot.	Canada	5-6 days	-	-	1.28-1.71	-	-	-	-	-	0.91-0.99 (441 nm)	-

Table IV-4: Average particle microphysical properties (namely volume concentration, effective radius, real and imaginary part of refractive index, and single scattering albedos) for the same selected thin layers within the smoke zone. The associate uncertainty for each variable corresponds to the standard deviation from the average solution.

	C_V ($\mu\text{m}^3\text{cm}^{-3}$)	r_{eff} (μm)	RRI	IRI	SSA 355 nm	SSA 532 nm
GR	17.3± 0.2	0.33± 0.02	1.496± 0.017	$(1.7\pm 0.4)\cdot 10^{-3}$	0.9820± 0.0002	0.9860± 0.0001
LE	10.1± 0.4	0.34± 0.03	1.480± 0.006	$(3\pm 1)\cdot 10^{-3}$	0.965 ± 0.006	0.972± 0.004
WA	34.3± 0.7	0.207± 0.006	1.473± 0.002	$(1.2\pm 0.3)\cdot 10^{-3}$	0.991 ± 0.001	0.99304± $5\cdot 10^{-5}$

Very low imaginary parts of the refractive index (*IRI*) with values form 0.0012 to 0.003 compared to 0.0094 ± 0.003 , given by Dubovik et al. (2002), and single scattering albedos close to 1 indicate a weak absorption by the particles, and therefore a low black carbon fraction, in disagreement with some previous works about biomass burning particles (Alados-Arboledas et al., 2011; Wandinger et al., 2002) but in agreement with others (Eck et al., 2009; Samaras et al., 2015). The spectral dependence of the *SSA* between 355 and 532 nm shows what could be considered an anomalous behaviour compared to some columnar retrievals (Dubovik et al., 2002b; Reid et al., 2005a, 2005b), where biomass burning aerosol *SSA* typically decreases with increasing measurement wavelength. However, the nearly constant or slightly positive spectral dependence is also found in other studies (Alados-Arboledas et al., 2011; Eck et al., 2009; Pereira et al., 2014). It is noteworthy that the refractive index is assumed wavelength-constant for the inversion algorithm used in this work, and thus the size distribution plays a major role in *SSA* retrieval. In the studied cases, it is found that the fine modes of the retrieved size distributions are broad (Figure IV-11), which implies a contribution of larger particles that cancels out the typically negative spectral dependence of *SSA*. The different

spectral behaviours and ranges of the *SSA* in the mentioned works are not only related to the aging process, because similar properties have been found for both fresh and aged biomass burning particles. These properties depend also on burning region and on fuel and combustion type.

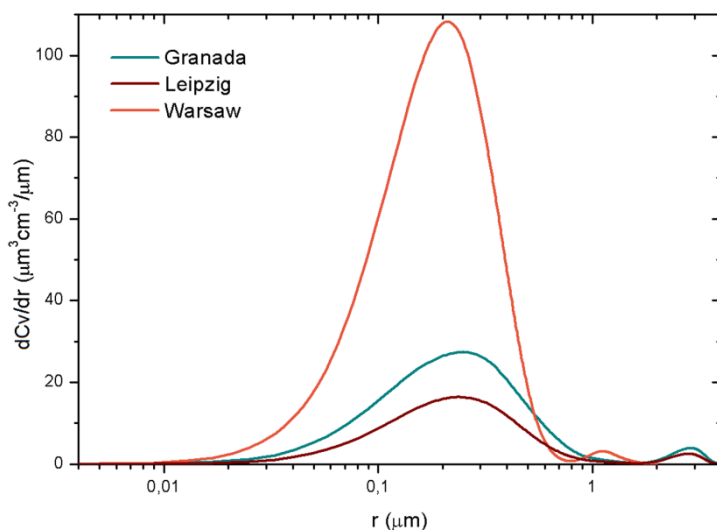


Figure IV-11: Volume particle size distributions retrieved for the selected points of the analyzed smoke plumes.

An important feature of these results is the similar intensive properties found for particles detected in GR and LE, as compared to those retrieved for WA. Such similarities and differences are consistent with the optical properties, and they are attributed to the different source region of the smoke plumes, as explained before. Additionally, the pathways of the plumes arriving at GR and LE did coincide up to a certain point, as also shown above.

The integrated volume concentration along the smoke layers (V_L) was also calculated in order to make a comparison with AERONET retrievals of integrated volume concentrations along the whole atmospheric column (V). A triangle-shape approximation was used for the C_V profile of the 1.8 km thick layer for GR and WA (at 4.3–6.1 and 1.5–3.3 km a.s.l., respectively), taking $C_V = 0$ at the points corresponding to the smoke layer top and the smoke layer bottom and the

calculated C_V values reported in Table IV-4 for the selected altitude. The integrated concentration for the case of LE was approximated using a rectangle-shape C_V profile of the 1.5 km thick layer (at 4.2–5.7 km a.s.l.). These approximations may be justified by looking at the shape of the particle extinction profiles in Figure IV-10. Fine and coarse mode distinction (V_L^f and V_L^c , respectively) was also calculated, using the same inflection points as those given by AERONET.

Table IV-5 shows the found values, which highlight again that the plume observed over WA was more intense (the V_L at this station doubles the values at the two other stations) and also that fine-mode particles were the most important ones. This mode represents 69 % of total V_L at GR, 63 % of total V_L at LE and 95 % of total V_L at WA.

Table IV-5: Concentration values integrated along each smoke layer. Superscripts ^f and ^c indicate fine and coarse mode separation, respectively.

	V_L ($\mu\text{m}^3 \mu\text{m}^{-2}$)	V_L^f ($\mu\text{m}^3 \mu\text{m}^{-2}$)	V_L^c ($\mu\text{m}^3 \mu\text{m}^{-2}$)
GR	0.016	0.011	0.005
LE	0.016	0.01	0.006
WA	0.038	0.036	0.002

Once the integrated concentration of each layer was calculated, an assessment of their impact on the total atmospheric column was made. Three AERONET microphysical retrievals were then selected, using the closest AERONET stations. For each station, the closest-in-time retrieval that according to the columnar AERONET retrieved properties showed a clear presence of the detected smoke plume was selected. The times were 06:29 UTC for Cerro de los Poyos (Granada), 17:31 UTC for Leipzig and 04:23 UTC for Belsk (Warsaw), corresponding to 03:30 h after lidar measurements at GR, 02:30 h before lidar measurements at LE and 03:20 h after lidar measurements at WA.

Table IV–6 shows the volume concentration in the whole atmospheric column (V) provided by AERONET, distinguishing among total, fine and coarse modes. It is seen that the fine-mode fraction is high in all cases, as it was observed for V_L in Table IV–5. It can also be seen that the smoke layer detected at GR during the night presented a V_L that represents 43 % of the total V observed during the afternoon, V_L at LE was 22 % of the V observed during the day and 57 % of the V during day at Belsk was observed for the smoke layer over WA.

Table IV–6: Columnar microphysical properties retrieved from AERONET inversions, which are the nearest in space and time to the analyzed lidar Raman measurements. GR: Cerro Poyos, 14.07.2013 06:29 UTC; LE: 17.07.2013 17:31 UTC; WA: Belsk, 09.07.2013 04:23 UTC. The UV wavelengths are 438 nm, 441 nm and 439 nm for GR, LE and WA, respectively. The VIS wavelengths are 676 nm, 675 nm and 675 nm for GR, LE and WA, respectively.

	r_{eff} (μm)	RRI	IRI	SSA (UV)	SSA (VIS)	V (μm^3 μm^{-2})	V^f (μm^3 μm^{-2})	V^c (μm^3 μm^{-2})
GR	0.253	1.5044	0.013	0.9395	0.9325	0.037	0.031	0.007
LE	0.24	1.43	0.0005	0.9955	0.9951	0.072	0.051	0.021
WA	0.23	1.52	0.014	0.9422	0.9214	0.067	0.049	0.018

The main intensive microphysical properties retrieved from the AERONET algorithm are also included in Table IV–6. The low absorption of the analyzed particles is confirmed, with very low IRI and very high SSA . The IRI included are the average values over all the wavelengths retrieved from photometers. The wavelengths at which SSA were obtained are different from lidar wavelengths, thus ultraviolet (UV) and visible (VIS) ranges are compared. SSA values appear to be almost spectrally independent but slightly decreasing with wavelength. This slope does not agree with the lidar retrieval presented previously in this section but does agree with other studies

using only columnar retrievals (Dubovik et al., 2002b; Reid et al., 2005a, 2005b).

Concerning the effective radii, discrepancies with values from Table IV–4 around 20, 30 and 10 % are found for GR, LE and WA, respectively. These differences are small taking into account the spatial and temporal differences among the measurements and also the volume investigated. Real refractive indices are also around 1.5 for photometric retrievals, although in LE an *RRI* of 1.43 was found. Imaginary parts of refractive index values showed larger differences with respect to values retrieved with lidar, which is also reflected in *SSA*. However, the *SSA* discrepancies remain less than 7 % and then still represent low particle absorption.

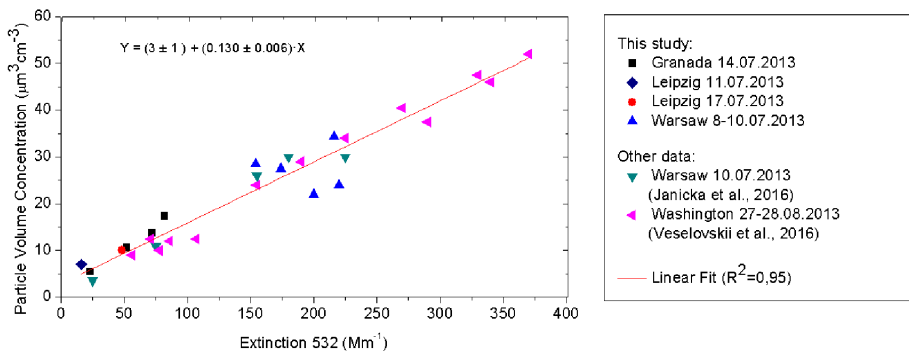


Figure IV–12: Scatter plot of the particle volume concentration as a function of the extinction coefficient at 532 nm. The red line represents the linear regression.

The experimental relationship between particle volume concentration and particle extinction coefficient at 532 nm is also analyzed in this study. In addition to the three cases illustrated in Figure IV–10, Table IV–2 and Table IV–4, three more cases for the same day in Granada, one more case for 11th July 2013 in Leipzig and four more cases for 8th–10th July 2013 in Warsaw were calculated with the UP algorithm. The points from the additional cases along with some points from other cases in literature (Janicka et al., 2017; Veselovskii et al., 2015b) were plotted, see Figure IV–12. It was found that a linear dependence can be deduced. A linear fit using α^a (532)

was calculated, obtaining $C_V (\mu\text{m}^3 \text{cm}^{-3}) = (3 \pm 1) (\mu\text{m}^3 \text{cm}^{-3}) + \alpha^a (0.130 \pm 0.006) (\mu\text{m})$ with $R^2 = 0.95$. The resulting linear parameters can be thus assumed to be representative of the approximation of volume concentration values in events of biomass burning particles transported from North America to Europe when α^a (532) is available. Nevertheless, this linear parameterization should only be applied for aerosol particles with similar chemical composition and affected by similar aging processes as the ones presented here due to the large dependence of the aerosol properties on these factors.

4.3 IMPROVING RAMAN LIDAR AEROSOL MICROPHYSICAL RETRIEVALS WITH STAR- AND LUNAR-PHOTOMETRY

We have seen in the previous sections of this chapter that multiwavelength Raman lidar measurements allow for stand-alone microphysical retrievals. The minimum requirement is having a '3+2' setup, i.e., with 3 β^a profiles (at 355, 532 and 1064 nm) and 2 α^a profiles (at 355 and 532 nm), as shown in different simulation studies (Böckmann et al., 2005; Müller et al., 2001; Veselovskii et al., 2002). However, not all existing lidar systems fulfill this requirement, it is, they miss one or several of these needed channels.

The aim of the work presented in this section is to find alternative lidar configurations that, in combination with star- or lunar-photometry measurements, are able to provide reasonably good inputs for microphysical retrievals. As this is an exploratory work, we have supposed that only one of the '3+2' lidar channels is missing, and we have proposed an alternative methodology and performed a sensitivity study.

The proposed approach consists on reconstructing the missing lidar profile using columnar AE of spectral AOD measured by star- or lunar-photometer, following Angström Equation (II-20):

$$\Gamma(\lambda_2, z) = \Gamma(\lambda_1, z) \cdot \left[\frac{\lambda_2}{\lambda_1} \right]^{-AE_{\Gamma}(\lambda_1, \lambda_2)} \quad (IV-4)$$

where Γ stands for α^a or β^a .

Therefore, the main assumption is that we can approximate this AE measured by the photometer for the whole atmospheric column, to the $AE(z)$ for each of the single aerosol layers. Moreover, we have to assume that the spectral dependence of AOD is the same for the optical properties measured with lidar at close wavelengths. These two assumptions imply that we are introducing some errors to the actual $AE(z)$ profiles and, consequently, to the input for the inversion of microphysical properties. An example of the differences between columnar AE_{AOD} and vertically resolved $AE_{\alpha}(z)$ is shown in Figure IV–13.

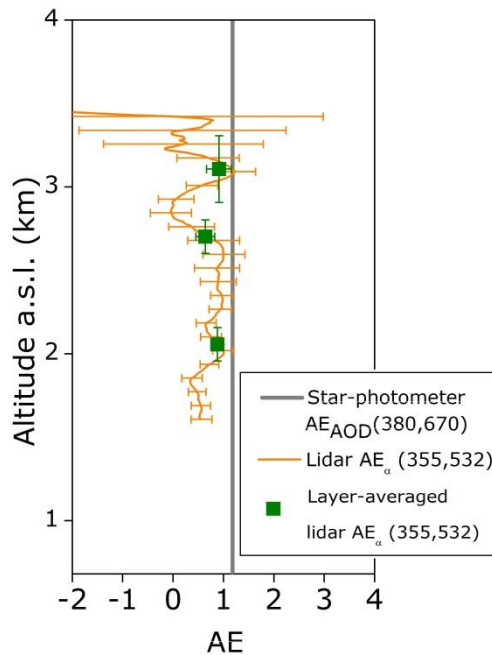


Figure IV–13: Example of a measured $AE_{\alpha}(z)$ profile derived from Raman lidar (orange) and the average values for some vertical layers (green), compared with the simultaneously-measured columnar AE_{AOD} from photometer (grey).

With this approach in mind, three different lidar channels substitution scenarios have been explored (shown schematically in Figure IV–14):

- Scenario I, or '3+1 (355)' configuration: when the lidar system has 3 β^a profiles but only one α^a profile at 355 nm. We can calculate the missing $\alpha^a(532)$ from $\alpha^a(355)$ using Equation (IV-4) with $AE_\alpha(355,532)$ from photometer AE_{AOD} at the closest wavelengths. Those wavelengths are (380,670) nm in the case of the star-photometer and (440,670) nm in the case of the lunar-photometer:

$$AE_\alpha(355,532, z) = AE_{AOD}(\lambda_1, \lambda_1) \forall z \quad (IV-5)$$

- Scenario II, or '3+1 (532)' configuration: when the lidar system has 3 β^a profiles but only one α^a profile at 532 nm. The missing $\alpha^a(355)$ is calculated from $\alpha^a(532)$ with the same $AE_\alpha(355,532)$ as in scenario I.
- Scenario III, or '2+2' configuration: when the missing channel is $\beta^a(1064)$. It is calculated from $\beta^a(532)$ following two different approaches that differ from each other in the assumed relation between measured AE_{AOD} and needed $AE_\beta(532,1064)$:

- a) The assumption taken is that $AE_\beta(532,1064)$ is equal to the measured AE_{AOD} at the closest wavelengths, that are (500,1020) nm for both photometer types:

$$AE_\beta(532,1064, z) = AE_{AOD}(500,1020) \forall z \quad (IV-6)$$

- b) $AE_\beta(532,1064)$ is not assumed to be equal but proportional to $AE_{AOD}(500,1020)$. The proportionality constant is assumed to be the same as the ratio between AE_α and AE_β :

$$\frac{AE_\beta(532,1064, z)}{AE_{AOD}(500,1020)} = \frac{AE_\beta(355,532, z)}{AE_\alpha(355,532, z)} \forall z \quad (IV-7)$$

The rest of combinations of one missing lidar channel would be $[\beta^a(355) + \beta^a(1064) + \alpha^a(355) + \alpha^a(532)]$ and $[\beta^a(532) + \beta^a(1064) + \alpha^a(355) + \alpha^a(532)]$. These scenarios have not been taken into account because they do not represent realistic lidar configurations (a Raman lidar system able to provide α^a at a certain λ always provides β^a at this λ , following Raman method described in section 2.3.1).

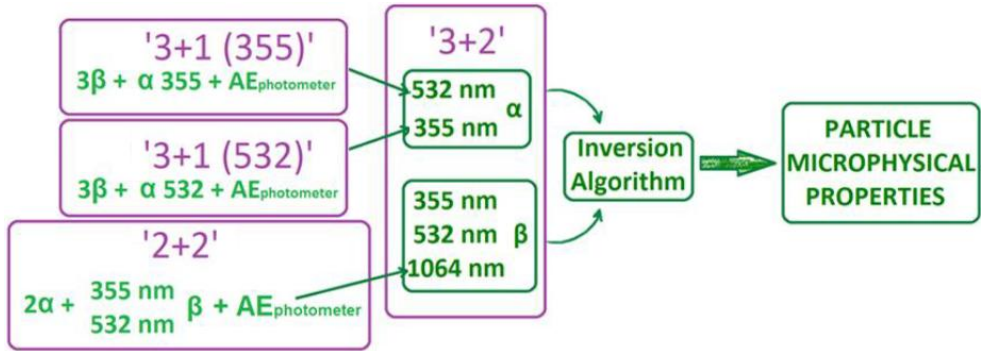


Figure IV–14: Scheme of the different proposed substitution scenarios.

4.3.1 Sensitivity study

In the first part of the work, the impact of the addition of certain noise to AE_α or AE_β on the inverted particle properties has been tested. This noise would correspond in a real case to the assumptions that the proposed methodology implies, as explained before. This study has been performed using simulated aerosol distributions, basing on simulations done in previous works such as Osterloh et al.(2013) and Müller et al. (2016).

Table IV–7: Selected parameters for the simulated log-normal distributions.

Distribution name	r_{med} (μm)	σ	r_{eff} (μm)	$r_{min} - r_{max}$ (μm)	C_S ($\mu\text{m}^2\text{cm}^{-3}$)	C_V ($\mu\text{m}^3\text{cm}^{-3}$)
1. Submicrometric	0.1	1.6	0.174	0.001-2.000	196	11
2. Micrometric	0.6	1.6	1.04	0.001-5.000	7036	2442

The simulations have been performed with UP software, that allows for creating aerosol distributions based on log-normal function, see Equation (II-11). Basing on the simulation works mentioned, two different monomodal distributions were selected, denoted here as *submicrometric distribution* (with r_{eff} of 0.174 μm) and *micrometric distribution* (with r_{eff} of 1.04 μm). Both distributions were normalized to have a total area C_N of 0.001 cm^{-3} . The selected parameters for both distributions,

and the resulting concentrations C_S and C_V are detailed in Table IV-7, and they are depicted with black lines in Figure IV-15.

Table IV-8: Selected *CRI* cases and obtained *SSA* at 355 and 532 nm for each of the distributions in Table IV-7.

<i>CRI</i> case	Submicrometric		Micrometric	
	SSA 355 nm	SSA 532 nm	SSA 355 nm	SSA 532 nm
A. 1.4+0.005i	0.9693	0.9667	0.8597	0.9015
B. 1.4+0.0075i	0.6862	0.6544	0.5146	0.5432
C. 1.5+0.005i	0.9721	0.9732	0.8536	0.8935
D. 1.6+0.05i	0.7943	0.8085	0.5477	0.5744

For each distribution, four different *CRI* cases were selected basing on physical and mathematical criteria. This means that the selected *CRI* are within the known ranges for different species, and that the kernel functions for the inversion problem are not too ill-posed (Osterloh et al., 2013). These four *CRI* cases, combined with the distributions determine certain values for *SSA*, according to Mie forward calculations. The selected *CRI* cases and the resulting *SSA* values are included in Table IV-8.

After the selection of this 2×4 initial situations (2 distributions and 4 *CRI* cases), the following procedure was followed (summarized in Figure IV-16):

1. Using UP software in forward calculation mode, the corresponding '3+2' optical setups were calculated for each situation, what we called *zero optical properties*. From them, the derived intensive aerosol properties (AE_α , AE_β and LR^α) were also calculated. The results are not shown in this section, but in the Appendix (Table VII-1 and Table VII-2).
2. With these 2×4 setups of undisturbed optical properties, the size distributions were then retrieved using UP software in inverse calculation mode. We called

them *zero retrievals* as they were obtained with the complete '3+2' setup, without substituting any channel with photometer information. The resulting distributions are shown in Figure IV-15 for all *CRI* cases, and the corresponding particle properties are included in the Appendix (Table VII-3 to Table VII-10).

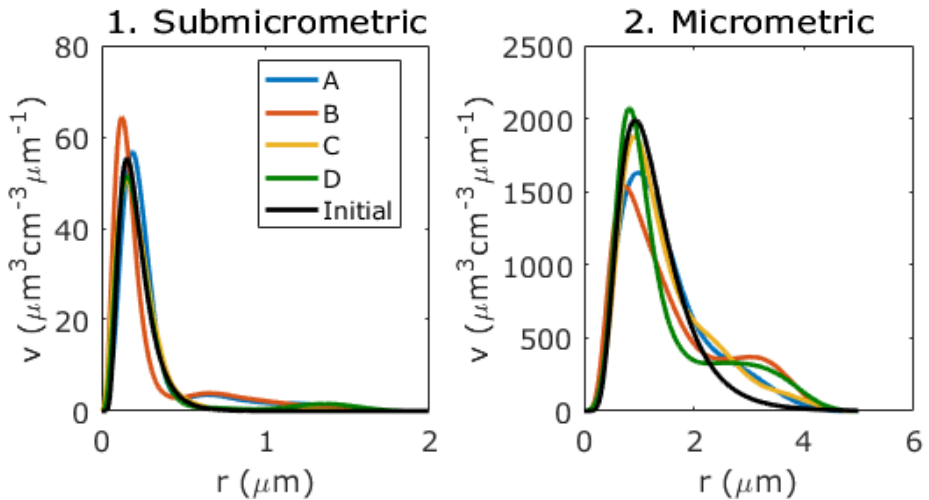


Figure IV-15: Initial log-normal size distributions (black lines), and the obtained distributions after "zero" retrieval for each *CRI* case.

3. After checking the level of error given by the software for these undisturbed cases, we proceeded to vary the AE_α and AE_β an amount of $\pm 5\%$ for each of the distributions, *CRI* cases and simulation scenarios. In this part of the work, scenario III was not divided into (a) and (b) since the reconstructed $AE_\beta(532,1064)$ is calculated by disturbing the zero case. The obtained disturbed optical properties are included in the Appendix (Table VII-11 and Table VII-12).
4. With these new $2 \times 4 \times 3$ setups of *disturbed optical properties* (for each distribution, *CRI* case and simulation scenario), the size distributions were retrieved. The corresponding particle properties are included in the Appendix (Table VII-13 to Table VII-18).
5. Finally, we compared the retrieved properties with the ones corresponding to zero retrieval. The reason for

comparing with zero retrieval instead of with the initial properties is that our comparison provides information on isolated impact of disturbing the Angström Exponents, apart from the error of the inversion itself.

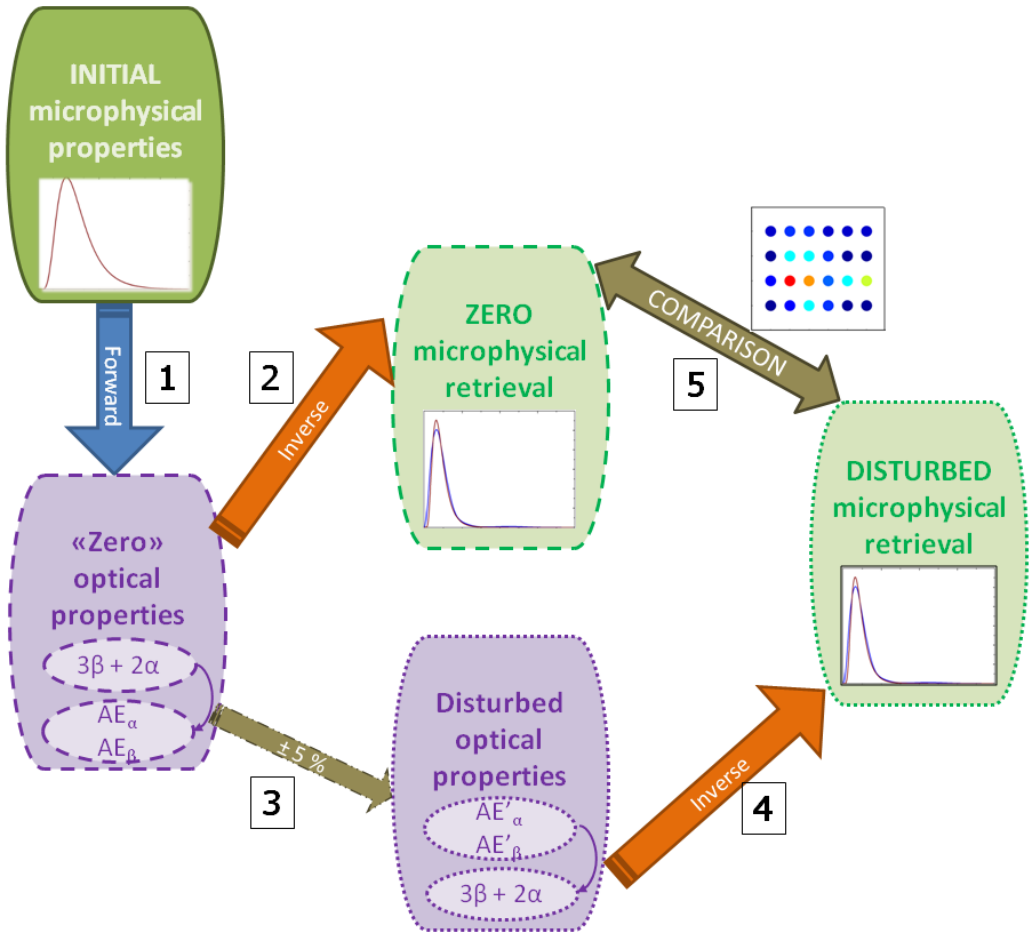


Figure IV-16: Scheme of the applied procedure. Steps were repeated for all possible distributions, *CRI* cases and simulation scenarios.

We will comment the results obtained step by step. Concerning the forward calculated optical properties in step 1 (Appendix, Table VII-1 and Table VII-2), it is important to notice that not all the initial situations represent realistic (or observed) aerosol properties. Although the selected *CRI* values are realistic themselves, certain combinations with the size distributions are not. In particular, *CRI* case B gives LR^a around 600-700 sr for micrometric distribution, what is far from the observed values

in literature between 15 and 100 sr, see e.g. Table 1 from (Müller et al., 2007a). The same *CRI* for the submicrometric distribution gives also high LR^a values (100-200 sr), although they are closer to the observed values. Despite that fact, these cases have been included in the sensitivity study, so that the theoretical work contemplates a wider scope.

Table IV–9: Summary of the retrieved differences between zero and initial particle properties.

	Submicrometric min.-max. relative error (%)	Micrometric min.-max. relative error (%)
<i>RRI</i>	0 - 3	0.5 - 2.5
<i>IRI</i>	2 - 61	5 - 16
r_{eff} (μm)	1.8 - 18	0.16 - 6
C_S ($\mu\text{m}^2\text{cm}^{-3}$)	7 - 36	0.08 - 2.4
C_V ($\mu\text{m}^3\text{cm}^{-3}$)	9 - 23	1.7 - 6
C_N (m^{-3})	0.6 - 20.5	0 - 4
SSA355 nm	0.7 - 27	0.16 - 6.4

In view of the results of step 2, i.e. the zero retrieved distributions (Figure IV–15), one can verify that even the undisturbed optical properties result in slightly different distributions, because of the inversion procedure. In those figures, it is also clear that the most unstable case is B, as anticipated before. From the derived particle properties (Appendix, Table VII–3 to Table VII–10), we observe differences (summarized in Table IV–9) in agreement with previous simulation and validation works with UP (Osterloh, 2011; Osterloh et al., 2011, 2013; Samaras, 2017; Samaras et al., 2015), although our number of cases is not representative for this purpose. The retrieved number concentrations (C_N) always differ from the initial concentration by 40 to 500%, as it was already warned by the mentioned studies. This is because even very small uncertainties in the Aitken part of the volume distribution lead to huge amplification in number when dividing by r^3 . In addition to this, the *IRI* relative differences are also usually very large because the values are small. For those

reasons, these two properties have been excluded from further analysis. The rest of the properties present relative differences below 5% in more than 75% of the cases, below 10% in more than 85% of the cases and below 25% in more than 95% of the analyzed values.

After disturbing the zero optical properties and retrieving the new distributions (steps 3 and 4), the particle properties were obtained for all the $2 \times 4 \times 3$ setups (Appendix, Table VII-13 to Table VII-18). The comparison described in step 5 was done, and the results have been depicted in Figure IV-17. In this figure, the matrices show with colors the relative differences between the disturbed retrievals and the zero retrieval. There are 3×2 subplots for the scenarios and distributions. In each subplot, each dot stands for a certain particle property (x axis) and a *CRI* case (y axis). In all cases, the deviations are below 20%, and almost all the data present deviations below 5% (dark blue dots). The least affected distribution is the micrometric one (probably because their extensive properties are higher in absolute amounts leading to lower relative errors). The simulation scenario that affected in least amount was scenario III, as we could expect since $\beta^a(1064)$ is usually much smaller and carries less weight in the inversion. The *CRI* case with lower deviation is case D, and the least affected parameter is *RRI*.

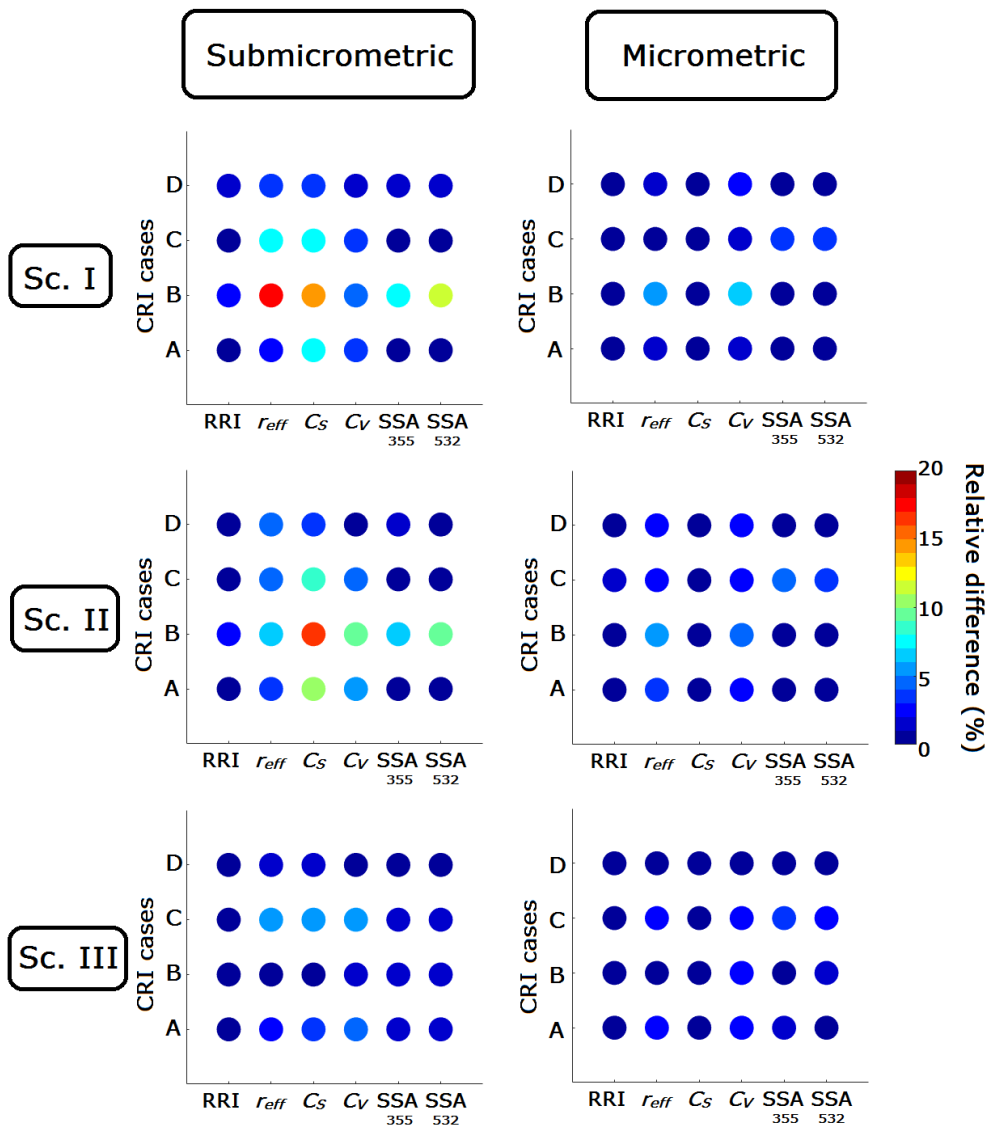


Figure IV-17: Relative differences between disturbed retrievals and zero retrieval, for the different initial distributions, *CRI* cases, simulation scenarios and particle properties.

4.3.2 Experimental cases

In the second part of the work, we used real cases measured with the multiwavelength Raman lidar system MULHACEN and the nocturnal photometers (triple CIMEL and EXCALIBUR star-photometer) at Granada station. Three cases are shown here, corresponding with fresh and aged biomass burning particles, and with anthropogenic particles. The selection of such cases is due to the fine and spherical nature of those particle types, what makes UP algorithm suitable for inversion analysis.

The procedure was similar to the simulation cases, with the difference that we did not select the size distributions and *CRI* values. Thus, we did not have the *initial* particle properties, but only the *zero* retrieved properties (i.e., the retrieval using the complete '3+2' setup). These properties constitute the reference values in this part of the study.

Case 1: Fresh biomass burning particles

The first analyzed case corresponds to an event of fresh smoke detected in Granada on 24th September 2007. The optical and microphysical analysis was already published by Alados-Arboledas et al. (2011) using another regularization algorithm (Müller et al., 1999a, 1999b; Veselovskii et al., 2002, 2004). For this work, we have recalculated the particle properties with UP algorithm and performed the channel substitution analysis. The nocturnal photometer that was measuring in Granada during this period was EXCALIBUR, and the Sun-sky photometer was CIMEL CE138-4 (see subsection 3.3.2).

The diurnal and nocturnal evolution of the *AOD* measured by the Sun- and star-photometers at 440 nm, together with the AE_{AOD} at 380-870 nm and 380-880 nm, respectively, is depicted in Figure IV-18. It shows an *AOD* increase around sunset on 24th September, with values around 0.5 and AE_{AOD} around 1.5. According to HYSPLIT backward-trajectory analysis, simulations with the NAAPS model and fire MODIS products, some smoke plumes arrived to Granada from a hot spot around 70 km apart, after a short transport time (24-36 h).

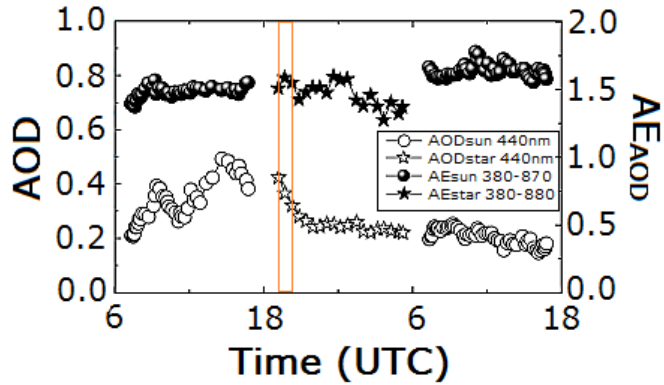


Figure IV-18: Column-integrated aerosol optical properties from Sun- and star-photometers for 24th and 25th September 2007. Orange box stands for the lidar analyzed period. Adapted from Alados-Arboledas et al. (2011).

Raman lidar measurements were taken during the night from 24th to 25th September, and the interval from 19:03 h UTC to 20:03 h UTC (orange box in Figure IV-18) was selected for the analysis. The simultaneous measurement selected from EXCALIBUR was at 19:42 h UTC, when $AOD(440)$ was 0.366 ± 0.018 and $AE_{AOD}(440,870)$ was 1.61 ± 0.10 .

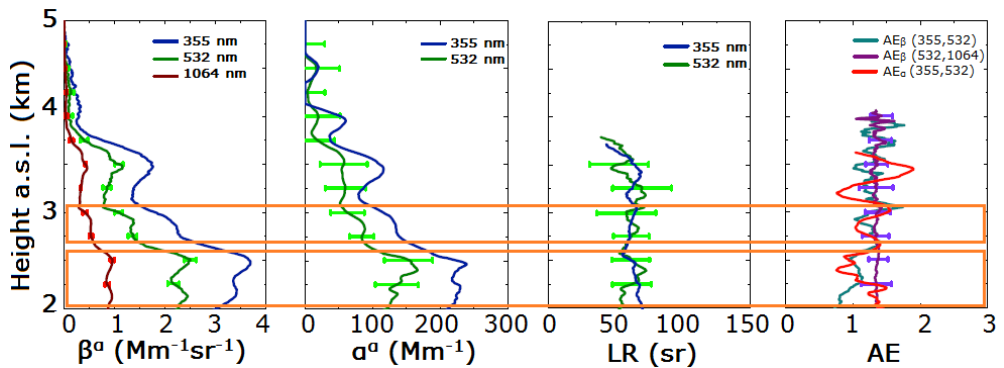


Figure IV-19: Vertical profiles of particle optical properties on 24th September 2007, 19:03-20:03 h UTC measured at Granada station. Orange boxes stand for the analyzed layers.

Figure IV-19 shows the obtained profiles of particle optical properties from lidar measurements. Two layers were selected for the study, centered at 2.300 and 2.875 km a.s.l., respectively (orange boxes in Figure IV-19). The criterion for the layer selection was to coincide with maximum values of extensive properties (α^a and β^a) and homogeneous regions in

terms of intensive properties (AE and LR^a). The averages of α^a and β^a at the different wavelengths formed thus the *zero optical properties*, i.e., the '3+2' setup for each layer. They are detailed in Table IV–10, together with their standard deviations within the layers. In Table IV–11, the averages of the corresponding intensive properties within those layers are detailed. LR^a values of 60-65 sr at both wavelengths are higher than the ones found in Section 4.2, what agrees with the fact that now we are analyzing medium-fresh smoke particles, according to Nicolae et al. (2013). AE values higher than 1 indicate the predominance of fine particles, as expected for this aerosol type and making this case suitable for analysis with UP software.

Table IV–10: Complete 3+2 setup of particle optical properties for each layer, with their standard deviations.

Height a.s.l. (km)	$\beta^a(355)$ ($Mm^{-1}sr^{-1}$)	$\beta^a(532)$ ($Mm^{-1}sr^{-1}$)	$\beta^a(1064)$ ($Mm^{-1}sr^{-1}$)	$\alpha^a(355)$ (Mm^{-1})	$\alpha^a(532)$ (Mm^{-1})
2.00–2.60	3.42±0.16	2.30±0.12	0.90±0.04	220±12	140±15
2.70-3.05	2.12±0.23	1.28±0.16	0.50±0.07	131±11	79±10

Table IV–11: Average intensive particle optical properties for each layer, with their standard deviations.

Height a.s.l. (km)	$LR^a(355)$ (sr)	$LR^a(532)$ (sr)	$AE_\alpha(355, 532)$	$AE_\beta(532, 1064)$
2.00–2.60	65±4	61±6	1.14±0.22	1.351±0.016
2.70-3.05	61.8±1.9	62±3	1.25±0.18	1.34±0.03

At these layers, we obtained then the reconstructed optical properties corresponding to each scenario (I, II, IIIa and IIIb), using the $AE_{AOD}(380,670)$ and $AE_{AOD}(500,1020)$ values from star-photometer, as explained before. The differences between the real AE values from Table IV–11 and the calculated in each scenario were between 3.5% and 30.1% (Table IV–12). The worst simulated was $AE_\alpha(355,532)$ for scenarios I and II, while

the simulation scenarios IIIa and IIIb gave $AE_{\beta}(532,1064)$ values closer than 10% to the measured ones.

Table IV–12: Relative differences between the simulated AE using star-photometer AE_{AOD} and the measured with lidar, for the different scenarios.

Height a.s.l. (km)	$AE_{\alpha}(355, 532)$ rel. diff. (%) Scenarios I and II	$AE_{\beta}(532, 1064)$ rel. diff. (%) Scenario IIIa	$AE_{\beta}(532, 1064)$ rel. diff. (%) Scenario IIIb
2.00–2.60	30.1	4.8	9.9
2.70–3.05	18.6	5.3	3.5

We then retrieved the particle properties with the UP software for the '3+2' setup and for the different simulation scenarios at both layers. In Figure IV–20, the results obtained are shown, together with the initial profiles of extensive optical properties.

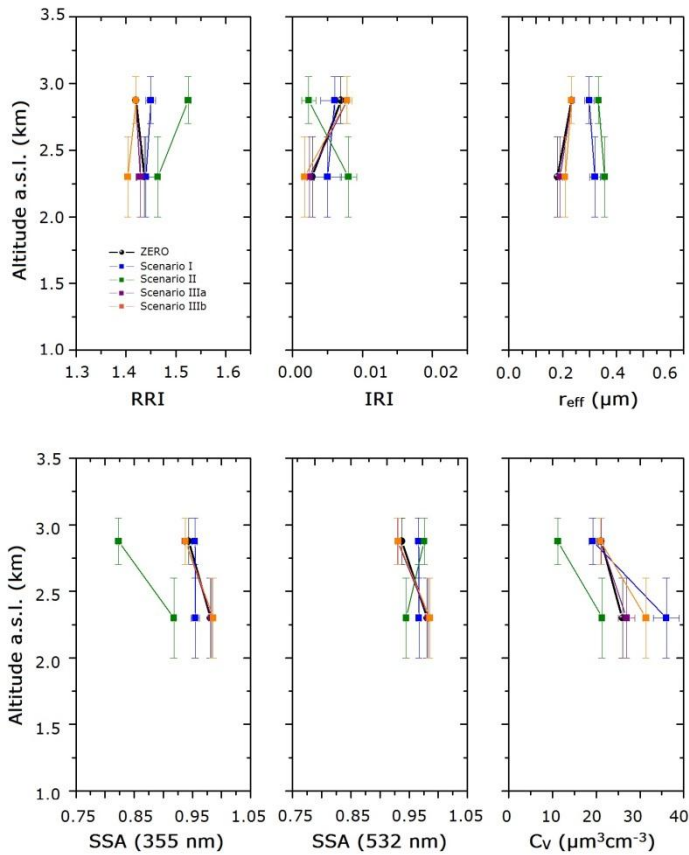


Figure IV–20: Results of the inversions with different combinations of input data derived from the different simulation scenarios.

For a better interpretation of the results in Figure IV–20, Table IV–13 summarizes the relative differences of each particle property for each scenario with respect to the zero retrieval, averaged for the two layers. The scenario that best reproduces the zero retrievals is III (a and b), and the worst is scenario II. The least affected particle properties are *RRI* and *SSA*, and the most affected is *IRI*.

Table IV–13: Mean deviations of each simulation scenario with respect to the zero retrieval, for each retrieved property.

	Scenario I Mean rel. diff. (%)	Scenario II Mean rel. diff. (%)	Scenario IIIa Mean rel. diff. (%)	Scenario IIIb Mean rel. diff. (%)
r_{eff}	53	70	2	8
<i>SSA</i> 355	2	10	0	1
<i>SSA</i> 532	2	4	0	1
C_V	24	32	2	11
<i>RRI</i>	1	5	0	1
<i>IRI</i>	46	126	14	26

Case 2: Mixed-aged biomass burning particles

The second analyzed case correspond to a measurement taken on 18th May 2016, within the framework of SLOPE I (Sierra Nevada Lidar Aerosol Profiling Experiment I). This was a field campaign carried out from May to September 2016 with the aim of gathering useful data for testing the retrieval schemes through inversion of remote sensing observations (de Arruda Moreira et al., 2018b; Bedoya-Velásquez et al., 2018; Benavent-Oltra, 2019; Horvath et al., 2018; Román et al., 2018). During this campaign, the triple photometer was in operation, and thus we will refer to it as *lunar-photometer* for the nocturnal measurements.

The diurnal and nocturnal evolution of the *AOD* measured by the Sun- and the lunar-photometers at 440 nm, together with the AE_{AOD} at 440-870 nm is depicted in Figure IV–21. It shows

$AOD(440)$ values increasing from around 0.2 during daytime on 18th May, reaching more than 0.3 at 21 h UTC. These values coincide with an AE_{AOD} increase (from 0.7 to 1.6), indicating the arrival of finer particles. According to satellite information and transport models (not shown here), the event was classified as biomass burning particles from North American forest fires.

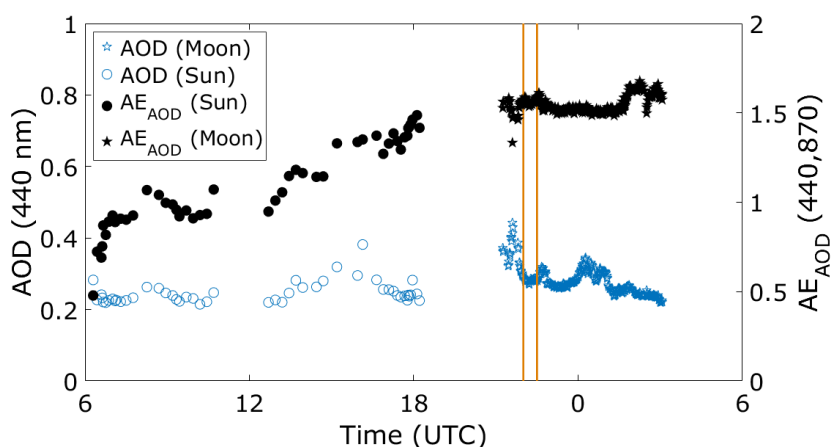


Figure IV-21: Column-integrated aerosol optical properties from Sun and lunar-photometers for 18th and 19th May 2016. Orange box stands for the lidar analyzed period.

The selected nocturnal Raman lidar measurements for this case were from 22:00 h UTC to 22:30 h UTC (orange box in Figure IV-21), and the average of all simultaneous photometer measurements within this interval (27 in total) was taken, obtaining that $AOD(440)$ was 0.282 ± 0.018 and $AE_{AOD}(440,870)$ was 1.56 ± 0.10 .

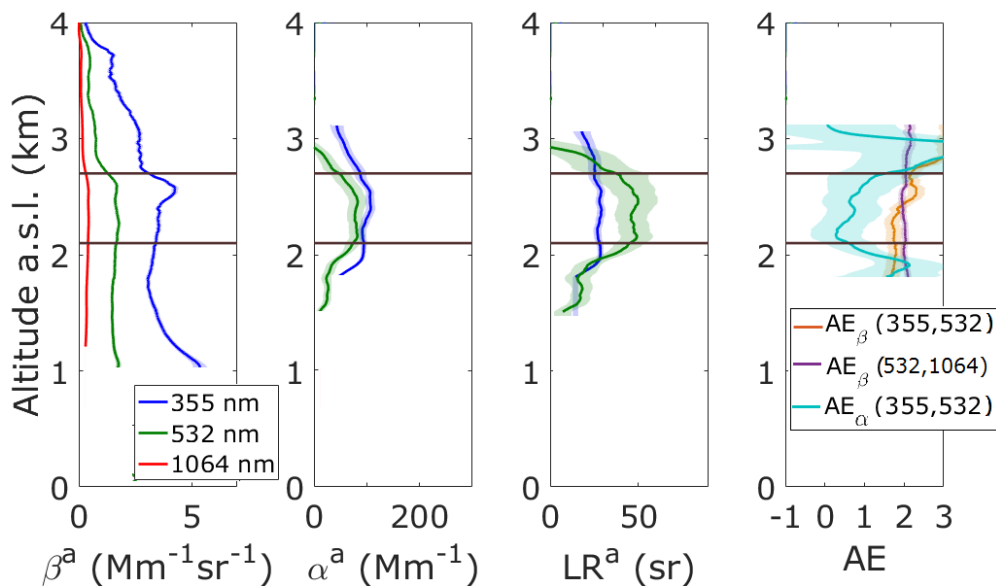


Figure IV-22: Vertical profiles of particle optical properties on 18th May 2016, 22:00-22:30 h UTC measured at Granada station. Brown lines stand for the analyzed layer top and bottom.

Figure IV-22 shows the obtained profiles of particle optical properties from lidar measurements. This time the layer selection criteria allowed us for selecting only one layer centered at 2.4 km a.s.l. The averaged zero optical properties, and their derived intensive properties are detailed in Table IV-14 and Table IV-15 respectively, together with their standard deviations. This case exhibits the same features of aged smoke as found in Section 4.2, in special with lower LR^a values and $CR_{LR} > 1$. AE values are also similar to the ones found in that Section, with AE_β more than 1 (even close to 2) and lower AE_α .

Table IV-14: Same as Table IV-10, for second experimental case and layer 2.1-2.7 km a.s.l.

$\beta^a(355)$ (Mm ⁻¹ sr ⁻¹)	$\beta^a(532)$ (Mm ⁻¹ sr ⁻¹)	$\beta^a(1064)$ (Mm ⁻¹ sr ⁻¹)	$\alpha^a(355)$ (Mm ⁻¹)	$\alpha^a(532)$ (Mm ⁻¹)
3.7±0.3	1.66±0.10	0.41±0.03	99±7	75±9

Table IV-15: Same as Table IV-11, for second experimental case and layer 2.1-2.7 km a.s.l.

$LR^\alpha(355)$ (sr)	$LR^\alpha(532)$ (sr)	$AE_\alpha(355, 532)$	$AE_\beta(532, 1064)$
27±4	45±8	0.7±0.5	2.02±0.19

In the same way as in the former experimental case, we reconstructed the different scenarios with the $AE_{AOD}(440,670)$ and $AE_{AOD}(500,1020)$ values from lunar-photometer. In this case, AE differences were much higher, between 24.9% and 130 % (Table IV-16). This was due to the high uncertainties in the lidar retrieved $AE_\alpha(355,532)$ for this case (see Figure IV-22). For example, if actual $AE_{AOD}(500,1020)$ were 1.2 (i.e., the mean measured value of 0.7 plus its error of 0.5), the relative differences for scenarios I and II would be 34 % instead of 130 %. Therefore, we have to be careful when interpreting the results in terms of these AE differences.

Table IV-16: Same as Table IV-12, for second experimental case and layer 2.1-2.7 km a.s.l.

$AE_\alpha(355, 532)$ rel. diff. (%) Scenarios I and II	$AE_\beta(532, 1064)$ rel. diff. (%) Scenario IIIa	$AE_\beta(532, 1064)$ rel. diff. (%) Scenario IIIb
130.0	24.9	113.1

The retrieved particle properties for the zero setup and for the different simulation scenarios were calculated and compared with the '3+2' retrievals (Table IV-17). In general terms, the scenario II presents the best accuracy, while scenarios I and III have similar differences (excepting for C_V , with 88 % difference for scenario I). The best retrieved properties are again RRI and SSA , with differences between 1 and 6 %, while IRI and C_V present the greatest differences.

Table IV-17: Same as Table IV-13, for experimental case 2.

	Scenario I Rel. diff. (%)	Scenario II Rel. diff. (%)	Scenario IIIa Rel. diff. (%)	Scenario IIIb Rel. diff. (%)
r_{eff}	11	13	16	10
SSA 355	2	3	7	3
SSA 532	1	2	6	4
C_v	88	10	13	35
RRI	1	2	1	1
IRI	22	33	78	67

Case 3: Local anthropogenic particles

This case corresponds to other set of measurements from SLOPE I. The analyzed day was 17th June 2016, when no transport event was detected, but the particles were from local anthropogenic sources. It could be confirmed (Figure IV-23) with the photometer AOD values around 0.1 at 440 nm and $AE_{AOD}(440,870)$ around 1, coinciding with the typical values for Granada urban background (Lyamani et al., 2010).

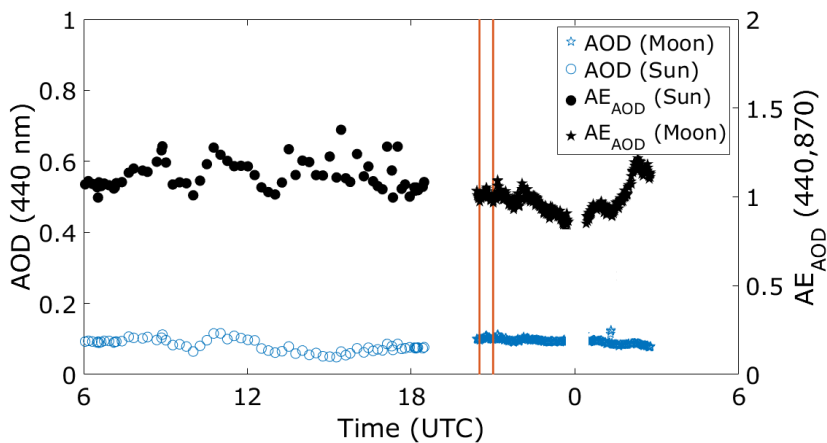


Figure IV-23: Same as Figure IV-21, for experimental case 3.

Raman lidar measurements from 20:30 h UTC to 21:00 h UTC were selected for the analysis, and the optical properties calculated are shown in Figure IV-24. The average of

simultaneous lunar-photometer measurement showed an $AOD(440)$ of 0.10 ± 0.01 and $AE_{AOD}(440,870)$ of 1.01 ± 0.10 .

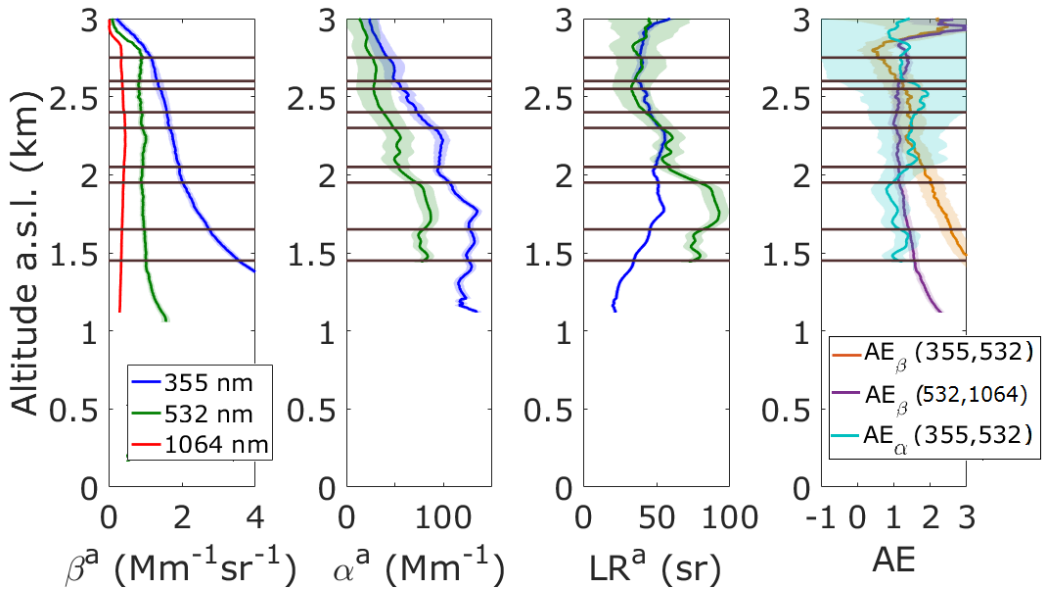


Figure IV-24: Vertical profiles of particle optical properties on 17th June 2016, 20:30-21:00 h UTC measured at Granada station. Brown lines stand for the analyzed layers top and bottom.

For the following analysis, we took five different layers along the vertical, and their averaged extensive and intensive particle optical properties are detailed in Table IV-18 and Table IV-19. Table IV-20 includes the differences found between the simulated AE using star-photometer AE_{AOD} and the measured with lidar, for the different scenarios and layers, that are less than 40% in all cases.

Table IV-18: Same as Table IV-10, for experimental case 3.

Height a.s.l. (km)	$\beta^a(355)$ ($Mm^{-1}sr^{-1}$)	$\beta^a(532)$ ($Mm^{-1}sr^{-1}$)	$\beta^a(1064)$ ($Mm^{-1}sr^{-1}$)	$\alpha^a(355)$ (Mm^{-1})	$\alpha^a(532)$ (Mm^{-1})
1.45-1.65	3.11 ± 0.24	1.000 ± 0.014	0.354 ± 0.005	128 ± 3	78 ± 3
1.65-1.95	2.37 ± 0.21	0.936 ± 0.018	0.384 ± 0.011	123 ± 9	83 ± 3
2.05-2.30	1.80 ± 0.07	0.96 ± 0.03	0.443 ± 0.011	96.3 ± 1.9	52.7 ± 2.0
2.40-2.55	1.51 ± 0.05	0.856 ± 0.024	0.398 ± 0.010	66 ± 5	32 ± 3
2.60-2.75	1.24 ± 0.04	0.871 ± 0.023	0.350 ± 0.010	48.1 ± 1.7	29.6 ± 1.1

Table IV–19: Same as Table IV–11, for experimental case 3.

Height a.s.l. (km)	$LR^{\alpha}(355)$ (sr)	$LR^{\alpha}(532)$ (sr)	$AE_{\alpha}(355, 532)$	$AE_{\beta}(532, 1064)$
1.45-1.65	41±4	76.5±2.0	1.23±0.15	1.50±0.04
1.65-1.95	51±3	89±3	0.97±0.10	1.28±0.07
2.05-2.30	53.2±2.1	57.4±2.2	1.49±0.08	1.12±0.03
2.40-2.55	43.3±1.5	37±3	1.79±0.09	1.11±0.03
2.60-2.75	38.4±1.7	38.3±1.8	1.20±0.03	1.31±0.07

Table IV–20: Relative differences between the simulated AE using star-photometer AE_{AOD} and the measured with lidar, for the different scenarios and layers.

Height a.s.l. (km)	$AE_{\alpha}(355, 532)$ rel. diff. (%) Scenarios I and II	$AE_{\beta}(532, 1064)$ rel. diff. (%) Scenario IIIa	$AE_{\beta}(532, 1064)$ rel. diff. (%) Scenario IIIb
1.45-1.65	0.4	45.0	25.1
1.65-1.95	27.4	35.8	51.3
2.05-2.3	17.3	26.4	23.9
2.4-2.55	31.1	25.5	41.4
2.6-2.75	2.7	37.2	53.9

Figure IV–25 shows the obtained inversion results for all properties, layers and scenarios. The averaged relative differences for each property and scenario are included in Table IV–21. We see that the least affected properties are the RRI and the SSA . On the other hand, the scenarios that affect the retrievals in least amount are again IIIa and IIIb.

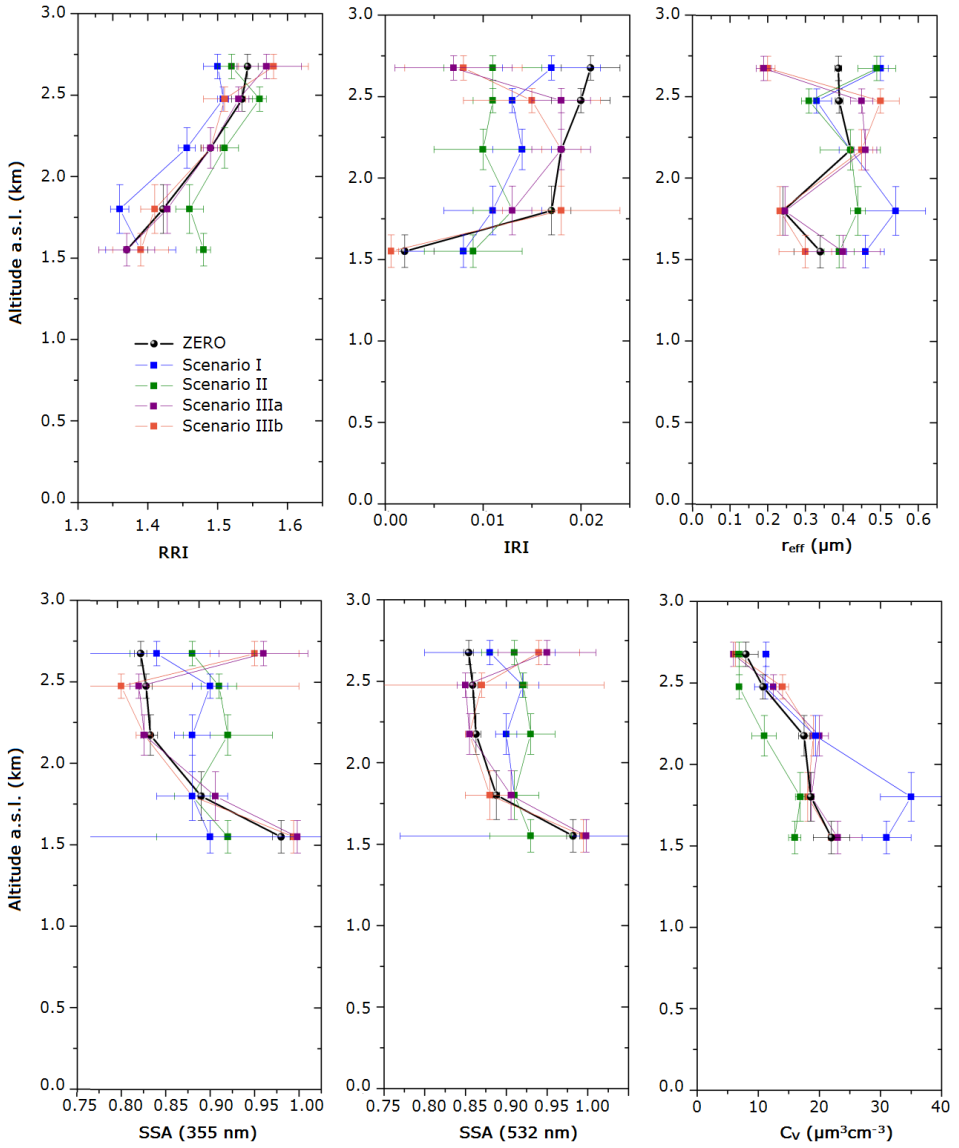


Figure IV-25: Same as Figure IV-20, for experimental case 3.

Table IV–21: Same as Table IV–13, for experimental case 3.

	Scenario I Mean rel. diff. (%)	Scenario II Mean rel. diff. (%)	Scenario IIIa Mean rel. diff. (%)	Scenario IIIb Mean rel. diff. (%)
r_{eff}	41	29	19	20
SSA 355	5	7	4	4
SSA 532	4	6	3	3
C_V	37	25	12	12
RRR	2.5	3	0.5	1.5
IRI	82	102	40	33

4.4 SUMMARY AND CONCLUSIONS

In this chapter, a hybrid regularization algorithm to retrieve aerosol microphysical particles has been systematically applied to real and simulated cases. This algorithm has been developed in the University of Potsdam (Germany) with graphical software to allow for interactive forward and inverse calculations based on Lorenz-Mie model for spherical particles. Thanks to this powerful tool, we were able to provide aerosol size distributions (and their derived particle size properties), particle complex refractive index and single scattering albedo from '3+2' Raman lidar datasets at different heights.

In section 4.2, a complete optical and microphysical analysis of biomass burning aerosol particles transported from North American forest fires to Europe was presented. The event occurred during July 2013, and Raman lidar data from three EARLINET stations (Granada, Leipzig and Warsaw) were used in order to obtain independent particle backscatter and extinction coefficient profiles and thus to apply the regularization algorithm.

The observed smoke layers, with thicknesses between 1 and 2 km, presented AOD (at 532 nm) that accounted for more than 40 % of total AOD at Granada, more than 30 % of total AOD at

Leipzig and more than 70 % of total *AOD* at Warsaw. Lidar ratios in the range 23–34 sr for 355 nm and 47–58 sr for 532 nm were obtained, which means a color ratio of lidar ratios around 2. These values, together with $AE_{\alpha}(355,532)$ ranging 0.20–0.98, are in agreement with other studies about biomass burning particle aging processes due to transport, although a minor effect was found for the Warsaw case.

Particle volume concentrations of 17.3 ± 0.2 , 10.1 ± 0.4 and $34.3 \pm 0.7 \mu\text{m}^3 \text{cm}^{-3}$ were found for the layer peaks at Granada, Leipzig and Warsaw, respectively. Effective radii between 0.207 and 0.34 μm were derived, with values that approximately fit an exponential dependence with transport time given in a previous article. The very low imaginary part of the complex refractive index (between 0.0012 and 0.003), and single scattering albedos of more than 0.96 and without significant spectral dependence, suggest that the analyzed particles present low absorption (and then low black carbon content) and wide particle size distributions.

Integrated volume concentrations were obtained by assuming some reasonable features of the volume concentration profiles within the smoke layers, finding values of 0.016–0.038 $\mu\text{m}^3 \mu\text{m}^{-2}$. This integration was compared to the retrieved concentrations obtained with passive remote sensing retrievals, which usually provide information about the properties integrated along the whole atmospheric column. Particularly, a comparison was made with microphysical retrievals from three nearby AERONET stations. The similarity among the majority of the obtained intensive properties for the smoke layers and for the total atmospheric column is an indication that the tropospheric structure and properties were determined by the smoke plumes during those events.

As a practical application of the results, an approximately linear dependence was found between particle volume concentrations and extinction coefficients at 532 nm for the analyzed layers, using also data from other studies. For the selected cases, this approximation is good and it can provide an estimation of the

particle volume concentrations using only extinction when inversion algorithms cannot be applied. Nevertheless, it must be taken with caution, since these factors are only strictly applicable for similar aerosol particles (in terms of sources and aging) and vertical distributions.

In section 4.3 we have proposed a methodology for using UP software and retrieve particle microphysical properties for cases or stations where one of the required '3+2' lidar channels is not available. The methodology consisted on reconstructing the missing channel with information from co-located star- or lunar-photometer, assuming certain equivalences between AE_{AOD} from photometer and AE_{α} or AE_{β} from lidar. Three reconstruction scenarios were defined (I, II and III), depending on the missing channel (α^a at 532 nm, α^a at 355 nm and β^a at 1064 nm, respectively). We have performed then a sensitivity study with both simulated and real cases.

We selected two different simulated monomodal aerosol size distributions (submicrometric and micrometric), and four different *CRI* for each distribution, and we calculated the optical properties for each reconstruction scenario and each distribution+*CRI* case. We observed that variations of 5 % in one of the *AE* introduced deviations less than 20 % in the retrieved microphysical properties. Moreover, in 95 % of the simulated cases, those deviations were less than 10 %. The results for the micrometric distribution were in general terms better than for the submicrometric, and the same can be stated for the refractive index case D (1.6+0.05i). For the real cases, using the photometer introduced variations in Angström Exponent between 3 and 40%, and we found that the deviations caused in the retrievals were less than 40 %.

It is to be said for both real and simulated cases, that the least affected parameters were the real part of the refractive index and the single scattering albedo. The best scenario was in general number III (it is, when β^a at 1064 nm is missing), and it is noticeable that no significant improvement was found if we

assume a more complex $AE_{AOD}-AE_{\beta}$ relationship (scenario IIIb) or if both AE are assumed to be equal (scenario IIIa).

In a future work, some bimodal distributions are going to be included for the simulations, and variations in AE up to 40 % will also be tested, as observed in real cases. More real cases must also be analyzed in order to perform a statistical study to evaluate which lidar configurations are the most appropriate and which microphysical parameters are less affected.

V INVERSIONS FOR NON-SPHERICAL PARTICLES

In the previous chapter, we have applied a hybrid regularization method to retrieve particle properties from so called '3+2' Raman lidar measurements. That method, as most of the regularization methods, use Mie theory to model aerosol particles as an ensemble of spheres, what usually provides fairly good results for submicrometric particles, as seen in literature and subsections 4.2 and 4.3. However, particle depolarization measurements allow for extending the model to non-spherical particles and, therefore, for describing realistic cases such as mineral dust particles and volcanic ashes.

As explained in section 2.2.1, the first non-spherical model approximation, i.e., the spheroidal model, seems to reproduce particle properties significantly better than spherical model (Kahnert and Kylling, 2004; Mishchenko et al., 1996, 1997). For this reason, several remote sensing inversion algorithms using spheroidal model have been applied, tested and validated in the recent decades (Böckmann and Osterloh, 2014; Dubovik et al., 2002a, 2006; Lopatin, 2013; Olmo et al., 2006, 2008;

Quirantes et al., 2012; Samaras, 2017; Samaras et al., 2016; Veselovskii et al., 2010). These algorithms model aerosol particles as a mixture of spherical and non-spherical components, but for simplicity shape and size are assumed to be independent.

In this chapter we analyze the potential of multiwavelength Raman depolarization lidar stand-alone retrievals of non-spherical particles properties. To that end, we use the software SphInX (Spheroidal Inversion Experiments), that adopts the spheroid-particle approximation with a simultaneous generalization of the size distribution to a shape-size distribution in two dimensions first proposed by Osterloh (2011) and Böckmann and Osterloh (2014). In section 5.1, this software and the mathematical algorithm behind it are briefly described to better understand its strengths and limitations.

In section 5.2, two experimental cases measured during SLOPE I campaign (described in section 4.3.2) are analyzed with this approach. The goal is to discuss the physical properties of two different aerosol types through the retrieval with SphInX and explore further the potential of this tool. It is important to stress the lack of a well-established consensus on modelling and inverting aerosol microphysics, especially when we include nonsphericity. This fact makes harder to find out how appropriate is the obtained retrieval in each case. Currently the world's most used software to derive columnar aerosol properties (although they are obtained for the whole atmospheric column, instead of vertically resolved) is provided by AERONET. Because of its worldwide use, and despite this tool provides different kind of information, we use AERONET data here in order to assess for the impact of the vertically resolved analyzed layers in the context of the columnar properties, in an effort to better understand the differences and limitations of both approaches.

Finally, section 5.3 includes the conclusions of our analysis and some proposals for further research in this field.

5.1 SPHINX SOFTWARE

The aim of this section is to give an insight into the algorithm and software used in this chapter. This software is based on the generalization of Mie model in two dimensions accounting for non-spherical particles. In this way, an ensemble of spheroids characterized by their volume-equivalent radius (r) and aspect ratio (a) is considered, and the aerosol volume shape-size distribution $v(r, a)$ is obtained by regularization (Böckmann and Osterloh, 2014).

The aerosol distribution is related to the optical properties $\Gamma(\lambda)$ through the generalization of Equation (IV-1):

$$\Gamma(\lambda) = \int_{a_{min}}^{a_{max}} \int_{r_{min}}^{r_{max}} K_{\Gamma, v}(r, \lambda, a, CRI) \cdot v(r, a) dr da \quad (V-1)$$

The Kernel functions $K_{\Gamma, v}(r, \lambda, a, CRI)$ for non-spherical particles are calculated from T-matrix theory (Mishchenko et al., 1996). For Raman lidar measurements, the ideal optical data setup would be $\beta^a(\lambda)$ at 355, 532 and 1064 nm, δ_p at the same wavelengths and $\alpha^a(\lambda)$ at the first two, also known as ' $3\beta + 2\alpha + 3\delta$ ' setup. In the case of MULHACEN data for this thesis, the available setup was ' $3\beta + 2\alpha + 1\delta$ ' (with δ_p at 532 nm), also shown to be enough for the retrieval of aerosol microphysical properties (Böckmann and Osterloh, 2014; Osterloh, 2011; Samaras, 2017; Samaras et al., 2016).

The algorithm used in SphInX has thus the aim of inverting Equation (V-1), which is an ill-posed problem of the same kind of the spherical case. The CRI is also unknown in this case and, thus, the strategy of defining a grid from which the best solution is chosen is also shared with UP software.

In the first step, for discretization of Equation (V-1) by collocation, the algorithm uses an extension of B-splines to two dimensions which are called *B-spline surfaces* (Deuffhard and Hohmann, 2003) of order d , $\phi^{(d)}(r, a)$. The distribution $v(r, a)$ is then approximated by a finite linear combination of such surfaces:

$$v_{p,q}(r, a) = \sum_{j=1}^p \sum_{k=1}^q b_{jk} \phi_{jk}^{(d)}(r, a) \quad (\text{V-2})$$

For illustration of B-spline surfaces, see Figure V-1.

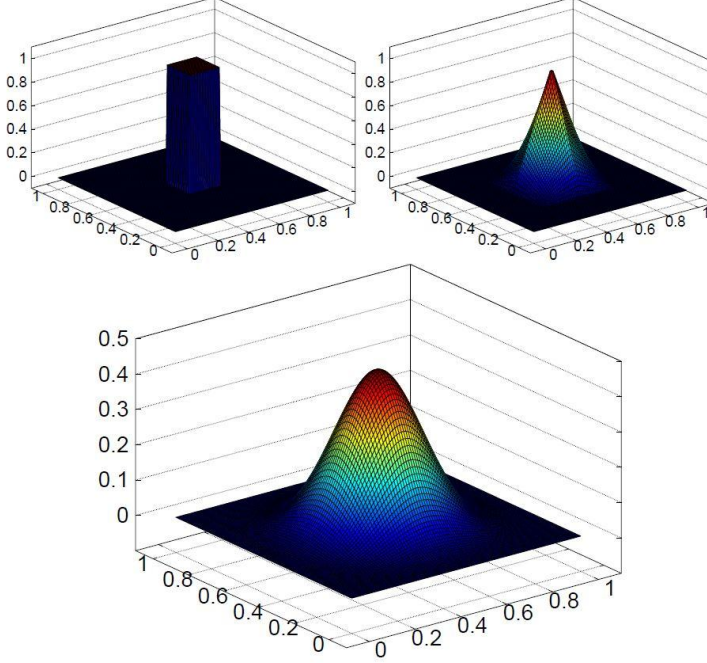


Figure V-1: Some particular 2-dimensional B-spline surfaces of orders 1, 2 and 4. From (Böckmann and Osterloh, 2012).

Then, an index reordering $L = F(j, k) = (k - 1)p + j$ is used to reduce the problem to determine the coefficients b_L from:

$$\sum_{L=1}^{p \cdot q} A_{iL} b_L = \Gamma_i \quad (\text{V-3})$$

where

$$A_{iL} = \int_{a_{min}}^{a_{max}} \int_{r_{min}}^{r_{max}} K_{\Gamma, \nu}(r, \lambda_i, a, CRI) \cdot \phi_L^{(d)}(r, a) dr da \quad (\text{V-4})$$

The advantage of B-spline collocation over other discretization methods, like *Galerkin* methods (Galerkin, 1915), is the lighter computational load of the first one and the better stability of the solutions. A more detailed discussion and description of the whole mathematical apparatus is given in Samaras (2017).

Unlike the UP algorithm, a precalculated database is used for the calculation of the kernel functions, for discrete (r, a) values.

This database has been produced by Mieschka tool (Rother and Kahnert, 2014) based on T-matrix method to avoid the computational cost which would otherwise limit the microphysical retrieval to an impractical point. The discretized B-splines are also precalculated in SphInX for certain values of spline point number (s) and degree (d), namely $s \in [3,20]$ and $d \in [2,6]$. However, in this case one can also use (s,d) values that are not in the database (although more computation time is needed) and the results are locally stored, expanding the database.

Another difference with UP algorithm is that several Regularization Methods (RM) and Parameter Choice Rules (PCR) combinations are available for solving the inversion problem, i.e., determining b_L from Equation (V-3). These combinations are:

- Truncated Singular Value Decomposition with discrepancy principle (TSVD-DP).
- Tikhonov regularization with L-curve method (Tikh-LC).
- Padé iteration with discrepancy principle (Padé-DP).
- Tikhonov regularization with the generalized cross validation method (Tikh-GCV).
- Tikhonov regularization with discrepancy principle (Tikh-DP).
- Padé iteration with L-curve method (Padé-LC).

TSVD (briefly explained in section 4.1) and Tikhonov regularization are widely used methods that can be found in most books about regularization, e.g. Hansen (2010), and have been used in other lidar inversion algorithms (Böckmann, 2001; Müller et al., 1999a). Padé iteration, in this context, is part of the so-called generalized Runge-Kutta regularization methods (Böckmann and Kirsche, 2006). The different PCR are also common in bibliography and the reason for choosing one of them in the algorithm is the presence or lack of a-priori error knowledge.

Samaras (2017) showed an overall better performance of Padé-DP combination, for a set of simulated monomodal

distributions. However, this improved performance strongly depends on the compared particle parameter, the quality of the input data and the simulated distribution. For that reason, we checked all the RM-PCR combinations for the cases analyzed in the following sections, and the best one was selected for each case in terms of least residual errors and best stability of the solution.

The software can be used in measurement and simulation modes, and consists of three (main) graphical user interfaces:

1. The SphInX-Configurator (analogous to UP setup phase): here the input optical data are specified (from a number of different lidar channel combinations), together with all initial calculation parameters, namely CRI grid, the $[r_{min}, r_{max}]$ and $[a_{min}, a_{max}]$ intervals and the parameter space to search (s, d) . The RM-PCR combination can also be selected in this step.



Figure V-2: Screen shot of the SphInX-Main panel, indicating the two main parts: solution grid with the scrutinized CRI values and some plot setting options (left), and shape-size distributions and their corresponding particle properties, retrieved in sequence for all selected (s, d) values (right). Adapted from Samaras (2017).

2. The SphInX-Main (analogous to UP computation phase, but with a specific user interface, Figure V–2): here one can visualize all the solutions in real-time while they are computed for all CRI values in the grid (left panel), and for all (s, d) values for the distributions (right panel). The user can perform here all preliminary tests (changing initial configuration), which are vital for the evaluation and interpretation of the final inversion. The computed particle properties that are used in this thesis are SSA , CRI , r_{eff} , C_v , C_s , and the shape properties a_{eff} and a_{width} .

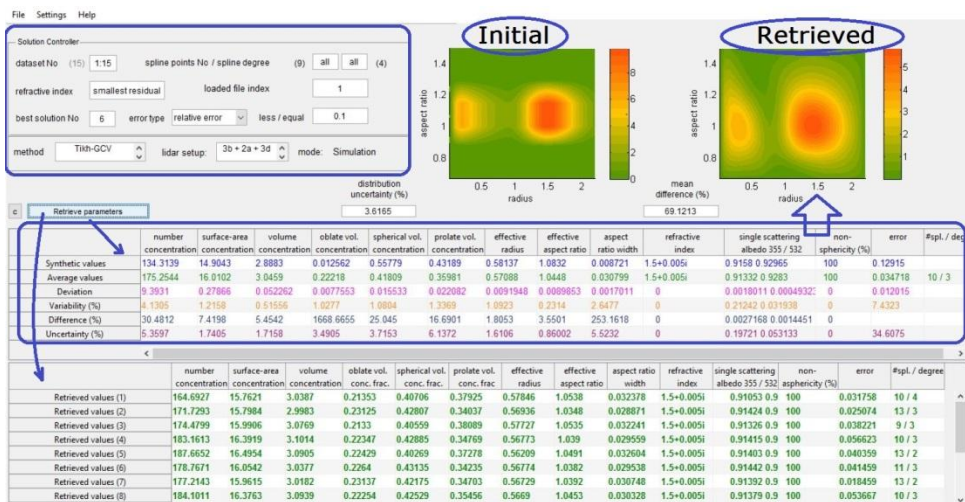


Figure V–3: Screen shot of the SphInX-MPP panel, indicating the main parts: solution controller (upper left panel), average retrieved and (if applicable) initial distributions (upper right part), averaged retrieved particle properties (middle table) and particle properties of each individual selected distribution (bottom table). Adapted from Samaras (2017).

3. The SphInX-MPP (similar to UP evaluation phase, although with other features, Figure V–3): here all retrieved particle properties are shown for each individual distribution (lower table with green numbers) and their average and error analysis (middle table). This error analysis panel is a new feature compared to UP software. It provides also the accuracy (in case of simulations) and standard deviation among the selected best distributions (called *Variability* in this software), but one can also run different inversions for several datasets

and the so-called *Uncertainty* (ratio of the standard deviation of the mean values of each parameter for each dataset over their overall mean) is also calculated. This is very useful e.g. for sensitivity analysis, but this feature has not been used in this thesis.

An important limitation to stress is the already mentioned use of a discrete precomputed database for the kernel functions $K_{\Gamma,v}(r, \lambda, a, CRI)$. This makes that the r range for inversion is limited to $2.2 \mu\text{m}$ (although with resolution up to $0.0113 \mu\text{m}$), the only available a values are $[0.67, 0.77, 0.87, 1, 1.15, 1.3, 1.5]$, and the available RRI and IRI values are $[1.33, 1.4, 1.5, 1.6, 1.7, 1.8]$ and $[0, 0.001, 0.005, 0.01, 0.03, 0.05, 0.1]$, respectively. The resolution gap in aspect ratio is handled by interpolation, what gives good results for shape-size distributions. For the CRI grid, this lack of resolution means that we might not find the exact CRI , but the closest neighbor from the database. However, simulations performed by Samaras (2017) showed that variations of the RRI have minor effects in the retrieved parameters C_s, C_v, r_{eff} and variations of the IRI add a percentage of 3-20 % in their uncertainty.

Finally, there is an important aspect to consider concerning the distribution comparison with other studies. Since there was no equivalent in the literature of a 2D particle distribution, Samaras (2017) introduced the *reduced volume size distribution*, defined as:

$$v_a(r) = \int_{a_{min}}^{a_{max}} v(r, a) da \quad (\text{V-5})$$

which can be compared with size distributions from other lidar regularization algorithms such as UP.

Moreover, size distributions in literature are many times defined for a logarithmic radius interval and for a certain layer with a thickness Δh , while $v_a(r)$ is defined for a single point. In order to interpret the retrieved distributions in that context, we can calculate a new distribution $v_{a,lnr}^{\Delta h}$ with the following conversions:

$$v_{a,\ln r} = v_a(\ln r') = v_a(r) \cdot \frac{dr}{d \ln r'} = v_a(r) \cdot r \quad (\text{V-6})$$

$$v_{a,\ln r}^{\Delta h} = v_a^{\Delta h}(\ln r') = \int_{z_1}^{z_1+\Delta h} v_a(\ln r', z) dz \approx \Delta h \cdot v_a(\ln r') \quad (\text{V-7})$$

where $r' = r(\mu\text{m})/1 \mu\text{m}$ and Δh is the thickness of the layer where the input optical properties ' $3\beta + 2\alpha + 1\delta'$ ' can be considered as constant. This is the reason why $v(r)$ has dimensions of $[\text{L}^3\text{L}^{-3}\text{L}^{-1}]$, usually $\mu\text{m}^3\text{cm}^{-3}\mu\text{m}^{-1}$, while $v_{a,\ln r}^{\Delta h}$ has dimensions of $[\text{L}^3\text{L}^{-2}]$, usually $\mu\text{m}^3\mu\text{m}^{-2}$. If several layers (with thicknesses Δh_i) are considered, a total distribution can be calculated as:

$$v_{a,\ln r}^{\Delta h} = \int_{z_1}^{z_1+\Delta h} v_a(\ln r', z) dz \approx \sum_i \Delta h_i \cdot v_{a,\ln r}^{\Delta h_i} \quad (\text{V-8})$$

5.2 EXAMPLE CASES

Two measurement cases were chosen from the database gathered during SLOPE I. In order to assess the performance of the regularization algorithm in different scenarios, cases with different aerosol types were selected, namely aged smoke and mineral dust. The smoke case was selected from the cases already analyzed with UP software, allowing for comparing both algorithms. The analyses of the cases are presented separately in the following subsections.

5.2.1 Case I: 18th May 2016

This case has been also analyzed with UP software in section 4.3.2, as it was used as test case for the methodology proposed in 4.3. As explained in that section, several aerosol plumes coming from North America (according to HYSPLIT backward trajectories) were detected in May 2016. Fire detection maps from satellite measurements indicated wide regions of active forest fires that seemed to be the source of the aerosol arriving to Granada.

In Figure V-4, optical profiles from Raman lidar measurements are depicted for this case, that corresponds to 18th May 2016 at 22:00-22:30 h UTC. Particle backscatter coefficient showed values up to $2 \text{ Mm}^{-1} \text{ sr}^{-1}$ at 532 nm in an aerosol layer centered

around 2.5 km a.s.l. Low δ_p at 532 nm (less than 8%) and strong spectral dependence of β^a , with AE_β around 2 indicated that the measured plume contained smoke particles from the North American forest fires and, thus, small spherical particles were expected, as described in the case from section 4.2 and agreeing with recent literature (e.g. Janicka et al., 2017; Janicka and Stachlewska, 2019; Nicolae et al., 2018; Osborne et al., 2019; Ritter et al., 2018; Sicard et al., 2019b; Vaughan et al., 2018).

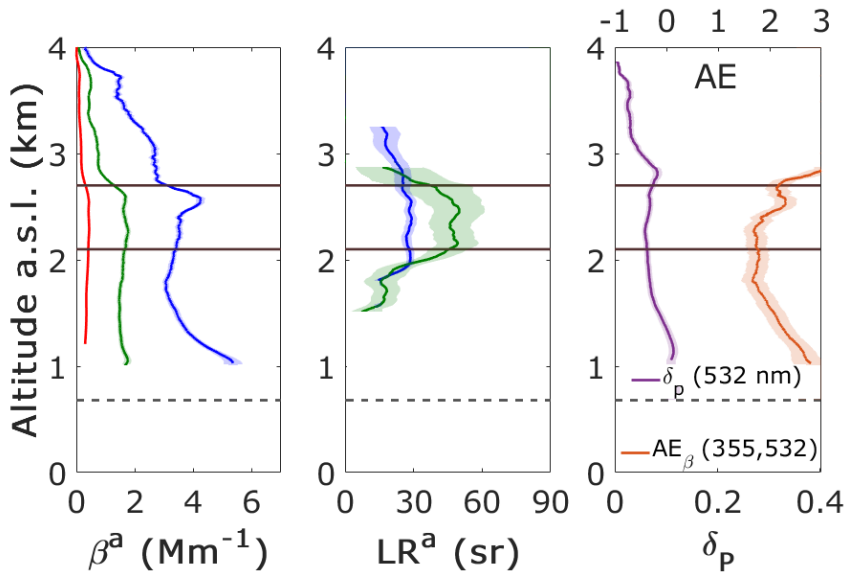


Figure V-4: Particle backscatter coefficient, particle lidar ratio, linear particle depolarization ratio and Angström Exponent profiles for 18th May 2016 at 22:00-22:30 UTC. Brown lines indicate top and bottom of the layer selected for microphysical analysis. Dashed grey lines indicate the altitude of Granada station.

A region from 2.1 to 2.7 km a.s.l. was selected with the criterion of homogeneous intensive properties (brown lines in Figure V-4) and its averaged optical properties were used as input for the regularization algorithm. These properties were already calculated in section 4.3.2 and detailed in Table IV-14 and Table IV-15. The particle lidar ratio values, with $LR^a(532) = 45 \pm 8$ sr and $LR^a(355) = 27 \pm 4$ sr (resulting in a $CR_{LR} = 1.7 \pm 0.5$), coincide with the aged smoke cases deeply studied in section 4.2. The AE_α and AE_β also reveal the same features as

the presented in that section, confirming the presence of aged smoke particles. The average δ_p within the analyzed layer (not included in Table IV-15) was 0.065 ± 0.007 .

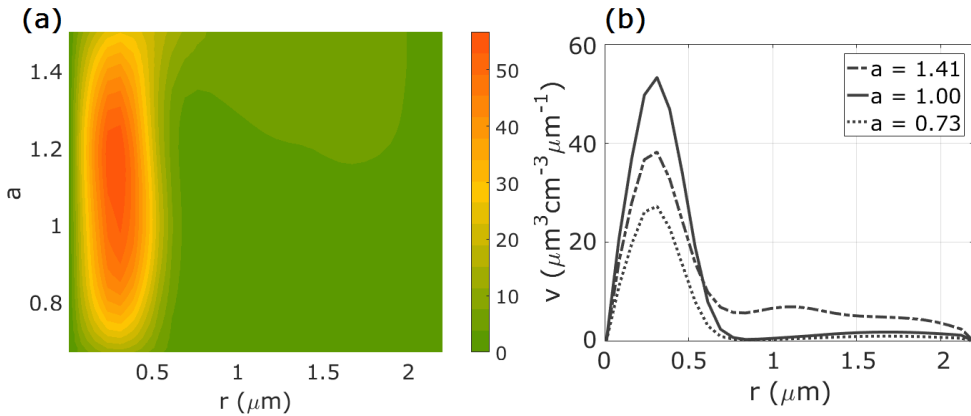


Figure V-5: Shape-size distribution retrieved for 18th May 2016, at 2.1-2.7 km a.s.l. (a) and size distributions for certain a values corresponding to prolate spheroids, spheres and oblate spheroids (b).

The next step with the ' $3\beta + 2\alpha + 1\delta'$ ' dataset was to determine the optimal initial parameters for the retrieval. This was achieved both using physical information and inversion stability test with the different available RM-PCR. The physical restriction consisted on the selection of a CRI grid with values from 1.4 to 1.7 for RI and from 0.001 to 0.03 for IRI . The reasons for this selection were that we found values around $RRI=1.5$ and $IRI=0.002$ for the aged smoke cases in section 4.2 and literature cited therein, and that the retrieval for this case with UP in section 4.3.2 was $RRI=1.474 \pm 0.012$ and $IRI=0.009 \pm 0.003$. Concerning the stability of the inversion with different retrieval methods, Padé-DP and Tikh-GCV were the ones with lower retrieval errors, and we finally selected the latter because the CRI solutions seemed more stable (meaning that close CRI grid points provided solutions with similar good quality).

The retrieved shape-size distribution (Figure V-5a) presents a single mode centered in $r_{mod}=0.31 \mu\text{m}$ (modal radius) and distributed in all shapes (with a peak in $a=1.07$), although a hint of a larger prolate mode is also visible with radii between 1

and $2 \mu\text{m}$, and $a \approx 1.4$. For a better interpretation of the 2D distribution, Figure V-5b shows single size distributions for selected a values corresponding to prolate spheroids ($a=1.41$), spheres ($a=1.00$) and oblate spheroids ($a=0.73$).

To our knowledge, the only work in literature with shape-sizes distributions of aged smoke is the study done by the algorithm and software developer (Samaras, 2017). In that work, 5 cases corresponding to aged biomass burning particles measured in Bucharest (Romania) were analyzed, and the intensive particle properties found were quite similar from case to case. The shape-size distribution for one of those cases is presented in that work, and it presents the same fine mode distributed along a -axis as in our case.

Samaras (2017) did not find the small prolate mode we did, though. It is true that the mode we found presents concentrations more than 5 times lower than the main fine mode. So, although it might be an algorithm artifact, this mode may also be real and related with the presence of different particle types in the present study. This case was indeed classified as 'mixed-aged smoke' in section 4.3.2, although we did not explain it in depth because it was not relevant for the sensitivity study there. The reasons for the classification were the found $r_{eff}=0.38 \mu\text{m}$ (larger than pure smoke particles in section 4.2 and literature therein) and also the analysis of the air masses advecting the particles. The backward trajectories ensemble from HYSPLIT model for this case (Figure V-6) actually reveal the possible presence of recirculated air masses from central Europe and also from local and regional areas.

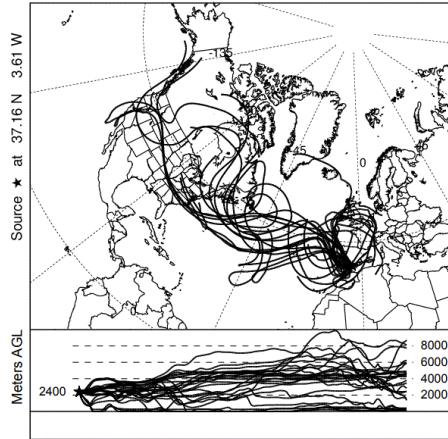


Figure V-6: Coordinates (black lines) of the ensembles of probable air masses' trajectories ending at the investigated layer on 18th May 2016 above Granada, calculated with HYSPLIT model.

The rest of the retrieved particle properties are included in Table V-1, where they are also compared with UP retrievals (for the same optical input data without δ_p information). UP retrievals from section 4.3.2 are labelled as 'UP_{4 μ m}', as this was the r_{max} selected for the retrieval. However, a new retrieval was run using $r_{max}=2.2 \mu\text{m}$ in order to have a better comparison with SphInX outputs. The results from one of the biomass burning cases analyzed by Samaras (2017) are also included in Table V-1, compared also with 'UP_{2 μ m}' ($r_{max}=2 \mu\text{m}$).

For our study, it is noteworthy that RRI retrieved with UP_{4 μ m} and with UP_{2.2 μ m} compares quite well with our findings for aged smoke, as discussed in section 4.2 and references therein (see Table IV-3 and Table IV-4), while SphInX-retrieved RRI presents a lower value. In Samaras' case, this low value is even more extreme, with the lowest possible RRI given by this software. This fact can be directly related with the discrete database used by SphInX (as explained in section 5.1), that seems to affect with a bias to lower RRI values in both analyzed cases.

The differences for IRI and the closely-related SSA , on the contrary, are within the standard deviations of each retrieval, being the maximum differences around 0.008 for IRI and 0.07 for SSA . Their values indicate very weakly absorbing particles, a

feature also observed in the study from section 4.2 and references therein (e.g. Eck et al., 2009; Samaras et al., 2015).

For r_{eff} , SphInX retrieval compares well with values from study in section 4.2, and presents differences of 9 % with $UP_{2.2\mu m}$ and 38 % with $UP_{4\mu m}$. The latter retrieval seems to overestimate r_{eff} , compared with SphInX and $UP_{2.2\mu m}$ retrievals, a conclusion that can also be inferred from Samaras (2017). Concerning shape retrievals, our $a_{eff}=1.126\pm 0.003$ and $a_{width}=0.048\pm 0.001$ values show the already discussed wide shape distribution with spherical particles and a slight predominance of prolate spheroids. It is important to note that these shape retrievals have only a difference of 2% with respect to those found by Samaras (2017) for the same aerosol type.

In contrast to the comparison between SphInX and UP in terms of r_{eff} , the C_v found with SphInX is closer to C_v from $UP_{4\mu m}$ than from $UP_{2.2\mu m}$. In any case, we trust on SphInX retrievals over that from UP, considering that SphInX includes more information (about particle shape) than UP. The differences on C_v between $UP_{4\mu m}$ and $UP_{2.2\mu m}$ are a result of the sizes covered in each retrieval, since the extended size range covered by $UP_{4\mu m}$ allows the inclusion of larger particles in the distribution. Therefore, we conclude that despite its size limitation, SphInX is able to reproduce the particle concentration as well as $UP_{4\mu m}$ by means of the additional shape information.

Table V-1: Particle properties retrieved with SphInX software for case 1, compared to UP retrievals for the same case and another BB case from Samaras (2017).

Reference / location	Inversion type	RRI	IRI	r_{eff} (μm)	a_{eff}	a_{width}	C_v ($\mu\text{m}^3\text{cm}^{-3}$)	C_s ($\mu\text{m}^2\text{cm}^{-3}$)	SSA 355 nm	SSA 532 nm
This study / Granada	UP _{4μm}	1.474±0.012	0.009±0.003	0.38±0.03	-	-	18.3±0.8	143±9	0.919±0.011	0.933±0.008
	UP _{2.2μm}	1.52±0.03	0.009±0.006	0.238±0.018	-	-	11.9±0.4	151±11	0.94±0.05	0.95±0.03
	SphInX	1.42±0.04	0.007±0.010	0.26±0.02	1.126±0.003	0.048±0.001	17.5±1.3	198±2	0.95±0.09	0.96±0.08
(Samaras, 2017) / Bucharest	UP _{2μm}	1.36±0.04	0.0024±0.0003	0.275±0.010	-	-	-	-	-	0.983±0.0001
	SphInX	1.33±0.00	0.004±0.005	0.241±0.003	1.102±0.005	0.047±0.002	9.30±0.03	116±2	-	0.97±0.04

The last part of this analysis was the comparison of the reduced distribution $v_{a,lnr}^{\Delta h}$, adapted from SphInX retrieval, with the corresponding UP distributions. For the conversion from $v(r, a)$ to $v_{a,lnr}^{\Delta h}$ we used Equations (V-5), (V-6) and (V-7) with $\Delta h=600$ m (the thickness of the analyzed layer). We chose this kind of representation because it allows for a better analysis of the size modes and its units can be directly used to assess for the impact of the analyzed layer on the total column. These columnar properties are usually measured by photometry and commonly retrieved with AERONET algorithm, as we will see in subsection 5.2.2. For the present case, this layer impact assessment was not possible since no columnar microphysical information temporally correlated with the lidar measurements was available with enough quality.

Figure V-7 shows the resulting $v_{a,lnr}^{\Delta h}$ distributions. We can observe that the three distributions show the relevance of the submicrometric mode, although the modal radii are slightly different. The intensity of this mode (in terms of concentration) seems underestimated by UP retrievals because of the missing shape information that SphInX includes, as we discussed for the integrated value, C_v . The second mode, with particles on the micrometric range, seems to be well resolved up to $2.2 \mu\text{m}$ by SphInX and $UP_{2.2\mu\text{m}}$. Meanwhile, $UP_{4\mu\text{m}}$ is able to reproduce larger particles contribution, but the sharp, intense peak is likely to be magnified by algorithm artifacts.

This kind of analysis demonstrates the potential of lidar inversion techniques to distinguish different submicrometric and micrometric particles contributions, even within thin layers that could not be deeply studied with other techniques like photometry.

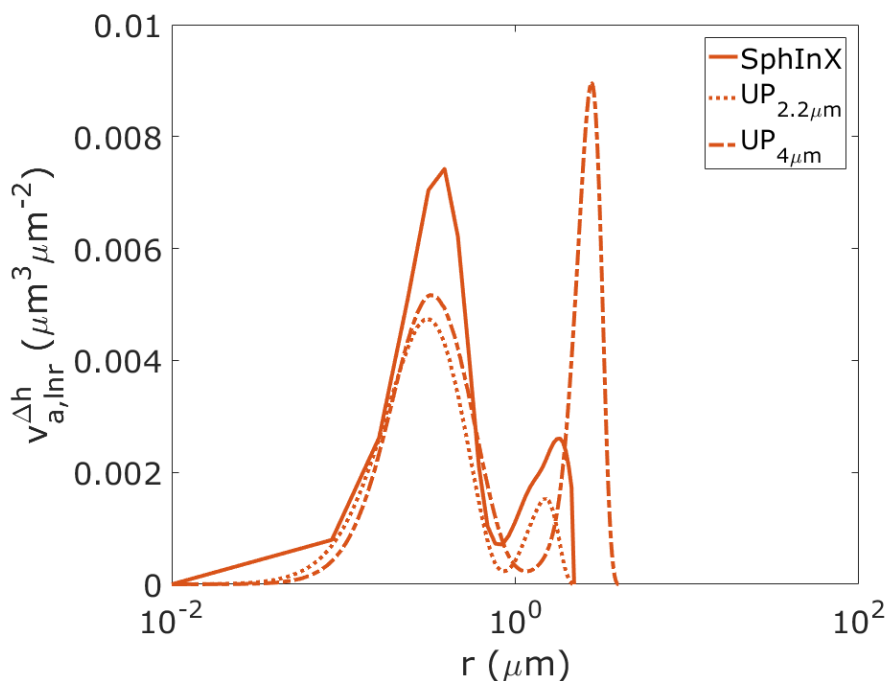


Figure V-7: Reduced logarithmic volume size distributions ($v_{a,lnr}$) adapted from SphInX retrieval for Case I, together with $v_{a,lnr}$ for $UP_{4\mu m}$ and $UP_{2.2\mu m}$.

5.2.2 Case II: 9th June 2016

The second analyzed case corresponds to a mineral dust plume coming from Sahara Desert, according to backward trajectories analysis (not shown here). The optical profiles for 9th June 2016 at 01:00-02:00 h UTC (Figure V-8) confirm the decoupled strong dust layer between 2.8 and 5.0 km a.s.l., with β^a larger than $5 \text{ Mm}^{-1}\cdot\text{sr}^{-1}$ at 532 nm. LR^a around 40-50 sr for both 355 and 532 nm channels, $AE_\beta(355,532)$ less than 0.5 and δ_p more than 0.30 at 532 nm reveal the presence of pure mineral dust particles in accordance to mineral dust studies with multiwavelength Raman and depolarization lidar (e.g. Bauer et al., 2011; Benavent-Oltra et al., 2017; Bravo-Aranda et al., 2013, 2015; Córdoba-Jabonero et al., 2011; Freudenthaler et al., 2009; Giannakaki et al., 2016; Granados-Muñoz et al., 2014, 2016; Guerrero-Rascado et al., 2009, 2008; Janicka et al., 2017; Mandija et al., 2016, 2017; Sicard

et al., 2019a; Soupiona et al., 2019; Tesche et al., 2011). This strong layer can be considered homogeneous in the view of its optical intensive properties, since LR^a (both wavelengths), $AE_\beta(355,532)$ and δ_p vary in ranges with standard deviations less than 7%.

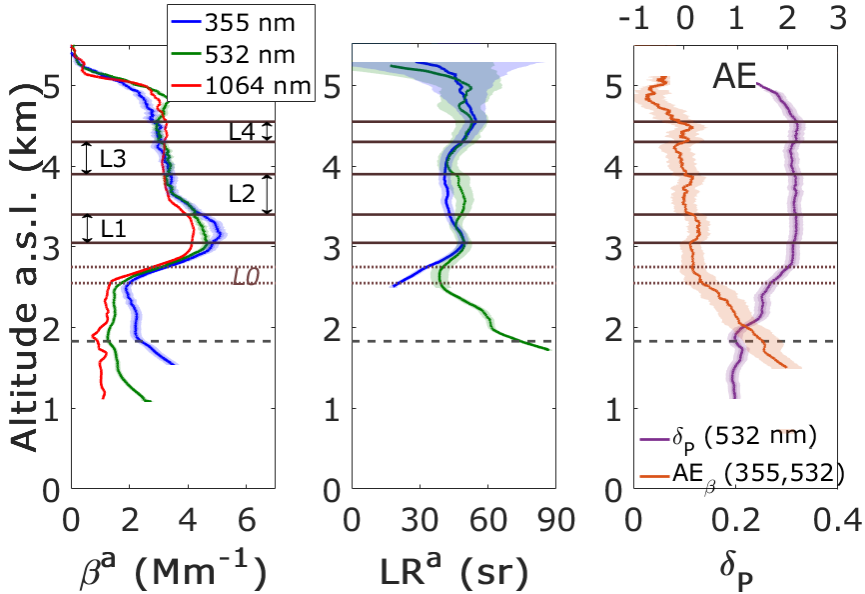
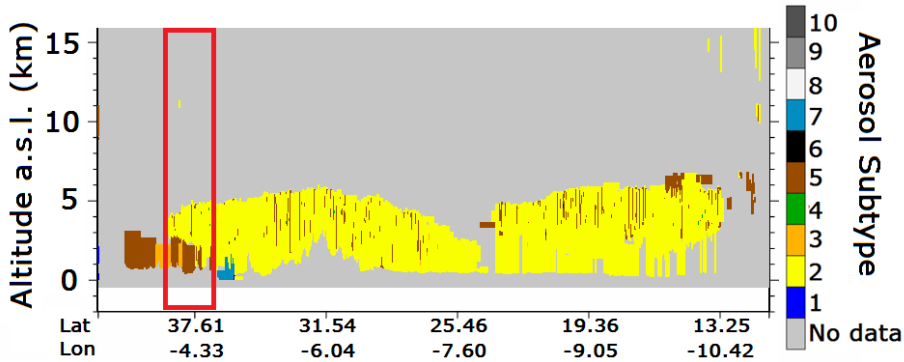


Figure V-8: Particle backscatter coefficient, lidar ratio, linear particle depolarization ratio and Angström Exponent profiles for 9th June 2016 at 01:00-02:00 UTC. Solid brown lines indicate top and bottom of the layers selected for microphysical analysis (L1-L4). Dotted brown lines indicate top and bottom of the layer analyzed by Soupiona et al. (2019), L0. Dashed grey lines indicate the altitude of Cerro Poyos station.

The aerosol layer below 2.8 km presented also enough intensity (with β^a around $2 \text{ Mm}^{-1} \cdot \text{sr}^{-1}$ at 532 nm) to be considered for analysis. The δ_p values around 20 % at 532 nm could indicate the presence of polluted mineral dust particles due to their mixing with the local aerosol background (Bravo-Aranda et al., 2015). In this case, a simultaneous overpass of CALIPSO satellite was available, what helped to confirm the two different dust types observed with the aerosol type product (Omar et al., 2009). In Figure V-9, the aerosol subtype product (version 4.10) for this overpass is shown, and the two different layers can be observed (yellow and brown labels). In the present analysis, only the pure dust layer is to be analysed,

as our intention is to test SphInX software for this pure aerosol type. However, Soupiona et al. (2019) analyzed the polluted layer from this profile with SphInX software since they were focused on highlighting the features of polluted dust against other pure dust cases.



1=marine 2=dust 3=polluted/continental smoke 4=clean continental 5=polluted dust
6=elevated smoke 7=dusty marine 8=PSC aerosol 9= volcanic ash 10=sulfate/other

Figure V-9: Aerosol Subtype product (version 4.10) corresponding to a section of a CALIPSO overpass on 9th June 2016 from 02:22 h to 02:35 h UTC. Red box corresponds to the detected aerosol layers over Granada.

For the microphysical retrieval, the pure dust layer was divided into 4 thin layers (L1-L4, depicted in Figure V-8 with brown lines), and the vertically-resolved optical properties were averaged within each layer. The averaged optical properties and their standard deviations are detailed in Table V-2 and Table V-3.

Table V-2: Extensive optical properties for 9th July 2016 at 01:00-02:00 h UTC, averaged for the all analyzed layers.

Layer base-top (km a.s.l.)	$\beta^a(355)$ ($\text{Mm}^{-1}\text{sr}^{-1}$)	$\beta^a(532)$ ($\text{Mm}^{-1}\text{sr}^{-1}$)	$\beta^a(1064)$ ($\text{Mm}^{-1}\text{sr}^{-1}$)	$\alpha^a(355)$ (Mm^{-1})	$\alpha^a(532)$ (Mm^{-1})
L1: 3.05-3.40	4.91±0.17	4.47±0.14	4.14±0.06	192±5	185±3
L2: 3.40-3.90	3.7±0.3	3.7±0.4	3.41±0.23	153±16	172±14
L3: 3.90-4.30	3.19±0.14	3.31±0.08	3.16±0.03	129±3	134±5
L4: 4.30-4.55	2.99±0.07	2.98±0.05	3.25±0.03	142±3	150±3

Table V-3: Intensive optical properties for 9th July 2016 at 01:00-02:00 h UTC, averaged for the all analyzed layers.

Layer base-top (km a.s.l.)	$LR^a(355)$ (sr)	$LR^a(532)$ (sr)	$\delta_p(532)$	$AE_\beta(355, 532)$
L1: 3.05-3.40	39.1±2.4	41.4±2.0	0.318±0.007	0.23±0.16
L2: 3.40-3.90	41±8	46±9	0.316±0.007	0.0±0.5
L3: 3.90-4.30	40±3	40.5±2.5	0.310±0.007	-0.09±0.17
L4: 4.30-4.55	47.5±2.1	50.3±1.9	0.319±0.008	0.01±0.10

We then proceeded to the inversion with SphInX software using the ' $3\beta + 2\alpha + 1\delta$ ' dataset for each layer. This time, the configured *CRI* grid had *RRI* between 1.33 and 1.7 and *IRI* between 0 and 0.01. Higher *IRI* values (meaning more intense absorption) were excluded as they have only been found in literature directly at the dust source (e.g. Wagner et al., 2012) or when the dust is mixed with absorbing particles like soot (e.g. Rodríguez et al., 2011; Schladitz et al., 2009; Valenzuela et al., 2012). The selected RM-PCR was again Tikh-GCV, since it was again more stable and with less errors, as in previous case.

Figure V-10 shows the retrieved shape-size distributions for each layer, and also some size distributions for selected *a* corresponding to spheres and prolate and oblate spheroids. All distributions look similar except for the absolute concentrations, and have in common the presence of two marked modes. The submicrometric mode, with $r_{mod}=0.46 \mu\text{m}$ for L1 and L3 and $r_{mod}=0.39 \mu\text{m}$ for L2 and L4 is spread along *a*-axis, but it is slightly shifted to prolate particles, for which the size distribution is also broader (see Figure V-10b, d, f, h for $a=1.41$). The micrometric mode is in the prolate part, with a peak in $r_{mod}=1.44 \mu\text{m}$ for all layers and $a_{mod}=1.21$ for L1 and $a_{mod}=1.24$ for L2-L4.

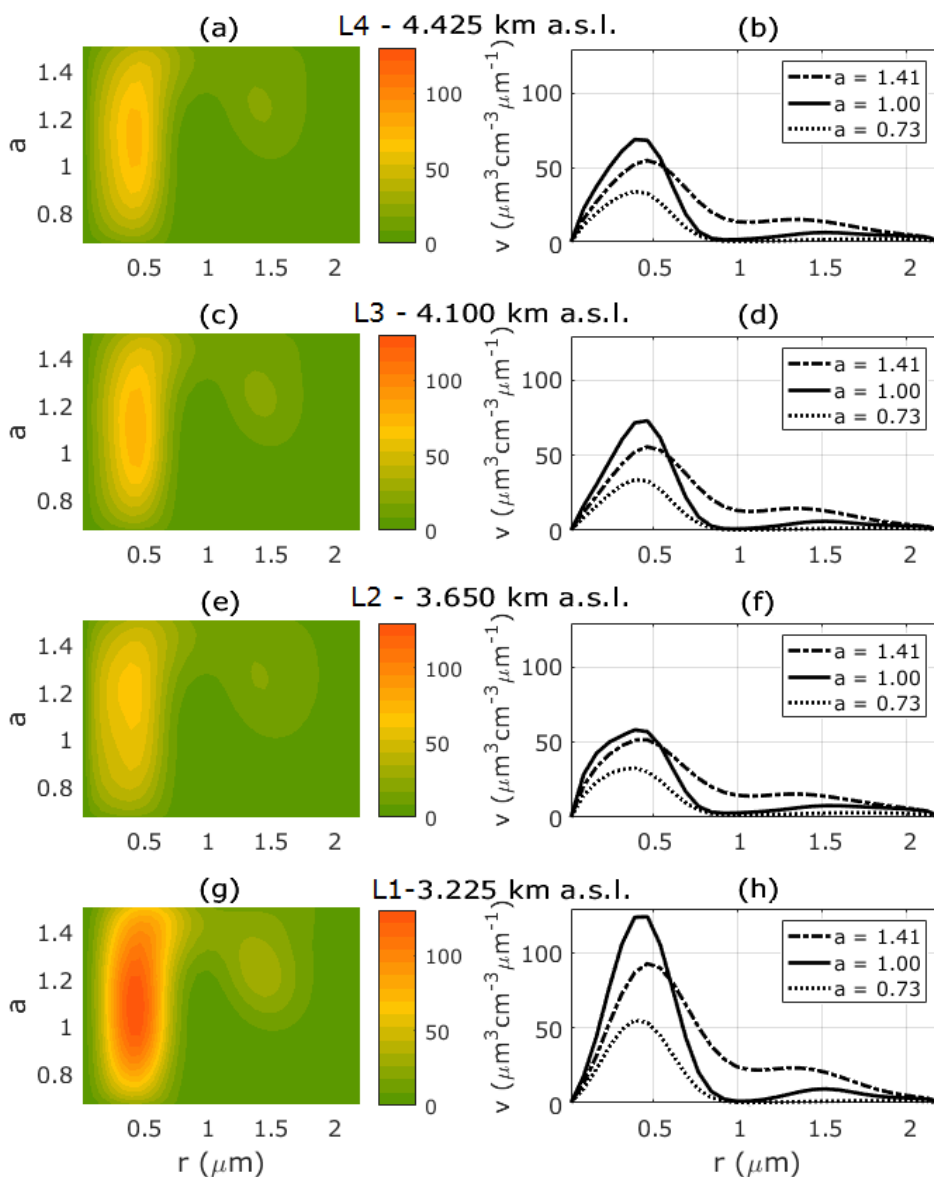


Figure V-10: Shape-size distributions for all analyzed layers on 9th June 2016 (a, c, e, g) and size distributions for certain a values corresponding to prolate spheroids, spheres and oblate spheroids (b, d, f, h).

Samaras (2017) analyzed also some dust cases with SphInX, one measured in Barbados Island, another in Potenza (Italy) and a case measured in Granada. The latter was presented with more detail by Soupiona et al. (2019), together with the

polluted layer from our profile (labelled as L0 in Figure V-8), and two more cases measured in Athens (Greece).

The shape-size distributions found by the cited works were quite diverse. Soupiona et al. (2019) found for pure dust cases distributions with 3 very distinct modes, two corresponding to prolate spheroidal particles with broad bimodal size distribution (similar to our case, see Figure V-10b ,d, f, h, prolate) and an additional contribution of spherical submicrometric particles. The distribution found by Samaras (2017) for measurements in Barbados was more similar to the one presented here, although it presented all particle shapes for both modes. In the same work, the distribution found for Potenza mainly presented a micrometric prolate mode and a submicrometric oblate mode.

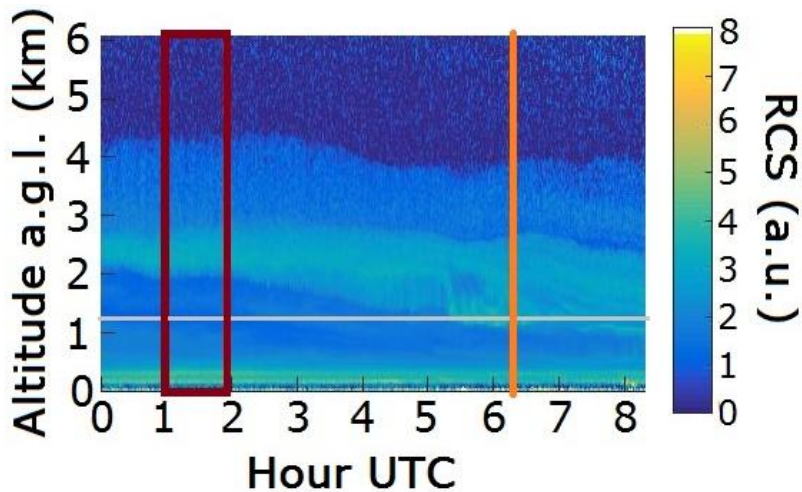


Figure V-11: Ceilometer RCS time evolution for 00:00 to 08:15 h UTC on 9th June 2016. Brown box stands for the analyzed lidar measurement interval, orange vertical line stands for the closest AERONET retrieval time, and grey horizontal line stands for altitude (a.g.l.) of Cerro Poyos photometer.

In Table V-4, the retrieved particle properties for our case are presented, together with the retrieved for pure dust cases by Samaras (2017) and Soupiona et al. (2019). AERONET retrievals (Level 2) are also included when available, in an effort to discuss lidar retrievals and their impact in the independently retrieved columnar properties. In our case, the AERONET retrieval corresponds to closest measuring time

(06:20 h UTC) from Cerro Poyos (12 km apart from Granada, 1830 m a.s.l.) in order to reduce the urban influence in the retrieved columnar properties. We assumed that aerosol load and type remained approximately constant from 02:00 h UTC (lidar measurement) to 06:20 h UTC, and we confirmed it by looking at the ceilometer signal. Figure V–11 shows the RCS time evolution during the studied night, and we can observe that the same aerosol layered structure is present at both lidar and photometer measuring times with minor differences.

It is worth to notice here that, despite the fact that the same aerosol type seems to be present, direct comparisons between lidar retrievals and AERONET are not feasible because of the inherent nature of the measured quantities. While lidar retrievals are focused in certain layers with homogeneous properties, AERONET retrieval corresponds to columnar properties measured from the ground (Cerro Poyos in this case). This means that AERONET retrieval contains the effective properties of the whole atmospheric particle composition, thus, being potentially affected by the polluted layer from Cerro Poyos altitude to the pure dust layer base. Our intention is then to demonstrate the capability of lidar technique to resolve vertical properties of specific layers and assess for their impact on the columnar properties. To be more specific, the integral of all the analyzed layers accounts for 53 % of the total integrated $\beta^a(532)$ and 55% of the total $AOD(532)$ (from Cerro Poyos altitude).

The retrieved vertical profiles of retrieved particle properties with SphInX are depicted in Figure V–12, where the properties found by Soupiona et al. (2019) for L0 (polluted dust) are also included. In that figure, the differences between the homogeneous pure dust layers and the polluted layer are clear.

Table V-4: Particle properties retrieved with SphInX software for case II, compared to AERONET retrievals for the same case and to other SphInX and AERONET retrievals for pure dust cases.

Ref.	Meas. location	Inversion type	RRI	IRI	r_{eff} (μm)	a_{eff}	a_{width}	C_v ($\mu\text{m}^3\text{cm}^{-3}$)	C_s ($\mu\text{m}^2\text{cm}^{-3}$)	SSA 355 nm	SSA 532 nm	
This study	Granada	Sph., L1	1.37±0.07	0.002±0.004	0.40±0.06	1.143±0.008	0.046±0.004	50±7	377±22	0.98±0.04	0.98±0.03	
		Sph., L2	1.48±0.10	0.008±0.004	0.34±0.07	1.142±0.013	0.048±0.003	32±9	280±24	0.93±0.04	0.94±0.03	
		Sph., L3	1.41±0.09	0.005±0.005	0.38±0.08	1.143±0.009	0.047±0.003	31±8	243±10	0.96±0.04	0.97±0.04	
		Sph., L4	1.43±0.09	0.006±0.005	0.35±0.08	1.141±0.004	0.047±0.003	31±9	262±14	0.95±0.04	0.95±0.04	
		AER.	1.43±0.05	0.001±0.001	0.72±0.02	-	-	-	-	-	0.95±0.03 (440 nm)	0.99±0.03 (675 nm)
		Sph.	1.4±0.0	0.004±0.002	0.40±0.02	1.18±0.05	0.084±0.007	26.4±1.9	199±6	-	0.96±0.03	
Samaras (2017)	Barbados island	AER.	1.52±0.02	0.0017±0.0004	1.30±0.09	-	-	-	-	-	0.96±0.01	
		Sph.	1.4±0.0	0.008±0.004	0.39±0.04	1.11±0.03	0.063±0.017	0.22±0.01	-	-	0.94±0.03	
		AER.	1.53±0.01	0.0032±0.0007	0.76±0.05	-	-	-	-	-	0.94±0.02	
Soupiona et al. (2019)	Athens	Sph.	1.4±0.0	0.004±0.002	0.32±0.01	1.18±0.06	0.06±0.01	16.1±1.6	152±12	-	0.97±0.01	
	Granada	Sph.	1.4±0.0	0.004±0.002	0.33±0.01	1.14±0.06	0.06±0.01	29±4	270±30	-	0.98±0.02	

The retrievals show in this case again that the *RRI* values seem to be underestimated if we recall the literature about it, giving values around 1.50-1.55 for mineral dust (Benavent-Oltra et al., 2017; Denjean et al., 2016; Kandler et al., 2009; Petzold et al., 2009; Wagner et al., 2012; Weinzierl et al., 2011). The *IRI* and *SSA* values agree for all cases with the cited literature and also with the AERONET columnar values, indicating weakly absorbing particles.

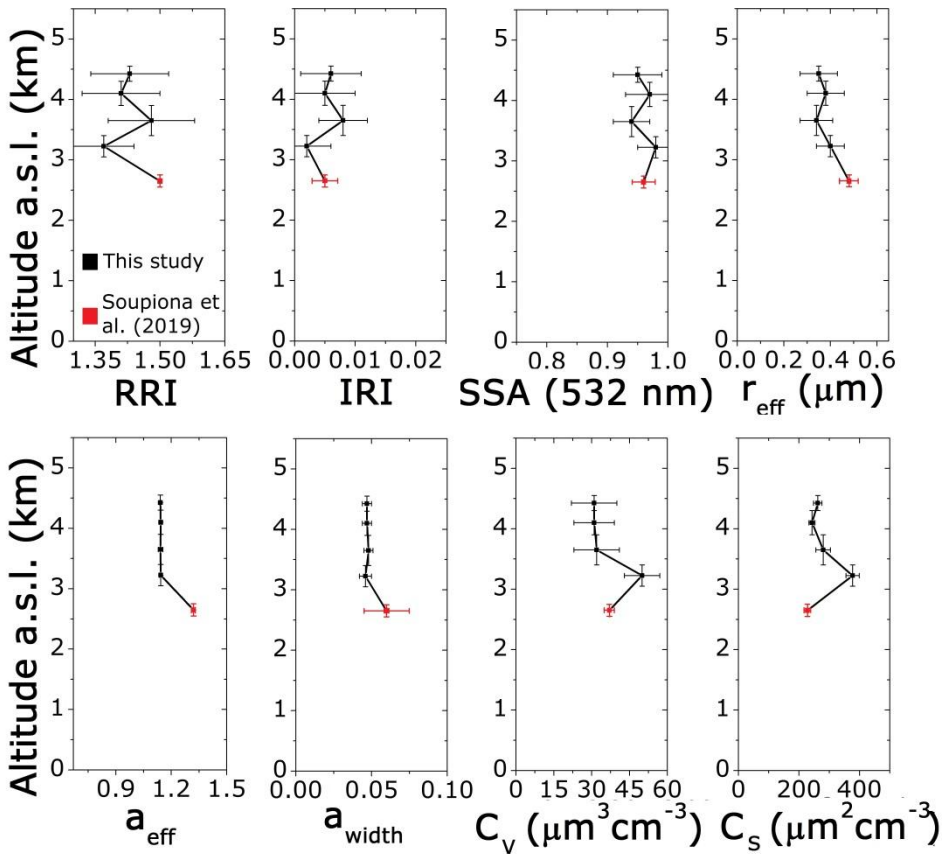


Figure V-12: Vertical profiles of particle optical and microphysical properties retrieved with SphInX software for case II. Red points indicate the layer corresponding to polluted dust (L0) that was analyzed by Soupiona et al. (2019).

The r_{eff} retrieved in our layers is very close to the one found by SphInX in the studies at Barbados and Potenza, and quite lower than the retrieved by AERONET. This is due to the fact of analyzing only a part of the atmospheric column with lidar

retrieval and to the limited radius range analyzed by SphInx, that is of special relevance in cases where coarse mode dominates.

Expanding this discussion about size retrieval, we calculated the reduced distribution $v_{a,lnr}^{\Delta h}$ of the total layer ensemble using Equations (V-5), (V-6) and (V-8) with the Δh_i values corresponding to the thickness of each layer L1-L4. In Figure V-13, the obtained distribution is depicted. We can observe a wide submicrometric mode with $r_{mod}=0.54 \mu\text{m}$ and a smaller micrometric mode with $r_{mod}=1.52 \mu\text{m}$. The coarser mode that is usually detected with other methodologies for dust particles cannot be fully detected with SphInX as we already discussed, therefore we cannot vertically resolve the contribution of each layer to the mode.

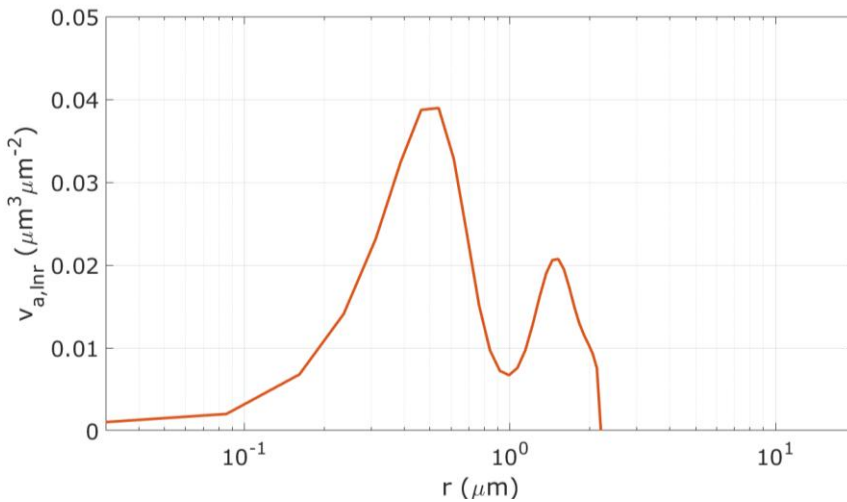


Figure V-13: Reduced logarithmic volume size distribution ($v_{a,lnr}$) for SphInX retrieval for Case II.

Notwithstanding this size limitation of SphInX retrieval, we have to strongly highlight the potential of this algorithm to discriminate between shape modes (even if we consider only sizes less than $2.2 \mu\text{m}$). In our case and in the rest of the cases in literature, the particle shape seems to be generally dominated by prolate spheroids, with a_{eff} between 1.11 and 1.18 in all cases. The a_{width} differs more among cases, what also gives an important information about the mentioned

differences between multimodal cases and cases with all present a (and thus higher a_{width}).

5.3 SUMMARY AND CONCLUSIONS

In this chapter, we explore a more complex algorithm that expands the scope of Mie model to account for non-spherical particle shape adding depolarization measurements to the '3+2' lidar setup. The application of this algorithm to real cases measured with MULHACEN lidar was possible thanks to the SphInX software developed in the University of Potsdam (Samaras, 2017). We were then able to retrieve the same particle properties as with the model in chapter IV, with the additional shape information through aspect ratio parameters (a_{eff} and a_{width}) and 2 dimensional shape-size distributions.

The first general comment that has to be mentioned is that we do not have experimental observations of such 2D distributions, and thus we can just compare our retrievals with other models or with the same model applied to similar data. In that sense, we analyzed two different widely studied aerosol types, namely biomass burning particles and mineral dust, and we compared the usual properties with recent literature. For comparing shape retrievals, we did it with the two only sources found with similar 2D distributions, i.e., Samaras (2017) and Soupiona et al. (2019).

For both cases, we observed that the RRI was not so well retrieved compared with literature. We find that the main reason for this fact is the discrete pre-computed kernel database that the software uses, making the algorithm choose the 'best neighbour' instead of the actual value of RRI .

From the biomass burning case, we were able to obtain particle properties that agree well with literature, with the added value of the shape information. Fine mode particles with $r_{eff}=0.26\pm 0.02$ μm and weak absorption properties were found, and the shape distribution indicated the mixture of all aspect ratios with a slight dominance of prolate spheroids. The retrieval was also compared to UP retrieval since the ensemble

could behave as spherical particles. The results indicate that the lack of shape information by UP makes it underestimate the volume concentration or overestimate r_{eff} (depending on the radius range selected) in order to compensate for this missing information.

From the dust case the main conclusion is that the limited size range of this method constrains its applicability to analyze only the submicrometric and micrometric particle size ranges. The information about absorption (*IRI* and *SSA*) seems to be well represented, though, and it is just the size properties (r_{eff}) the affected ones. We could not compare the retrieved volume concentration with any independent dataset, but this algorithm is likely to underestimate it because of this lack of size information. If we focus just on the part well represented by the algorithm, we found a bimodal particle distribution with a submicrometric mode ($r_{mod}=0.46 \mu\text{m}$) spread over all aspect ratios with a more importance for prolate particles, and a medium mode of purely prolate spheroidal particles.

Those conclusions lead to the necessity of improving the computed database with a greater size range and with a denser *CRI* grid. Including such an extended database to SphInX software would create the ideal tool to completely distinguish completely multiple shape and size modes without losing any information.

Finally, an important drawback of this algorithm needs to be mentioned. This is the necessity of comparing manually and iteratively the results retrieved using different RM-PCR and different initial inversion parameters (spline points, degree, *CRI* grid) because the best configuration differs from one single case to another. That means that more analysis and interpretation time is needed, diminishing then the usability of the software in an automatical mode. However, the great importance of the added information provided by this software makes it worth to continue the research on this line in order to be able to find common criteria to select good and realistic retrievals.

PART III

WIND AND TURBULENCE PROFILING

VI CHARACTERIZATION OF THE ATMOSPHERIC BOUNDARY LAYER WITH DOPPLER LIDAR

Wind and turbulence are key variables in understanding the complex processes in the ABL. High resolution numerical weather prediction models require measured wind speed and direction profiles (World-Meteorological-Organization, 2018). Moreover, those wind profiles measured over a particular site provide valuable information about local transport or to validate homogeneity assumptions for studies comparing close sites (e.g. Bedoya-Velásquez et al., 2018; Benavent-Oltra, 2019).

On the other hand, it is important to characterize and understand turbulence mechanisms and sources due to their complex interactions with other meteorological variables. Turbulence has also a role in new aerosol particle formation (Wehner et al., 2010) and cloud microphysics (Pinsky et al., 2008). An important application of social interest is the prediction of urban pollution events. In particular, the

meteorological and orographic features in Granada produce special conditions in its ABL (de Arruda Moreira et al., 2018b; Bedoya-Velásquez et al., 2019). Especially during winter, long periods with low wind, dry air and stable conditions cause serious air pollution events (e.g. Lyamani et al., 2012).

In this chapter, a statistical study has been carried out to characterize the ABL over Granada in terms of mean horizontal wind and turbulence sources. Some particular study cases have also been analyzed to show the potential of ABL classification scheme to characterize different situations. This analysis has also been applied to two experimental campaigns carried out in two different rural sites in Spain and Poland.

In section 6.1, the methodology to retrieve wind vector field from Doppler lidar measurements is presented as well as the software toolbox developed by Manninen (2019b) to systematically derive different ABL properties.

The horizontal wind product calculated for a 2-year database is used in section 6.2 to perform a statistical analysis of the wind field over Granada. Mean hourly wind profiles for each season are calculated, looking for similarities and differences in the observed trends. Wind rose plots are also presented for different height ranges during day and nighttime, in order to extend the existing information on surface winds in Granada (presented in chapter III).

In section 6.3, the ABL classification scheme is applied over three different sites, namely Granada, an olive orchard in Úbeda (south Spain) and a peatland in Rzecin (Poland). The study in this subsection combines some study cases with a statistical analysis similar to the one conducted by Manninen et al. (2018).

Finally, we present in section 6.4 the conclusions of the whole analysis and some open issues for future research.

6.1 WIND RETRIEVAL AND ABL CLASSIFICATION

In this section, we first describe the physical and mathematical basis of the method to retrieve wind vector field from Doppler lidar measurements (subsection 6.1.1). Later, the different calculation steps and derived products of the software package *Halo lidar toolbox* are explained (subsection 6.1.2). The package, developed in the FMI (Helsinki, Finland) and freely available (Manninen, 2019b), is able to read and calibrate Doppler lidar signals from Halo systems and calculate different wind and turbulent quantities to end up with a classification of the boundary layer mixing sources.

6.1.1 Wind vector field retrieval

The wind is a three dimensional vector field that generally depends on time and space, $\vec{U}(x, y, z, t) = (u, v, w)$. Therefore, the instantaneous measurement of wind at a particular position requires the determination of three vector components. A Doppler lidar system, as explained in section 2.3.2, is able to measure only the projection of the wind vector along the laser beam line of sight (LOS), i.e., the radial velocity v_r . However, assuming a stationary and horizontally homogeneous wind field, i.e. $\vec{U}(x, y, z, t) \sim \vec{U}(z)$, it is possible to estimate the full wind vector from several consecutive Doppler lidar radial measurements. It can be easily shown, by rotation of coordinate system, that the measured v_r by a beam with a certain elevation angle φ and azimuth θ (with respect to North direction) shows a sine-like behaviour:

$$v_r(z) = u(z) \sin \theta \cos \varphi + v(z) \cos \theta \cos \varphi + w(z) \sin \varphi \quad (\text{VI-1})$$

The minimum number of linearly independent v_r measurements to obtain the (u, v, w) wind components is three. One of the usual Doppler lidar scanning techniques, known as *Doppler beam swinging* or DBS, is based on that fact. It consists of measuring v_r in the vertical direction (v_{r1}), tilted to the East (v_{r2} , $\theta = 90^\circ$) and tilted to the North (v_{r3} , $\theta = 0^\circ$) with the same

elevation, as depicted in Figure VI-1, upper part. The wind components are obtained, for each range bin of the laser beam (s), as follows:

$$\begin{cases} u(z) = [v_{r2}(s) - v_{r1}(s) \sin \varphi] / \cos \varphi \\ v(z) = [v_{r3}(s) - v_{r1}(s) \sin \varphi] / \cos \varphi \\ w(z) = v_{r1}(z) \end{cases} \quad (\text{VI-2})$$

where $z = s \cdot \sin \varphi$ for u and v , and $z = s$ for w . This method allows for very fast scanning, but it may easily yield to unrealistic measurements if the wind field is non-homogeneous. For this reason, it is advisable to take more measurements and perform a least-square approach retrieval scheme for the wind components. The most widely used method is the *Velocity-Azimuth display* or VAD, based on the classic technique described by Browning and Wexler (1968). It consists of measuring v_r with a fixed elevation and several azimuth angles, what is known as a conical scan (Figure VI-1, lower part).

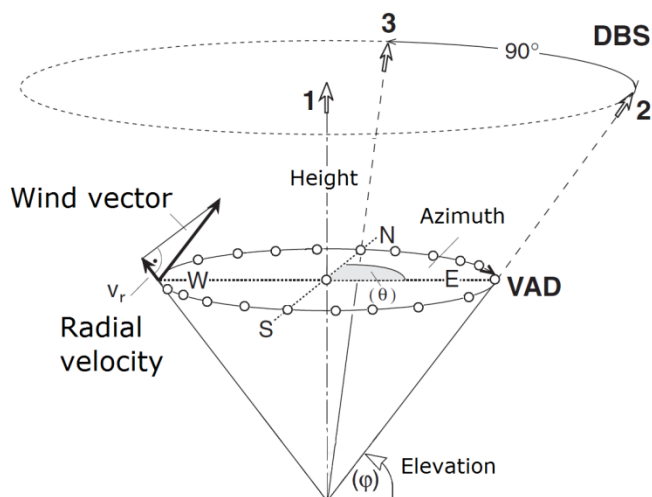


Figure VI-1: Schematic of the scan technique of a Doppler lidar. Lower part: VAD scan; upper part: DBS scan. Adapted from Werner (2005).

One can fit the v_r measured with the conical scheme for each height bin $z = s \cdot \sin \varphi$ to a function of type:

$$v_r(z) = a(z) + b(z) \cos[\theta - \theta_{max}(z)] \quad (\text{VI-3})$$

with offset a , amplitude b and phase shift θ_{max} , see Figure VI-2. We can then get the 3D wind vector for each height bin as:

$$\begin{cases} u(z) = -b(z)\sin \theta_{max}(z)/\cos \varphi \\ v(z) = -b(z)\cos \theta_{max}(z)/\cos \varphi \\ w(z) = -a(z)/\sin \varphi \end{cases} \quad (\text{VI-4})$$

The horizontal wind speed is then:

$$U_H(z) = \sqrt{u(z)^2 + v(z)^2} = b(z)/\cos \varphi \quad (\text{VI-5})$$

and the wind direction, in the meteorological sense (e.g., 90° means wind *from* East):

$$d(z) = \theta_{max}(z) \quad (\text{VI-6})$$

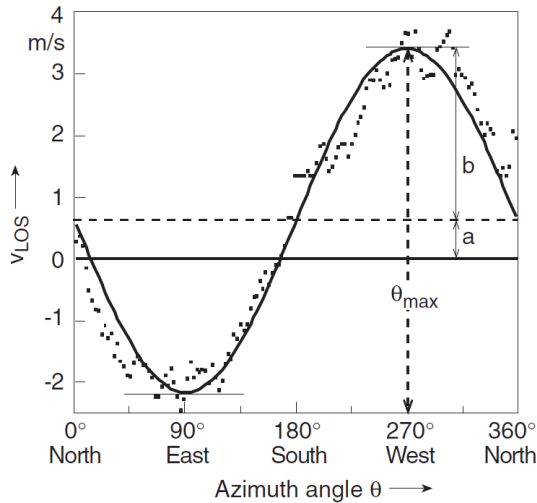


Figure VI-2: Example of sine fitting of the radial wind velocity with the use of the VAD technique. From Werner (2005).

This sinusoidal fitting approach has the advantage of providing a quite simple method for retrieving 3D mean wind field, but also for assessing the goodness of the retrieval in terms of the homogeneity assumption. In this sense, Päsche et al. (2015) proposed the use of the coefficient of determination R^2 of the fitting as a quality control parameter for wind reconstruction, rejecting retrievals with $R^2 < 0.95$. Moreover, the deviations from the ideal sinusoidal shape can provide also valuable information, as they are due to several processes such as wind field divergence or deformation, instrumental noise and

turbulence (Browning and Wexler, 1968). Therefore, the residuals of the VAD fit can be used as a proxy for turbulence estimation, as in the method developed by Vakkari et al. (2015).

The VAD retrieval can be also formulated in terms of a regularization problem. Equation (VI-1) can also be written in matrix form as:

$$A \cdot \vec{U} = \vec{V}_r \quad (\text{VI-7})$$

where $\vec{V}_r = (v_{r1}, v_{r2}, \dots, v_{rn})$ is a vector containing the measured radial velocities and A is a matrix whose rows are comprised of the unit vectors along the n pointing directions with azimuth angles $\theta_i, i = 1, \dots, n$:

$$A = \begin{pmatrix} \sin \theta_1 \cos \varphi & \cos \theta_1 \cos \varphi & \sin \varphi \\ \sin \theta_2 \cos \varphi & \cos \theta_2 \cos \varphi & \sin \varphi \\ \dots & \dots & \dots \\ \sin \theta_n \cos \varphi & \cos \theta_n \cos \varphi & \sin \varphi \end{pmatrix} \quad (\text{VI-8})$$

Equation (VI-7) is an overdetermined linear system that can be solved by regularization with singular value decomposition (SVD), instead of the sinus fitting with so-called normal equations (Boccippio, 1995; Päsche et al., 2015). Thanks to SVD retrieval method, an additional quality control parameter can be calculated, the *condition number*, that accounts for the numerical stability of the retrieval. The problem is numerically stable, or well-conditioned, when the degree of collinearity among the Doppler velocity measurements used for the retrieval is relatively weak, as is well known in regression analysis (see e.g. Belsley et al., 1980).

The precision of the retrieved wind speed and direction from VAD technique can be obtained if the random uncertainty of the radial velocity measurements (in general composed by a turbulent term and an instrumental precision term) are known. Usually this uncertainty is not known, and then some assumptions are needed. The two main approaches followed by the software used in this thesis (*Halo lidar toolbox*, described below in subsection 6.1.2) are (i) the assumption that v_r

precision is isotropic and (ii) the neglect of turbulence and calculation of instrumental precision from SNR. A detailed description can be found in Newsom et al. (2017).

As already mentioned before, DBS scanning procedure is faster than VAD when single beam lidar is used, as only three beam positions are needed. However, the strong homogeneity assumption frequently leads to wrong measurements. The number of azimuth angles used for VAD scan is also critical in the same way, directly affecting the retrieval stability through the condition number. The selected elevation angle (φ) for the scans does not directly affect the retrieval quality, but limitates the height resolution and measurement range.

For those reasons, some tests were carried out before setting up the Doppler lidar system used in this thesis (section 3.2) for regular measurements. The tests were performed with consecutive DBS scan and VAD scans at different elevation angles (from 20° to 80°) and different number of equidistant azimuth points (3, 6, 12 and 24). The results revealed large differences (more than 70 % in many cases) of the retrieved U_H by DBS compared with VAD and a reference wind measurement from co-located radiosoundings. The results for the number of azimuth points in VAD scans showed that the retrievals with 12 points were optimal in terms of short measurement time and stable profiles. We did not obtain a clear optimal value for the elevation angle, since similarly good retrievals were obtained for φ between 60° and 80°. Lower scans showed to improve the resolution in the first hundreds of meters (as shown e.g. by Vakkari et al., 2015), but that kind of measurements were not needed for the studies carried out during this thesis, and therefore their use will be explored in future works. As a result of those tests and the review of some recent literature (Manninen et al., 2018; Marke et al., 2018; Päsche et al., 2015), the final measurement protocol adopted was VAD scans at $\varphi=75^\circ$ and 12 azimuth points.

6.1.2 ABL classification with Halo lidar toolbox

Most of the Doppler lidar analysis done in this thesis has been based on products from *Halo lidar toolbox*, a software package developed in the FMI which is freely available from GitHub website (Manninen, 2019b). The aim of this toolbox is to provide a robust tool to produce harmonized Doppler lidar retrievals applied to measurements from different sites using methods presented in peer-reviewed articles (Harvey et al., 2013; ICAO, 2005; Kleiner et al., 2014; Manninen et al., 2016, 2018; Newsom et al., 2017; O'Connor et al., 2010; Päscke et al., 2015; Rimoldini, 2014; Vakkari et al., 2019) and providing consistent uncertainty estimates. Such harmonization on calculated quantities and used methods is essential to create a broad catalogue of ABL datasets in order to address the gap in between the understanding of the ABL physics and their representation in high resolution climate and numerical weather prediction models (Baklanov and Grisigono, 2008).

The processing chain followed by the toolbox is schematically presented in Figure VI-3. It consists of several scripts that process the measured Doppler lidar data, starting on the necessary preprocessing explained in section 3.5, and culminating in a complete ABL classification (Manninen et al., 2018).

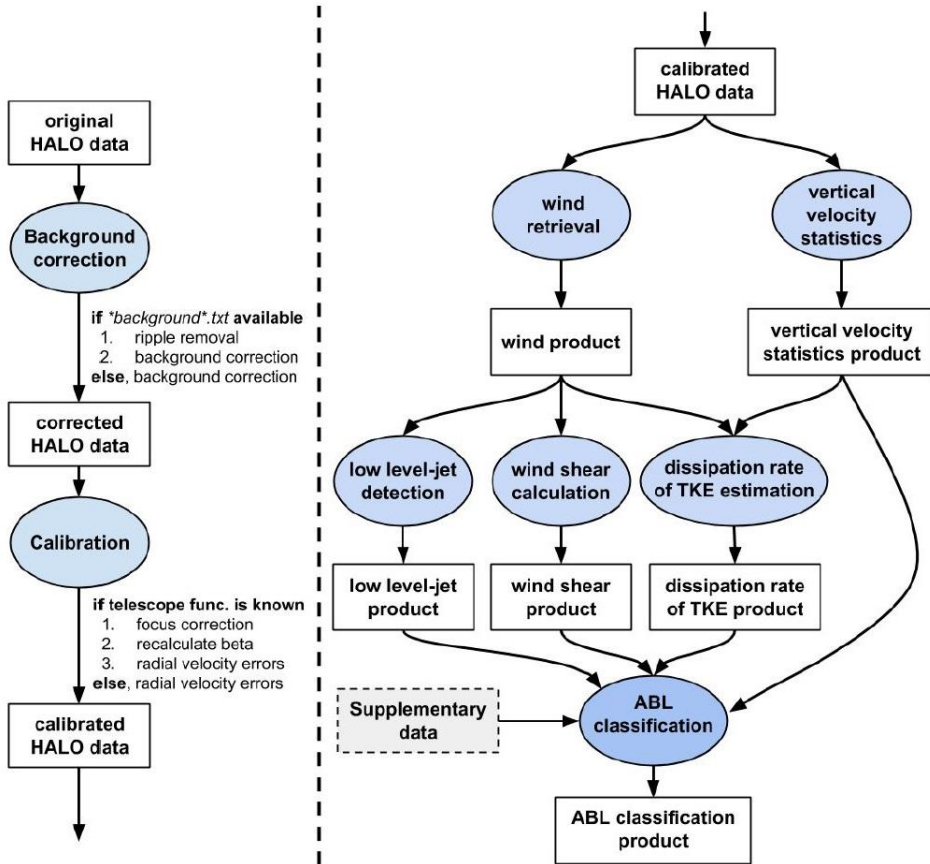


Figure VI-3: Sketch diagram of the Halo lidar toolbox processing chain illustrating the data processing steps from the original uncorrected data to the ABL classification product. In the version used in this thesis, the low level-jet detection algorithm was still not implemented. From Manninen (2019a)

In this thesis, only the horizontal wind product (whose retrieval is detailed in the previous subsection) and the ABL classification product have been systematically used. Nevertheless, the rest of the quantities calculated in the chain are required for the ABL classification and, thus, they are briefly described below:

1. The raw data files are read and background artefacts are corrected with method published by Manninen et al. (2016) and Vakkari et al. (2019). The focus correction is also applied to the signal as explained in section 3.5. The

instrumental precision of radial velocities are estimated with the method given by Rye and Hardesty (1997) and Pearson et al. (2009), and attenuated backscatter coefficient β_{att} with uncertainties are also calculated by

$$\sigma_{\beta} = \frac{1}{\sqrt{n_p}} \left(1 + \frac{1}{|SNR|} \right) \quad (\text{VI-9})$$

where n_p is the number of pulses per ray (Manninen et al., 2018).

2. From VAD scans files, the wind vector profiles are obtained with the methods described by Newsom et al. (2017) and Päsche et al. (2015) and explained in previous subsection. The errors due to random instrumental noise and overall errors are also calculated following method by Newsom et al. (2017). DBS scan measurements can also be processed, but they have not been considered in this thesis because of the aforementioned limitations.
3. The vertical velocity statistical momenta, i.e., variance, skewness and kurtosis (Equations II-2, II-3 and II-4) are calculated from vertically pointing measurements at 3, 30, and 60 min resolutions. The statistics which are unbiased by random noise and sample size are calculated as given by Rimoldini (2014) and standard errors are estimated with a bootstrap method described by Kleiner et al. (2014).
4. Wind shear vector is also calculated, as it can also be a source of turbulent mixing. This vector is calculated from the changes in u and v wind components with height (e.g. ICAO, 2005), as:

$$\vec{sh} = \frac{\Delta \vec{U}_H}{\Delta z} = \left(\frac{\Delta u}{\Delta z}, \frac{\Delta v}{\Delta z} \right) \quad (\text{VI-10})$$

and therefore its module is:

$$sh = \frac{\sqrt{\Delta u^2 + \Delta v^2}}{\Delta z} \quad (\text{VI-11})$$

5. The dissipation rate of the Turbulent Kinetik Energy, ε , is calculated from vertically pointing measurements using

the method presented by O'Connor et al. (2010). This quantity is defined as the rate at which the turbulence energy is absorbed by breaking the eddies down into smaller eddies until it is ultimately converted into heat by viscous forces (Garrat, 1992), following Kolmogorov (1941) hypothesis. This quantity is then used as an indicator of turbulent mixing, instead of the combination of vertical skewness and variance (Hogan et al., 2009). The method used also provides an uncertainty estimate for ε (O'Connor et al., 2010).

6. Finally, all the previously calculated quantities are combined following the decision tree in Figure VI-4 to create a bitfield-based classification mask. This method was created by Manninen et al. (2018) following the profile-based Doppler lidar method introduced by Harvey et al. (2013).

A more detailed description of the definitions and calculations for each product can be found in the cited literature. All modules read the input and write the results into netcdf files.

The processing chain has two more utilities, namely *cloud product* and *beta-velocity covariance product*, that have been recently added and then have not been used in this thesis. The first product contains information on cloud base height and velocity and provides an improved cloud mask for the rest of products. The second product contains the calculated covariance between the attenuated backscatter coefficient (β_{att}) and the vertical velocity (w) based on the method described in Engelmann et al. (2008).

The ABL classification mask is based on objectively assigning a dominant source for the turbulent mixing, and is complemented by another mask (from the same generated bitfield) identifying turbulence coupling to the surface and/or clouds.

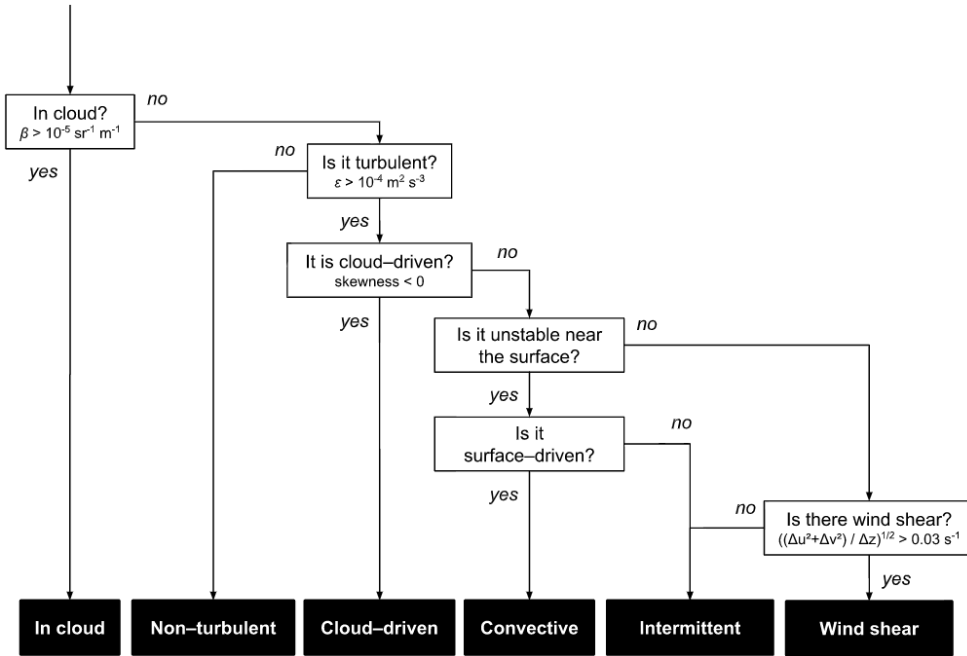


Figure VI-4: Schematic of the atmospheric boundary layer turbulent mixing source decision tree. From Manninen et al. (2018).

Before classifying the profiles according to the decision tree, precipitation cases are identified and excluded from further analysis. The precipitation detection is performed from the vertical velocity data with the criterion that the whole vertical profile (with an averaging window of 9 min and 210 m) presents fall velocities < -1 m/s. The rest of profiles are analyzed firstly in terms of calibrated β_{att} in order to limit the rest of calculations to the height ranges with enough atmospheric signal. A simple cloud detection algorithm is also applied in this step, using the threshold $\beta_{att}(cloud) > 10 \text{ Mm}^{-1}\text{sr}^{-1}$ from the literature (e.g. Harvey et al., 2013; Hogan et al., 2009; Westbrook et al., 2010).

After that, the presence of turbulence is obtained from ε with a threshold $\varepsilon(turbulent) > 10^{-5} \text{ m}^2 \cdot \text{s}^{-3}$ or $\varepsilon(turbulent) > 10^{-4} \text{ m}^2 \cdot \text{s}^{-3}$, depending whether the classified heights are below cloud or they are connected to surface. All remaining range gates where $\varepsilon > 10^{-5} \text{ m}^2 \cdot \text{s}^{-3}$ but there is no cloud- or surface-connection are labelled as *unconnected*. More details on the application of these thresholds can be found in Manninen et al. (2018).

All range gates with surface-connected turbulent behaviour during daytime (sunrise and sunset times are calculated) are classified as dominated by convective mixing, in the absence of ancillary measurements. During nighttime, when ABL is assumed to be neutral or stably stratified (e.g. Garrat, 1992), wind-shear derived turbulence is searched with a threshold $sh > 0.03 \text{ s}^{-1}$ (Manninen, 2019a).

Range gates that are classified as turbulent but are unconnected (to surface or cloud) during daytime, and not related to wind shear during nighttime, are labelled as *intermittent* since turbulence is assumed to arise from other intermittent sources (Lothon et al., 2014).

6.2 STATISTICAL CHARACTERIZATION OF HORIZONTAL WIND FIELD OVER GRANADA

6.2.1 Methodology and data availability

The study in this section was carried out with the horizontal wind speed and direction profiles obtained from VAD measurements. We used the VAD calculation module from Halo lidar toolbox (subsection 6.1.2) to derive the wind product in order to have standard, homogenized retrievals. The measurements were taken in a regular basis consisting of conical scans with 12 measurement positions with same elevation of 75° and equidistant azimuth angles. Subsequent scans were separated by 10 min. With this procedure, we gathered a 2-year database, from 3rd May 2016 to 2nd May 2018.

To investigate the seasonal changes in the diurnal wind cycle, the database was divided into four seasons: winter (December to February, *DJF*), spring (March to May, *MAM*), summer (June to August, *JJA*) and autumn (September to November, *SOM*). For each season, we averaged wind profiles within 1-hour time intervals, but no range averaging (i.e., with the original range resolution of 30 m). The time interval of 1 hour was selected following the averaging time used in most meteorological and air quality models (US-EPA, 2000). With this approach, we

aimed to have a mean diurnal evolution of the horizontal wind speed and direction at different altitudes.

The wind averaging was carefully tackled because of its vector nature, and it is worth to be mentioned here. Depending on the application, the wind measurements may be vector- or scalar-averaged (Atmospheric Research and Technology LLC, 2013; Grange, 2014). For a single wind retrieval from Halo lidar toolbox, both the orthogonal wind components (u, v, w) and the horizontal polar components (wind speed and direction) are provided. In scalar-averaging horizontal wind data, individual wind speeds and directions are separately averaged to obtain what we will call \overline{U}_H and \bar{d} . In vector-averaging, individual u and v components are averaged to obtain \bar{u} and \bar{v} and, then, the *resultant vector* mean wind speed and direction are calculated as:

$$\overline{U}_{RV} = \sqrt{\bar{u}^2 + \bar{v}^2} \quad (\text{VI-12})$$

$$\bar{d}_{RV} = \tan^{-1}\left(\frac{\bar{u}}{\bar{v}}\right) + k \quad (\text{VI-13})$$

where k is a correction to keep d between 0° and 360° , and depends on the sign of \bar{u} and \bar{v} .

Scalar-averaging of wind direction may lead to wrong results, due to the 'circular' nature of this quantity (meaning that both 0° and 360° correspond to northerly wind). If we average two d values close to North (e.g. 359° and 1°), the scalar average results in a wrong southerly wind (with $d=180^\circ$). Therefore, the vector-averaging has always been used here for wind direction calculations at all time resolutions.

On the other hand, mean wind speed may be valid from both averaging types, depending on the selected time interval. Vector-averaging may provide wrong wind speeds when wind direction variance is large. As an illustrative example, if we had a constant wind from N at 5 m/s for 5 min followed by a similar period of constant wind with the same speed from S, the vector-averaged speed would be 0 m/s, whereas the scalar-averaged speed would be 5 m/s, that is the result that best represent the actual wind speed. For short averaging time as

the 1-hour period selected, this effect can be negligible since direction variance can be assumed to be small. However, for an averaging as the one in the present study, where we averaged the same 1-hour period for all days within a season and several years, associated wind directions are likely to compensate, and therefore the scalar-averaging has to be performed.

Scalar-averaging also allows for direct calculation of standard deviation of the averaged data, while this is not straightforward for vector-averaging. Several methods for estimating the standard deviation of the wind direction have been proposed and evaluated (Mardia, 1975; Mori, 1986; Turner, 1986; Yamartino, 1984), but the implied assumptions and approximations were not suitable for the scope of the present study.

Therefore, the wind averages we took and that are presented in this study were scalar-averaged wind speed ($\overline{U_H}$, hereinafter simply referred as U_H) and vector-averaged wind direction (\overline{d}_{RV} , hereinafter referred as d). They must not be interpreted as the polar components of any mean wind vector, but have to be discussed as separated quantities.

An additional criterion was used to ensure statistical representativity of the averages. Wind retrieval was not available for certain range gates where the quality of the retrieval was not enough (in terms of R^2 and condition number), where precipitation or fog was detected or if there were no measurements (because of technical issues). With this in mind, we calculated the fraction of the data from the total analyzed period that were available for each hour of the day and range gate, and we selected the ones with more than 60 % availability to perform the statistical analysis. The results of this calculation are shown in Figure VI-5 for each season. It can be observed that the highest altitudes with this criterion (red lines) are reached during summer and the lowest during winter. This fact was expected (if no technical issues are taken into account), as in Granada the ABL height, and consequently the height with enough SNR, is higher in summer than in

winter (de Arruda Moreira et al., 2018b; Bedoya-Velásquez et al., 2019; Granados-Muñoz et al., 2012).

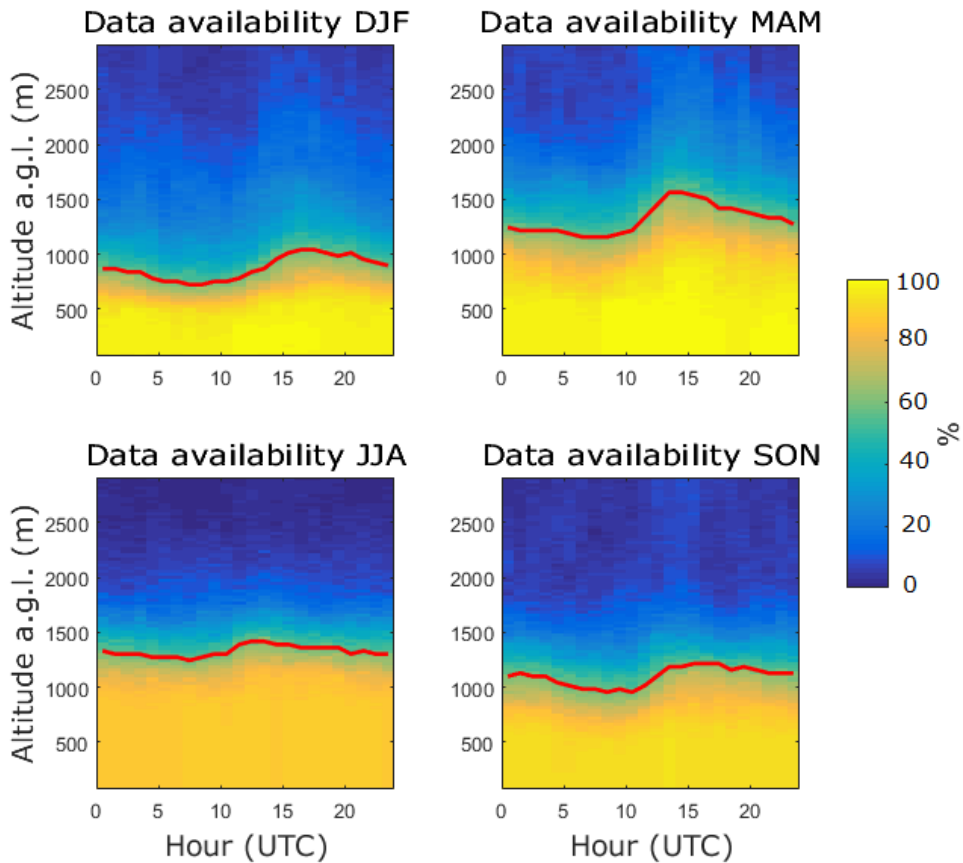


Figure VI-5: Fraction of available data from 3rd May 2016 to 2nd May 2018, divided by hours and range gates. Red lines stand for the heights were data availability drops to 60 %.

The last part of the study was a wind rose analysis of the wind database, without any seasonal division. To this end, and considering the data availability from Figure VI-5, we divided the hourly averaged profiles into three height regions: 100-340 m a.g.l., 340-580 m a.g.l. and 580-820 m a.g.l. We also distinguished between two time intervals: 'Daytime' from 07:30 to 17:00 h UTC and 'Nighttime' from 21:30 to 03:00 h UTC. The reason for using these intervals is that they ensure that we are including only hours when it is daytime or nighttime during the whole year, excluding twilight (defined when the Sun has an elevation angle over -18° , American

Meteorological Society, 2000) and transition times (see Figure VI-6).

With this height and time intervals, a total of six different wind roses were calculated with 22.5° angle intervals and the wind speed intervals: 0-0.5 m/s, 0.5-1 m/s, 1-1.5 m/s, 1.5-2 m/s, 2-5 m/s, 5-10 m/s and ≥ 10 m/s.

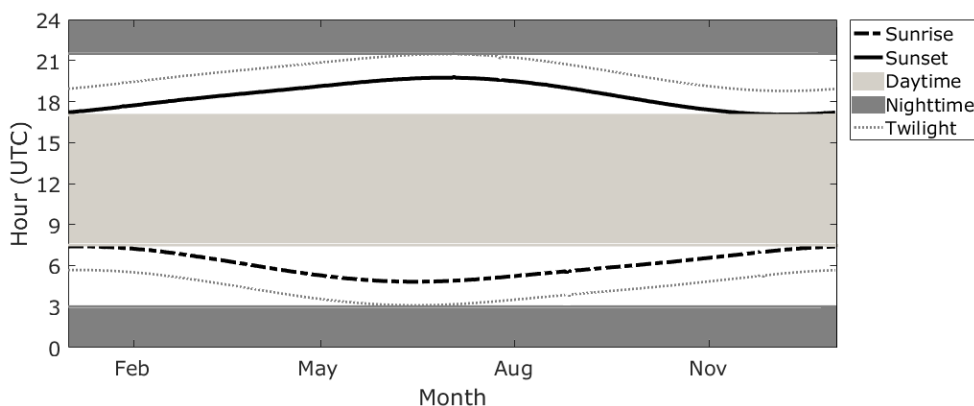


Figure VI-6: Sun graph for Granada, showing sunrise (dashed line), sunset (solid line) and twilight (dotted lines) hours for the whole year. Dark and light grey shaded areas correspond to the hours when it is always night or daytime, respectively.

6.2.2 Results

We applied the seasonal analysis to the whole database from 3rd May 2016 to 2nd May 2018. The results show some seasonal differences mostly during daytime, with calm winter and more windy spring and summer for all altitudes. During nighttime, the winds were low (less than 1 m/s in average) for all seasons.

Figure VI-7(a, d, f, i, k, n, p, s) shows the time evolution of the mean hourly wind speed and direction profiles, from 100 m a.g.l. to the maximum available altitude gate (according to Figure VI-5). We selected two intervals for each season and we called them 'day' and 'night', although in this case the criterion was not based on sunrise or sunset times. It was done by directly identifying strong direction and/or speed gradients in the height-time average plots. The selected intervals are included in Table VI-1 and depicted with orange (night) and blue (day) boxes in Figure VI-7(a, d, f, i, k, n, p, s). We then

calculated the mean profiles (and also the standard deviation for the wind speed, ΔU_H) within such intervals, and the results are shown in Figure VI-7(b, c, e, g, h, j, l, m, o, q, r, t).

Table VI-1: Selected hours for 'Day' and 'Night' time intervals for the averaged profiles at each season.

	DJF	MAM	JJA	SON
'Day' interval (h UTC)	10 - 18	10 - 22	10 - 21	9 - 20
'Night' interval (h UTC)	20 - 9	23 - 7	1 - 8	22 - 7

From wind speed plots Figure VI-7(a, b, c, f, g, h, k, l, m, p, q, r), we can observe that average U_H increases with height during nighttime for all seasons (from 2-3 m/s up to 5-6 m/s in winter, summer and autumn and up to 9 m/s in spring). Meanwhile, diurnal average U_H starts from 3-4 m/s at the lowest analyzed heights, then presents a slight increase around 200 m a.g.l. (especially in spring and summer) and remains constant before a final increase at high altitudes, reaching 6 m/s in winter, summer and autumn and 10 m/s in spring. Wind speeds at the highest analyzed altitudes do not present diurnal differences for any season. The altitudes where this constant pattern was reached were around 440 m a.g.l., 940 m a.g.l., 1230 m a.g.l. and 1080 m a.g.l. for winter, spring, summer and autumn, respectively.

Standard deviations also increase with height, from around 1.5 m/s up to 5 m/s in all seasons with the exception of spring, when ΔU_H reaches 7 m/s. This means that, during the analyzed period, wind speeds presented more diverse values at higher altitudes, specially in spring. However, no significant differences were observed between diurnal and nocturnal standard deviations.

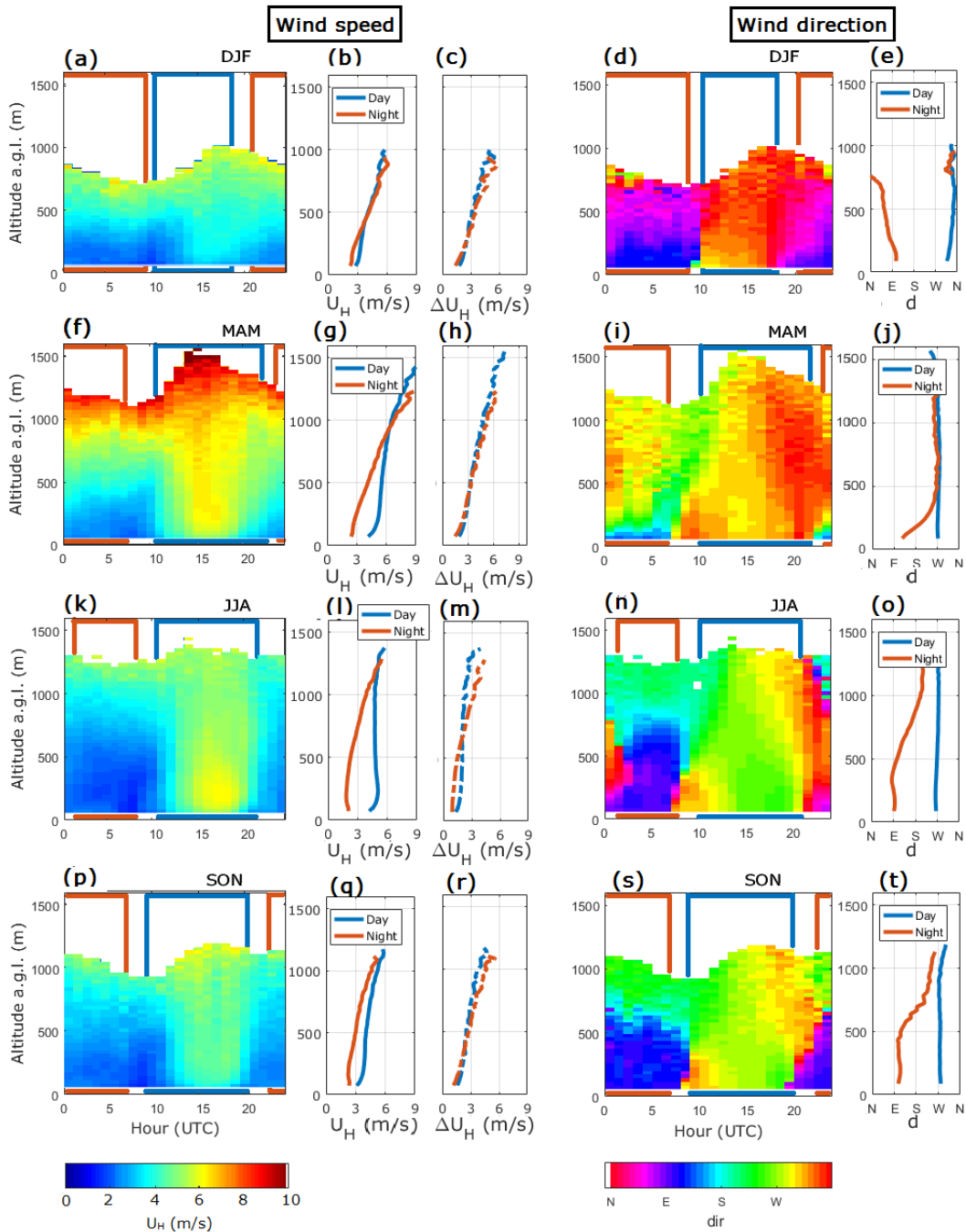


Figure VI-7: (a, d, f, i, k, n, p, s) Hourly averages of horizontal wind speed and direction vertical profiles for all seasons. (b, g, l, q) Diurnal and nocturnal averaged wind speed profiles and (c, h, m, r) their standard deviations. (e, j, o, t) Diurnal and nocturnal averaged wind direction profiles.

Direction plots (Figure VI-7d, e, i, j, n, o, s, t) also show marked diurnal and seasonal differences, as well as contrast between the first 800 m and altitudes above. In winter, the mean diurnal wind came from NW close to the surface and from N at higher altitudes, while the mean nocturnal wind came from SE close to surface and from E at higher altitudes. In spring, most of the time we had winds coming from W and NW, with the exception of the nocturnal wind close to the surface, that came from S. Summer and autumn presented similar direction patterns, with mean diurnal winds coming from W and SW, and nocturnal winds coming from E below 500 m a.g.l. and from SW above this altitude.

As second part of the study, Figure VI-8 includes all the wind roses from 1-h averaged wind data at three different height ranges and two common time intervals ('Daytime', 07:30-17:00 h UTC and 'Nighttime', 21:30-03:00 h UTC), using the two-year database. In the lowest height interval (Figure VI-8e, f), there is a clear prevalence of NW diurnal winds with speeds mostly >2 m/s and a strong change to ESE (East-Southeast) and weaker nocturnal winds. Figure VI-9 shows those wind directions in the context of the local orography. This pattern is consistent with the katabatic winds that we would expect at that height range due to slope effects, although a deeper analysis would be needed to detect such winds.

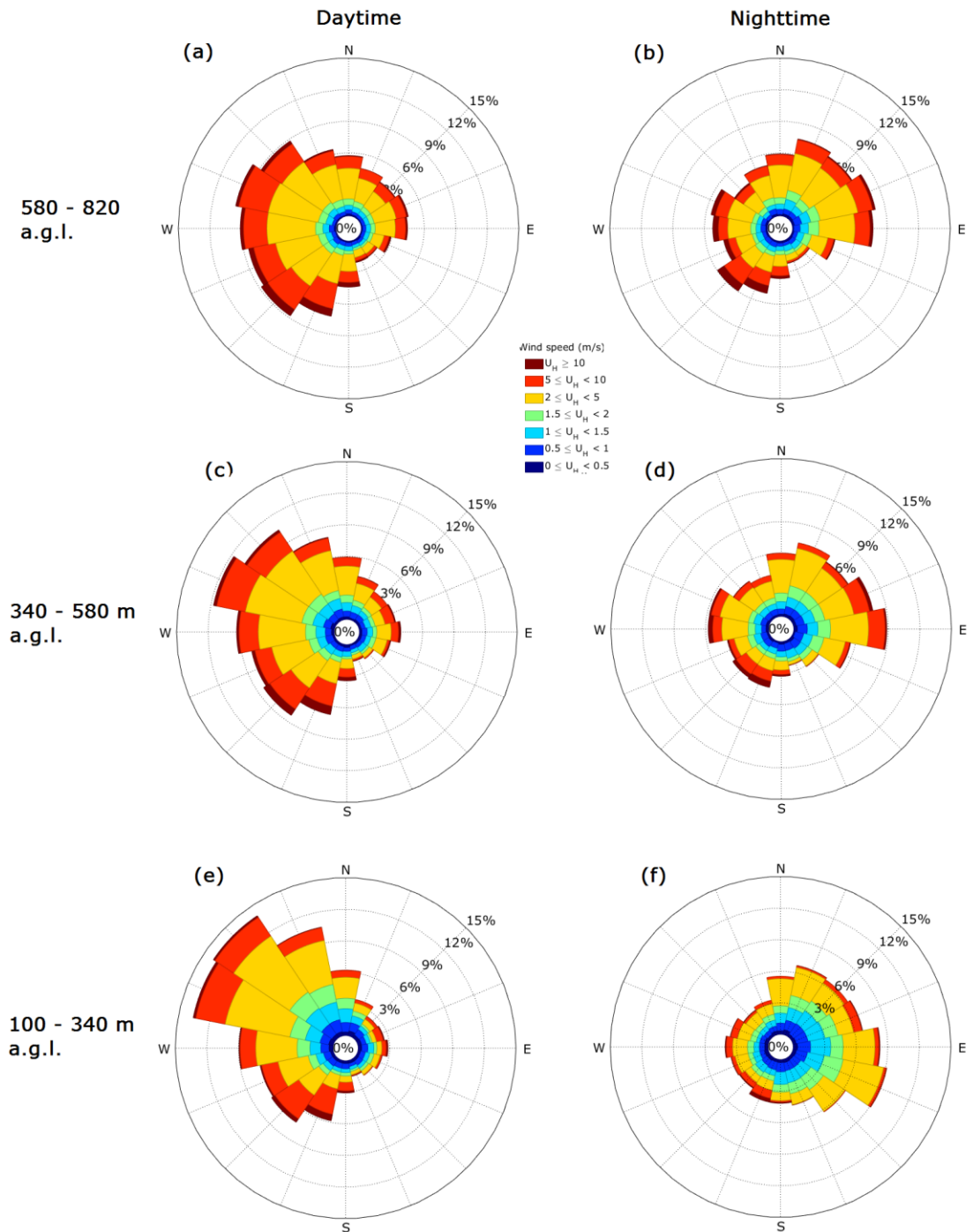


Figure VI-8: Wind roses showing the prevailing wind speeds and directions in Granada in three different height ranges, distinguishing between daytime (a, c, e) and nighttime (b, d, f).

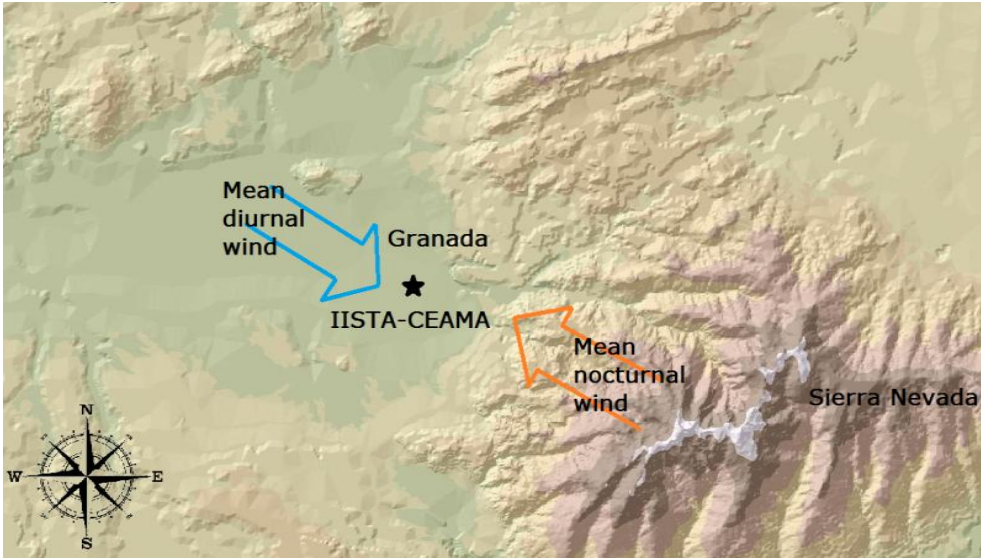


Figure VI-9: Representation of the prevailing wind directions for diurnal and nocturnal periods and the lowest height range (100-340 m a.g.l.) in the context of the measurements location. Image adapted from Granada Geophysical Information System website (siggra.dipgra.es/siggra/maps/view/1).

This pattern is not exactly preserved at higher altitudes (Figure VI-8a-d), although there are similarities. The diurnal wind is also dominated by NW direction, although the frequency distributions spread and there is higher contribution of W and SW winds. The peak of the nocturnal winds moves towards E at higher altitudes and a slight SW contribution also appears in the highest interval.

Coming back to the site description from a climatological point of view done in chapter III, a similar day / nighttime pattern is observed, although it is turned slightly to N-S direction instead of NW-SE (Figure III-2). Taking into account that those data correspond to surface measurements, this pattern is consistent with the prevailing nocturnal wind direction shifting towards E with height (Figure VI-8b, d, f). However, this could also be due to the relative position of the measurement station used for that climatology with respect to the mountain and the city (Armillá airbase station, see Figure III-1).

Finally, as a common feature for all heights and interval times, strong winds (more than 10 m/s, represented with brown color) are not frequent but they come mostly from SW when present. This is parallel to Sierra Nevada mountain, meaning that the wind coming from this direction is more likely to have higher speeds without orographic limitation.

6.3 CHARACTERIZATION OF THE ABL TURBULENT SOURCES OVER THREE SITES

The characterization of the ABL under different conditions is important for weather and climate models, but also for wind energy applications or air quality studies. As we reviewed in section 2.1, the definition of this layer is still ambiguous although there have been recent efforts to harmonise and standardise the criteria (e.g. Bravo-Aranda et al., 2019). One of the most important features that make ABL description complex is the turbulent mixing, responsible for the redistribution of momentum, mass, temperature and humidity within this layer (Oke, 1992). The sources of turbulent mixing exhibit significant temporal and spatial variations, and include buoyancy (that produces upwards convective mixing), wind shear (mechanical mixing) or radiative cooling in stratocumulus clouds (producing top-down convective mixing).

For those reasons, the turbulent mixing source identification and classification method described in section 6.1.2 represents a powerful tool to study and deeply analyze certain ABL scenarios, or to create long-term databases of vertically resolved ABL classification. Manninen et al. (2018) showed the performance of the ABL classification product on a daily basis when applied to two particular stations, namely Jülich (Germany) and Hyytiälä (Finland). They presented an example of a clear-sky day in Jülich, where the convective ABL could be properly developed, and a cloud-topped example in Hyytiälä, where the clouds avoided any possible convection. A statistical study was also performed for those stations, finding clear

differences in the main sources and their seasonal and diurnal cycles due to the different locations.

In this sense, the aim of the present section is to use the same standard and objective classification methodology to characterize very different locations and situations. In particular, we present two particular study cases applied to an olive orchard environment in southern Spain, and a statistical analysis to characterize the urban ABL of Granada over all seasons, and the rural ABL in a peatland environment in Poland during summer.

6.3.1 Methodology

For the analysis of single cases, we chose some of the products obtained with the Halo toolbox, namely TKE dissipation rate (ε), wind shear (sh), vertical velocity skewness (S_w) and the ABL classification product. They have been selected because they provide information on turbulence presence (high ε values), direction of the turbulent movements (positive or negative S_w), mechanical turbulent sources (sh) and the final classification mask applied (see section 6.1.2).

For the statistical analysis, the database was split into seasons as in section 6.2. Then, for each time of the day (with 3 min resolution, as it was the maximum available by the software), the frequency of occurrence of each source of mixing from the BL-classification product was calculated for each season and range gate. This kind of analysis allows for characterizing the diurnal cycle of the ABL in terms of prevailing mixing sources.

6.3.2 Additional experimental sites: AMAPOLA and POLIMOS campaigns

The study presented in this subsection includes a the 2-year database from UGR station, but also some measurements taken in two additional experimental sites with different features. Those measurements were taken during the following field campaigns:

- AMAPOLA (Atmospheric Monitoring of Aerosol Particle Fluxes in Olive Orchard) was carried out from 18th to 29th

May 2016, with the main focus of testing the combination of in-situ and remote sensing observations of aerosol particle fluxes. It was coordinated by GFAT group and funded in the framework of ACTRIS-2 project. The Halo Doppler lidar was one of the instruments installed in an already existing ICOS (Integrated Carbon Observation System) experimental site located in an irrigated olive orchard in Úbeda (Spain, 37.90° N, 3.31° W, 370 m a.s.l.). The site presents Mediterranean climate, with mean annual temperature of 16°C and mean annual precipitation of 495 mm. Predominant surface winds come from NW during day and from S and SE at night (Chamizo et al., 2017). This kind of crop is one of the most important in the Mediterranean basin, particularly in southern Spain. Therefore, its study and characterization is important in order to account for its impact on the global soil carbon cycle linked to anthropogenic climate change.

- POLIMOS-2018 (Polish Radar and Lidar Mobile Observation System 2018) was performed from March to November 2018 with the goal of assessing the impact of atmospheric optical properties on terrestrial ecosystem functioning (Harenda et al., 2018). It was coordinated by the Institute of Geophysics of the University of Warsaw (Poland) and funded by the European Space Agency. The measurements were carried out at the PolWET site in Rzecin village (52.75° N, 16.30° E, 54 m a.s.l.), where the Doppler lidar was installed from 24th May to 24th September 2018. The ecosystem is a peatland with average air temperature of 8.5°C, annual precipitation of 526 mm and prevailing western surface wind (Chojnicki et al., 2007). Peatlands are a special type of wetland that represents one of the largest natural terrestrial carbon store and have a strong interaction with the climate system (Lappalainen, 1996).

6.3.3 Results

Case studies

In this subsection, we first show two examples of the complete diurnal ABL analysis that can be carried out thanks to the selected variables. The focus of the studied cases is on differences between clear sky and cloud-topped ABL, and therefore we will not repeat the analysis for the different sites. We chose two cases from AMAPOLA campaign, because they presented the same conditions (they were close in time, and the aerosol load, temperatures, etc. were similar) except for the cloud cover.

Figure VI-10 shows temporal evolution of ε , S_w , sh and ABL classification obtained from the Halo toolbox processing chain for 28th April 2016, as an example when the ABL was not topped by clouds. Sunrise was at 05:26 h UTC that day, and sunset was at 18:56 h UTC.

The temporal evolution of ε (Figure VI-10a) indicates that turbulence started in the very low layers around sunrise and created a turbulent layer that grew until reaching about 2000 m a.g.l. at noon. This morning turbulent growing layer also agrees with positive skewness (Figure VI-10c) and the BL-classification mask labelled those range gates as having 'convective mixing' as turbulence source (Figure VI-10d). Data above 1200 m were quite noisy, indicating that there was not enough signal to obtain reliable measurement. Therefore, it seems that the turbulent ABL could have grown above the maximum altitude reached by the Doppler lidar, and the constant behaviour shown by this layer from 12 h UTC to around 18 h UTC may not reproduce the actual ABL height. Wind shear vector (Figure VI-10b) displayed strong variations from 0 up to 0.06 s^{-1} inside this convective growing layer, but the algorithm always assumes that convective mixing dominates when present.

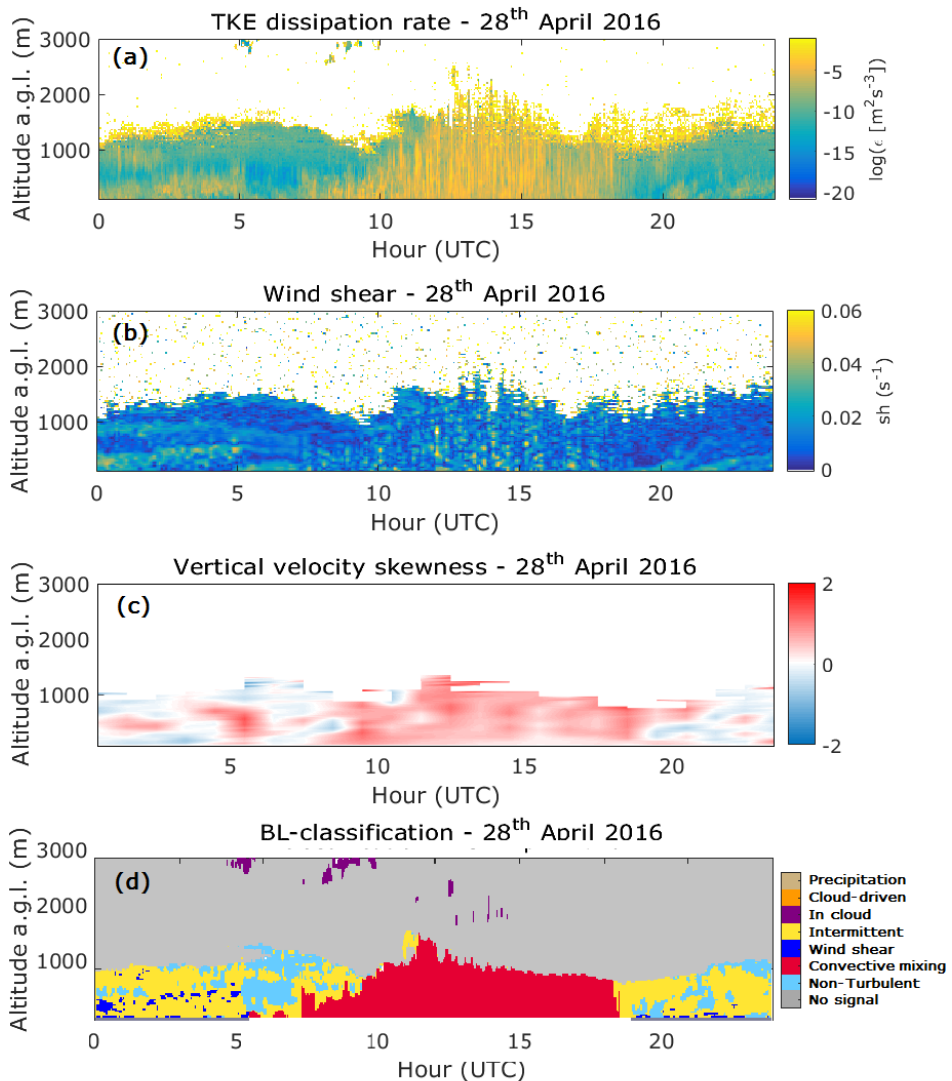


Figure VI-10: Time evolution of the vertical profiles of (a) TKE dissipation rate, (b) wind shear, (c) vertical velocity skewness and (d) BL classification, calculated from Doppler lidar measurements on 28th April 2018 during AMAPOLA campaign.

In the hours before sunrise and after sunset, ϵ seemed more stratified, with still high values close to the surface and in an elevated layer around 1000 m a.g.l. From midnight until sunrise, two layers (approximately coinciding with high ϵ layers at the surface and around 1000 m a.g.l.) appeared with wind shear values more than $0.02 s^{-1}$. They coincided with negative skewness values (blue areas before 5 h UTC in Figure VI-10c),

with a layer of positive skewness in between. The BL-classification mask labelled those range gates as turbulent, with source in wind shear (for the corresponding altitudes) or intermittent sources.

The second analyzed case corresponds to 23rd April 2016, also during AMAPOLA campaign. In this case, some low clouds were present, interacting with the ABL turbulence evolution. Figure VI-11 shows the same products as Figure VI-10 for this case. The 'in-cloud' label in ABL-classification mask plot (Figure VI-11d) revealed the cloud presence during almost the whole day. Some precipitation was also detected at some hours (golden vertical lines before 5 h UTC and at some short periods between 11:00 h and 17:30 h UTC).

The first effect of the clouds seemed to be the delay on the convective mixing. Although sunrise was at 05:19 h UTC for this case, the first detected convective range gate was around 07:30 h UTC. From that time, the layer started developing with positive skewness (Figure VI-11c) and high ε (Figure VI-11a). Moreover, the growth of this convective layer was stopped when its altitude reached the clouds at 1500 m a.g.l., with a layer immediately below the clouds with negative skewness that could break down the convective pattern. This process is depicted in Figure VI-11d with orange colour and label 'cloud-driven' turbulence.

Another important feature to point out is the stratified structure that wind shear presented before convection begins. However, the formed layers did not present wind shear values over the threshold of 0.03 s^{-1} , and therefore were not taken into account as turbulence source.

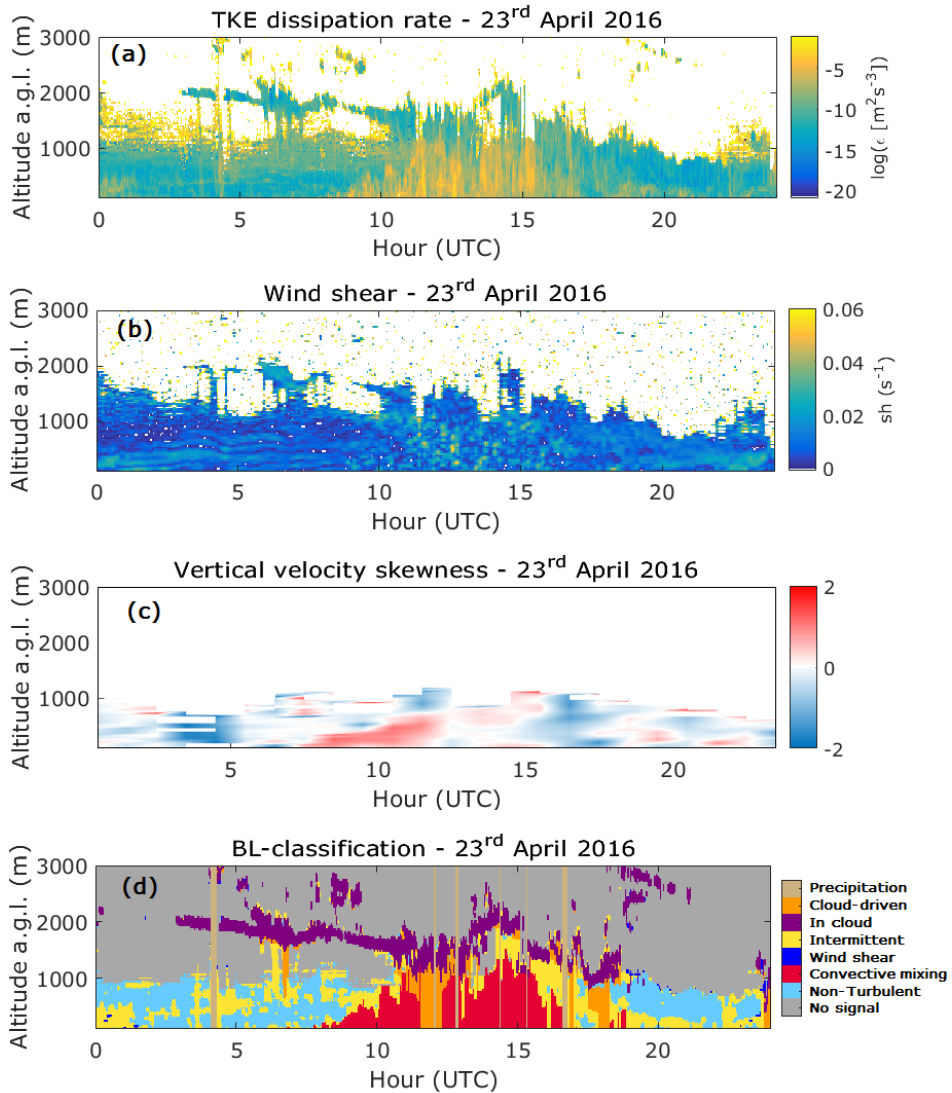


Figure VI-11: Same as Figure VI-10, Doppler lidar measurements on 23rd April 2018 during AMAPOLA campaign.

Statistical analysis from Granada and POLIMOS campaign

In this part, we first used the data gathered at Granada station from 3rd May 2016 to 2nd May 2018, covering two complete years. Figure VI-12 displays the relative occurrence frequency of three of the turbulent source types, namely 'convective mixing' (Figure VI-12a, d, g, j), 'intermittent' (Figure VI-12b, e, h, k) and 'wind shear' (Figure VI-12c, f, i, l), with respect to

time of the day and altitude. The rest of the categories ('precipitation', 'cloud-driven', 'in-cloud' and 'non-turbulent') presented frequencies that did not follow any clear pattern for the analyzed data. Subplots from the different rows correspond to the distinguished seasons.

The convective mixing frequency plots show a clear diurnal evolution of the range gates with the most frequency (red coloured). This mechanism usually starts with sunrise in the lowest heights and is more frequent at growing altitudes up to a maximum. In spring (d) and summer (g), this maximum height seems to remain constant from around 12 h to 17 h UTC, but the effect mentioned in the clear-sky example from previous section has to be noticed. It is likely that the system did not receive signal with enough SNR above a certain altitude (that can go down to 1000 or 1500 m a.g.l.) to perform the complete analysis for the ABL classification and, therefore, the convective ABL growth could not be detected above that altitude. This effect does not occur in autumn (j) and winter (a), when the maximum height of the convective ABL is frequently registered around 16 h and 15 h, respectively.

Wind shear plots only present frequency values during the nighttime, since convective mixing is assumed to dominate the surface-driven turbulence when it is present (although there may be also wind shear). The season with highest frequency of wind shear-driven turbulence is autumn, when this mechanism is responsible for more than 20 % of the detected turbulence below 500 m a.g.l. around 20 h UTC. This result is in agreement with the high mean wind speeds calculated in the previous subsection for the same data (Figure VI-7p), that are likely related to low level jets (strong winds concentrated within a narrow stream typically in the lower 2-3 km of the troposphere, American Meteorological Society, 2000). For spring and summer, wind-shear is responsible for around 10 % of the detected turbulence in the same time interval (around 20 h UTC) at low altitudes, and around 500 m a.g.l. after 00 h UTC. In winter, that period before early morning is the one with highest wind shear frequency.

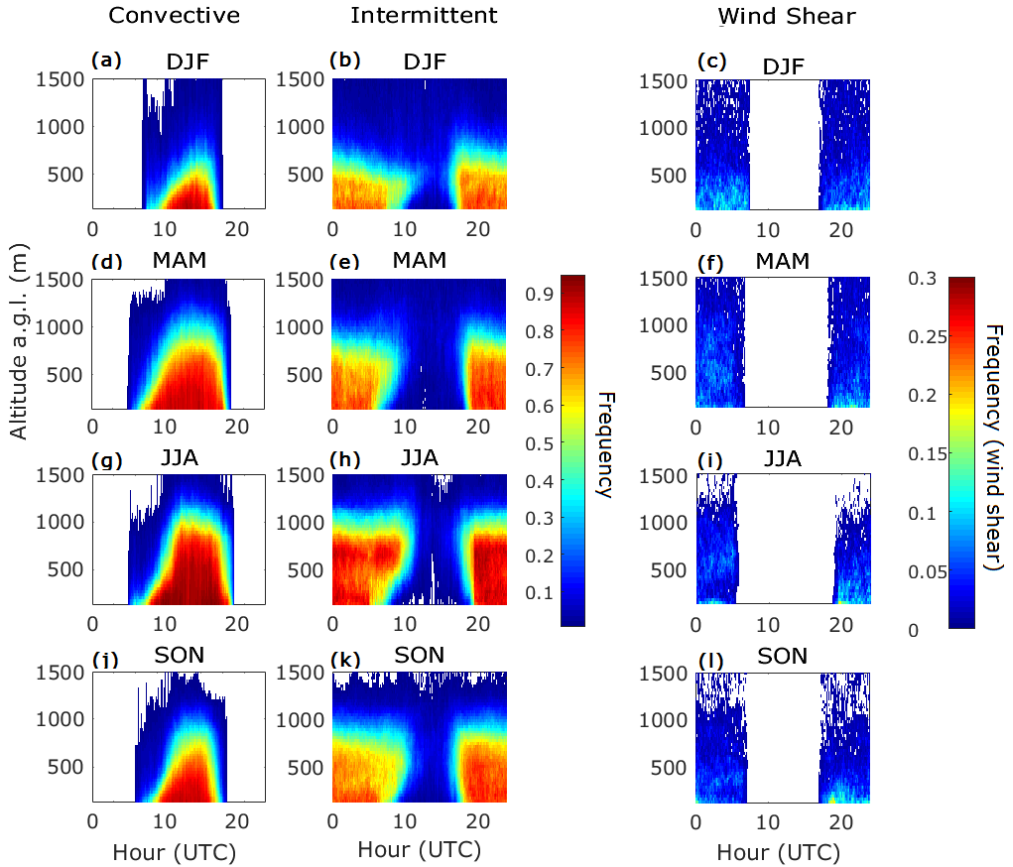


Figure VI-12: Frequency of occurrence of the three main labelled turbulence sources for each time and range gates, and for each season at Granada station from 3rd May 2016 to 2nd May 2018. Wind shear plots (c, f, i, l) have a different colour scale.

The ‘intermittent’ category, given to range gates with turbulence that is not related to the rest of sources, has been also represented in Figure VI-12 because of its high frequencies (particularly when there is no convection). Since this category can not be properly investigated with the methodology used here, we are not able to discuss the reason of this in depth. However, we found important to highlight its presence and the need for further research. A possible reason of the high frequencies might be the need for finding a different wind shear threshold for this location (Manninen, 2019a), but there also must be another source that is not properly detected with this method.

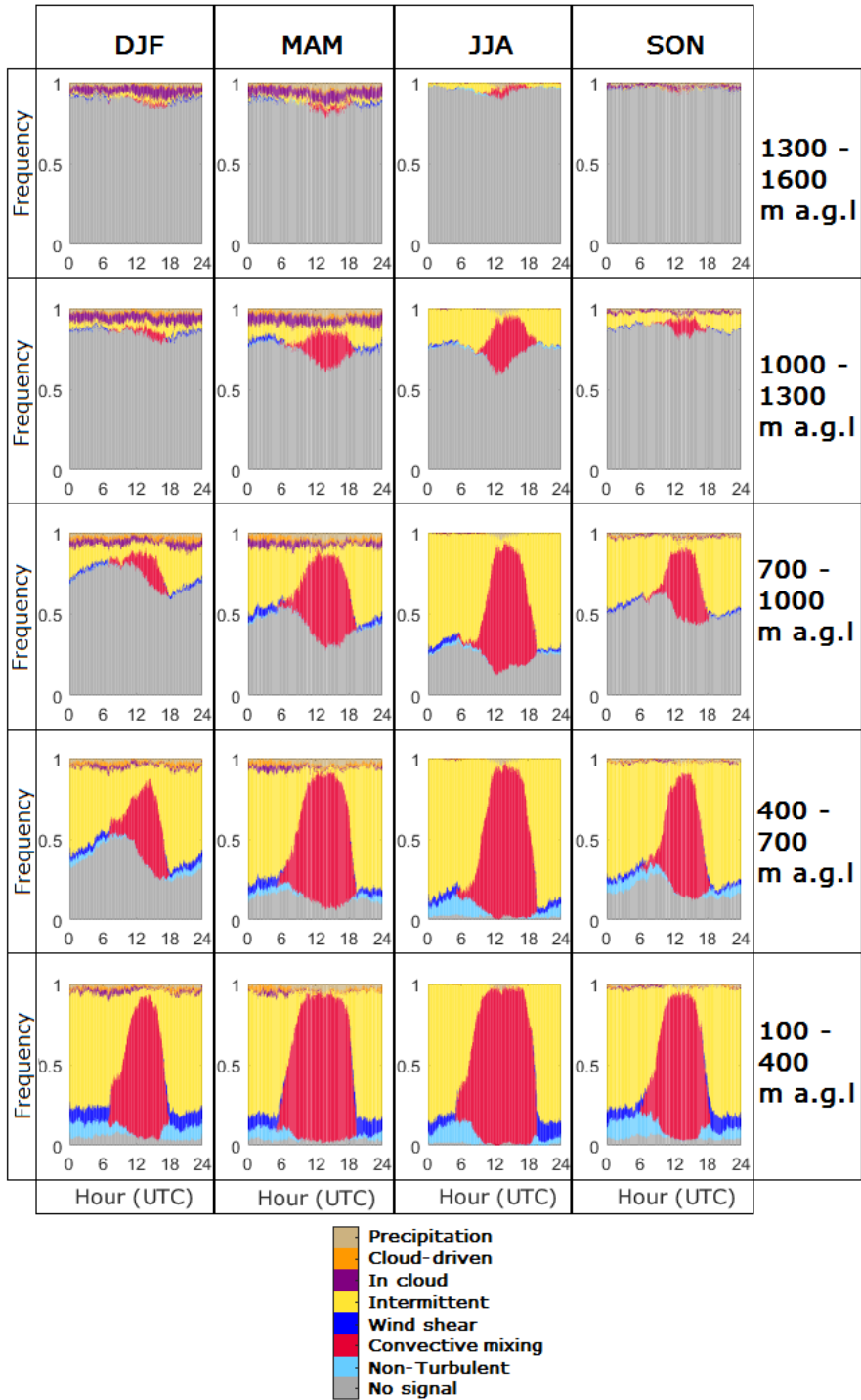


Figure VI-13: Diurnal cycle of the observed frequency of occurrence of each labelled turbulent source, for each season and calculated for five different height ranges at Granada station from 3rd May 2016 to 2nd May 2018.

In Figure VI-13 we investigate the diurnal and seasonal behaviour of the assigned mixing sources, but taking into account all the possible given labels. For this analysis, we have taken five different range intervals and calculated the accumulated frequency of each source type with 3-min time resolution. The amount of missing data at different heights presents diurnal dependence directly related to ABL height, as expected since SNR is usually much higher inside the ABL.

This figure clearly shows the strong diurnal variation in convective mixing and also its seasonal dependence, typical features for ABL in the mid-latitudes (e.g. de Arruda Moreira et al., 2018b; Baars et al., 2008). The frequency of this turbulent mechanism is almost 100 % in the central hours for altitudes up to 700 m a.g.l. in summer, and a bit lower (but still high) in spring. This feature was not showed for the analysis shown by Manninen et al. (2018) for Germany and Finland, where the surface-connected convective mixing was dominant during the central hours, but there was no negligible contribution of non-turbulent and cloud-driven turbulence cases.

Clouds frequency is very low for almost all subplots in Figure VI-13, and almost absent in summer. However, it has to be noticed that the full cloud cover is not necessarily captured with this analysis, since there might be ABL-associated clouds above the maximum selected range of 1600 m a.g.l. In-cloud and cloud-driven cases are more frequent during winter and spring for altitudes above 1000 m a.g.l., with constant frequencies of 5-10 %.

Wind shear is detected for all seasons during nighttime at low altitudes, as we could already observe in Figure VI-12. Nevertheless, turbulence classified as intermittent is the most frequently detected during nighttime. This feature was opposite for the high latitude scenario analyzed by Manninen et al. (2018), where the contribution of intermittent sources was mainly during central hours in spring and summer. In contrast, for the mid-latitude site (Germany) analyzed in that study, the results were similar to our analysis for Granada, although the

frequency of intermittent sources was much less, in favour of non-turbulent cases.

A similar study was performed for the data gathered during POLIMOS campaign, from 24th May to 24th September 2018 in Rzecin peatland. Figure VI-14 and Figure VI-15 show the same analysis as Figure VI-12 and Figure VI-13. For this case, we have not split the data into seasons, since the database corresponded only to 4 months in summer and beginning of autumn. In addition, Figure VI-15 was calculated over slightly different altitude ranges with respect to the study for Granada (Figure VI-13). The ranges were selected so that the ABL development could be properly analyzed and compared despite the differences in their average daily maximum ABL height.

The probability of convective mixing with height (Figure VI-14a) presents a diurnal cycle quite similar to the one observed for Granada in spring (Figure VI-12d). This cycle is also observed in Figure VI-15 for all altitude ranges, with frequency decreasing with height.

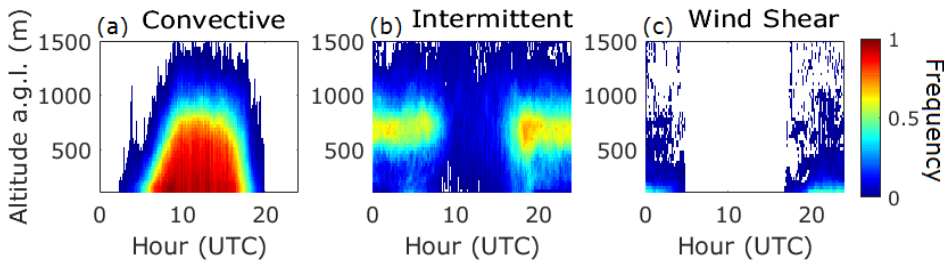


Figure VI-14: Frequency of occurrence of the three main labelled turbulence sources for each time and range gates at Rzecin station from 24th May to 24th September 2018.

We can observe that, for this peatland environment, wind shear is mainly concentrated in the first hundreds of meters, with higher frequencies (more than 40 %) than in Granada (note the different colour scale for Figure VI-12c, f, i, l and Figure VI-14c). This source identification seems to reduce the amount of nocturnal cases labelled as intermittent for those low heights (see Figure VI-14b), although this is also because less turbulence is detected (see 'Non-turbulent' bars in Figure VI-15e). In this case, the most frequency of intermittent

sources is detected between around 600 m and 900 m a.g.l. (Figure VI-14b and Figure VI-15c).

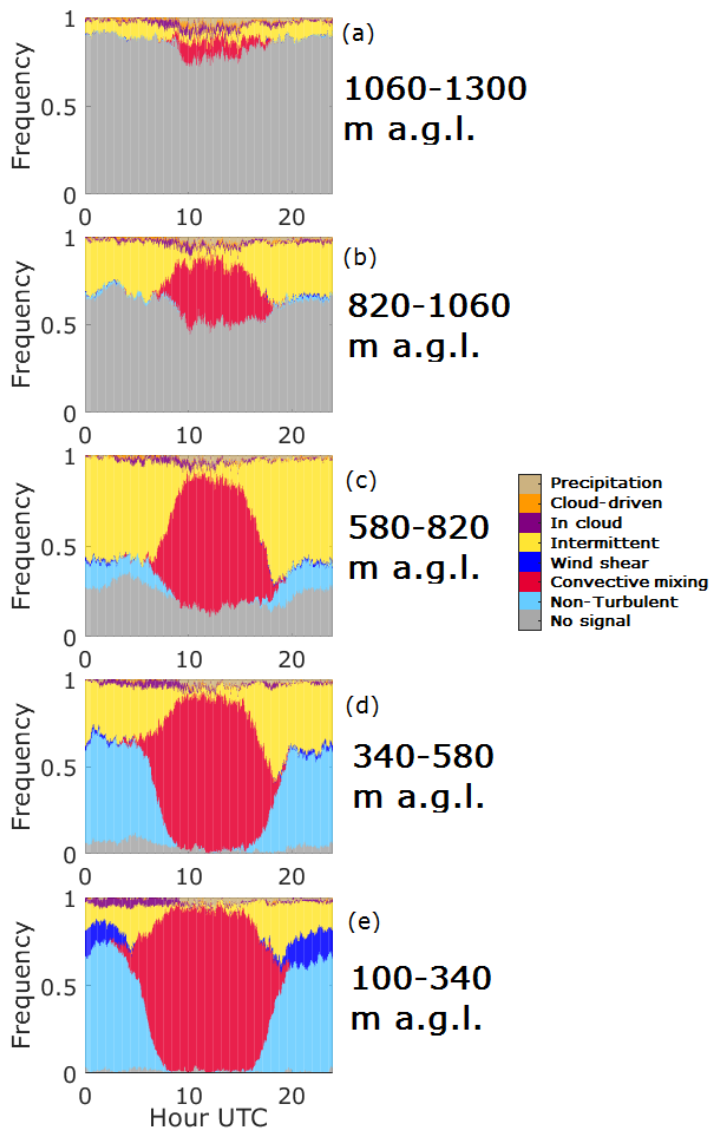


Figure VI-15: Diurnal cycle of the observed frequency of occurrence of each labelled turbulent source, calculated for five different height ranges at Rzecin station from 24th May to 24th September 2018.

6.4 CONCLUSIONS AND FUTURE WORK

In this chapter, we applied Doppler lidar technique to characterize wind field and ABL turbulent properties with high temporal and vertical resolution. The analyzed ABL properties were obtained thanks to Halo lidar toolbox, a software package developed at FMI (Helsinki, Finland) that allows for continuous, automatic and standardized retrievals. With this methodology, we were able to gather a 2-year database of wind field and turbulence measurements for Granada, and also participate in two field campaigns in different environments.

The statistical analysis of the horizontal wind over Granada included in subsection 6.2 allowed for obtaining diurnal and seasonal patterns of the mean profiles from 100 to around 1000 m a.g.l. From this study, we can conclude that the general trend is to have diurnal wind from NW and with highest velocities in spring and summer, and weak nocturnal winds from SE.

This clear pattern in wind direction is consistent with the expected katabatic wind at the analyzed altitudes due to the interaction between the city of Granada and the close mountain range of Sierra Nevada. However, to have a more complete description of this particular effect and separate it from other patterns, a deeper analysis should be done. A *Principal Component Analysis* would fit this kind of study, since we could isolate this katabatic pattern and correlate it with other mechanisms, and we could also detect other typical situations that contribute to the average behaviour described here.

The analysis of the turbulent sources was first performed using single cases measured during AMAPOLA campaign. The clear-sky case showed a typical situation where ABL is fully developed during daytime due to convection, with high turbulent activity (in terms of ε) and strong positive skewness indicating frequent and powerful updrafts. The cloud-topped case showed the strong influence that clouds can have on ABL development, avoiding it to reach the same maximum height

and introducing top-down movements as important contribution to mixing.

For Granada database and POLIMOS campaign, the turbulent sources were analyzed statistically. For Granada, we could characterize the seasonal and diurnal behaviour of the convective mixing, and also detect the seasons, altitudes and times when wind shear becomes an important turbulence source. For Rzecin site during POLIMOS campaign, the turbulent sources analysis reveals a similar behaviour of the convective mixing mechanism, but the wind shear was located at lower altitudes. An important feature we came across was the high frequency found in Granada of intermittent turbulence, that can not be further analyzed with this methodology. In Rzecin, this kind of turbulence was mainly detected in a certain altitude range and in a less amount.

We can also draw some conclusions from the combined analysis of sections 6.2 and 6.3. In particular, we can observe that in Granada, the nocturnal wind profiles are more stratified in terms of wind direction, while the diurnal profiles are more homogeneous in coincidence with the hours of maximum convective mixing frequency. Moreover, regions where wind shear is frequently detected coincide with high average winds with direction gradients.

This chapter lets some open issues, that motivates us to do further research to exploit the potential of the measured Doppler lidar data. The combination with other instrument or techniques may be useful for investigating the sources of the detected nocturnal turbulence, in particular in Granada urban environment. To this end, a clear improvement would be to integrate a low level jet detection algorithm (e.g. Tuononen et al., 2017) in order to discriminate it from other sources. Moreover, wind shear threshold sensitivity tests (Manninen, 2019a) should be carried out for these sites, in order to better interpret wind shear-affected regions.

Finally, we believe that there is a clear application of this kind of information in air quality and pollutant dispersion studies.

The poor air quality events are closely related to the capability of the ABL to mix and disperse the emitted pollutants, a complex issue that Doppler lidar measurements can clearly help to understand.

PART IV

CONCLUSIONS

VII CONCLUSIONS AND OUTLOOK

This thesis addresses the vertical profiling of different atmospheric properties using lidar technique, a general objective that has been successfully fulfilled. The main lidar systems used were a multiwavelength Raman lidar with depolarization capabilities (MULHACEN) and a Doppler lidar. The measurements performed with MULHACEN were used to retrieve aerosol optical profiles with Raman algorithm, and microphysical profiles with two regularization algorithms, UP (based on Mie model for spherical particles) and SphInX (based on T-matrix model for spheroids) developed in the University of Potsdam (Germany). The measurements from Doppler lidar were the input for a chain of several algorithms, the Halo lidar toolbox developed in the Finnish Meteorological Institute (Helsinki, Finland), to calculate 3D wind field and turbulent properties within the ABL.

Thanks to this approach with multiple applied algorithms, we were able to understand and implement these techniques to describe events and situations of different nature from several points of view. We have improved the capability of GFAT group to retrieve a number of atmospheric quantities with high spatial and temporal resolution. With those properties, we have

been able to characterize and analyze several complex situations, and we can also apply the algorithms systematically in order to have long and robust databases for further studies.

The conclusions of each study developed in this thesis have been presented throughout the different chapters. However, the aim of this chapter is to highlight the main aspects of each work and link them to the objectives we proposed in chapter I.

The first group of results was linked with the improvement of measuring and processing techniques. We implemented a new setup in MULHACEN in order to measure rotational Raman signal at UV branch, with the advantages of the enhanced SNR and the negligible wavelength shift between elastic and Raman returns. The improved measurements have been shown to have enough quality to retrieve particle backscatter and extinction coefficient profiles both during day and nighttime, with a significant temporal resolution improvement and with only additional uncertainties of less than 2 % and 4 % for α^a and β^a , respectively.

As part of the instrumental improvements, we applied several post-processing algorithms to the Doppler lidar measured signal. We corrected the background signal artifacts due to the instrumental response and to the measurement protocol itself, allowing the detection of weaker signals with a lower SNR threshold. We then applied a calibration of the Doppler lidar signal in terms of focus height and lens diameter of the optical system. We calibrated with a systematic procedure based on comparing the corrected signals with a co-located ceilometer, being able to calculate attenuated backscatter.

The second group of results is related to the study of aerosol transport processes and the characterization of aerosol optical and microphysical properties with spherical model. The most remarkable work done in the sense was the analysis of strong events of long-range transported biomass burning aerosol, that were detected during July 2013 at three EARLINET stations. Satellite observations from MODIS and CALIOP instruments, as well as modelling tools such as HYSPLIT and NAAPS, were used

to estimate the sources and transport paths of those North American forest fire smoke particles. The multiwavelength Raman lidar technique was applied to obtain vertically resolved particle optical properties, and further inversion of those properties with UP software allowed for retrieving microphysical information on the studied particles.

The results highlighted the presence of elevated smoke layers of 1–2 km thickness, accounting for more than 30 % of the total *AOD* in all cases. The retrieved optical and microphysical features were typical for different aging degrees: color ratio of lidar ratios around 2, AE_α less than 1, r_{eff} of 0.3 μm and large values of *SSA*, nearly spectrally independent. The intensive microphysical properties were compared with columnar retrievals from co-located AERONET stations, and the intensity of the layers was also characterized in terms of particle volume concentration, establishing an experimental relationship between this magnitude and the particle extinction coefficient.

A second study that we presented in the framework of microphysical inversions with spherical model was the use of star- and lunar-photometry for Raman lidar microphysical retrievals. We proposed a methodology for using UP regularization software for cases or stations where one of the required '3+2' lidar channels is not available. A sensitivity study of this methodology was carried out for three different scenarios, two initial particle size distributions and four *CRI*. The results showed that most simulated cases presented errors less than 10 % with respect to retrievals with complete setup.

We also validated the methodology with measurement cases, finding deviations up to 40 %. However, those higher deviations were due to the fact that variations in the input were between 3 and 40 % for the measurement cases, as opposed to the constant 5 % error introduced in the simulation inputs. For both simulated and measured cases, it was noticeable that the best retrieved particle properties were the real part of *CRI* and the *SSA*. The latter is of special relevance since it is directly related to particle absorption, one of the

aerosol properties that still present large uncertainties in global models and a key target of important research projects and infrastructures as ACTRIS. Therefore, the proposed methodology will help to significantly increase the global databases of particle absorption properties (in addition to the rest of particle properties), since stations equipped with nocturnal photometers will be able to apply it although their Raman lidars do not fulfill the '3+2' requirements.

As part of the aerosol optical and microphysical characterization and transport studies, we also investigated the use of the SphInX software for non-spherical particles by adding depolarization measurements to the '3+2' input. Since this software is more recent than UP, our work was focused on carefully analyze and compare the retrievals in order to optimize the quality of the results. We selected a case with biomass burning particles that could also be analyzed with UP software in order to highlight the added value of SphInX software. We found that this model improves the size retrieval in terms particle volume concentration and effective radius, in addition to provide new shape information with the 'size-shape distribution' and the effective aspect ratio.

We also selected a mineral dust case as typical example of non-spherical particles. Although this aerosol type is characterized by particle sizes exceeding the application limit of the lidar technique, constraining the analyzed part of the total distribution to submicrometric and micrometric particles, we found positive points that make this a worthwhile methodology. The main point is that we found reasonably well retrieved aerosol absorption properties, in particular *IRI* and *SSA*, the key target (as already mentioned before) of most of current aerosol research.

The last set of results is vinculated to Doppler lidar measurements and their use to characterize the ABL. We analyzed data from three different locations using the products calculated with Halo lidar toolbox. A general conclusion that can be drawn from this whole part is that this software chain

provides an automatical, reliable and robust tool to obtain standardized ABL products with high temporal and spatial resolution.

We performed a statistical description of the horizontal wind field over Granada for two years in a height range from 100 m a.g.l. to around 1000 m a.g.l. The general trend obtained was mean diurnal wind from NW with mean speed around 3-4 m/s at low altitudes and 6-10 m/s at higher altitudes, and weaker mean nocturnal wind from SE with similar height dependence. Wind speed standard deviations indicated that the wind variability throughout the studied seasons also increased with height. The differences among the different seasons were also studied, finding the highest speeds during spring, and the lowest in winter.

The last work of this part was the analysis of turbulent properties of the ABL, starting with a characterization of clear sky versus cloud topped ABL. The first situation showed a clear development of the layer during daytime due to convective mixing from the surface, while the cloud presence in the second situation produced top-down mixing that did not allow the convective mechanism to rise the ABL to the same height as the previous case.

As a culmination of the Doppler lidar software chain, the ABL-classification product combines the information of all the rest of variables and provides a mask indicating the source and type of mixing for each time and range gate within the ABL. We calculated this product for the available databases of two complete years in Granada and 4 summer months in Rzecin (Poland). We found that both places shared similar convective behaviour during daytime, as is usual for mid-latitude locations. The wind shear-driven turbulence appeared to be more important for Rzecin rural site, although the results for this mechanism in Granada together with the high frequency of detection of 'intermittent' turbulence (not due to any of the labelled sources) made us consider the need for further analysis of those two types.

We have presented deep analyses of quite diverse atmospheric situations from different points of view in the framework of aerosol and Doppler lidar techniques. However, further research is still needed in order to progress in the studies carried out in this thesis, with the focus in the following topics:

- We will implement the rotational Raman channel also for the 532 nm branch in MULHACEN. Basing on the work with 355 nm, we expect successful results for nighttime optical retrievals, although the diurnal measurements will need to be tackled carefully due to the higher background radiation at this wavelength.
- Regarding the Doppler lidar focus correction, in a further step in collaboration with FMI group, the algorithm will be improved to better reject wrong cases, for instance those with strong aerosol extinction, and to be able to perform faster calibrations with extended databases. We will also explore the effect of the wavelength difference and the use of multiwavelength lidar data instead of ceilometer for the comparisons.
- The proposed methodology for combining Raman lidar and nocturnal photometry will be tested for more complex or extreme scenarios, including bimodal distributions and higher input error levels to meet the actual observations. A statistical study will be performed with more real cases to evaluate the most appropriate lidar configurations and the least affected microphysical properties. In addition to this, the method can be easily extended to non-spherical cases using SphInX software.
- A Principal Component Analysis of the horizontal winds over Granada will be performed to isolate and quantify the relevance of the katabatic winds with respect to other situations that contribute to the average behaviour.
- We will analyze in depth the sources of the detected nocturnal turbulence over Granada by implementing a low-level jet detection scheme and testing the wind-shear threshold applied.

CONCLUSIONES Y PERSPECTIVAS

Esta tesis aborda el perfilado vertical de distintas propiedades atmosféricas usando la técnica lidar, un objetivo general que ha sido llevado a cabo con éxito. Los principales sistemas lidar utilizados fueron un lidar Raman multiespectral con despolarización (MULHACEN) y un lidar Doppler. Las medidas realizadas con MULHACEN se usaron para obtener perfiles de propiedades ópticas con el algoritmo Raman, de propiedades microfísicas con dos algoritmos de regularización, UP (basado en el modelo de Mie para partículas esféricas) y SphInX (basado en el modelo T-matrix para esferoides), desarrollados en la Universidad de Potsdam (Alemania). Las medidas de lidar Doppler se usaron como datos de entrada de una cadena de varios algoritmos, *Halo lidar toolbox* desarrollada en el Instituto Meteorológico Finlandés (Helsinki, Finlandia), para calcular campo 3D de viento y propiedades turbulentas de la ABL.

Gracias a este enfoque con múltiples algoritmos pudimos comprender e implementar estas técnicas para describir eventos y situaciones de distinta naturaleza bajo varios puntos de vista. Hemos mejorado la capacidad del grupo GFAT de obtener un gran número de variables atmosféricas con gran resolución espacial y temporal. Con estas propiedades, hemos

sido capaces de caracterizar y analizar varias situaciones complejas, y podemos también aplicar los algoritmos de forma sistemática para tener bases de datos extensas y robustas para posteriores estudios.

Las conclusiones de cada estudio desarrollado en esta tesis ya han sido presentadas a lo largo de los distintos capítulos. Sin embargo, el objetivo del presente capítulo es destacar los aspectos principales de cada trabajo y vincularlos con los objetivos propuestos en el capítulo I.

El primer grupo de resultados estuvo vinculado con la mejora de las técnicas de medida y procesamiento. Se implementó una nueva configuración en MULHACEN para medir la señal Raman rotacional en la rama UV, con las ventajas de una mayor SNR y una variación despreciable de longitud de onda entre las señales Raman y elástica. Las medidas mejoradas han demostrado tener suficiente calidad para obtener perfiles de retrodispersión y extinción de partículas tanto durante el día como la noche, con una importante mejora de la resolución temporal y con las únicas incertidumbres añadidas de menos de 2 % y 4 % para α^a y β^a , respectivamente.

Como parte de las mejoras instrumentales, hemos aplicado varios algoritmos de procesamiento de la señal medida con lidar Doppler. Se corrigieron los artefactos en la señal de fondo debidos a la respuesta instrumental y al protocolo de medida en sí, permitiendo la detección de señales más débiles con un umbral de SNR menor. También se aplicó una calibración de la señal lidar Doppler según la altura focal y el diámetro de la lente del sistema óptico. Se calibró el sistema con un procedimiento sistemático basado en la comparación de las señales corregidas con un ceilómetro cercano, siendo así capaces de calcular el coeficiente de retrodispersión atenuado.

El segundo grupo de resultados está relacionado con el estudio de los procesos de transporte de aerosol y la caracterización de propiedades ópticas y microfísicas con el modelo esférico. El trabajo más destacable en este sentido fue el análisis de intensos eventos de partículas de combustión de biomasa

transportadas a gran distancia, que fueron detectadas en julio de 2013 en tres estaciones EARLINET. Se utilizaron observaciones de satélite de los instrumentos MODIS y CALIOP, así como herramientas de modelización como HYSPLIT y NAAPS, para estimar las fuentes y las trayectorias de transporte de esas partículas de humo de incendios en Norte América. La técnica lidar Raman multiespectral se aplicó para obtener propiedades ópticas de las partículas con resolución vertical, y la posterior inversión de estas propiedades con el software UP permitió obtener información microfísica de las partículas estudiadas.

Los resultados señalaron la presencia de capas de humo elevadas de 1-2 km de espesor, que suponían más de un 30 % del *AOD* total en todos los casos. Las propiedades ópticas y microfísicas obtenidas fueron las típicas para distintos grados de envejecimiento de las partículas: razón de color de razones lidar en torno a 2, AE_α menor de 1, r_{eff} de 0.3 μm y altos valores de *SSA*, casi espectralmente independientes. Las propiedades microfísicas intensivas se compararon con los resultados en columna de estaciones próximas de AERONET, y la intensidad de las capas se caracterizó también según la concentración volúmica de partículas, estableciendo una relación experimental entre esta magnitud y el coeficiente de extinción de partículas.

Un segundo estudio que se presenta en el marco de las inversiones microfísicas con el modelo esférico fue el uso de fotometría lunar y estelar para las inversiones con lidar Raman. Propusimos una metodología para usar el programa de regularización UP para casos o estaciones donde uno de los canales lidar '3+2' necesarios no está disponible. Se llevó a cabo un estudio de sensibilidad para tres escenarios diferentes, dos distribuciones de tamaño iniciales y cuatro *CRI*. Los resultados mostraron que la mayoría de los casos simulados presentaron errores menores del 10 % con respecto a los cálculos con la configuración completa.

También se validó la metodología con casos medidos, encontrando desviaciones hasta del 40 %. Sin embargo, estas mayores desviaciones se debieron al hecho de que las variaciones en los datos de entrada eran entre el 3 y el 40 % para los casos de medida, en contraposición al error constante del 5 % que se introdujo para las simulaciones. Tanto para casos simulados como medidos se puede destacar que las propiedades mejor obtenidas fueron la parte real del *CRI* y el *SSA*. Este último resulta de especial relevancia porque está directamente relacionado con la absorción de partículas, una de las propiedades del aerosol que aún presenta grandes incertidumbres en los modelos globales, y es un objetivo clave en proyectos de investigación e infraestructuras importantes como ACTRIS. Por tanto, la metodología propuesta ayudará a aumentar significativamente las bases de datos globales de propiedades de absorción del aerosol (además del resto de propiedades), ya que las estaciones equipadas con fotómetros nocturnos podrán obtenerlas aunque sus sistemas lidar Raman no cumplan el requisito '3+2'.

Como parte de los estudios de transporte y caracterización óptica y microfísica, también se investigó el uso del software SphInX para partículas no esféricas añadiendo medidas de despolarización. Ya que este programa es más reciente que UP, nuestro trabajo se centró en analizar minuciosamente y comparar las inversiones para optimizar la calidad de los resultados. Seleccionamos un caso con partículas de combustión de biomasa que pudo ser también analizado con UP para destacar el valor añadido de SphInX. Se obtuvo que este modelo mejoró las inversiones de tamaño, en concreto la concentración volúmica de partículas y el radio efectivo, además de proporcionar nueva información sobre la forma de las partículas con la '*size-shape distribution*' y la razón de aspecto efectiva.

También seleccionamos un caso de polvo mineral como ejemplo típico de partículas no esféricas. Aunque este tipo de aerosol se caracteriza por tamaños de partículas por encima del límite de aplicación de la técnica lidar, restringiendo la

parte analizada de la distribución total a las partículas submicrométricas y micrométricas, encontramos aspectos positivos que la hacen una metodología útil. El punto principal es que se encontraron propiedades de absorción de aerosol razonables, en particular *IRI* y *SSA*, los objetivos clave (como se ha mencionado antes) de la mayoría de la investigación actual en aerosol.

El último grupo de resultados está vinculado a las medidas lidar Doppler y su uso para caracterizar la ABL. Se analizaron data de tres localizaciones diferentes usando los productos calculados con la *Halo lidar toolbox*. Una conclusión general que se puede sacar de esta parte completa es que la cadena de procesamiento proporciona una herramienta automática, fiable y robusta para obtener productos estandarizados de la ABL con gran resolución espacial y temporal.

Se realizó una descripción estadística del campo de viento horizontal sobre Granada durante dos años en un rango de alturas desde 100 m s.n.s. hasta alrededor de 1000 m s.n.s. La tendencia general obtenida fue un viento medio diurno del noroeste con velocidades medias en torno a 3-4 m/s a baja altura y 6-10 m/s a mayores alturas, y un viento medio más débil del sureste con dependencia similar con la altura. Las desviaciones estándar en la velocidad del viento indicaron que la variabilidad del viento a lo largo de las estaciones del año estudiadas también aumenta con la altura. Las diferencias entre distintas épocas del año también se estudiaron, encontrando las mayores velocidades durante primavera, y las menores en invierno.

El último trabajo de esta parte fue el análisis de propiedades turbulentas de la ABL, empezando por la caracterización de situación de cielo despejado frente a cubierta de nubes. La primera situación mostró un claro desarrollo de la ABL durante el día debido a la mezcla convectiva desde la superficie, mientras que la presencia de nubes en la segunda situación produjo mezcla de arriba abajo que no permitió al mecanismo

convectivo elevar la ABL a la misma altura que el caso despejado.

Como culminación de la cadena de procesado de lidar Doppler, el producto de clasificación de la ABL combina información de todo el resto de variables y proporciona una máscara indicando la fuente y el tipo de mezcla para cada instante e intervalo de alturas en la ABL. Se calculó este producto para las bases de datos disponibles para dos años completos en Granada y 4 meses en verano en Rzecin (Polonia). Se encontró que ambos lugares compartían un comportamiento convectivo similar durante el día, como es común en latitudes medias. La turbulencia debida a cizalla del viento resultó ser más frecuente en el entorno rural de Rzecin, aunque los resultados para este mecanismo en Granada junto con la alta frecuencia de detección de turbulencia 'intermitente' (no debida a ninguno de los tipos estudiados) nos hizo considerar la necesidad de un mayor análisis para estos dos tipos.

Hemos presentado análisis profundos de situaciones atmosféricas diversas desde diferentes puntos de vista en el marco de las técnicas lidar de aerosol y Doppler. Sin embargo, se necesita aún más estudio para progresar en los análisis llevados a cabo en esta tesis, con especial atención en los siguientes temas:

- Se implementará el canal Raman rotacional también en la rama de 532 nm de MULHACEN. Basándonos en el trabajo para 355 nm, se esperan resultados exitosos para medidas nocturnas, aunque las medidas diurnas tendrán que ser cuidadosamente enfocadas debido a la mayor radiación de fondo a esta longitud de onda.
- En cuanto a la corrección del foco del lidar Doppler, en un paso posterior en colaboración con el grupo FMI, se mejorará el algoritmo para rechazar casos no válidos, por ejemplo con extinción de partículas muy intensa, y para realizar calibraciones más rápidas para extensas bases de datos. También se explorará el efecto de la diferencia de longitud de onda y el uso de lidar

multiespectral en lugar de ceilómetro para las comparaciones.

- La metodología propuesta para combinar lidar Raman y fotometría nocturna se probará con escenarios más complejos y extremos, incluyendo distribuciones bimodales y niveles de error iniciales mayores para representar las observaciones reales. Se realizará un estudio estadístico con más casos reales para evaluar las configuraciones lidar más apropiadas y las propiedades microfísicas menos afectadas. Además, el método se puede extender fácilmente a los casos no esféricos con SphIX.
- Se realizará un Análisis de Componentes Principales de los vientos horizontales sobre Granada, para aislar y cuantificar la relevancia de los vientos catabáticos con respecto a otras situaciones que contribuyen al comportamiento medio.
- Analizaremos en profundidad las fuentes de la turbulencia nocturna detectada en Granada, implementando un esquema de detección de *low-level jet* y comprobando el umbral de cizalla de viento utilizado.

APPENDIX

TABLES RELATED TO PARTICLE OPTICAL AND
MICROPHYSICAL PROPERTIES SIMULATIONS

The following tables correspond to simulated and retrieved particle optical and microphysical properties from section 4.3.1.

7.1 FORWARD CALCULATIONS

Table VII-1: Particle optical extensive properties obtained with Mie forward calculation from the initial distributions and *CRI* values described in section 4.3.1.

Distr.	<i>CRI</i> case	$\alpha^a(355)$ (Mm^{-1})	$\beta^a(355)$ ($Mm^{-1}sr^{-1}$)	$\alpha^a(532)$ (Mm^{-1})	$\beta^a(532)$ ($Mm^{-1}sr^{-1}$)	$\beta^a(1064)$ ($Mm^{-1}sr^{-1}$)
1 (submic.)	A	104.2	1.187	59.1	0.739	0.343
	B	102.1	0.351	65.8	0.361	0.292
	C	128.8	2.568	81.9	1.285	0.518
	D	140.0	1.626	102.3	0.995	0.595
2 (mic.)	A	4115.3	122.026	4447.4	119.846	77.261
	B	4089.0	5.796	4354.2	7.116	9.617
	C	4098.5	173.594	4319.6	267.664	247.290
	D	4077.6	31.494	4266.5	69.923	110.816

Table VII-2: Particle optical intensive properties obtained with Mie forward calculation from the initial distributions and *CRI* values described in section 4.3.1.

Distr.	<i>CRI</i> case	$LR^a(355)$ (sr)	$LR^a(532)$ (sr)	AE_α (355, 532)	AE_β (355, 532)	AE_β (355, 1064)	AE_β (532, 1064)
1 (submic.)	A	87.8	80.0	1.40	1.17	1.13	1.11
	B	290.6	182.4	1.09	-0.07	0.17	0.31
	C	50.2	63.7	1.12	1.71	1.46	1.31
	D	86.1	102.8	0.77	1.21	0.92	0.74
2 (mic.)	A	33.7	37.1	-0.19	0.04	0.42	0.63
	B	705.5	611.9	-0.16	-0.51	-0.46	-0.43
	C	23.6	16.1	-0.13	-1.07	-0.32	0.11
	D	129.5	61.0	-0.11	-1.97	-1.15	-0.66

7.2 ZERO RETRIEVALS

Table VII-3: Particle optical and microphysical properties retrieved with inverse calculation from the initial optical properties in Table VII-1, compared to the initial properties, for submicrometric distribution and *CRI* case A.

	Initial	Zero retrieval	Absolute error	Relative error (%)
<i>RRI</i>	1.4	1.357 ± 0.005	-0.043	-3.07
<i>IRI</i>	0.005	0.002 ± 0.001	-0.003	-60.00
r_{eff} (μm)	0.174	0.205 ± 0.018	0.031	17.82
C_S (μm ² cm ⁻³)	196	210 ± 30	14.000	7.14
C_V (μm ³ cm ⁻³)	11.3	13.9 ± 0.5	2.600	23.01
C_N (m ⁻³)	0.001002	0.0016 ± 0.0021	0.001	59.68
SSA 355 nm	0.9693	0.9834 ± 0.0005	0.014	1.45
SSA 532 nm	0.9667	0.9815 ± 0.0006	0.015	1.53

Table VII-4: Particle optical and microphysical properties retrieved with inverse calculation from the initial optical properties in Table VII-1, compared to the initial properties, for submicrometric distribution and *CRI* case B.

	Initial	Zero retrieval	Absolute error	Relative error (%)
<i>RRI</i>	1.4	1.38 ± 0.01	-0.020	-1.43
<i>IRI</i>	0.075	0.121 ± 0.011	0.046	61.33
r_{eff} (μm)	0.174	0.150 ± 0.005	-0.024	-13.79
C_S (μm ² cm ⁻³)	196	267 ± 8	71.000	36.22
C_V (μm ³ cm ⁻³)	11.3	13.3 ± 0.4	2.000	17.70
C_N (m ⁻³)	0.001002	0.0039 ± 0.004	0.003	289.22
SSA 355 nm	0.686	0.545 ± 0.002	-0.141	-20.55
SSA 532 nm	0.654	0.483 ± 0.004	-0.171	-26.15

Table VII-5: Particle optical and microphysical properties retrieved with inverse calculation from the initial optical properties in Table VII-1, compared to the initial properties, for submicrometric distribution and *CRI* case C.

	Initial	Zero retrieval	Absolute error	Relative error (%)
<i>RRI</i>	1.5	1.484 ± 0.017	-0.016	-1.07
<i>IRI</i>	0.005	0.0028 ± 0.0024	-0.002	-44.00
r_{eff} (μm)	0.174	0.157 ± 0.009	-0.017	-9.77
C_S (μm ² cm ⁻³)	196	243 ± 16	47.000	23.98
C_V (μm ³ cm ⁻³)	11.3	12.7 ± 0.017	1.400	12.39
C_N (m ⁻³)	0.001002	0.006 ± 0.003	0.005	498.80
<i>SSA</i> 355 nm	0.9721	0.9836 ± 0.0005	0.012	1.18
<i>SSA</i> 532 nm	0.9732	0.9843 ± 0.0005	0.011	1.14

Table VII-6: Particle optical and microphysical properties retrieved with inverse calculation from the initial optical properties in Table VII-1, compared to the initial properties, for submicrometric distribution and *CRI* case D.

	Initial	Zero retrieval	Absolute error	Relative error (%)
<i>RRI</i>	1.6	1.6 ± 0.03	0.000	0.00
<i>IRI</i>	0.05	0.051 ± 0.006	0.001	2.00
r_{eff} (μm)	0.174	0.171 ± 0.006	-0.003	-1.72
C_S (μm ² cm ⁻³)	196	215 ± 8	19.000	9.69
C_V (μm ³ cm ⁻³)	11.3	12.3 ± 0.5	1.000	8.85
C_N (m ⁻³)	0.001002	0.0020 ± 0.0005	0.001	99.60
<i>SSA</i> 355 nm	0.7943	0.7892 ± 0.0019	-0.005	-0.64
<i>SSA</i> 532 nm	0.8085	0.8028 ± 0.0021	-0.006	-0.71

Table VII-7: Particle optical and microphysical properties retrieved with inverse calculation from the initial optical properties in Table VII-1, compared to the initial properties, for micrometric distribution and *CRI* case A.

	Initial	Zero retrieval	Absolute error	Relative error (%)
<i>RRI</i>	1.4	1.393 ± 0.014	-0.007	-0.50
<i>IRI</i>	0.005	0.0042 ± 0.0004	-0.001	-16.00
r_{eff} (μm)	1.04139	1.09 ± 0.10	0.049	4.67
C_S (μm ² cm ⁻³)	7035.97	6940 ± 150	-95.970	-1.36
C_V (μm ³ cm ⁻³)	2442.39	2500 ± 30	57.610	2.36
C_N (m ⁻³)	0.00100048	0.0014 ± 0.0004	0.0004	39.93
SSA 355 nm	0.859654	0.877 ± 0.003	0.017	2.02
SSA 532 nm	0.901455	0.9148 ± 0.0017	0.013	1.48

Table VII-8: Particle optical and microphysical properties retrieved with inverse calculation from the initial optical properties in Table VII-1, compared to the initial properties, for micrometric distribution and *CRI* case B.

	Initial	Zero retrieval	Absolute error	Relative error (%)
<i>RRI</i>	1.4	1.383 ± 0.025	-0.017	-1.21
<i>IRI</i>	0.075	0.071 ± 0.012	-0.004	-5.33
r_{eff} (μm)	1.04139	1.05 ± 0.19	0.009	0.83
C_S (μm ² cm ⁻³)	7035.97	6870 ± 130	-165.970	-2.36
C_V (μm ³ cm ⁻³)	2442.39	2400 ± 500	-42.390	-1.74
C_N (m ⁻³)	0.00100048	0.0017 ± 0.0005	0.001	69.92
SSA355 nm	0.514636	0.5363 ± 0.0018	0.022	4.21
SSA 532 nm	0.543227	0.578 ± 0.004	0.035	6.40

Table VII-9: Particle optical and microphysical properties retrieved with inverse calculation from the initial optical properties in Table VII-1, compared to the initial properties, for micrometric distribution and *CRI* case C.

	Initial	Zero retrieval	Absolute error	Relative error (%)
<i>RRI</i>	1.5	1.503 ± 0.009	0.007	0.47
<i>IRI</i>	0.005	0.0053 ± 0.0016	0.000	6.00
r_{eff} (μm)	1.04139	1.10 ± 0.07	0.059	5.63
C_S (μm ² cm ⁻³)	7035.97	7030 ± 100	-5.970	-0.08
C_V (μm ³ cm ⁻³)	2442.39	2580 ± 20	137.610	5.63
C_N (m ⁻³)	0.00100048	0.003 ± 0.003	0.002	199.86
<i>SSA</i> 355 nm	0.853563	0.848 ± 0.005	-0.006	-0.65
<i>SSA</i> 532 nm	0.893472	0.87 ± 0.003	-0.006	-0.72

Table VII-10: Particle optical and microphysical properties retrieved with inverse calculation from the initial optical properties in Table VII-1, compared to the initial properties, for micrometric distribution and *CRI* case D.

	Initial	Zero retrieval	Absolute error	Relative error (%)
<i>RRI</i>	1.6	1.64 ± 0.05	0.040	2.50
<i>IRI</i>	0.05	0.055 ± 0.008	0.005	10.00
r_{eff} (μm)	1.04139	1.04 ± 0.13	-0.001	-0.13
C_S (μm ² cm ⁻³)	7035.97	6970 ± 80	-65.970	-0.94
C_V (μm ³ cm ⁻³)	2442.39	2400 ± 300	-42.390	-1.74
C_N (m ⁻³)	0.00100048	0.0018 ± 0.0005	0.001	79.91
<i>SSA</i> 355 nm	0.547708	0.5477 ± 0.0003	0.0000	0.00
<i>SSA</i> 532 nm	0.574372	0.5753 ± 0.0010	0.001	0.16

7.3 NOISE ADDITION

Table VII-11: Disturbed values of $AE_\alpha(355,532)$ with +5% and -5% (superscripts + and -, respectively), and the calculated $\alpha^a(532)$ and $\alpha^a(355)$, corresponding to scenarios I and II, for the two distributions and all *CRI* values described in section 4.3.1.

Distr.	<i>CRI</i> case	AE_α^+ (355, 532)	AE_α^- (355, 532)	α_+^a (532) (Mm ⁻¹)	α_-^a (532) (Mm ⁻¹)	α_+^a (355) (Mm ⁻¹)	α_-^a (355) (Mm ⁻¹)
1 (submic.)	A	1.47	1.33	57.5	60.8	107.2	101.3
	B	1.14	1.03	64.4	67.3	104.4	99.9
	C	1.18	1.06	80.0	83.7	131.8	125.9
	D	0.81	0.74	100.8	104.0	142.2	137.8
2 (mic.)	A	-0.20	-0.18	4464.6	4430.1	4099.4	4131.3
	B	-0.16	-0.15	4367.9	4340.5	4076.1	4101.8
	C	-0.14	-0.12	4331.0	4308.3	4087.8	4109.3
	D	-0.12	-0.11	4276.2	4256.9	4068.3	4086.8

Table VII-12: Disturbed values of $AE_\alpha(532,1064)$ with +5% and -5% (superscripts + and -, respectively), and the calculated $\beta^a(1064)$, corresponding to scenario III, for the two distributions and all *CRI* values described in section 4.3.1.

Distr.	<i>CRI</i> case	AE_β^+ (532, 1064)	AE_α^- (532, 1064)	β_+^a (1064) (Mm ⁻¹ sr ⁻¹)	β_-^a (1064) (Mm ⁻¹ sr ⁻¹)
1 (submic.)	A	1.16	1.05	0.330	0.357
	B	0.32	0.29	0.289	0.295
	C	1.38	1.25	0.495	0.542
	D	0.78	0.71	0.580	0.610
2 (mic.)	A	0.44	0.40	75.583	78.976
	B	-0.46	-0.41	9.763	9.473
	C	0.12	0.11	246.313	248.271
	D	-0.70	-0.63	113.397	108.294

7.4 DISTURBED RETRIEVALS

Table VII-13: Particle optical and microphysical properties retrieved with inverse calculation from the initial optical properties in Table VII-1 and the $\alpha^a(532)$ for submicrometric distribution and scenario I in Table VII-11. Relative errors with respect to zero retrieval are depicted in Figure IV-17.

Sc.	CRI case	RRI	IRI	r_{eff} (μm)	C_S ($\mu\text{m}^2\text{cm}^{-3}$)	C_V ($\mu\text{m}^3\text{cm}^{-3}$)	C_N (m^{-3})	SSA 355 nm	SSA 532 nm
I ⁺	A	1.354	0.002	0.2	220	14.2	0.0018	0.9831	0.981
	B	1.346	0.111	0.139	305	14.1	0.0049	0.535	0.468
	C	1.489	0.002	0.146	251	12.23	0.0092	0.9861	0.9866
	D	1.583	0.047	0.168	222	12.4	0.0030	0.7991	0.808
I ⁻	A	1.369	0.0032	0.21	190	13.1	0.00101	0.9777	0.976
	B	1.407	0.098	0.192	228	13	0.00340	0.618	0.575
	C	1.4862	0.0032	0.1685	214.7	12.206	0.002071	0.9812	0.9823
	D	1.58	0.047	0.181	207	12.5	0.00190	0.798	0.814

Table VII-14: Particle optical and microphysical properties retrieved with inverse calculation from the initial optical properties in Table VII-1 and the $\alpha^a(532)$ for micrometric distribution and scenario I in Table VII-11. Relative errors with respect to zero retrieval are depicted in Figure IV-17.

Sc.	CRI case	RRI	IRI	r_{eff} (μm)	C_S ($\mu\text{m}^2\text{cm}^{-3}$)	C_V ($\mu\text{m}^3\text{cm}^{-3}$)	C_N (m^{-3})	SSA 355 nm	SSA 532 nm
I ⁺	A	1.395	0.0041	1.08	6920	2480	0.0015	0.8819	0.919
	B	1.394	0.077	0.94	6800	2100	0.002	0.5349	0.5780
	C	1.52	0.0072	1.10	6990	2570	0.002	0.8120	0.8570
	D	1.64	0.056	1	6960	2300	0.0016	0.5498	0.5754
I ⁻	A	1.389	0.0039	1.11	6910	2550	0.00170	0.8845	0.921
	B	1.38	0.069	1.06	6870	2400	0.0019	0.5384	0.5790
	C	1.519	0.007	1.09	6970	2530	0.004	0.819	0.863
	D	1.65	0.056	1.04	6980	2400	0.0023	0.5509	0.5725

Table VII-15: Particle optical and microphysical properties retrieved with inverse calculation from the initial optical properties in Table VII-1 and the $\alpha^a(355)$ for submicrometric distribution and scenario II in Table VII-11. Relative errors with respect to zero retrieval are depicted in Figure IV-17.

Sc.	CRI case	RRI	IRI	r_{eff} (μm)	C_S ($\mu\text{m}^2\text{cm}^{-3}$)	C_V ($\mu\text{m}^3\text{cm}^{-3}$)	C_N (m^{-3})	SSA 355 nm	SSA 532 nm
II ⁺	A	1.354	0.002	0.191	230	14.3	0.003	0.9851	0.9831
	B	1.336	0.11	0.139	320	14.8	0.0052	0.5280	0.46
	C	1.479	0.0018	0.151	257.4	12.9	0.0082	0.9891	0.9894
	D	1.599	0.049	0.17	219	12.4	0.0021	0.7959	0.8041
II ⁻	A	1.374	0.0035	0.206	187	12.8	0.0011	0.975	0.97317
	B	1.413	0.107	0.159	232	12.3	0.0041	0.6004	0.5566
	C	1.493	0.004	0.165	216	11.8	0.003	0.9773	0.9788
	D	1.571	0.044	0.184	202	12.4	0.0014	0.8047	0.817

Table VII-16: Particle optical and microphysical properties retrieved with inverse calculation from the initial optical properties in Table VII-1 and the $\alpha^a(355)$ for micrometric distribution and scenario II in Table VII-11. Relative errors with respect to zero retrieval are depicted in Figure IV-17.

Sc.	CRI case	RRI	IRI	r_{eff} (μm)	C_S ($\mu\text{m}^2\text{cm}^{-3}$)	C_V ($\mu\text{m}^3\text{cm}^{-3}$)	C_N (m^{-3})	SSA 355 nm	SSA 532 nm
II ⁺	A	1.387	0.0042	1.13	6980	2630	0.0012	0.8737	0.912
	B	1.39	0.075	0.95	6780	2200	0.0019	0.5371	0.5820
	C	1.52	0.007	1.11	6970	2580	0.003	0.8170	0.861
	D	1.64	0.057	0.99	6930	2280	0.0017	0.5489	0.5738
II ⁻	A	1.396	0.004	1.06	6910	2500	0.0019	0.885	0.921
	B	1.379	0.069	1.03	6880	2400	0.0021	0.5384	0.580
	C	1.525	0.0081	1.05	6980	2450	0.006	0.803	0.8491
	D	1.65	0.056	1.04	7000	2400	0.0022	0.5499	0.5720

Table VII-17: Particle optical and microphysical properties retrieved with inverse calculation from the initial optical properties in Table VII-1 and the $\beta^a(1064)$ for submicrometric distribution and scenario III in Table VII-12. Relative errors with respect to zero retrieval are depicted in Figure IV-17.

Sc.	CRI case	RRI	IRI	r_{eff} (μm)	C_S ($\mu\text{m}^2\text{cm}^{-3}$)	C_V ($\mu\text{m}^3\text{cm}^{-3}$)	C_N (m^{-3})	SSA 355 nm	SSA 532 nm
III ⁺	A	1.361	0.0014	0.205	193	13.1	0.001	0.99	0.9888
	B	1.379	0.117	0.151	268	13.5	0.0039	0.551	0.49
	C	1.4810 3	0.0015 5	0.1637	219.89	11.999	0.0022	0.9909	0.9913
	D	1.61	0.051	0.169	218	12.3	0.0022	0.7874	0.8007
III ⁻	A	1.359	0.0042	0.216	203	14.4	0.001	0.969	0.9645
	B	0.377	0.116	0.151	269	13.5	0.0039	0.553	0.493
	C	1.507	0.0062	0.1453	248.6	12.04	0.0094	0.9651	0.9664
	D	1.592	0.049	0.173	217	12.4	0.003	0.7929	0.8068

Table VII-18: Particle optical and microphysical properties retrieved with inverse calculation from the initial optical properties in Table VII-1 and the $\beta^a(1064)$ for micrometric distribution and scenario III in Table VII-12. Relative errors with respect to zero retrieval are depicted in Figure IV-17.

Sc.	CRI case	RRI	IRI	r_{eff} (μm)	C_S ($\mu\text{m}^2\text{cm}^{-3}$)	C_V ($\mu\text{m}^3\text{cm}^{-3}$)	C_N (m^{-3})	SSA 355 nm	SSA 532 nm
III ⁺	A	1.395	0.0039	1.05	6870	2400	0.0019	0.901	0.923
	B	1.38	0.069	1.05	6810	2400	0.0018	0.5442	0.589
	C	1.517	0.007	1.10	6990	2560	0.0030	0.8190	0.8650
	D	1.65	0.056	1.02	6960	2400	0.0017	0.5509	0.5747
III ⁻	A	1.396	0.0041	1.08	6920	2500	0.0014	0.8811	0.917
	B	1.389	0.074	1.07	6870	2500	0.0024	0.535	0.5763
	C	1.52	0.0076	1.05	6980	2450	0.004	0.810	0.856
	D	1.64	0.055	1.04	6970	2400	0.0018	0.5511	0.5753

LIST OF SYMBOLS AND ABBREVIATIONS

Symbol / Abbreviation	Full name	Usual units
a.g.l.	Above ground level	-
a.s.l.	Above sea level	-
σ_{ab}	Absorption coefficient	m^{-1}
β^a	Aerosol (or particle) backscatter coefficient	$m^{-1}sr^{-1}$ or $Mm^{-1}sr^{-1}$
α^a	Aerosol (or particle) extinction coefficient	m^{-1} or Mm^{-1}
LR^a	Aerosol (or particle) lidar ratio	sr
AOD	Aerosol optical depth	Unitless
AERONET	Aerosol Robotic Network	-
ACTRIS	Aerosol, Clouds and Trace Gases Research Infrastructure	-
AEMET	Agencia Estatal de Meteorología	-
An	Analog detection	-
AGORA	Andalusian Global Observatory of the Atmosphere	-
AE_q	Angström Exponent (q -related)	Unitless
a_{width}	Aspect ratio width	Unitless
ABL	Atmospheric boundary layer	-
ABLH	Atmospheric boundary layer height	Km
AMAPOLA	Atmospheric Monitoring of Aerosol Particle Fluxes in Olive Orchard	-
β_{att}	Attenuated backscatter coefficient	$m^{-1}sr^{-1}$ or $Mm^{-1}sr^{-1}$
σ_{β}	Attenuated backscatter coefficient uncertainty	-

Symbol / Abbreviation	Full name	Usual units
APD	Avalanche photodiode detector	-
β	Backscatter coefficient	$\text{m}^{-1}\text{sr}^{-1}$ or $\text{Mm}^{-1}\text{sr}^{-1}$
R	Backscattering ratio	Unitless
ϕ	B-spline function	-
CALIPSO	Cloud-Aerosol Lidar and Infrared Pathfinder Satellite Observation	-
CALIOP	Cloud-Aerosol Lidar with Orthogonal Polarization	-
V	Columnar volume concentration	$\mu\text{m}^3\mu\text{m}^{-2}$
CRI	Complex refractive index	Unitless
CNR-IMAA	Consiglio Nazionale delle Ricerche - Istituto di Metodologie per l'Analisi Ambientale	-
K_{Γ}	Cross section (of Γ)	cm^2
DM	Dichroic mirror	-
DP	Discrepancy Principle	-
ε	Dissipation rate of the Turbulent Kinetic Energy	m^2s^{-3}
DBS	Doppler beam swinging	-
a_{eff}	Effective aspect ratio	Unitless
r_{eff}	Effective radius	μm
ERIC	European Research Infrastructure Consortium	-
EARLINET	European Aerosol Research Lidar Network	-
α	Extinction coefficient	m^{-1} or Mm^{-1}
FMI	Finnish Meteorological Institute	-
f_h	Focus height	M
FT	Free Troposphere	-
f	Frequency	Hz
GCV	Generalized cross validation method	-

Symbol / Abbreviation	Full name	Usual units
GRASP	Generalized Retrieval of Atmosphere and Surface Properties	-
GDAS	Global Data Assimilation System	-
GFAT	Grupo de Física de la Atmósfera	-
r_h	Horizontal spheroidal semiaxis	μm
d	Horizontal wind direction	$^\circ$
U_H	Horizontal wind speed	m s^{-1}
HYSPLIT	Hybrid Single-Particle Lagrangian Integrated Trajectory	-
ICENET	Iberian Ceilometer Network	-
IRI	Imaginary part of refractive index	Unitless
IR	Infrared	-
IAA	Instituto Andaluz de Astrofísica	-
IISTA-CEAMA	Instituto Interuniversitario de Investigación del Sistema Tierra en Andalucía – Centro Andaluz de Medio Ambiente	-
INOE	Institutul Național de Cercetare-Dezvoltare pentru Optoelectronică	-
IPCC	Intergovernmental Panel on Climate Change	-
ICOS	Integrated Carbon Observation System	-
β_{KF}^a	Klett-Fernald aerosol backscatter coefficient	$\text{m}^{-1}\text{sr}^{-1}$ or $\text{Mm}^{-1}\text{sr}^{-1}$
K_q	Kurtosis (of q)	Unitless
LALINET	Latin American Lidar Network	-
V_L	Layer-integrated volume concentration	$\mu\text{m}^3\mu\text{m}^{-2}$
LC	L-curve method	-
l	Lens diameter	m

Symbol / Abbreviation	Full name	Usual units
LiCal	Lidar Calibration Centre	-
LiCoTest	Lidar Components Testing Laboratory	-
LiReQA	Lidar Remote Quality Assurance	-
LIRIC	Lidar-Radiometer Inversion Code	-
Lidar	Light detection and ranging	-
δ_p	Linear particle depolarization ratio	Unitless
v_{LOS}	Line-of-sight velocity	m/s
LO	Local oscillator	-
LMU	Ludwig Maximilians University	-
C_M	Mass particle concentration	$\mu\text{g cm}^{-3}$
$m(r) / m(r, a)$	Mass particle size (and shape) distribution	$\mu\text{g cm}^{-3}\mu\text{m}^{-1}$
r_{med}	Median radius	μm
a_{mod}	Modal aspect ratio	-
r_{mod}	Modal radius	μm
MODIS	Moderate Resolution Imaging Spectroradiometer	-
β^m	Molecular backscatter coefficient	$\text{m}^{-1}\text{sr}^{-1}$ or $\text{Mm}^{-1}\text{sr}^{-1}$
α^m	Molecular extinction coefficient	m^{-1} or Mm^{-1}
δ^m	Molecular linear depolarization ratio	Unitless
NOAA	National Oceanographic and Atmospheric Administration	-
NRL	Naval Research Laboratory	-
NAAPS	Navy Aerosol Analysis and Prediction System	-
C_N	Numeric particle concentration	cm^{-3}
$n(r) / n(r, a)$	Numeric particle size (and shape) distribution	$\text{cm}^{-3}\mu\text{m}^{-1}$
OD	Optical depth	Unitless
OT	Optical thickness	Unitless
OA	Organic aerosol	-

Symbol / Abbreviation	Full name	Usual units
PCR	Parameter choice rule	-
a	Particle aspect ratio	Unitless
r	Particle radius	μm
x	Particle size parameter	Unitless
Pc	Photon-counting	-
PBS	Polarizing beam splitter	-
POLIMOS	Polish Radar and Lidar Mobile Observation System	-
PBAPs	Primary biological aerosol particles	-
RR	Pure rotational Raman	-
v_r	Radial velocity	m/s
RF	Radiative forcing	-
β_R^a	Raman aerosol backscatter coefficient	$\text{m}^{-1}\text{sr}^{-1}$ or $\text{Mm}^{-1}\text{sr}^{-1}$
RCS	Range corrected signal	arbitrary units
RRI	Real part of refractive index	Unitless
RIMA	Red Ibérica de Medida fotométrica de Aerosoles	-
v_a	Reduced volume particle size distribution	$\mu\text{m}^3\text{cm}^{-3}\mu\text{m}^{-1}$
RM	Regularization method	-
σ_{sc}	Scattering coefficient	m^{-1}
SLOPE	Sierra Nevada Lidar Aerosol Profiling Experiment	-
SNR	Signal-to-Noise Ratio	-
SSA	Single scattering albedo	Unitless
SVD	Singular Value Decomposition	-
S_q	Skewness (of q)	Unitless
SphInX	Spheroidal Inversion Experiments (regularization software)	-
C_s	Surface particle concentration	$\mu\text{m}^2\text{cm}^{-3}$
$s(r) / s(r, a)$	Surface particle size (and shape) distribution	$\mu\text{m}^2\text{cm}^{-3}\mu\text{m}^{-1}$
TSVD	Truncated Singular Value Decomposition	-

Symbol / Abbreviation	Full name	Usual units
UV	Ultraviolet	-
UTC	Universal Time Coordinated	-
UP	University of Potsdam (regularization software)	-
σ_q^2	Variance (of q)	$[q]^2$
VAD	Velocity-Azimuth display	
r_v	Vertical spheroidal semiaxis	μm
w	Vertical wind	m/s
VR	Vibrational-rotational Raman	-
VIS	Visible	-
C_v	Volume particle concentration	$\mu\text{m}^3\text{cm}^{-3}$
$v(r) / v(r, a)$	Volume particle size (and shape) distribution	$\mu\text{m}^3\text{cm}^{-3}\mu\text{m}^{-1}$
λ	Wavelength	nm or μm
sh	Wind shear	s^{-1}

ACKNOWLEDGEMENTS

This thesis has been directly funded by Spanish Ministry of Education, Culture and Sport (currently, the Ministry of Education and Vocational Training) through grant FPU14/03684. However, a number of institutions and researchers have also contributed with their financial, professional and academic support.

I would first like to thank my supervisors, Prof. Dr. Lucas Alados-Arboledas and Dr. Juan Luis Guerrero-Rascado, for sharing with me their expertise and providing guidance and feedback throughout this project. I especially appreciate their trust in my abilities and their willingness to develop my career as a researcher. They have also financially supported my attendance to several international meetings, conferences, workshops and research internships. This financial support has come from the Spanish Government through TRIAEROMONITOR and CLARIN projects and from the European Union through ACTRIS and ACTRIS-2 projects and Erasmus + Programme.

Furthermore I want to thank the rest of GFAT team and all the scientists that have stayed with us during those years, for their exceptional advice and help, and for their work in instrument operation, measurement gathering and data analysis to create the databases used in this thesis. In particular, I am grateful to

the people that worked for AMAPOLA and SLOPE campaigns and to Dr. Juan Antonio Bravo-Aranda for developing INDRA software. I have to especially mention Dr. Jose Antonio Benavent-Oltra, Dr. Andrés Bedoya-Velásquez, Dr. Gregori de Arruda Moreira, Dr. Anderson Guedes, Manuela Hoyos-Restrepo and Cristian Soto-Ormeño for their work with the lidar systems. I am also thankful to the University of Granada, the IISTA and all its member's staff.

I must also acknowledge the University of Potsdam and the Finnish Meteorological Institute for hosting me during my research internships. On the one hand, to Prof. Dr. Christine Böckmann and her team for providing insight and knowledge of the regularization theory and application, to Dr. Lukas Osterloh and Dr. Lars Schneidenbach for developing UP software, and to Dr. Stefanos Samaras for developing SphInX software. On the other hand, to Dr. Ewan O'Connor and his team for their instruction in Doppler lidar field, and to Dr. Antti Manninen for developing Halo lidar toolbox.

I owe my gratitude to Dr. Iwona Stachlewska and Dr. Holger Baars for the fruitful cooperation we had in my first publication, and to the rest of coauthors for their data analyses and reviews. The review of this thesis by Dr. Jana Preißler and Dr. Francisco Navas-Guzmán is also gratefully acknowledged.

I am again grateful to Dr. Iwona Stachlewska, and also to Dr. Chojnicki and their team during POLIMOS 2018 for giving me the opportunity and the means and support to participate in that field campaign. And special thanks to Juan Andrés Casquero-Vera for his side-by-side work.

I also appreciate the technical and scientific support offered by Dr. George Georgousis and the rest of Raymetrics team, and also by Dr. Guy Pearson, Justin Eackock and Halo Photonics team.

I express gratitude to the NOAA Air Resources Laboratory (ARL) for the HYSPLIT transport and dispersion model. I thank those at NRL-Monterey that have helped in the development of the NAAPS model and the MODIS team for the use of FIRMS

data. Acknowledgements are also due for NASA–EOS team members for providing CALIOP and CALIPSO datasets. I acknowledge those members of Granada, Leipzig and Belsk teams for maintaining and supporting the instruments from the AERONET network used in this thesis, and B. Holben and the AERONET team for the use of the retrievals and data availability. Appreciation is also due to GOA-UVA team for photometer calibrations with particular mention of Dr. África Barreto for nocturnal *AOD* data processing and Dr. Roberto Román for the fruitful cooperation and data availability.

I am also indebted to José C. Díaz Montes for the graphical design and printing of the thesis cover.

To conclude, I cannot stress enough the invaluable personal support of many people, that has undoubtedly been crucial for the completion of this thesis. Putting it down in writing would not be sufficient to thank each of them.

REFERENCES

- Aitchison, J. and Brown, J. A. C.: The Lognormal Distribution Function, Cambridge University Press, Cambridge, UK., 1957.
- Alados-Arboledas, L., Müller, D., Guerrero-Rascado, J. L., Navas-Guzmán, F., Pérez-Ramírez, D. and Olmo, F. J.: Optical and microphysical properties of fresh biomass burning aerosol retrieved by Raman lidar, and star-and sun-photometry, *Geophys. Res. Lett.*, doi:10.1029/2010GL045999, 2011.
- Allen, M. R., Dube, O. P., Solecki, W., Aragón-Durand, F., Cramer, W., Humphreys, S., Kainuma, M., Kala, J., Mahowald, N., Mulugetta, Y., Perez, R., Wairiu, M. and Zickfeld, K.: Framing and Context, in *Global Warming of 1.5°C. An IPCC Special Report on the impacts of global warming of 1.5°C above pre-industrial levels and related global greenhouse gas emission pathways, in the context of strengthening the global response to the threat of climate change*, edited by V. Masson-Delmotte, P. Zhai, H.-O. Pörtner, D. Roberts, J. Skea, P. R. Shukla, A. Pirani, W. Moufouma-Okia, C. Péan, R. Pidcock, S. Connors, J. B. R. Matthews, Y. Chen, X. Zhou, M. I. Gomis, E. Lonnoy, T. Maycock, M. Tignor, and T. Waterfield, In Press., 2018.
- Althausen, D., Engelmann, R., Baars, H., Heese, B., Ansmann, A., Müller, D. and Komppula, M.: Portable raman lidar pollyxt for automated profiling of aerosol backscatter, extinction, and depolarization, *J. Atmos. Ocean. Technol.*, 26(11), 2366–2378, doi:10.1175/2009JTECHA1304.1, 2009.
- American Meteorological Society: *Glossary of Meteorology*, Second., American Meteorological Society., 2000.
- Ancellet, G., Pelon, J., Totems, J., Chazette, P., Bazureau, A., Sicard, M., Di Iorio, T., Dulac, F. and Mallet, M.: Long-range transport and mixing of aerosol sources during the 2013 North American biomass burning episode: Analysis of multiple lidar observations in the western Mediterranean basin, *Atmos. Chem. Phys.*, 16, 4725–4742, doi:10.5194/acp-16-4725-2016, 2016.
- Andreae, M. O.: Biomass burning: Its history, use and distribution and its impact on environmental quality and global climate, in *Global Biomass Burning: Atmospheric, Climatic and Biospheric Implication*, edited by J. S. Levine, pp. 3–21, MIT Press,

Cambridge, Mass., 1991.

- Andreae, M. O. and Rosenfeld, D.: Aerosol-cloud-precipitation interactions. Part 1. The nature and sources of cloud-active aerosols, *Earth-Science Rev.*, 89, 13–41, doi:10.1016/j.earscirev.2008.03.001, 2008.
- Ångström, A.: Techniques of Determining the Turbidity of the Atmosphere, *Tellus*, 13, 214–223, doi:10.1111/j.2153-3490.1961.tb00078.x, 1961.
- Ansmann, A., Riebesell, M. and Weitkamp, C.: Measurement of atmospheric aerosol extinction profiles with a Raman lidar, *Opt. Lett.*, doi:10.1364/OL.15.000746, 1990.
- Ansmann, A., Riebesell, M., Wandinger, U., Weitkamp, C., Voss, E., Lahmann, W. and Michaelis, W.: Combined raman elastic-backscatter LIDAR for vertical profiling of moisture, aerosol extinction, backscatter, and LIDAR ratio, *Appl. Phys. B Photophysics Laser Chem.*, doi:10.1007/BF00348608, 1992a.
- Ansmann, A., Wandinger, U., Riebesell, M., Weitkamp, C. and Michaelis, W.: Independent measurement of extinction and backscatter profiles in cirrus clouds by using a combined Raman elastic-backscatter lidar, *Appl. Opt.*, doi:10.1364/AO.31.007113, 1992b.
- Ansmann, A., Bösenberg, J., Chaikovsky, A., Comerón, A., Eckhardt, S., Eixmann, R., Freudenthaler, V., Ginoux, P., Komguem, L., Linné, H., Márquez, M. Á. L., Matthias, V., Mattis, I., Mitev, V., Müller, D., Music, S., Nickovic, S., Pelon, J., Sauvage, L., Sobolevsky, P., Srivastava, M. K., Stohl, A., Torres, O., Vaughan, G., Wandinger, U. and Wiegner, M.: Long-range transport of Saharan dust to northern Europe: The 11-16 October 2001 outbreak observed with EARLINET, *J. Geophys. Res. Atmos.*, 108(D24), 4783, doi:10.1029/2003jd003757, 2003.
- Ansmann, A., Baars, H., Chudnovsky, A., Mattis, I., Veselovskii, I., Haarig, M., Seifert, P., Engelmann, R. and Wandinger, U.: Extreme levels of Canadian wildfire smoke in the stratosphere over central Europe on 21-22 August 2017, *Atmos. Chem. Phys.*, 18, 11831–11845, doi:10.5194/acp-18-11831-2018, 2018.
- Antuña-Marrero, J. C., Landulfo, E., Estevan, R., Barja, B., Robock, A., Wolfram, E., Ristori, P., Clemesha, B., Zaratti, F., Forno, R., Armandillo, E., Bastidas, Á. E., De Frutos Baraja, Á. M.,

- Whiteman, D. N., Quel, E., Barbosa, H. M. J., Lopes, F., Montilla-Rosero, E. and Guerrero-Rascado, J. L.: LALINET: The first Latin American-born regional atmospheric observational network, *Bull. Am. Meteorol. Soc.*, doi:10.1175/BAMS-D-15-00228.1, 2017.
- de Arruda Moreira, G., Guerrero-Rascado, J. L., Benavent-Oltra, J. A., Ortiz-Amezcuca, P., Román, R., Esteban Bedoya-Velásquez, A., Bravo-Aranda, J. A., Olmo-Reyes, F. J., Landulfo, E. and Alados-Arboledas, L.: Analyzing the turbulence in the Planetary Boundary Layer by the synergic use of remote sensing systems: Doppler wind lidar and aerosol elastic lidar, *Atmos. Chem. Phys. Discuss.*, doi:10.5194/acp-2018-276, 2018a.
- de Arruda Moreira, G., Guerrero-Rascado, J. L., Bravo-Aranda, J. A., Benavent-Oltra, J. A., Ortiz-Amezcuca, P., Róman, R., Bedoya-Velásquez, A. E., Landulfo, E. and Alados-Arboledas, L.: Study of the planetary boundary layer by microwave radiometer, elastic lidar and Doppler lidar estimations in Southern Iberian Peninsula, *Atmos. Res.*, 213, 185–195, doi:10.1016/J.ATMOSRES.2018.06.007, 2018b.
- Arshinov, Y., Bobrovnikov, S., Serikov, I., Ansmann, A., Wandinger, U., Althausen, D., Mattis, I. and Müller, D.: Daytime operation of a pure rotational Raman lidar by use of a Fabry–Perot interferometer, *Appl. Opt.*, doi:10.1364/ao.44.003593, 2005.
- Arya, S. P.: Atmospheric boundary layer and its parameterization, in *Wind Climate in Cities*, edited by J. E. Cermak, pp. 41–66, Kluwer, Dordrecht., 1995.
- Atmosphere, U. S. C. on E. to the S.: U.S. Standard Atmosphere, National Oceanic and Atmospheric Administration, Washington DC., 1976.
- Atmospheric Research and Technology LLC: Vector vs. Scalar Averaging of Wind Data, [online] Available from: http://www.sodar.com/FYI/vector_vs_scalar.html, 2013.
- Baars, H., Ansmann, A., Engelmann, R. and Althausen, D.: Continuous monitoring of the boundary-layer top with lidar, *Atmos. Chem. Phys.*, doi:10.5194/acp-8-7281-2008, 2008.
- Baars, H., Kanitz, T., Engelmann, R., Althausen, D., Heese, B., Komppula, M., Preißler, J., Tesche, M., Ansmann, A., Wandinger, U., Lim, J.-H., Young Ahn, J., Stachlewska, I. S., Amiridis, V., Marinou, E., Seifert, P., Hofer, J., Skupin, A., Schneider, F., Bohlmann, S., Foth, A., Bley, S., Pfüller, A.,

Giannakaki, E., Lihavainen, H., Viisanen, Y., Kumar Hooda, R., Pereira, S. N., Bortoli, D., Wagner, F., Mattis, I., Janicka, L., Markowicz, K. M., Achtert, P., Artaxo, P., Pauliquevis, T., Souza, R. A. F., Prakesh Sharma, V., Gideon Van Zyl, P., Paul Beukes, J., Sun, J., Rohwer, E. G., Deng, R., Mamouri, R.-E. and Zamorano, F.: An overview of the first decade of PollyNET: An emerging network of automated Raman-polarization lidars for continuous aerosol profiling, *Atmos. Chem. Phys.*, 16(8), 5111–5137, doi:10.5194/acp-16-5111-2016, 2016.

Baklanov, A. and Grisigono, B.: *Atmospheric boundary layers: Nature, theory and applications to environmental modelling and security*, Springer, New York., 2008.

Baklanov, A. A., Grisogono, B., Bornstein, R., Mahrt, L., Zilitinkevich, S. S., Taylor, P., Larsen, S. E., Rotach, M. W. and Fernando, H. J. S.: The nature, theory, and modeling of atmospheric planetary boundary layers, *Bull. Am. Meteorol. Soc.*, 92(2), 123–128, doi:10.1175/2010BAMS2797.1, 2011.

Barreto, A., Román, R., Cuevas, E., Pérez-Ramírez, D., Berjón, A. J., Kouremeti, N., Kazadzis, S., Gröbner, J., Mazzola, M., Toledano, C., Benavent-Oltra, J. A., Doppler, L., Juryšek, J., Almansa, A. F., Victori, S., Maupin, F., Guirado-Fuentes, C., González, R., Vitale, V., Goloub, P., Blarel, L., Alados-Arboledas, L., Woolliams, E., Taylor, S., Antuña, J. C. and Yela, M.: Evaluation of night-time aerosols measurements and lunar irradiance models in the frame of the first multi-instrument nocturnal intercomparison campaign, *Atmos. Environ.*, 202, 190–211, doi:10.1016/j.atmosenv.2019.01.006, 2019.

Barreto, Á., Cuevas, E., Granados-Muñoz, M. J., Alados-Arboledas, L., Romero, P. M., Gröbner, J., Kouremeti, N., Almansa, A. F., Stone, T., Toledano, C., Román, R., Sorokin, M., Holben, B., Canini, M. and Yela, M.: The new sun-sky-lunar Cimel CE318-T multiband photometer – A comprehensive performance evaluation, *Atmos. Meas. Tech.*, doi:10.5194/amt-9-631-2016, 2016.

Bauer, S., Bierwirth, E., Esselborn, M., Petzold, A., Macke, A., Trautmann, T. and Wendisch, M.: Airborne spectral radiation measurements to derive solar radiative forcing of Saharan dust mixed with biomass burning smoke particles, *Tellus, Ser. B Chem. Phys. Meteorol.*, doi:10.1111/j.1600-0889.2011.00567.x, 2011.

Bedoya-Velásquez, A. E., Navas-Guzmán, F., Granados-Muñoz, M. J.,

- Titos, G., Román, R., Andrés Casquero-Vera, J., Ortiz-Amezcuca, P., Antonio Benavent-Oltra, J., De Arruda Moreira, G., Montilla-Rosero, E., Hoyos, C. D., Artiñano, B., Coz, E., Olmo-Reyes, F. J., Alados-Arboledas, L. and Guerrero-Rascado, J. L.: Hygroscopic growth study in the framework of EARLINET during the SLOPE i campaign: Synergy of remote sensing and in situ instrumentation, *Atmos. Chem. Phys.*, doi:10.5194/acp-18-7001-2018, 2018.
- Bedoya-Velásquez, A. E., Navas-Guzmán, F., de Arruda Moreira, G., Román, R., Cazorla, A., Ortiz-Amezcuca, P., Benavent-Oltra, J. A., Alados-Arboledas, L., Olmo-Reyes, F. J., Foyo-Moreno, I., Montilla-Rosero, E., Hoyos, C. D. and Guerrero-Rascado, J. L.: Seasonal analysis of the atmosphere during five years by using microwave radiometry over a mid-latitude site, *Atmos. Res.*, doi:10.1016/j.atmosres.2018.11.014, 2019.
- Belegante, L., Antonio Bravo-Aranda, J., Freudenthaler, V., Nicolae, D., Nemuc, A., Ene, D., Alados-Arboledas, L., Amodeo, A., Pappalardo, G., D'Amico, G., Amato, F., Engelmann, R., Baars, H., Wandinger, U., Papayannis, A., Kokkalis, P. and Pereira, S. N.: Experimental techniques for the calibration of lidar depolarization channels in EARLINET, *Atmos. Meas. Tech.*, doi:10.5194/amt-11-1119-2018, 2018.
- Belsley, D. A., Kuh, E. and Welsch, R. E.: *Regression diagnostics: Identifying influential observations and sources of collinearity*, John Wiley and Sons, Hoboken, New Jersey., 1980.
- Benavent-Oltra, J. A.: *Synergetic use of active and passive remote sensing techniques to retrieve vertical profiles of atmospheric aerosol properties during day- and night-time*, University of Granada, Spain., 2019.
- Benavent-Oltra, J. A., Román, R., Granados-Munõz, M. J., Pérez-Ramírez, D., Ortiz-Amezcuca, P., Denjean, C., Lopatin, A., Lyamani, H., Torres, B., Guerrero-Rascado, J. L., Fuertes, D., Dubovik, O., Chaikovsky, A., Olmo, F. J., Mallet, M. and Alados-Arboledas, L.: Comparative assessment of GRASP algorithm for a dust event over Granada (Spain) during ChArMEx-ADRIMED 2013 campaign, *Atmos. Meas. Tech.*, doi:10.5194/amt-10-4439-2017, 2017.
- Boccippio, D. J.: A Diagnostic Analysis of the VVP Single-Doppler Retrieval Technique, *J. Atmos. Ocean. Technol.*, 12, 230–248, doi:10.1175/1520-0426(1995)012<0230:adaotv>2.0.co;2, 1995.

- Böckmann, C.: Hybrid regularization method for the ill-posed inversion of multiwavelength lidar data in the retrieval of aerosol size distributions, *Appl. Opt.*, doi:10.1364/ao.40.001329, 2001.
- Böckmann, C. and Kirsche, A.: Iterative regularization method for lidar remote sensing, *Comput. Phys. Commun.*, 174, 607–615, doi:10.1016/j.cpc.2005.12.019, 2006.
- Böckmann, C. and Osterloh, L.: Inversion of two-dimensional spheroidal particle distributions from backscatter, extinction and depolarization profiles via regularization, in *Ninth International Symposium on Tropospheric Profiling.*, 2012.
- Böckmann, C. and Osterloh, L.: Runge-Kutta type regularization method for inversion of spheroidal particle distribution from limited optical data, *Inverse Probl. Sci. Eng.*, doi:10.1080/17415977.2013.830615, 2014.
- Böckmann, C., Müller, D., Wandinger, U. and Ansmann, A.: Microphysical particle parameters from extinction and backscatter lidar data by inversion with regularization: simulation., *Appl. Opt.*, doi:10.1364/ao.40.001329, 2001.
- Böckmann, C., Mironova, I., Müller, D., Schneidenbach, L. and Nessler, R.: Microphysical aerosol parameters from multiwavelength lidar, *J. Opt. Soc. Am. A Opt. Image Sci. Vis.*, 22(3), 518–528, doi:10.1364/JOSAA.22.000518, 2005.
- Bohren, C. and Huffman, D.: *Absorption and Scattering of Light by Small Particles*, Wiley, New York., 1983.
- Bösenberg, J.: Ground-based differential absorption lidar for water-vapor and temperature profiling: methodology, *Appl. Opt.*, doi:10.1364/ao.37.003845, 1998.
- Bosque Maurel, J.: El clima de Granada, *Estud. Geográficos*, 20(74), 145–147, 1959.
- Boucher, O., Randall, D., Artaxo, P., Bretherton, C., Feingold, G., Forster, P., Kerminen, V.-M., Kondo, Y., Liao, H., Lohmann, U., Rasch, P., Satheesh, S. K., Sherwood, S., Stevens, B. and Zhang, X. Y.: Clouds and Aerosols, in *Climate Change 2013: The Physical Science Basis. Contribution of Working Group I to the Fifth Assessment Report of the Intergovernmental Panel on Climate Change*, edited by T. F. Stocker, D. Qin, G.-K. Plattner, M. Tignor, S. K. Allen, J. Boschung, A. Nauels, Y. Xia, V. Bex, and P. M. Midgley, pp. 571–657, Cambridge University Press,

- Cambridge, United Kingdom and New York, USA., 2013.
- Bragg, W. H. and Bragg, W. L.: The reflection of X-rays by crystals, in Proceedings of the Royal Society of London A., 1913.
- Brasseur, G. and Granier, C.: Mount Pinatubo aerosols, chlorofluorocarbons, and ozone depletion, *Science* (80-.), 257(5074), 1239–1242, doi:10.1126/science.257.5074.1239, 1992.
- Bravo-Aranda, J. A., Navas-Guzmán, F., Guerrero-Rascado, J. L., Pérez-Ramírez, D., Granados-Muñoz, M. J. and Alados-Arboledas, L.: Analysis of lidar depolarization calibration procedure and application to the atmospheric aerosol characterization, *Int. J. Remote Sens.*, doi:10.1080/01431161.2012.716546, 2013.
- Bravo-Aranda, J. A., Titos, G., Granados-Muñoz, M. J., Guerrero-Rascado, J. L., Navas-Guzmán, F., Valenzuela, A., Lyamani, H., Olmo, F. J., Andrey, J. and Alados-Arboledas, L.: Study of mineral dust entrainment in the planetary boundary layer by lidar depolarisation technique, *Tellus, Ser. B Chem. Phys. Meteorol.*, doi:10.3402/tellusb.v67.26180, 2015.
- Bravo-Aranda, J. A., Kotthaus, S., Coen, M. C., Haeffelin, M., Cimini, D., O’connor, E. J., Hervo, M., Guerrero-Rascado, J. L., Costa, M. J. and Schween, J. H.: Review of the atmospheric boundary layer structure, *Prep.*, 2019.
- Browning, K. A. and Wexler, R.: The Determination of Kinematic Properties of a Wind Field Using Doppler Radar, *J. Appl. Meteorol.*, 7, 105–113, doi:10.1175/1520-0450(1968)007<0105:tdokpo>2.0.co;2, 1968.
- Cairo, F., Di Donfrancesco, G., Adriani, A., Pulvirenti, L. and Fierli, F.: Comparison of various linear depolarization parameters measured by lidar, *Appl. Opt.*, 38(21), 4425–4432, doi:10.1364/ao.38.004425, 1999.
- Cariñanos, P., Casares-Porcel, M. and Quesada-Rubio, J. M.: Estimating the allergenic potential of urban green spaces: A case-study in Granada, Spain, *Landsc. Urban Plan.*, doi:10.1016/j.landurbplan.2013.12.009, 2014.
- Cariñanos, P., Adinolfi, C., Díaz de la Guardia, C., De Linares, C. and Casares-Porcel, M.: Characterization of Allergen Emission Sources in Urban Areas, *J. Environ. Qual.*, 45(1), 244–52, doi:10.2134/jeq2015.02.0075, 2016.

- Cazorla, A., Andrés Casquero-Vera, J., Román, R., Luis Guerrero-Rascado, J., Toledano, C., Cachorro, V. E., Orza, J. A. G., Cancillo, M. L., Serrano, A., Titos, G., Pandolfi, M., Alastuey, A., Hanrieder, N. and Alados-Arboledas, L.: Near-real-time processing of a ceilometer network assisted with sun-photometer data: Monitoring a dust outbreak over the Iberian Peninsula, *Atmos. Chem. Phys.*, doi:10.5194/acp-17-11861-2017, 2017.
- Chaikovsky, A., Dubovik, O., Holben, B., Bril, A., Goloub, P., Tanré, D., Pappalardo, G., Wandinger, U., Chaikovskaya, L., Denisov, S., Grudo, J., Lopatin, A., Karol, Y., Lapyonok, T., Amiridis, V., Ansmann, A., Apituley, A., Allados-Arboledas, L., Biniotoglou, I., Boselli, A., D'Amico, G., Freudenthaler, V., Giles, D., Granados-Muñoz, M. J., Kokkalis, P., Nicolae, D., Oshchepkov, S., Papayannis, A., Rita Perrone, M., Pietruczuk, A., Rocadenbosch, F., Sicard, M., Slutsker, I., Talianu, C., De Tomasi, F., Tsekeri, A., Wagner, J. and Wang, X.: Lidar-Radiometer Inversion Code (LIRIC) for the retrieval of vertical aerosol properties from combined lidar/radiometer data: Development and distribution in EARLINET, *Atmos. Meas. Tech.*, 9, 1181–1205, doi:10.5194/amt-9-1181-2016, 2016.
- Chamizo, S., Serrano-Ortiz, P., López-Ballesteros, A., Sánchez-Cañete, E. P., Vicente-Vicente, J. L. and Kowalski, A. S.: Net ecosystem CO₂ exchange in an irrigated olive orchard of SE Spain: Influence of weed cover, *Agric. Ecosyst. Environ.*, 239, 51–64, doi:10.1016/j.agee.2017.01.016, 2017.
- Chen, H., Chen, S., Zhang, Y., Guo, P., Chen, H. and Chen, B.: Robust calibration method for pure rotational Raman lidar temperature measurement, *Opt. Express*, doi:10.1364/oe.23.021232, 2015.
- Chojnicki, B. H., Urbaniak, M., Józefczyk, D., Augustin, J. and Olejnik, J.: Measurements of gas and heat fluxes at Rzecin wetland, in *Wetlands: Monitoring, Modeling and Management*, edited by T. Okruszko, E. Malby, J. Szatyłowicz, D. Swiatek, and W. Kotowski, pp. 125–131, Taylor & Francis, London, England., 2007.
- Compaan, A., Wagoner, A. and Aydinli, A.: Rotational Raman scattering in the instructional laboratory, *Am. J. Phys.*, doi:10.1080/09692299408434272, 1994.
- Córdoba-Jabonero, C., Sorribas, M., Guerrero-Rascado, J. L., Adame, J. A., Hernández, Y., Lyamani, H., Cachorro, V., Gil, M.,

- Alados-Arboledas, L., Cuevas, E. and De La Morena, B.: Synergetic monitoring of Saharan dust plumes and potential impact on surface: A case study of dust transport from Canary Islands to Iberian Peninsula, *Atmos. Chem. Phys.*, doi:10.5194/acp-11-3067-2011, 2011.
- David, R. and Holmgren, P.: *Global Ecological Zoning for TheGlobal Forest Resources Assessment 2000, Final Report*, Food and Agriculture Organization of the United Nations, Forestry Department, Rome., 2001.
- Denjean, C., Cassola, F., Mazzino, A., Triquet, S., Chevaillier, S., Grand, N., Bourriane, T., Momboisse, G., Sellegri, K., Schwarzenbock, A., Freney, E., Mallet, M. and Formenti, P.: Size distribution and optical properties of mineral dust aerosols transported in the western Mediterranean, *Atmos. Chem. Phys.*, doi:10.5194/acp-16-1081-2016, 2016.
- Deuflhard, P. and Hohmann, A.: *Numerical Analysis in Modern Scientific Computing. An Introduction*, Springer, New York., 2003.
- Draxler, R., Stunder, B., Rolph, G., Stein, A. and Taylor, A.: *HYSPLIT4 users guide, Hysplit4 User's Guid. Version 4.9*, 2009.
- Dubovik, O. and King, M. D.: A flexible inversion algorithm for retrieval of aerosol optical properties from Sun and sky radiance measurements, *J. Geophys. Res. Atmos.*, doi:10.1029/2000JD900282, 2000.
- Dubovik, O., Smirnov, A., Holben, B. N., King, M. D., Kaufman, Y. J., Eck, T. F. and Slutsker, I.: Accuracy assessments of aerosol optical properties retrieved from Aerosol Robotic Network (AERONET) Sun and sky radiance measurements, *J. Geophys. Res. Atmos.*, doi:10.1029/2000JD900040, 2000.
- Dubovik, O., Holben, B. N., Lapyonok, T., Sinyuk, A., Mishchenko, M. I., Yang, P. and Slutsker, I.: Non-spherical aerosol retrieval method employing light scattering by spheroids, *Geophys. Res. Lett.*, 29(10), doi:10.1029/2001GL014506, 2002a.
- Dubovik, O., Holben, B., Eck, T. F., Smirnov, A., Kaufman, Y. J., King, M. D., Tanré, D. and Slutsker, I.: Variability of Absorption and Optical Properties of Key Aerosol Types Observed in Worldwide Locations, *J. Atmos. Sci.*, doi:10.1175/1520-0469(2002)059<0590:VOAAOP>2.0.CO;2, 2002b.
- Dubovik, O., Sinyuk, A., Lapyonok, T., Holben, B. N., Mishchenko,

- M., Yang, P., Eck, T. F., Volten, H., Muñoz, O., Veihelmann, B., van der Zande, W. J., Leon, J. F., Sorokin, M. and Slutsker, I.: Application of spheroid models to account for aerosol particle nonsphericity in remote sensing of desert dust, *J. Geophys. Res. Atmos.*, 111(D11), doi:10.1029/2005JD006619, 2006.
- Dubovik, O., Lapyonok, T., Litvinov, P., Herman, M., Fuertes, D., Ducos, F., Torres, B., Derimian, Y., Huang, X., Lopatin, A., Chaikovsky, A., Aspetsberger, M. and Federspiel, C.: GRASP: a versatile algorithm for characterizing the atmosphere, *SPIE Newsroom*, 25, doi:10.1117/2.1201408.005558, 2014.
- Eck, T. F., Holben, B. N., Reid, J. S., Sinyuk, A., Hyer, E. J., O'Neill, N. T., Shaw, G. E., Vande Castle, J. R., Chapin, F. S., Dubovik, O., Smirnov, A., Vermote, E., Schafer, J. S., Giles, D., Slutsker, I., Sorokine, M. and Newcomb, W. W.: Optical properties of boreal region biomass burning aerosols in central Alaska and seasonal variation of aerosol optical depth at an Arctic coastal site, *J. Geophys. Res. Atmos.*, 114(11), doi:10.1029/2008JD010870, 2009.
- Elachi, C.: Introduction to the Physics and Techniques of Remote Sensing, edited by J. A. Kong, John Wiley & Sons., 1987.
- Emeis, S.: Analytical Description and Vertical Structure of the Atmospheric Boundary Layer, in *Surface-Based Remote Sensing of the Atmospheric Boundary Layer*, pp. 9–32, Springer, Dordrecht., 2011.
- Engelmann, R., Wandinger, U., Ansmann, A., Müller, D., Žeromskis, E., Althausen, D. and Wehner, B.: Lidar observations of the vertical aerosol flux in the planetary boundary layer, *J. Atmos. Ocean. Technol.*, 25, 1296–1306, doi:10.1175/2007JTECHA967.1, 2008.
- Engelmann, R., Kanitz, T., Baars, H., Heese, B., Althausen, D., Skupin, A., Wandinger, U., Komppula, M., Stachlewska, I. S., Amiridis, V., Marinou, E., Mattis, I., Linné, H. and Ansmann, A.: The automated multiwavelength Raman polarization and water-vapor lidar Polly<sup>XT&/sup>: the neXT generation, *Atmos. Meas. Tech.*, 9(4), 1767–1784, doi:10.5194/amt-9-1767-2016, 2016.
- Etminan, M., Myhre, G., Highwood, E. J. and Shine, K. P.: Radiative forcing of carbon dioxide, methane, and nitrous oxide: A significant revision of the methane radiative forcing, *Geophys.*

- Res. Lett., 43(24), 12614–12623, doi:10.1002/2016GL071930, 2016.
- Fernald, F. G.: Analysis of atmospheric lidar observations: some comments, *Appl. Opt.*, doi:10.1364/AO.23.000652, 1984.
- Fernald, F. G., Herman, B. M. and Reagan, J. A.: Determination of Aerosol Height Distributions by Lidar, *J. Appl. Meteorol.*, 11, 482–489, doi:10.1175/1520-0450(1972)011<0482:doahdb>2.0.co;2, 1972.
- Fiebig, M., Stohl, A., Wendisch, M., Eckhardt, S. and Petzold, A.: Dependence of solar radiative forcing of forest fire aerosol on ageing and state of mixture, *Atmos. Chem. Phys.*, 3, 881–891, doi:10.5194/acp-3-881-2003, 2003.
- Flamant, C., Pelon, J., Flamant, P. H. and Durand, P.: Lidar determination of the entrainment zone thickness at the top of the unstable marine atmospheric boundary layer, *Boundary-Layer Meteorol.*, 83(2), 247–284, doi:10.1023/A:1000258318944, 1997.
- Frehlich, R.: Performance of maximum likelihood estimators of mean power and doppler velocity with a priori knowledge of spectral width, *J. Atmos. Ocean. Technol.*, 1999.
- Freudenthaler, V.: About the effects of polarising optics on lidar signals and the $\Delta 90$ calibration, *Atmos. Meas. Tech.*, doi:10.5194/amt-9-4181-2016, 2016.
- Freudenthaler, V., Esselborn, M., Wiegner, M., Heese, B., Tesche, M., Ansmann, A., Müller, D., Althausen, D., Wirth, M., Fix, A., Ehret, G., Knippertz, P., Toledano, C., Gasteiger, J., Garhammer, M. and Seefeldner, M.: Depolarization ratio profiling at several wavelengths in pure Saharan dust during SAMUM 2006, *Tellus, Ser. B Chem. Phys. Meteorol.*, doi:10.1111/j.1600-0889.2008.00396.x, 2009.
- Freudenthaler, V., Linné, H., Chaikovski, A., Rabus, D. and Groß, S.: EARLINET lidar quality assurance tools, *Atmos. Meas. Tech. Discuss.*, doi:10.5194/amt-2017-395, 2018.
- Fromm, M. D. and Servranckx, R.: Transport of forest fire smoke above the tropopause by supercell convection, *Geophys. Res. Lett.*, 30, 1542, doi:10.1029/2002GL016820, 2003.
- Galerkin, B. G.: Expansions in stability problems for elastic rods and plates, in *Vestnik inzhenorov* 19, pp. 897–908., 1915.

- Garrat, J. R.: The atmospheric boundary layer, edited by J. T. Houghton, M. J. Rycroft, and A. J. Dessler, Cambridge University Press., 1992.
- Geer, I. W., Ed.: Glossary of Weather and Climate, American Meteorological Society., 1996.
- Giannakaki, E., Van Zyl, P. G., Müller, D., Balis, D. and Komppula, M.: Optical and microphysical characterization of aerosol layers over South Africa by means of multi-wavelength depolarization and Raman lidar measurements, *Atmos. Chem. Phys.*, doi:10.5194/acp-16-8109-2016, 2016.
- Di Girolamo, P., Marchese, R., Whiteman, D. N. and Demoz, B. B.: Rotational Raman Lidar measurements of atmospheric temperature in the UV, *Geophys. Res. Lett.*, doi:10.1029/2003GL018342, 2004.
- Di Girolamo, P., Behrendt, A. and Wulfmeyer, V.: Spaceborne profiling of atmospheric temperature and particle extinction with pure rotational Raman lidar and of relative humidity in combination with differential absorption lidar: performance simulations--erratum, *Appl. Opt.*, doi:10.1364/ao.45.004909, 2006.
- Goldsmith, J. E. M., Blair, F. H., Bisson, S. E. and Turner, D. D.: Turn-key Raman lidar for profiling atmospheric water vapor, clouds, and aerosols, *Appl. Opt.*, doi:10.1364/ao.37.004979, 1998.
- Granados-Muñoz, M. J., Navas-Guzmán, F., Bravo-Aranda, J. A., Guerrero-Rascado, J. L., Lyamani, H., Fernández-Gálvez, J. and Alados-Arboledas, L.: Automatic determination of the planetary boundary layer height using lidar: One-year analysis over southeastern Spain, *J. Geophys. Res. Atmos.*, doi:10.1029/2012JD017524, 2012.
- Granados-Muñoz, M. J., Guerrero-Rascado, J. L., Bravo-Aranda, J. A., Navas-Guzmán, F., Valenzuela, A., Lyamani, H., Chaikovsky, A., Wandinger, U., Ansmann, A., Dubovik, O., Grudo, J. O. and Alados-Arboledas, L.: Retrieving aerosol microphysical properties by Lidar-Radiometer Inversion Code (LIRIC) for different aerosol types, *J. Geophys. Res.*, 119(8), 4836–4858, doi:10.1002/2013JD021116, 2014.
- Granados-Muñoz, M. J., Navas-Guzmán, F., Bravo-Aranda, J. A., Guerrero-Rascado, J. L., Lyamani, H., Valenzuela, A., Titos, G., Fernández-Gálvez, J. and Alados-Arboledas, L.: Hygroscopic

- growth of atmospheric aerosol particles based on active remote sensing and radiosounding measurements: Selected cases in southeastern Spain, *Atmos. Meas. Tech.*, 8, 705–718, doi:10.5194/amt-8-705-2015, 2015.
- Granados-Muñoz, M. J., Bravo-Aranda, J. A., Baumgardner, D., Guerrero-Rascado, J. L., Pérez-Ramírez, D., Navas-Guzmán, F., Veselovskii, I., Lyamani, H., Valenzuela, A., Olmo, F. J., Titos, G., Andrey, J., Chaikovsky, A., Dubovik, O., Gil-Ojeda, M. and Alados-Arboledas, L.: A comparative study of aerosol microphysical properties retrieved from ground-based remote sensing and aircraft in situ measurements during a Saharan dust event, *Atmos. Meas. Tech.*, 9(3), 1113–1133, doi:10.5194/amt-9-1113-2016, 2016.
- Grange, S. K.: Technical note: Averaging wind speeds and directions., 2014.
- Grieshop, A. P., Logue, J. M., Donahue, N. M. and Robinson, A. L.: Laboratory investigation of photochemical oxidation of organic aerosol from wood fires 1: Measurement and simulation of organic aerosol evolution, *Atmos. Chem. Phys.*, 9, 1263–1277, doi:10.5194/acp-9-1263-2009, 2009a.
- Grieshop, A. P., Donahue, N. M. and Robinson, A. L.: Laboratory investigation of photochemical oxidation of organic aerosol from wood fires 2: Analysis of aerosol mass spectrometer data, *Atmos. Chem. Phys.*, 9, 2227–2240, doi:10.5194/acp-9-2227-2009, 2009b.
- Grund, C. J., Banta, R. M., George, J. L., Howell, J. N., Post, M. J., Richer, R. A. and Weickmann, A. M.: High-resolution doppler lidar for boundary layer and cloud research, *J. Atmos. Ocean. Technol.*, doi:10.1175/1520-0426(2001)018<0376:HRDLFB>2.0.CO;2, 2001.
- Guerrero-Rascado, J. L., Ruiz, B. and Alados-Arboledas, L.: Multi-spectral Lidar characterization of the vertical structure of Saharan dust aerosol over southern Spain, *Atmos. Environ.*, doi:10.1016/j.atmosenv.2007.12.062, 2008.
- Guerrero-Rascado, J. L., Olmo, F. J., Avilés-Rodríguez, I., Navas-Guzmán, F., Pérez-Ramírez, D., Lyamani, H. and Arboledas, L. A.: Extreme saharan dust event over the southern iberian peninsula in september 2007: Active and passive remote sensing from surface and satellite, *Atmos. Chem. Phys.*, doi:10.5194/acp-9-8453-2009, 2009.

- Guerrero-Rascado, J. L., Olmo, F. J., Molero, F., Navas-Guzmán, F., Costa, M. J., Silva, A. M., Pujadas, M., Sicard, M. and Alados-Arboledas, L.: Aerosol direct radiative effects of a transatlantic biomass burning plume over Granada, Spain, in IV Reunión Española de Ciencia y Tecnología del Aerosol-RECTA, pp. C7-1-C7-6., 2010a.
- Guerrero-Rascado, J. L., Costa, M. J., Bortoli, D., Silva, A. M., Lyamani, H. and Alados-Arboledas, L.: Infrared lidar overlap function: an experimental determination, *Opt. Express*, 18(19), 20350–20359, doi:10.1364/oe.18.020350, 2010b.
- Guerrero-Rascado, J. L., Olmo, F. J., Molero, F., Navas-Guzmán, F., Costa, M. J., Silva, A. M., Pujadas, M., Sicard, M. and Alados-Arboledas, L.: Characterization of atmospheric aerosols for a long-range transport of biomass-burning from North America over the Iberian Peninsula, in Proceedings of the 25th International Laser Radar Conference, pp. 580–583., 2011a.
- Guerrero-Rascado, J. L., Müller, D., Navas-Guzmán, F., Pérezramírez, D. and Alados-Arboledas, L.: First results of aerosol microphysical properties by 3+2 raman lidar at earlinet granada station, *Rom. Reports Phys.*, 56, 467–474, 2011b.
- Guerrero-Rascado, J. L., Navas-Guzmán, F., Díaz, J. A., Bravo-Aranda, J. A. and Alados-Arboledas, L.: Quality assurance at the EARLINET Granada station: Characterization of the optical subsystem for a multichannel Raman lidar, *Óptica Pura y Apl.*, 44, 19–23, 2011c.
- Guerrero-Rascado, J. L., Landulfo, E., Antuña, J. C., de Melo Jorge Barbosa, H., Barja, B., Bastidas, Á. E., Bedoya, A. E., da Costa, R. F., Estevan, R., Forno, R., Gouveia, D. A., Jiménez, C., Larroza, E. G., da Silva Lopes, F. J., Montilla-Rosero, E., de Arruda Moreira, G., Nakaema, W. M., Nisperuza, D., Alegria, D., Múnera, M., Otero, L., Papandrea, S., Pallota, J. V., Pawelko, E., Quel, E. J., Ristori, P., Rodrigues, P. F., Salvador, J., Sánchez, M. F. and Silva, A.: Latin American Lidar Network (LALINET) for aerosol research: Diagnosis on network instrumentation, *J. Atmos. Solar-Terrestrial Phys.*, doi:10.1016/j.jastp.2016.01.001, 2016.
- Haarig, M., Engelmann, R., Ansmann, A., Veselovskii, I., Whiteman, D. N. and Althausen, D.: 1064nm rotational Raman lidar for particle extinction and lidar-ratio profiling: Cirrus case study, *Atmos. Meas. Tech.*, doi:10.5194/amt-9-4269-2016, 2016.

- Haarig, M., Ansmann, A., Baars, H., Jimenez, C., Veselovskii, I., Engelmann, R. and Althausen, D.: Extreme levels of Canadian wildfire smoke in the stratosphere over central Europe – Part 2: Lidar study of depolarization and lidar ratios at 355, 532, and 1064 nm and of microphysical properties, *Atmos. Chem. Phys. Discuss.*, 18, 11847–11861, doi:10.5194/acp-2018-358, 2018.
- Hadamard, J.: *Lectures on the Cauchy Problem in Linear Partial Differential Equations*, Yale University Press, New Haven., 1923.
- Hallquist, M., Wenger, J. C., Baltensperger, U., Rudich, Y., Simpson, D., Claeys, M., Dommen, J., Donahue, N. M., George, C., Goldstein, A. H., Hamilton, J. F., Herrmann, H., Hoffmann, T., Iinuma, Y., Jang, M., Jenkin, M. E., Jimenez, J. L., Kiendler-Scharr, A., Maenhaut, W., McFiggans, G., Mentel, T. F., Monod, A., Prévôt, A. S. H., Seinfeld, J. H., Surratt, J. D., Szmigielski, R. and Wildt, J.: The formation, properties and impact of secondary organic aerosol: Current and emerging issues, *Atmos. Chem. Phys.*, 9, 5155–5236, doi:10.5194/acp-9-5155-2009, 2009.
- Hamamatsu, P.: *Photon Counting Using Photomultiplier Tubes*, Japan., 2005.
- Hansen, P. C.: *Discrete Inverse Problems, Insight and Algorithms*, SIAM., 2010.
- Harenda, K. M., Poczta, P., Szczepanik, D., Wang, D., Stachlewska, I. S. and Chojnicki, B. H.: Strategy for Multidimensional Peatland Ecosystem Analysis in the Context of the Atmospheric Properties, ITM Web Conf., 23, doi:10.1051/itmconf/20182300014, 2018.
- Harvey, N. J., Hogan, R. J. and Dacre, H. F.: A method to diagnose boundary-layer type using doppler lidar, *Q. J. R. Meteorol. Soc.*, 139, 1681–1693, doi:10.1002/qj.2068, 2013.
- Haywood, J. and Boucher, O.: Estimates of the direct and indirect radiative forcing due to tropospheric aerosols: A review, *Rev. Geophys.*, doi:10.1029/1999RG000078, 2000.
- Haywood, J. and Schulz, M.: Causes of the reduction in uncertainty in the anthropogenic radiative forcing of climate between IPCC (2001) and IPCC (2007), *Geophys. Res. Lett.*, 34, L20701, 2007.

- Hill, C.: Coherent focused lidars for Doppler sensing of aerosols and wind, *Remote Sens.*, doi:10.3390/rs10030466, 2018.
- Hobbs, P. V.: Direct Radiative Forcing by Smoke from Biomass Burning, *Science* (80-.), 275, 1776–1778, doi:10.1126/science.275.5307.1777, 1997.
- Hogan, R. J., Grant, A. L. M., Illingworth, A. J., Pearson, G. N. and O'Connor, E. J.: Vertical velocity variance and skewness in clear and cloud-topped boundary layers as revealed by Doppler lidar, *Q. J. R. Meteorol. Soc.*, 135, 635–643, doi:10.1002/qj.413, 2009.
- Holben, B. N., Eck, T. F., Slutsker, I., Tanré, D., Buis, J. P., Setzer, A., Vermote, E., Reagan, J. A., Kaufman, Y. J., Nakajima, T., Lavenu, F., Jankowiak, I. and Smirnov, A.: AERONET - A federated instrument network and data archive for aerosol characterization, *Remote Sens. Environ.*, doi:10.1016/S0034-4257(98)00031-5, 1998.
- Holben, B. N., Eck, T. F., Slutsker, I., Smirnov, A., Sinyuk, A., Schafer, J., Giles, D. and Dubovik, O.: Aeronet's Version 2.0 quality assurance criteria, in *Remote Sensing of the Atmosphere and Clouds.*, 2006.
- Holton, J. R.: *An Introduction to Dynamic Meteorology*, 3rd Editio., Academic Press, San Diego., 1992.
- Horvath, H.: Influence of atmospheric aerosols on the radiation balance, in *Atmospheric particles*, edited by R. M. Harrison and R. van Grieken, John Wiley & Sons., 1998.
- Horvath, H., Alados Arboledas, L. and Olmo Reyes, F. J.: Angular scattering of the Sahara dust aerosol, *Atmos. Chem. Phys.*, 18(23), 17735–17744, doi:10.5194/acp-18-17735-2018, 2018.
- ICAO: *Manual on Low-level Wind Shear*, . Doc 9817 AN/449, 2005.
- Illingworth, A. J., Hogan, R. J., O'Connor, E. J., Bouniol, D., Brooks, M. E., Delanoë, J., Donovan, D. P., Eastment, J. D., Gaussiat, N., Goddard, J. W. F., Haefelin, M., Klein Baltinik, H., Krasnov, O. A., Pelon, J., Piriou, J. M., Protat, A., Russchenberg, H. W. J., Seifert, A., Tompkins, A. M., van Zadelhoff, G. J., Vinit, F., Willen, U., Wilson, D. R. and Wrench, C. L.: Cloudnet: Continuous evaluation of cloud profiles in seven operational models using ground-based observations, *Bull. Am. Meteorol. Soc.*, doi:10.1175/BAMS-88-6-883, 2007.
- Inaba, H.: Detection of atoms and molecules by Raman scattering

- and resonance fluorescence, in *Laser Monitoring of the Atmosphere*, edited by E. D. Hinkley, pp. 153–232, Springer-Verlag, Beling., 1976.
- IPCC: Global Warming of 1.5 °C - SR15. [online] Available from: <https://www.ipcc.ch/sr15/>, 2018.
- Jacobson, M. Z.: Strong radiative heating due to the mixing state of black carbon in atmospheric aerosols, *Nature*, doi:10.1038/35055518, 2001.
- Janicka, L. and Stachlewska, I. S.: Properties of biomass burning aerosol mixtures derived at fine temporal and spatial scales from Raman lidar measurements: Part I optical properties, *Atmos. Chem. Phys. Discuss.*, doi:10.5194/acp-2019-207, 2019.
- Janicka, L., Stachlewska, I. S., Veselovskii, I. and Baars, H.: Temporal variations in optical and microphysical properties of mineral dust and biomass burning aerosol derived from daytime Raman lidar observations over Warsaw, Poland, *Atmos. Environ.*, 169, 162–174, doi:10.1016/j.atmosenv.2017.09.022, 2017.
- Jost, H. J., Drdla, K., Stohl, A., Pfister, L., Loewenstein, M., Lopez, J. P., Hudson, P. K., Murphy, D. M., Cziczo, D. J., Fromm, M., Bui, T. P., Dean-Day, J., Gerbig, C., Mahoney, M. J., Richard, E. C., Spichtinger, N., Pittman, J. V., Weinstock, E. M., Wilson, J. C. and Xueref, I.: In-situ observations of mid-latitude forest fire plumes deep in the stratosphere, *Geophys. Res. Lett.*, 31, L11101, doi:10.1029/2003GL019253, 2004.
- Kahnert, M. and Kylling, A.: Radiance and flux simulations for mineral dust aerosols: Assessing the error due to using spherical or spheroidal model particles, *J. Geophys. Res. D Atmos.*, 109(D9), 2156–2202, doi:10.1029/2003JD004318, 2004.
- Kandler, K., Schütz, L., Deutscher, C., Ebert, M., Hofmann, H., Jäckel, S., Jaenicke, R., Knippertz, P., Lieke, K., Massling, A., Petzold, A., Schladitz, A., Weinzierl, B., Wiedensohler, A., Zorn, S. and Weinbruch, S.: Size distribution, mass concentration, chemical and mineralogical composition and derived optical parameters of the boundary layer aerosol at Tinfou, Morocco, during SAMUM 2006, *Tellus, Ser. B Chem. Phys. Meteorol.*, 61(1), 32–50, doi:10.1111/j.1600-0889.2008.00385.x, 2009.
- Kieffer, H. H. and Stone, T. C.: *The Spectral Irradiance of the Moon*,

- Astron. J., doi:10.1086/430185, 2005.
- Kim, D. and Cha, H.: Rotational Raman Lidar: Design and Performance Test of Meteorological Parameters (Aerosol Backscattering Coefficients and Temperature), *J. Korean Phys. Soc.*, doi:10.3938/jkps.51.352, 2007.
- Kirsche, A. and Böckmann, C.: Padé iteration method for regularization, *Appl. Math. Comput.*, 180, 648–663, doi:10.1016/j.amc.2006.01.011, 2006.
- Kleiner, A., Talwalkar, A., Sarkar, P. and Jordan, M. I.: A scalable bootstrap for massive data, *J. R. Stat. Soc. Ser. B Stat. Methodol.*, 76(4), 795–816, doi:10.1111/rssb.12050, 2014.
- Klett, J. D.: Stable analytical inversion solution for processing lidar returns, *Appl. Opt.*, doi:10.1364/AO.20.000211, 1981.
- Kolgotin, A. and Müller, D.: Theory of inversion with two-dimensional regularization: profiles of microphysical particle properties derived from multiwavelength lidar measurements, *Appl. Opt.*, 47(25), 4472–4490, doi:10.1364/ao.47.004472, 2008.
- Kolmogorov, A. N.: The Local Structure of Turbulence in Incompressible Viscous Fluid for Very Large Reynolds' Numbers, *Dokl. Akad. Nauk SSSR*, 30, 301–305, 1941.
- Kovalev, V. A. and Eichinger, W. E.: *Elastic Lidar Theory, Practice, and Analysis Methods*, Wiley Interscience., 2004.
- Lappalainen, E.: General review on world peatland and peat resources, in *Global Peat Resources*, edited by E. Lappalainen, pp. 53–55, International Peat Society and Geological Survey of Finland, Jyska, Finland., 1996.
- Li, H., Yang, Y., Hu, X. M., Huang, Z., Wang, G., Zhang, B. and Zhang, T.: Evaluation of retrieval methods of daytime convective boundary layer height based on lidar data, *J. Geophys. Res.*, doi:10.1002/2016JD025620, 2017.
- Lindelöw, P.: *Fiber based coherent lidars for remote wind sensing*, Technical University of Denmark., 2008.
- Lohmann, U. and Feichter, J.: Global indirect aerosol effects: A review, *Atmos. Chem. Phys.*, 5, 715–737, 2005.
- Lopatin, A.: *Enhanced Remote Sensing of atmospheric aerosol by joint inversion of active and passive remote sensing observations*, University of Lille., 2013.

- Lothon, M., Lohou, F., Pino, D., Couvreux, F., Pardyjak, E. R., Reuder, J., Vilà-Guerau De Arellano, J., Durand, P., Hartogensis, O., Legain, D., Augustin, P., Gioli, B., Lenschow, D. H., Faloon, I., Yagüe, C., Alexander, D. C., Angevine, W. M., Bargain, E., Barrié, J., Bazile, E., Bezombes, Y., Blay-Carreras, E., Van De Boer, A., Boichard, J. L., Bourdon, A., Butet, A., Campistron, B., De Coster, O., Cuxart, J., Dabas, A., Darbieu, C., Deboudt, K., Delbarre, H., Derrien, S., Flament, P., Fourmentin, M., Garai, A., Gibert, F., Graf, A., Groebner, J., Guichard, F., Jiménez, M. A., Jonassen, M., Van Den Kroonenberg, A., Magliulo, V., Martin, S., Martinez, D., Mastrorillo, L., Moene, A. F., Molinos, F., Moulin, E., Pietersen, H. P., Piguet, B., Pique, E., Román-Cascón, C., Rufin-Soler, C., Saïd, F., Sastre-Marugán, M., Seity, Y., Steeneveld, G. J., Toscano, P., Traullé, O., Tzanos, D., Wacker, S., Wildmann, N. and Zaldei, A.: The BLLAST field experiment: Boundary-Layer late afternoon and sunset turbulence, *Atmos. Chem. Phys.*, 14(10), 931–960, doi:10.5194/acp-14-10931-2014, 2014.
- Lyamani, H., Olmo, F. J. and Alados-Arboledas, L.: Physical and optical properties of aerosols over an urban location in Spain: Seasonal and diurnal variability, *Atmos. Chem. Phys.*, doi:10.5194/acp-10-239-2010, 2010.
- Lyamani, H., Fernández-Gálvez, J., Pérez-Ramírez, D., Valenzuela, A., Antón, M., Alados, I., Titos, G., Olmo, F. J. and Alados-Arboledas, L.: Aerosol properties over two urban sites in South Spain during an extended stagnation episode in winter season, *Atmos. Environ.*, 62, 424–432, doi:10.1016/j.atmosenv.2012.08.050, 2012.
- Malm, W. C.: Introduction to Visibility (Classic Reprint), Fb&c Limited. [online] Available from: <https://books.google.es/books?id=0thUswEACAAJ>, 2017.
- Mandija, F., Guerrero-Rascado, J. L., Lyamani, H., Granados-Muñoz, M. J. and Alados-Arboledas, L.: Synergic estimation of columnar integrated aerosol properties and their vertical resolved profiles in respect to the scenarios of dust intrusions over Granada, *Atmos. Environ.*, 145, 439–454, doi:10.1016/j.atmosenv.2016.09.045, 2016.
- Mandija, F., Sicard, M., Comerón, A., Alados-Arboledas, L., Guerrero-Rascado, J. L., Bravo-Aranda, J. A., Bravo-Aranda, J. A., Granados-Muñoz, M. J., Lyamani, H., Muñoz Porcar, C., Rocadenbosch, F., Rodríguez, A., Valenzuela, A. and García

- Vizcaíno, D.: Origin and pathways of the mineral dust transport to two Spanish EARLINET sites: Effect on the observed columnar and range-resolved dust optical properties, *Atmos. Res.*, 187, 69–83, doi:10.1016/j.atmosres.2016.12.002, 2017.
- Manninen, A. J.: Developing methods for Doppler lidar to investigate atmospheric boundary layer, University of Helsinki. [online] Available from: urn:ISBN:978-952-7276-19-8, 2019a.
- Manninen, A. J.: Halo lidar toolbox, Github [online] Available from: https://github.com/manninenaj/HALO_lidar_toolbox (Accessed 1 March 2019b), 2019.
- Manninen, A. J., O’Connor, E. J., Vakkari, V. and Petäjä, T.: A generalised background correction algorithm for a Halo Doppler lidar and its application to data from Finland, *Atmos. Meas. Tech.*, doi:10.5194/amt-9-817-2016, 2016.
- Manninen, A. J., Marke, T., Tuononen, M. and O’Connor, E. J.: Atmospheric Boundary Layer Classification With Doppler Lidar, *J. Geophys. Res. Atmos.*, 123, 8172–8189, doi:10.1029/2017JD028169, 2018.
- Mardia, K. V.: Statistics of Directional Data, *J. R. Stat. Soc. Ser. B Stat. Methodol.*, 37(3), 349–393 [online] Available from: <https://www.jstor.org/stable/2984782>, 1975.
- Marke, T., Crewell, S., Schemann, V., Schween, J. H. and Tuononen, M.: Long-term observations and high-resolution modeling of midlatitude nocturnal boundary layer processes connected to low-level jets, *J. Appl. Meteorol. Climatol.*, 57, 1155–1170, doi:10.1175/JAMC-D-17-0341.1, 2018.
- Markowicz, K. M., Chilinski, M. T., Lisok, J., Zawadzka, O., Stachlewska, I. S., Janicka, L., Rozwadowska, A., Makuch, P., Pakszys, P., Zielinski, T., Petelski, T., Posyniak, M., Pietruczuk, A., Szkop, A. and Westphal, D. L.: Study of aerosol optical properties during long-range transport of biomass burning from Canada to Central Europe in July 2013, *J. Aerosol Sci.*, 101, 156–173, doi:10.1016/j.jaerosci.2016.08.006, 2016.
- Martins, J. V., Artaxo, P., Liousse, C., Reid, J. S., Hobbs, P. V. and Kaufman, Y. J.: Effects of black carbon content, particle size, and mixing on light absorption by aerosols from biomass burning in Brazil, *J. Geophys. Res. Atmos.*, 103, 32041–3205, doi:10.1029/98JD02593, 1998.
- Mattis, I., D’Amico, G., Baars, H., Amodeo, A., Madonna, F. and

- Iarlori, M.: EARLINET Single Calculus Chain - Technical - Part 2: Calculation of optical products, *Atmos. Meas. Tech.*, 9(7), 3009–3029, doi:10.5194/amt-9-3009-2016, 2016.
- Mie, G.: Beiträge zur Optik trüber Medien, speziell kolloidaler Metallösungen, *Ann. Phys.*, 330(3), 337–445, doi:10.1002/andp.19083300302, 1908.
- Mishchenko, M., Hovenier, J. and Travis, L., Eds.: *Light Scattering by Nonspherical Particles*, Academic Press, San Diego., 2000.
- Mishchenko, M. I., Travis, L. D. and Mackowski, D. W.: T-matrix computations of light scattering by nonspherical particles: A review, *J. Quant. Spectrosc. Radiat. Transf.*, 55(5), 535–575, doi:10.1016/0022-4073(96)00002-7, 1996.
- Mishchenko, M. I., Travis, L. D., Kahn, R. A. and West, R. A.: Modeling phase functions for dustlike tropospheric aerosols using a shape mixture of randomly oriented polydisperse spheroids, *J. Geophys. Res. Atmos.*, 102, 16831–16847, doi:10.1029/96jd02110, 1997.
- Montávez, J. P., Rodríguez, A. and Jiménez, J. I.: A study of the Urban Heat Island of Granada, *Int. J. Climatol.*, doi:10.1002/1097-0088(20000630)20:8<899::AID-JOC433>3.0.CO;2-I, 2000.
- Mori, Y.: Evaluation of several “single-pass” estimators of the mean and the standard deviation of wind direction., *J. Clim. Appl. Meteorol.*, 25, 1387–1397, doi:10.1175/1520-0450(1986)025<1387:EOSPEO>2.0.CO;2, 1986.
- mpimet.mpg.de: Max-Planck-Institut für Meteorologie, Raman Lidar [online] Available from: mpimet.mpg.de (Accessed 17 June 2019), n.d.
- Müller, D., Wandinger, U. and Ansmann, A.: Microphysical particle parameters from extinction and backscatter lidar data by inversion with regularization: simulation., *Appl. Opt.*, 1999a.
- Müller, D., Wandinger, U. and Ansmann, A.: Microphysical particle parameters from extinction and backscatter lidar data by inversion with regularization: Theory, *Appl. Opt.*, 38, 2346–2357, 1999b.
- Müller, D., Wandinger, U., Althausen, D. and Fiebig, M.: Comprehensive particle characterization from three-wavelength Raman-lidar observations: case study, *Appl. Opt.*, 40, 4863–4869, doi:10.1364/ao.40.004863, 2001.

- Müller, D., Mattis, I., Wandinger, U., Ansmann, A., Althausen, D. and Stohl, A.: Raman lidar observations of aged Siberian and Canadian forest fire smoke in the free troposphere over Germany in 2003: Microphysical particle characterization, *J. Geophys. Res. D Atmos.*, 110(17), 75–90, doi:10.1029/2004JD005756, 2005.
- Müller, D., Ansmann, A., Mattis, I., Tesche, M., Wandinger, U., Althausen, D. and Pisani, G.: Aerosol-type-dependent lidar ratios observed with Raman lidar, *J. Geophys. Res. Atmos.*, 112, 2156–2202, doi:10.1029/2006JD008292, 2007a.
- Müller, D., Mattis, I., Ansmann, A., Wandinger, U., Ritter, C. and Kaiser, D.: Multiwavelength Raman lidar observations of particle growth during long-range transport of forest-fire smoke in the free troposphere, *Geophys. Res. Lett.*, 34(5), doi:10.1029/2006GL027936, 2007b.
- Müller, D., Böckmann, C., Kolgotin, A., Schneidenbach, L., Chemyakin, E., Rosemann, J., Znak, P. and Romanov, A.: Microphysical particle properties derived from inversion algorithms developed in the framework of EARLINET, *Atmos. Meas. Tech.*, 9(10), 5007–5035, doi:10.5194/amt-9-5007-2016, 2016.
- Myhre, G., Shindell, D., Bréon, F.-M., Collins, W., Fuglestedt, J., Huang, J., Koch, D., Lamarque, J.-F., Lee, D., Mendoza, B., Nakajima, T., Robock, A. and Stephens, G.: Anthropogenic and Natural Radiative Forcing, in *Climate Change 2013: The Physical Science Basis. Contribution of Working Group I to the Fifth Assessment Report of the Intergovernmental Panel on Climate Change*, edited by T. F. Stocker, D. Qin, G.-K. Plattner, M. Tignor, S. K. Allen, J. Boschung, A. Nauels, Y. Xia, V. Bex, and P. M. Midgley, Cambridge University Press, Cambridge, United Kingdom and New York, USA., 2013.
- Myhre, G., Aas, W., Cherian, R., Collins, W., Faluvegi, G., Flanner, M., Forster, P., Hodnebrog, Ø., Klimont, Z., Lund, M. T., Mülmenstädt, J., Lund Myhre, C., Olivié, D., Prather, M., Quaas, J., Samset, B. H., Schnell, J. L., Schulz, M., Shindell, D., Skeie, R. B., Takemura, T. and Tsyro, S.: Multi-model simulations of aerosol and ozone radiative forcing due to anthropogenic emission changes during the period 1990-2015, *Atmos. Chem. Phys.*, 17(4), 2709–2720, doi:10.5194/acp-17-2709-2017, 2017.
- Navas-Guzmán, F., Guerrero-Rascado, J. L. and Alados-Arboledas,

- L.: Retrieval of the lidar overlap function using Raman signals, *Óptica Pura y Apl.*, 44, 71–75, 2011.
- Navas-Guzmán, F., Müller, D., Bravo-Aranda, J. A., Guerrero-Rascado, J. L., Granados-Muñoz, M. J., Pérez-Ramírez, D., Olmo, F. J. and Alados-Arboledas, L.: Eruption of the Eyjafjallajökull Volcano in spring 2010: Multiwavelength Raman lidar measurements of sulphate particles in the lower troposphere, *J. Geophys. Res. Atmos.*, 118, 1–10, doi:10.1002/jgrd.50116, 2013a.
- Navas-Guzmán, F., Bravo-Aranda, J. A., Guerrero-Rascado, J. L., Granados-Muñoz, M. J. and Alados-Arboledas, L.: Statistical analysis of aerosol optical properties retrieved by Raman lidar over Southeastern Spain, *Tellus, Ser. B Chem. Phys. Meteorol.*, doi:10.3402/tellusb.v65i0.21234, 2013b.
- Newsom, R. K.: Doppler lidar handbook., 2012.
- Newsom, R. K., Alan Brewer, W., Wilczak, J. M., Wolfe, D. E., Oncley, S. P. and Lundquist, J. K.: Validating precision estimates in horizontal wind measurements from a Doppler lidar, *Atmos. Meas. Tech.*, 10, 1229–1240, doi:10.5194/amt-10-1229-2017, 2017.
- Nicolae, D., Nemuc, A., Müller, D., Talianu, C., Vasilescu, J., Belegante, L. and Kolgotin, A.: Characterization of fresh and aged biomass burning events using multiwavelength Raman lidar and mass spectrometry, *J. Geophys. Res. Atmos.*, 118(7), 2956–2965, doi:10.1002/jgrd.50324, 2013.
- Nicolae, D., Vasilescu, J., Talianu, C., Binietoglou, I., Nicolae, V., Andrei, S. and Antonescu, B.: A neural network aerosol-typing algorithm based on lidar data, *Atmos. Chem. Phys.*, 18, 14511–14537, doi:10.5194/acp-18-14511-2018, 2018.
- O'Connor, E. J., Illingworth, A. J., Brooks, I. M., Westbrook, C. D., Hogan, R. J., Davies, F. and Brooks, A. B. J.: A method for estimating the turbulent kinetic energy dissipation rate from a vertically pointing doppler lidar, and independent evaluation from balloon-borne in situ measurements, *J. Atmos. Ocean. Technol.*, 27, 1652–1664, doi:10.1175/2010JTECHA1455.1, 2010.
- Oke, T. R.: Boundary layer climates, Second Edi., Routledge, London., 1992.
- Olmo, F. J., Quirantes, A., Alcántara, A., Lyamani, H. and Alados-

- Arboledas, L.: Preliminary results of a non-spherical aerosol method for the retrieval of the atmospheric aerosol optical properties, *J. Quant. Spectrosc. Radiat. Transf.*, 100, 305–314, doi:10.1016/j.jqsrt.2005.11.047, 2006.
- Olmo, F. J., Quirantes, A., Lara, V., Lyamani, H. and Alados-Arboledas, L.: Aerosol optical properties assessed by an inversion method using the solar principal plane for non-spherical particles, *J. Quant. Spectrosc. Radiat. Transf.*, 109(8), 1504–1516, doi:10.1016/j.jqsrt.2007.12.019, 2008.
- Omar, A. H., Winker, D. M., Kittaka, C., Vaughan, M. A., Liu, Z., Hu, Y., Trepte, C. R., Rogers, R. R., Ferrare, R. A., Lee, K.-P., Kuehn, R. E. and Hostetler, C. A.: The CALIPSO automated aerosol classification and lidar ratio selection algorithm, *J. Atmos. Ocean. Technol.*, 26(10), 1994–2014, doi:10.1175/2009JTECHA1231.1, 2009.
- Ortiz-Amezcuca, P., Guerrero-Rascado, J. L., Granados-Muñoz, M. J., Bravo-Aranda, J. A. and Alados-Arboledas, L.: Characterization of atmospheric aerosols for a long range transport of biomass burning particles from canadian forest fires over the southern iberian peninsula in july 2013, *Opt. Pura y Apl.*, doi:10.7149/OPA.47.1.43, 2014.
- Ortiz-Amezcuca, P., Luis Guerrero-Rascado, J., Granados-Munõz, M. J., Benavent-Oltra, J. A., Böckmann, C., Samaras, S., Stachlewska, I. S., Janicka, L., Baars, H., Bohlmann, S. and Alados-Arboledas, L.: Microphysical characterization of long-range transported biomass burning particles from North America at three EARLINET stations, *Atmos. Chem. Phys.*, doi:10.5194/acp-17-5931-2017, 2017.
- Osborne, M., Malavelle, F. F., Adam, M., Buxmann, J., Sugier, J., Marengo, F. and Haywood, J.: Saharan dust and biomass burning aerosols during ex-hurricane Ophelia: Observations from the new UK lidar and sun-photometer network, *Atmos. Chem. Phys.*, 19(6), 3557–3578, doi:10.5194/acp-19-3557-2019, 2019.
- Osterloh, L.: Retrieving Aerosol Microphysical Properties from Multiwavelength Lidar Data, University of Potsdam (Germany)., 2011.
- Osterloh, L., Pérez, C., Böhme, D., Baldasano, J. M., Böckmann, C., Schneidenbach, L. and Vicente, D.: Parallel software for retrieval of aerosol distribution from LIDAR data in the

- framework of EARLINET-ASOS, *Comput. Phys. Commun.*, 180(11), 2095–2102, doi:10.1016/j.cpc.2009.06.011, 2009.
- Osterloh, L., Böckmann, C., Mamouri, R. E. and Papayannis, A.: An adaptive base point algorithm for the retrieval of aerosol microphysical properties, *Open Atmos. Sci. J.*, 5(1), 61–73, doi:10.2174/1874282301105010061, 2011.
- Osterloh, L., Böckmann, C., Nicolae, D. and Nemuc, A.: Regularized inversion of microphysical atmospheric particle parameters: Theory and application, *J. Comput. Phys.*, 237, 79–94, doi:10.1016/j.jcp.2012.11.040, 2013.
- Pappalardo, G., Amodeo, A., Pandolfi, M., Wandinger, U., Ansmann, A., Bösenberg, J., Matthias, V., Amiridis, V., De Tomasi, F., Frioud, M., Iarlori, M., Komguem, L., Papayannis, A., Rocadenbosch, F. and Wang, X.: Aerosol lidar intercomparison in the framework of the EARLINET project 3 Raman lidar algorithm for aerosol extinction, backscatter, and lidar ratio, *Appl. Opt.*, doi:10.1364/AO.43.005370, 2004.
- Pappalardo, G., Mona, L., D’Amico, G., Wandinger, U., Adam, M., Amodeo, A., Ansmann, A., Apituley, A., Alados Arboledas, L., Balis, D., Boselli, A., Bravo-Aranda, J. A., Chaikovsky, A., Comeron, A., Cuesta, J., De Tomasi, F., Freudenthaler, V., Gausa, M., Giannakaki, E., Giehl, H., Giunta, A., Grigorov, I., Groß, S., Haeffelin, M., Hiebsch, A., Iarlori, M., Lange, D., Linné, H., Madonna, F., Mattis, I., Mamouri, R. E., McAuliffe, M. A. P., Mitev, V., Molero, F., Navas-Guzman, F., Nicolae, D., Papayannis, A., Perrone, M. R., Pietras, C., Pietruczuk, A., Pisani, G., Preißler, J., Pujadas, M., Rizi, V., Ruth, A. A., Schmidt, J., Schnell, F., Seifert, P., Serikov, I., Sicard, M., Simeonov, V., Spinelli, N., Stebel, K., Tesche, M., Trickl, T., Wang, X., Wagner, F., Wiegner, M. and Wilson, K. M.: Four-dimensional distribution of the 2010 Eyjafjallajökull volcanic cloud over Europe observed by EARLINET, *Atmos. Chem. Phys.*, 13, 4429–4450, doi:10.5194/acp-13-4429-2013, 2013.
- Pappalardo, G., Amodeo, A., Apituley, A., Comeron, A., Freudenthaler, V., Linné, H., Ansmann, A., Bösenberg, J., D’Amico, G., Mattis, I., Mona, L., Wandinger, U., Amiridis, V., Alados-Arboledas, L., Nicolae, D. and Wiegner, M.: EARLINET: Towards an advanced sustainable European aerosol lidar network, *Atmos. Meas. Tech.*, doi:10.5194/amt-7-2389-2014, 2014.
- Pappalardo, G., Freudenthaler, V., Nicolae, D., Mona, L., Belegante,

- L. and D'Amico, G.: Lidar Calibration Centre, Eur. Phys. J. Conf., 119(9–10), 19003, 2016.
- Päschke, E., Leinweber, R. and Lehmann, V.: An assessment of the performance of a 1.5 μm Doppler lidar for operational vertical wind profiling based on a 1-year trial, Atmos. Meas. Tech., 8, 22151–2266, doi:10.5194/amt-8-2251-2015, 2015.
- Pearson, G., Davies, F. and Collier, C.: An analysis of the performance of the UFAM pulsed Doppler lidar for observing the boundary layer, J. Atmos. Ocean. Technol., doi:10.1175/2008JTECHA1128.1, 2009.
- Pereira, S. N., Preißler, J., Guerrero-Rascado, J. L., Silva, A. M. and Wagner, F.: Forest fire smoke layers observed in the free troposphere over Portugal with a multiwavelength Raman lidar: Optical and microphysical properties, Sci. World J., 2014, doi:10.1155/2014/421838, 2014.
- Pérez-Ramírez, D., Aceituno, J., Ruiz, B., Olmo, F. J. and Alados-Arboledas, L.: Development and calibration of a star photometer to measure the aerosol optical depth: Smoke observations at a high mountain site, Atmos. Environ., doi:10.1016/j.atmosenv.2007.06.009, 2008.
- Peterson, D., Hyer, E. and Wang, J.: Quantifying the potential for high-altitude smoke injection in the north american boreal forest using the standard MODIS fire products and subpixel-based methods, J. Geophys. Res., 119, 3401–3419, doi:10.1002/2013JD021067, 2014.
- Petzold, A., Rasp, K., Weinzierl, B., Esselborn, M., Hamburger, T., Dörnbrack, A., Kandler, K., Schütz, L., Knippertz, P., Fiebig, M. and Virkkula, A.: Saharan dust absorption and refractive index from aircraft-based observations during SAMUM 2006, Tellus, Ser. B Chem. Phys. Meteorol., doi:10.1111/j.1600-0889.2008.00383.x, 2009.
- Pinsky, M., Khain, A. and Krugliak, H.: Collisions of Cloud Droplets in a Turbulent Flow. Part V: Application of Detailed Tables of Turbulent Collision Rate Enhancement to Simulation of Droplet Spectra Evolution, J. Atmos. Sci., 65(di), 357–374, doi:10.1175/2007jas2358.1, 2008.
- Preißler, J., Wagner, F., Guerrero-Rascado, J. L. and Silva, A. M.: Two years of free-tropospheric aerosol layers observed over Portugal by lidar, J. Geophys. Res. Atmos., 118(9), 3676–3686, doi:10.1002/jgrd.503502013, 2013.

- Quijano, A. L., Sokolik, I. N. and Toon, O. B.: Radiative heating rates and direct radiative forcing by mineral dust in cloudy atmospheric conditions, *J. Geophys. Res. Atmos.*, 105, doi:10.1029/2000JD900047, 2000.
- Quirantes, A., Olmo, F. J., Lyamani, H., Valenzuela, A. and Alados-Arboledas, L.: Investigation of fine and coarse aerosol contributions to the total aerosol light scattering: Shape effects and concentration profiling by Raman lidar measurements, *J. Quant. Spectrosc. Radiat. Transf.*, 113, 2593–2600, doi:10.1016/j.jqsrt.2012.08.010, 2012.
- Reid, J. S., Koppmann, R., Eck, T. F. and Eleuterio, D. P.: A review of biomass burning emissions part II: intensive physical properties of biomass burning particles, *Atmos. Chem. Phys.*, 5(799–825), 2005a.
- Reid, J. S., Eck, T. F., Christopher, S. A., Koppmann, R., Dubovik, O., Eleuterio, D. P., Holben, B. N., Reid, E. A. and Zhang, J.: A review of biomass burning emissions part III: intensive optical properties of biomass burning particles, *Atmos. Chem. Phys.*, 5, 827–849, doi:10.5194/acp-5-827-2005, 2005b.
- Rimoldini, L.: Weighted skewness and kurtosis unbiased by sample size and Gaussian uncertainties, *Astron. Comput.*, 5, 1–8, doi:10.1016/j.ascom.2014.02.001, 2014.
- Ritter, C., Angeles Burgos, M., Böckmann, C., Mateos, D., Lisok, J., Markowicz, K. M., Moroni, B., Cappelletti, D., Udusti, R., Maturilli, M. and Neuber, R.: Microphysical properties and radiative impact of an intense biomass burning aerosol event measured over Ny-Ålesund, Spitsbergen in July 2015, *Tellus, Ser. B Chem. Phys. Meteorol.*, 70(1), 1–23, doi:10.1080/16000889.2018.1539618, 2018.
- Rodgers, C. D.: *Inverse Methods for Atmospheric Sounding - Theory and Practice*, edited by F. W. Taylor, World Scientific., 2000.
- Rodríguez, S., Alastuey, A., Alonso-Pérez, S., Querol, X., Cuevas, E., Abreu-Afonso, J., Viana, M., Pérez, N., Pandolfi, M. and De La Rosa, J.: Transport of desert dust mixed with North African industrial pollutants in the subtropical Saharan Air Layer, *Atmos. Chem. Phys.*, 11, 6663–6685, doi:10.5194/acp-11-6663-2011, 2011.
- Rolph, G. D.: Real-time environmental applications and display system (READY), [online] Available from: <http://www.ready.noaa.gov> (Accessed 31 January 2017),

2016.

- Román, R., Benavent-Oltra, J. A., Casquero-Vera, J. A., Lopatin, A., Cazorla, A., Lyamani, H., Denjean, C., Fuertes, D., Pérez-Ramírez, D., Torres, B., Toledano, C., Dubovik, O., Cachorro, V. E., de Frutos, A. M., Olmo, F. J. and Alados-Arboledas, L.: Retrieval of aerosol profiles combining sunphotometer and ceilometer measurements in GRASP code, *Atmos. Res.*, doi:10.1016/j.atmosres.2018.01.021, 2018.
- Rother, T. and Kahnert, M.: *Electromagnetic Wave Scattering on Nonspherical Particles*, 2nd Editio., Springer., 2014.
- Rye and Hardesty, R. M.: Discrete Spectral Peak Estimation in Incoherent Backscatter Heterodyne Lidar. I: Spectral Accumulation and the Cramer-Rao Lower Bound, *IEEE Trans. Geosci. Remote Sens.*, doi:10.1109/36.210440, 1993a.
- Rye, B. J. and Hardesty, R. M.: Discrete Spectral Peak Estimation in Incoherent Backscatter Heterodyne Lidar. II: Correlogram Accumulation, *IEEE Trans. Geosci. Remote Sens.*, doi:10.1109/36.210441, 1993b.
- Rye, B. J. and Hardesty, R. M.: Estimate optimization parameters for incoherent backscatter heterodyne lidar, *Appl. Opt.*, 36(36), 9425–9436, 1997.
- Samaras, S.: Microphysical retrieval of non-spherical aerosol particles using regularized inversion of multi-wavelength lidar data, University of Potsdam (Germany)., 2017.
- Samaras, S., Nicolae, D., Böckmann, C., Vasilescu, J., Biniotoglou, I., Labzovskii, L., Toanca, F. and Papayannis, A.: Using Raman-lidar-based regularized microphysical retrievals and Aerosol Mass Spectrometer measurements for the characterization of biomass burning aerosols, *J. Comput. Phys.*, 299, 156–174, doi:10.1016/j.jcp.2015.06.045, 2015.
- Samaras, S., Böckmann, C. and Nicolae, D.: Combined sphere-spheroid particle model for the retrieval of the microphysical aerosol parameters via regularized inversion of lidar data, *EPJ Web Conf.*, 119 [online] Available from: <https://doi.org/10.1051/epjconf/201611923022>, 2016.
- Schladitz, A., Müller, T., Kaaden, N., Massling, A., Kandler, K., Ebert, M., Weinbruch, S., Deutscher, C. and Wiedensohler, A.: In situ measurements of optical properties at Tinfou (Morocco) during the Saharan Mineral Dust Experiment SAMUM 2006, *Tellus B*

- Chem. Phys. Meteorol., 61(1), 64–78, doi:10.1111/j.1600-0889.2008.00397.x, 2009.
- Seinfeld, J. H. and Pandis, S. N.: Atmospheric Chemistry and Physics, Wiley Interscience., 1998.
- Shifrin, K. S.: Analytical Inverse Methods for Aerosol Retrieval, in Exploring the Atmosphere by Remote Sensing Techniques, edited by R. Guzzi, Springer., 2003.
- Sicard, M., Comerón, A., Fernández, A., Bedoya-Velásquez, A. E., Rodríguez-Gómez, A., Artiñano, B., Muñoz-Porcar, C., Bortoli, D., Rocadenbosch, F., Molero, F., Martínez-Lozano, J. A., Benavent-Oltra, J. A., Gómez-Amo, J. L., Guerrero-Rascado, J. L., Alados-Arboledas, L., Pujadas, M., Costa, M. J., Granados-Muñoz, M. J., Potes, M., Ortiz-Amezcuca, P., Salvador, P., Utrillas, P., Barragán, R., Román, R., Salgado, R., Basart, S. and Salgueiro, V.: Extreme, wintertime Saharan dust outbreak intrusion in the Iberian Peninsula: lidar monitoring and evaluation of dust forecast models during the February 2017 event, Atmos. Res., 2019a.
- Sicard, M., Granados-Muñoz, M. J., Alados-Arboledas, L., Barragán, R., Bedoya-Velásquez, A. E., Benavent-Oltra, J. A., Bortoli, D., Comerón, A., Córdoba-Jabonero, C., Costa, M. J., del Águila, A., Fernández, A. J., Guerrero-Rascado, J. L., Jorba, O., Molero, F., Muñoz-Porcar, C., Ortiz-Amezcuca, P., Papagiannopoulos, N., Potes, M., Pujadas, M., Rocadenbosch, F., Rodríguez-Gómez, A., Román, R., Salgado, R., Salgueiro, V., Sola, Y. and Yela, M.: Ground/space, passive/active remote sensing observations coupled with particle dispersion modelling to understand the inter-continental transport of wildfire smoke plumes, Remote Sens. Environ., 232, 111294, doi:10.1016/J.RSE.2019.111294, 2019b.
- Soupiona, O., Samaras, S., Ortiz-Amezcuca, P., Böckmann, C., Papayannis, A., de Arruda Moreira, G., Benavent-Oltra, J. A., Guerrero-Rascado, J. L., Bedoya-Velásquez, A. E., Olmo-Reyes, F. J., Román, R., Kokkalis, P., Mylonaki, M., Alados-Arboledas, L., Papanikolaou, C. A. and Foskinis, R.: Retrieval of optical and microphysical properties of transported Saharan dust over Athens and Granada based on multi-wavelength Raman Lidar measurements: study of the mixing processes, Atmos. Environ., in review, 2019.
- Stein, A. F., Draxler, R. R., Rolph, G. D., Stunder, B. J. B., Cohen, M. D. and Ngan, F.: NOAA's hysplit atmospheric transport and

- dispersion modeling system, *Bull. Am. Meteorol. Soc.*, 96(12), 2059–2077, doi:10.1175/BAMS-D-14-00110.1, 2015.
- Stull, R. B.: *An Introduction to Boundary Layer Meteorology*, Springer, New York., 1988.
- Tesche, M., Gross, S., Ansmann, A., Müller, D., Althausen, D., Freudenthaler, V. and Esselborn, M.: Profiling of Saharan dust and biomass-burning smoke with multiwavelength polarization Raman lidar at Cape Verde, *Tellus, Ser. B Chem. Phys. Meteorol.*, doi:10.1111/j.1600-0889.2011.00548.x, 2011.
- Titos, G., Jefferson, A., Sheridan, P. J., Andrews, E., Lyamani, H., Alados-Arboledas, L. and Ogren, J. A.: Aerosol light-scattering enhancement due to water uptake during the TCAP campaign, *Atmos. Chem. Phys.*, 14, 7031–7043, doi:10.5194/acp-14-7031-2014, 2014a.
- Titos, G., Lyamani, H., Pandolfi, M., Alastuey, A. and Alados-Arboledas, L.: Identification of fine (PM₁) and coarse (PM₁₀₋₁) sources of particulate matter in an urban environment, *Atmos. Environ.*, doi:10.1016/j.atmosenv.2014.03.001, 2014b.
- Titos, G., Lyamani, H., Cazorla, A., Sorribas, M., Foyo-Moreno, I., Wiedensohler, A. and Alados-Arboledas, L.: Study of the relative humidity dependence of aerosol light-scattering in southern Spain, *Tellus, Ser. B Chem. Phys. Meteorol.*, 66, 24536, doi:10.3402/tellusb.v66.24536, 2014c.
- Titos, G., Cazorla, A., Zieger, P., Andrews, E., Lyamani, H., Granados-Muñoz, M. J., Olmo, F. J. and Alados-Arboledas, L.: Effect of hygroscopic growth on the aerosol light-scattering coefficient: A review of measurements, techniques and error sources, *Atmos. Environ.*, 141, 494–507, doi:10.1016/j.atmosenv.2016.07.021, 2016.
- Titos, G., del Águila, A., Cazorla, A., Lyamani, H., Casquero-Vera, J. A., Colombi, C., Cuccia, E., Gianelle, V., Močnik, G., Alastuey, A., Olmo, F. J. and Alados-Arboledas, L.: Spatial and temporal variability of carbonaceous aerosols: Assessing the impact of biomass burning in the urban environment, *Sci. Total Environ.*, doi:10.1016/j.scitotenv.2016.11.007, 2017.
- Trefethen, L. N. and Bau, D.: *Numerical Linear Algebra*, SIAM., 1997.
- Tuononen, M., O'Connor, E. J., Sinclair, V. A. and Vakkari, V.: Low-level jets over Utö, Finland, based on Doppler lidar

- observations, *J. Appl. Meteorol. Climatol.*, 56(9), 2577–2594, doi:10.1175/JAMC-D-16-0411.1, 2017.
- Turner, D. B.: Comparison of three methods for calculating the standard deviation of the wind direction., *J. Clim. Appl. Meteorol.*, 25, 703–707, 1986.
- US-EPA (United States Environmental Protection Agency): *Meteorological Monitoring Guidance for Regulatory Modeling Applications.*, 2000.
- Vakkari, V., O'Connor, E. J., Nisantzi, A., Mamouri, R. E. and Hadjimitsis, D. G.: Low-level mixing height detection in coastal locations with a scanning Doppler lidar, *Atmos. Meas. Tech.*, 8, 1875–1885, doi:10.5194/amt-8-1875-2015, 2015.
- Vakkari, V., Manninen, A. J., O'Connor, E. J., Schween, J. H., Van Zyl, P. G. and Marinou, E.: A novel post-processing algorithm for Halo Doppler lidars, *Atmos. Meas. Tech.*, doi:10.5194/amt-12-839-2019, 2019.
- Valenzuela, A., Olmo, F. J., Lyamani, H., Antón, M., Quirantes, A. and Alados-Arboledas, L.: Classification of aerosol radiative properties during African desert dust intrusions over southeastern Spain by sector origins and cluster analysis, *J. Geophys. Res. Atmos.*, 117, D06214, doi:10.1029/2011JD016885, 2012.
- Vaughan, G., Wareing, D. P., Pepler, S. J., Thomas, L. and Mitev, V.: Atmospheric temperature measurements made by rotational Raman scattering, *Appl. Opt.*, doi:10.1364/ao.32.002758, 1993.
- Vaughan, G., Draude, A. P., Ricketts, H. M. A., Schultz, D. M., Adam, M., Sugier, J. and Wareing, D. P.: Transport of Canadian forest fire smoke over the UK as observed by lidar, *Atmos. Chem. Phys.*, 18(15), 11375–11388, doi:10.5194/acp-18-11375-2018, 2018.
- Veselovskii, I., Kolgotin, A., Griaznov, V., Müller, D., Wandinger, U. and Whiteman, D. N.: Inversion with regularization for the retrieval of tropospheric aerosol parameters from multiwavelength lidar sounding, *Appl. Opt.*, 41(18), 3685–3699, doi:10.1364/AO.41.003685, 2002.
- Veselovskii, I., Kolgotin, A., Griaznov, V., Müller, D., Franke, K. and Whiteman, D. N.: Inversion of multiwavelength Raman lidar data for retrieval of bimodal aerosol size distribution, *Appl.*

Opt., doi:10.1364/ao.43.001180, 2004.

- Veselovskii, I., Dubovik, O., Kolgotin, A., Lapyonok, T., Di Girolamo, P., Summa, D., Whiteman, D. N., Mishchenko, M. and Tanré, D.: Application of randomly oriented spheroids for retrieval of dust particle parameters from multiwavelength lidar measurements, *J. Geophys. Res. Atmos.*, 115(D21), doi:10.1029/2010JD014139, 2010.
- Veselovskii, I., N Whiteman, D., Korenskiy, M., Suvorina, A., Kolgotin, A., Lyapustin, A., Wang, Y., Chin, M., Bian, H., Kucsera, T. L., Pérez-Ramírez, D. and Holben, B.: Characterization of forest fire smoke event near Washington, DC in summer 2013 with multi-wavelength lidar, *Atmos. Chem. Phys.*, 15, 1647–1660, doi:10.5194/acp-15-1647-2015, 2015a.
- Veselovskii, I., Whiteman, D. N., Korenskiy, M., Suvorina, A. and Perez-Ramirez, D.: Use of rotational Raman measurements in multiwavelength aerosol lidar for evaluation of particle backscattering and extinction, *Atmos. Meas. Tech.*, doi:10.5194/amt-8-4111-2015, 2015b.
- Viedma Muñoz, M.: Análisis de los direcciones de los vientos en Andalucía, *Nimbus*, 1, 153–168, 1998.
- Wagner, R., Ajtai, T., Kandler, K., Lieke, K., Linke, C., Müller, T., Schnaiter, M. and Vragel, M.: Complex refractive indices of Saharan dust samples at visible and near UV wavelengths: A laboratory study, *Atmos. Chem. Phys.*, 12, 2491–2512, doi:10.5194/acp-12-2491-2012, 2012.
- Wandinger, U. and Ansmann, A.: Experimental determination of the lidar overlap profile with Raman lidar, *Appl. Opt.*, doi:10.1364/AO.41.000511, 2002.
- Wandinger, U., Müller, D., Böckmann, C., Althausen, D., Matthias, V., Bösenberg, J., Weiß, V., Fiebig, M., Wendisch, M., Stohl, A. and Ansmann, A.: Optical and microphysical characterization of biomass-burning and industrial-pollution aerosols from multiwavelength lidar and aircraft measurements, *J. Geophys. Res. Atmos.*, 107(21), doi:10.1029/2000JD000202, 2002.
- Wang, Y.: An efficient gradient method for maximum entropy regularizing retrieval of atmospheric aerosol particle size distribution function, *J. Aerosol Sci.*, 39(4), 305–322, doi:10.1016/j.jaerosci.2007.11.008, 2008.
- Wang, Y., Fan, S. and Feng, X.: Retrieval of the aerosol particle size

- distribution function by incorporating a priori information, *J. Aerosol Sci.*, 38(8), 885–901, doi:10.1016/j.jaerosci.2007.06.005, 2007.
- Waterman, P. C.: Matrix Formulation of Electromagnetic Scattering, *Proc. IEEE*, 53(8), 805–812, doi:10.1109/PROC.1965.4058, 1965.
- Wehner, B., Siebert, H., Ansmann, A., Ditas, F., Seifert, P., Stratmann, F., Wiedensohler, A., Apituley, A., Shaw, R. A., Manninen, H. E. and Kulmala, M.: Observations of turbulence-induced new particle formation in the residual layer, *Atmos. Chem. Phys.*, 10, 4319–4330, doi:10.5194/acp-10-4319-2010, 2010.
- Weinzierl, B., Sauer, D., Esselborn, M., Petzold, A., Veira, A., Rose, M., Mund, S., Wirth, M., Ansmann, A., Tesche, M., Gross, S. and Freudenthaler, V.: Microphysical and optical properties of dust and tropical biomass burning aerosol layers in the Cape Verde region-an overview of the airborne in situ and lidar measurements during SAMUM-2, *Tellus, Ser. B Chem. Phys. Meteorol.*, doi:10.1111/j.1600-0889.2011.00566.x, 2011.
- Werner, C.: Doppler Wind Lidar, in *Lidar: range-resolved optical remote sensing of the atmosphere*, edited by C. Weitkamp, pp. 325–353, Springer, New York., 2005.
- Westbrook, C. D., Illingworth, A. J., O'Connor, E. J. and Hogan, R. J.: Doppler lidar measurements of oriented planar ice crystals falling from supercooled and glaciated layer clouds, *Q. J. R. Meteorol. Soc.*, 136, 260–276, doi:10.1002/qj.528, 2010.
- Whitby, K. and Cantrell, B.: Fine particles, in *International Conference on Environmental Sensing and Assessment*, Institute of Electrical and Electronic Engineers (IEEE), Las Vegas, NV., 1976.
- Whiteman, D. N.: Examination of the traditional Raman lidar technique I Evaluating the temperature-dependent lidar equations, *Appl. Opt.*, doi:10.1364/AO.42.002571, 2003a.
- Whiteman, D. N.: Examination of the traditional Raman lidar technique II Evaluating the ratios for water vapor and aerosols, *Appl. Opt.*, doi:10.1364/ao.42.002593, 2003b.
- Winker, D. M., Vaughan, M. A., Omar, A., Hu, Y., Powell, K. A., Liu, Z., Hunt, W. H. and Young, S. A.: Overview of the CALIPSO mission and CALIOP data processing algorithms, *J. Atmos.*

Ocean. Technol., 26(11), 2310–2323,
doi:10.1175/2009JTECHA1281.1, 2009.

World-Meteorological-Organization: Statement of Guidance for High Resolution Numerical Weather Prediction (NWP). Technical Report., 2018.

Wu, D., Wang, Z., Wechsler, P., Mahon, N., Deng, M., Glover, B., Burkhart, M., Kuestner, W. and Heesen, B.: Airborne compact rotational Raman lidar for temperature measurement, *Opt. Express*, doi:10.1364/oe.24.0a1210, 2016.

Yamartino, R. J.: A comparison of several 'single-pass' estimators of the standard deviation of wind direction., *J. Clim. Appl. Meteorol.*, 23, 1362–1366, doi:10.1175/1520-0450(1984)023<1362:ACOSPE>2.0.CO;2, 1984.

Zeyn, J., Lahmann, W. and Weitkamp, C.: Remote daytime measurements of tropospheric temperature profiles with a rotational Raman lidar, *Opt. Lett.*, 21(16), 1301, doi:10.1364/ol.21.001301, 2008.

SHORT CV OF THE AUTHOR

BACKGROUND

University of Granada:

BSc in Physics (2014)

MSc in Geophysics and Meteorology
(2015)

SCIENTIFIC IDs

Scopus Author ID: 56071053100

ORCID: 0000-0001-7842-2260

Researcher ID: L-6857-2017

Personal web: portizamezcua.com

SCIENTIFIC IMPACT (Scopus)

Nr. of citations: 61 Nr. of papers: 11

h-index: 5 i10-index: 3

PUBLICATIONS

SICARD, M. et al. Remote Sens. Environ.
2019

SOUPIONA, O. et al. Atmos. Environ. 2019

DE ARRUDA MOREIRA, G. et al. Atmos.
Chem. Phys. 2019

QUIRANTES, A. et al. Atmos. Res. 2019

FERNÁNDEZ, A.J. et al. Atmos. Res. 2019

BEDOYA-VELÁSQUEZ, A.E. et al. Atmos.
Res. 2019

DE ARRUDA MOREIRA, G. et al. Atmos. Res.
2018

BEDOYA-VELÁSQUEZ, A.E. et al. Atmos.
Chem. Phys. 2018

BENAVENT-OLTRA, J.A. et al. Atmos. Meas.
Tech. 2017

ORTIZ-AMEZCUA, P. et al. Atmos. Chem.
Phys. 2017

ORTIZ-AMEZCUA, P. et al. Óptica Pura y
Aplicada. 2014

TEACHING

Degree in Environmental Sciences,
University of Granada:

Energy Management and Renewables
(2016-17, 2018-19)

Physics (2017-18)

Degree in Physics, University of
Granada:

Mechanics and Waves (2018-19)

